University of Southampton

Faculty of Engineering and Physical Sciences

School of Chemistry

High-Throughput Discovery of Anode Catalysts for Direct Sodium Borohydride Fuel Cells

Abdulrahman Faraj Alharbi

Thesis for Degree of Doctor of Philosophy

July 2019

University of Southampton

Abstract

Faculty of Engineering and Physical Sciences

SCHOOL OF CHEMISTRY

THESIS FOR DEGREE OF PHILOSOPHY

High-Throughput Discovery of Anode Catalysts for Direct Sodium Borohydride Fuel Cells

by

Abdulrahman Faraj Alharbi

Combinatorial synthesis and high-throughput characterization and electrochemical screening methods have been used to accelerate the design and optimization of binary alloy catalysts for the anode of the Direct Borohydride Fuel Cell. Single metal catalysts are shown to have limited effectiveness, in agreement with previous literature. In principle, the direct oxidation of the BH_4^- ion is accompanied by the transfer of eight electrons. Competing electrochemical oxidation reactions[1-3], and the spontaneous catalytic hydrolysis of BH_4^- hinder the exploitation of the eight electron reaction. The order of the catalytic activity for the direct oxidation of the BH_4^- ion in alkali environment on pure metals as reflected in the onset potential *vs.* SHE for the reaction was found to be Au (-0.43 V_{SHE}) > Ag (-0.21 V_{SHE}) > Pt (0.04 V_{SHE}) > Ni (+0.62 V_{SHE}) > Cu (+0.7 V_{SHE}). Pt hydrolysed BH_4^- producing H_2 which was electro-oxidised at -0.7 V_{SHE}, competing with direct BH_4^- oxidation. The catalytic activity of the Ni and Cu towards the direct BH_4^- oxidation reaction (BOR) was found to be sharply affected by the passivation layer formed by the adsorption of O_2/OH.

The intent was to modify the catalytic properties of the pure metals by alloying through both electronic and ensemble effects, lowering the overpotential for the eight-electron process and reducing the parasitic effects of competing catalytic pathways, and hindering O_2/OH adsorption.

A wide gradient of compositions of Au-Ni, Au-Cu, and Au-Pt alloy catalysts (unannealed and annealed) were synthesized by High Throughput Physical Vapor Deposition (HT-PVD). High Throughput bulk/surface methods including Energy Dispersive X-ray Spectroscopy (EDX), X-ray Diffraction (XRD) and X-ray Photon Spectroscopy (XPS) were used to characterise the alloy catalysts as a function of composition. To efficiently determine the best alloy catalysts for the direct BOR, High Throughput

Electrochemical Screening method was used. Additionally, a High Throughput Hydrogen Probe method was developed to monitor H_2 evolution on the Au-Pt alloy catalysts. This method was found to be effective in determining the lowest/highest H_2 evolution as a function of composition. New anode alloy catalysts were discovered and can catalyse the BOR at low over potential. The optimum Au-Ni alloy composition was found to be at composition Ni_{35}-Au_{65} offering a higher electrode activity for the direct BOR among other binary alloy catalysts. The Au-Cu alloy catalysts were found to be affected by the addition of Cu on the Au-Cu alloy catalysts. The activity of the $Cu_{78.3}$-$Au_{21.7}$ (unannealed) was found to be higher than pure Au. In order to evaluate the electrocatalytic activity on the Au-Pt alloy catalysts, the H_2 evolution was successfully detected as a function of composition using High Throughput Hydrogen Probe. This experimental approach proved that the BOR on the Au-Pt alloy catalysts was strongly influenced by the competing H_2 oxidation reaction produced by the spontaneous catalytic hydrolysis reaction.

Table of Contents

LIST OF FIGURES

List of Tables

Declaration of Authorship

Abdulrahman Faraj Alharbi

High-Throughput Discovery of Anode Catalysts for Direct Sodium Borohydride Fuel Cells

I declare that this thesis and the work presented in it are my own and has been generated by me as the result of my own original research.

I confirm that:

This work was done wholly or mainly while in candidature for a research degree at this University;

Where any part of this thesis has previously been submitted for a degree or any other qualification at this University or any other institution, this has been clearly stated;

Where I have consulted the published work of others, this is always clearly attributed;

Where I have quoted from the work of others, the source is always given. With the exception of such quotations, this thesis is entirely my own work;

I have acknowledged all main sources of help;

Where the thesis is based on work done by myself jointly with others, I have made clear exactly what was done by others and what I have contributed myself;

None of this work has been published before submission

Signature: Date: July,2019

Acknowledgement

First and foremost, I would like to thank my supervisor Professor Brian Hayden for his support, kind guidance, encouragement and scientific discussions given me the confidence required to complete this project.

I would also like to thank Dr Guy Denuault for his discussions and guidelines led me to develop the High Throughput Hydrogen Probe Technique.

I express my deepest gratitude to the group of Advanced Composite Materials Facilities for their help, insightful criticism, patience and support during the period of this project. I extent my thanks to Dr Jin Yao for interesting conversation about the High Throughput characterization methods and the High Throughput Synthesis.

I would also like to thank the mechanical workshop and glassblowers who have been very helpful on many ways to design the hydrogen probe.

I would like also to thank the Government of Saudi Arabia for their financial support.

Heartfelt thanks go to my parents for their love, encouragement and unlimited support.

Thanks also goes to my uncle Abullah for his help and support.

Finally, but far from least, is my wife, her tireless efforts and patience made the completion of this thesis possible.

Definitions and Abbreviations

AFM	Atomic Force Microscopy
BOR	BOR reaction
B_E	Binding energy
CA	Chronoamperometry
CAE	Constant analyser energy
CE	Chemical-electrochemical
CV	Cyclic voltammetry
DBFCs	Direct borohydride fuel cells
DMFCs	Direct methanol fuel cells
E_k	Kinetic energy
e-beam	Electron beam
ECE	Electrochemical-chemic-electrochemical
EDX	Energy Dispersive X-ray Spectroscopy
EOR	Ethanol oxidation reaction
E°	Equilibrium potential
F_A	Relative sensitivity factor
Fcc	Face centred cubic
Fct	Face centred tetragonal
GADDS	General area detector diffraction system
HER	Hydrogen evolution reaction
HT-ECS	High Throughput Electrochemical Screening
HT-PVD	High Throughput Physical Vapour Deposition
I_A	Peak area

K-cells	Knudsen-cells
MBE	Molecular beam epitaxy
PEMFCs	Polymer electrolyte fuel cells
OER	Oxygen evolution reaction
ORR	Oxygen reduction reaction
SECM	Scanning electrochemical microscopy
SEM	Scanning electron microscope
SCE	Saturated calomel reference electrode
SHE	Standard hydrogen electrode
SIMS	Secondary-ion mass spectrometry
UHV	Ultra-High Vacuum
UME	Ultra-micro-electrode
XRD	X-ray Diffraction
XPS	X-ray Photoelectron Spectroscopy
hv	Photoelectron energy
ΔG_{OH}	Free energy of adsorption of OH_{ads}
ΔG_{H}	Free energy of adsorption of H_{ads}

Chapter 1 Introduction

For many decades, there has been a global dependence and reliance on oil, in all its forms, as a source of energy, whilst simultaneously ignoring the environmental damage it causes. According to many experts, sources of oil may become depleted[4], and consequently, alternative sources of energy or "renewable energies" will be needed. Many researchers and scientists are currently investigating renewable energy, with their focus on creating clean energies that are sustainable and ideally derived from renewable sources. This should help break the dependence on fossil fuel exploitation, mitigate extensively detrimental climate change and achieve resource efficiency. This is being done in the expectation of regaining some of what has been lost, namely a climate free of pollution and a clean marine environment. To this end, researchers and scientists are heavily focused on fuel cells, which are regarded as a renewable and clean energy source that can be used not only to supply energy but also to dispense with oil and its hazardous waste, which have become life threatening for many in this world[5]. As a result, many scientists and researchers are working on the development of effective catalysts to increase the efficiency and performance of fuel cells, in order to meet the requirements of the consumers of clean energy, both at the individual and industrial levels.

1.1 Catalysis

Catalysis is the process by which a change in the rate of a chemical reaction occurs by introducing a catalyst that lowers the activation barrier and provides an alternative pathway without being consumed in the process. The path of a chemical reaction consists of three important phases: reactants, transition state (extremely unstable state) and products. In the catalysed reaction, the catalyst forms a complex with the reactant, which allows its activation barrier to be lower than that of the transition state of the uncatalysed reaction[6].

Catalysis can be classified as homogenous or heterogeneous catalysis based on the physical state of the existing substances. Homogenous catalysis is the process where a reactant and the involved catalyst exist in the same phases, as in the case of reactions between gases (the oxidation of sulphur dioxide by oxygen using nitrogen oxides as a catalyst), reactions between liquids (reaction between acids and bases), enzymatic processes and co-ordination complexes (polyester condensations)[7]. Heterogeneous catalysis is the process where both materials have different phases as in the case of electro-catalysis where electron transfer reactions occur between reactants (liquid phase) and a metal surface (solid phase). A heterogeneous catalytic reaction depends on critical steps that must occur while the reactants and products transfer to and from the catalyst surface (on which the reaction effectively takes place). This includes (1) mass

transport of reactants from the bulk of the solution phase to the interface of the catalyst, (2) diffusion of the reactants to the active sites, (3) adsorption of reactants on the active sites, (4) a catalytic reaction of the adsorbed species to take place at the active sites, (5) desorption of products from the active sites, and (6) mass transport of products into the bulk of the solution phase[8].

Much effort has been made in conducting a variety of research studies to design the ideal catalysts. Modern catalysis involves three important aspects, which are catalysts synthesis, catalyst characterisation and catalytic kinetics[8]. The synthesis of the catalyst has a dramatic effect on the activity, selectivity and stability of varieties of catalyst materials for certain reactions. For example, the synthesis of bimetallic catalysts offers unique catalytic properties[9]. Alloying alters the structure and composition of a catalyst and thus changes its properties. The selectivity and the reactivity of an alloy's catalyst are the main parameters that govern the performance of the catalyst. They are frequently regarded as ensemble effects and ligand effects[9]. The ensemble effects occur when active sites are blocked by incorporating a secondary metal. Some chemical reactions need an ensemble of a small number of adjacent active sites to take place, and therefore the selectivity towards these chemical reactions can be modified accordingly[9-10].

The effect of introducing an additional metal to change the catalytic properties by direct electronic interaction between components of the alloy is usually referred to as ligand effects. This type of electronic modification affects the surface local density of states and the d-band energies shift[11]. Norskov et. al extensively studied the role of the so-called d-band (centre) model[12], which simply describes the trends of catalytic activity based on the interaction of adsorbate energy levels with the d-band of a transition metal surface. Due to this interaction, bonding and antibonding states are created which, in turn, affect the potential barrier for adsorption and the adsorption energy. The strength of the adsorption energy can be predicted based on the d-band centre shift with respect to the position of the Fermi level. An upward shift of the d-band centre indicates high activity while a downward shift indicates a less active metal. Therefore, Norskov et. al proposed a Volcano plot on various metals, which shows the most efficient catalysts for hydrogen adsorption by measuring the exchange current density of the hydrogen evolution reaction[13].

The d-band model can be applied to alloy materials. Modification of the structure and composition of the alloy surface affects the d-band centre shifts that could change the strength of the bond between the surface of the metal catalyst and the adsorbate (reactants). As a result, intermediate properties between those of pure metals or even unique bimetallic properties can potentially be made[9]. Au-Pd is an interesting example of the electronic/ ensemble effects, and Au can be used as a modifier to improve the catalytic performance. H_2 adsorption as well as CO

adsorption on the Au-Pd catalysts have been studied in more detail using combinatorial high throughput synthesis and screening[14]. It has been found that annealing the Au-Pd alloy results in an Au-enriched surface that increases the catalytic activity for the CO and reduces the selectivity towards the H_2 adsorption as a function of composition. This study clearly showed that the design of ideal catalysts largely depends on the method of catalyst preparation.

1.2 Low Temperature Fuel Cells

Fuel cells, which convert the chemical energy stored in a fuel into electrical energy, are promising candidates for future energy use characterised by their high converted efficiency and low emissions at low operating temperature. Efficiency as high as 60% can be extracted from the fuel without the need for the combustion process[15-16]. Unlike battery technology, fuel cells do not require recharging. Energy is produced on demand as long as the fuel cells are supplied with fuel (e.g., hydrogen) and oxidant (air or oxygen). Naturally, the electrical energy cannot be produced without the existence of electro-catalytic electrodes that work as anodes and cathodes and are separated by an ion conducting electrolyte. The anode is the negative electrode at which H_2 is oxidised, producing protons and electrons. The released electrons are conducted to the anode through an external circuit providing current. The cathode is the positive electrode where O_2 molecules are reduced and combined with the produced electrons and protons to form water[16].

Many scientists have been working on the development of fuel cells using different types of low temperature fuel cells since they were discovered by Sir William Robert Grove[17]. Sir Grove used water to produce electrical energy. Water was electrolysed into hydrogen and oxygen by an electric current releasing electrical energy. Fuel cells can be classified by their main internal parts. This includes the individual type of each fuel, the oxidant, the electrolyte or the operating temperature. One of the most investigated types is the polymer electrolyte fuel cell (PEFC)[18]. PEFCs are composed of a proton exchange membrane (Nafion) and electrode materials as catalysts (Pt). The distinctive feature of this type of fuel cell is that it operates at low temperatures between 80 and 100 °C. However, issues related to one of the cell components exist, namely anode poisoning, results in a reduction of the cell performance[19]. The anode is poisoned at below 150 °C[20] because of the carbon monoxide (CO) that is present in the fuel. The CO is adsorbed on the electrode surface blocking active sites. Efforts have been made to prevent this issue by using a reformer to produce pure H_2[21] or by using hydrogen storage materials[22]. However, this will require more efficient systems to be applied to the small portable electronic devices, which is a complication, since most of the reforming systems and hydrogen storage materials are still under development[23].

Direct methanol fuel cells (DMFCs) are classified as a low operating temperature fuel cell. The positive side to this is that methanol is easily stored and requires no fuel processing compared to the H_2 in the PEFCs[24]. Moreover, methanol is widely available since it can be extracted from different sources such as oil, natural gas and coal. However, further investigation is needed in order to develop the DMFCs system. Although using liquid methanol directly as fuel helps to overcome processing, CO (a reaction intermediate) can be formed during the oxidation reaction of the methanol. The CO can be adsorbed on the surface (Pt) resulting in catalyst poisoning, and this consequently reduces the catalyst performance to complete the full methanol oxidation process. Therefore, an appropriate low-cost catalyst is still required to remove the adsorbed CO on the Pt surface to increase the reaction rate[25]. Another limitation in the use of methanol fuel is the crossover of methanol from anode to cathode which results in low open circuit voltage and a reduction in power density[18, 26-27].

1.3 Direct Sodium Borohydride Fuel Cells

Recently, Direct Borohydride Fuel Cells (DBFCs) have received increasing attention due to their many favourable features. The open circuit voltage for the DBFC is 1.64 V, which is higher than PEMFC and DMFC (1.23 V and 1.21 V, respectively). The oxidation of the borohydride (BH_4^-) ion is accompanied by the transfer of eight electrons, while the oxidation of the hydrogen and the methanol fuel are two and six electrons, respectively. The maximum theoretical conversion efficiency (ηmax) (the ratio between the change in the Gibbs free energy (ΔG_{cell})and the change in the enthalpy ΔH_{cell} (Equation 1-1)[28] of the DBFC is 0.91 Wh kg^{-1}, which is similar to the DMFCs (0.92 Wh kg^{-1}), but higher than the PEMFC (0.83 Wh kg^{-1}) [29, 30].

$$\eta(\max) = \frac{\Delta G(\text{cell})}{\Delta H(\text{cell})} \qquad \text{Equation 1-1}$$

The DBFCs consist of fuel ($NaBH_4$) and an oxidant (O_2, air) or H_2O_2, which are used to generate power. The fuel is chemically stable as a concentrated basic solution[18]. The $NaBH_4$ and its product, i.e. borate (BO_2^-), are regarded as non-toxic and environmentally safe materials. Moreover, the borate can be recycled to generate BH_4^-. The fuel can be stored and transported easily[30]. In addition, the DBFCs can be applied to small electronic devices and portable devices[31] with high power density[30].

The electrodes' reactions are given as follows:

a. The half reaction of the direct oxidation of the BH_4^- ion is accompanied by the transfer of eight electrons:

$$BH_4^- + 8OH^- \rightarrow BO_2^- + 6H_2O + 8e^- \qquad E° = -1.24\ V_{SHE} \qquad \text{Equation 1-2}$$

b. The half reaction of O_2 reduction is the combination of the electrons and water:

$$2O_2 + 4H_2O + 8e^- \rightarrow 8OH^- \qquad E^\circ = 0.4\ V_{SHE} \qquad \text{Equation 1-3}$$

c. The net reaction of the cell is:

$$BH_4^- + 2O_2 \rightarrow BO_2^- + 2H_2O \qquad E^\circ_{,cell} = 1.64\ V \qquad \text{Equation 1-4}$$

Sodium borohydride ($NaBH_4$) consists of 10.6 wt. % hydrogen and was first discovered in the 1950s and used as a reducing agent. It was also used for hydrogen generation[32]. The BH_4^- (at room temperature) reacts with water, kinetically at a slow rate, liberating four moles of hydrogen (Equation 1-5). Simultaneously, the hydrolysis was found to be decreased by increasing the pH of the solution.

$$BH_4^- + 2H_2O \rightarrow BO_2^- + 4H_2 \qquad \text{Equation 1-5}$$

The rate of hydrolysis of the $NaBH_4$ is a function of both the pH of the solution and electrode materials. Steven et al. studied the rate of the generated hydrogen at different concentrations of $NaBH_4$ in the alkaline medium $NaOH_{aq}$ using a ruthenium, Ru, catalyst[33]. In order to determine the hydrolysis rate, different concentrations of sodium hydroxide solutions including 0.25 M, 1.3 M and 2.8 M were used separately. The variation of both $NaBH_4$ weight percentage and the Ru catalyst loading were constant for each part. The authors found that the rate of hydrogen generation decreased by doubling the rate when a higher concentration (2.8 M) of NaOH was used in the electrolyte solution.

It will be shown that the catalytic spontaneous hydrolysis reaction is a major problem encountered by the DBFCs. Not only does it limit the selection of the solution to a strong alkaline solution, but it also interferes with the electrode type selection. It is therefore expected that there will be competition between a partial hydrolysis reaction (catalytic hydrolysis) and the direct oxidation of the borohydride on the surface of the electrode, and that the rate of each reaction depends largely on the electrode's activity.

1.3.1 The Direct Oxidation of the Borohydride Reaction

The type of electrode material influences the direct oxidation of the borohydride. In principle, the oxidation of the BH_4^- ion is accompanied by the transfer of eight electrons (Equation 1-2). However, because of the hydrolysis of the borohydride, the effective use of the 8-e^- direct oxidation process can be hindered depending on the anode type. For some anode materials, both reactions (the direct oxidation of borohydride and hydrolysis of the borohydride) may take place[1-3]. The hydrolysis reaction is not completely suppressed even at a high pH [34], as it can be catalysed by a number of metals and their compounds[35] and the product (H_2) (BH_3OH^-) (Equations 1-6 and

1-7) are further oxidised at a more negative potential than the BH_4^- ion[36]. The Borate (BO_2^-), the production of the second reaction, is considered as a non-electro active species.

I. $BH_4^- + H_2O \rightarrow BH_3OH^- + H_2$ Equation 1-6

II. $BH_3OH^- + H_2O \rightarrow BO_2^- + 3H_2$ Equation 1-7

The situation is further complicated by the formation of hydrogen that arises from the reduction of water electrochemically. The equilibrium potential of the 8-e^- oxidation of borohydride is 300 mV more negative than the equilibrium potential of the reduction of water to hydrogen (-0.828 V *vs*. SHE) under identical conditions. Therefore, thermodynamics predict that a mixed potential is developed at the anode of both anodic reactions (the direct oxidation reaction and the formed hydrogen)[35, 37]. Experimentally, it has been found that these competitive reactions contribute to the reduction of the total number of electrons transferred associated with BH_4^- ion[37] (Equation 1-8).

$BH_4^- + (x)\ OH^- \rightarrow BO^-_2 + (x-2)\ H_2O + (4-(1/2)\ x)\ H_2 + xe^-$ Equation 1-8

This equation has been suggested in numerous studies[1, 29, 38]. Here x represents the total number of electrons transferred during the oxidation of the BH_4^- ion. It will become apparent in the next section that not every electrode gives the total practical number of electrons transferred.

In the literature, catalysts are classified as either catalytic or non-catalytic with respect to the quasi-spontaneously catalytic hydrolysis[3]. Non-catalytic metals such as Au[39], Ag[40], Hg[41] and Zn[42] oxidise the BH_4^- ion at lower overpotential and the reported electron transfer value is close to the theoretical electron-transfer number. On the other hand, metals such as Pt[39], Pd[43], Ni[44] and Cu[45] oxidise BH_4^- at a higher overpotential and a number of electrochemical oxidation reactions can take place (see above). The electro-oxidation mechanism of the BH_4^- ion on materials such as Pt, Ru and Ni have been regarded as a four electro-oxidation process, whilst materials such as Hg and Au have been regarded as an eight electro-oxidation process[3]. For metals such as Ni and Cu, oxygen on OH is also adsorbed at the surface, which will sharply influence the catalytic activity.

1.3.2 Pure Catalyst Materilas for Direct BOR

In the 1960s, a number of catalyst materials were used for the oxidation of borohydride in an alkaline solution. Initially, it was Maurice and his co-workers who examined Ni electrodes using sintered Ni of 80% porosity[46]. They found that a large amount of hydrogen gas was produced due to the hydrolysis occurring during the oxidation process. Elder et al. also studied the oxidation of borohydride on a number of electrodes including Pt, Ni, Cu and carbon using potentiostatic methods[34]. Their study was carried out to demonstrate how the rate of hydrolysis of borohydride varies under different conditions. The authors found that the hydrolysis rate increased with

increasing temperature and decreased by increasing the hydroxide ion concentration in the solution. They also reported, in their study, that both Cu and Ni are inactive catalysts towards the BH_4^- ion, as there was no clear indication of an electrochemical process that contributes to the direct oxidation of the borohydride at low potential, and the oxidation process does not occur until the electrode potential reaches the oxygen evolution region. As for the studies carried out on the Pd electrode, Elder et al. also reported a large current occurring at more negative potential values and this was attributed to the oxidation of H_2 formed by the catalytic hydrolysis of the borohydride.

Numerous studies have been conducted on Au to identify its behaviour towards the borohydride ion. Okinaka et al. was the first to investigate this in the early 1970s[47]. Okinaka's experiment was conducted under specific conditions (T= 75 °C and 0.2M KOH solution as background), allowing a large rate of hydrolysis. In the early 1990s, Bard and his co-workers studied the catalyst behaviour of ultra-microelectrode Au using 0.01 M of $NaBH_4$ in highly concentrated basic solution (1 M of NaOH)[48]. Their investigation included a study of a reaction mechanism of the electro-oxidation of the BH_4^- using fast-scan cyclic voltammetry (CV) and scanning electrochemical microscopy (SECM). They found that the 8-electron oxidation process of the direct borohydride reaction on Au undergoes a multistage process (2-electron oxidation process followed by a 6-electron oxidation process). When the electrode reactions were studied at a slow scan rate (100 mV/s), a single anodic peak was found to take place at high potential (between -0.12 and +0.38 V *vs.* SHE) corresponding to the BH_4^- oxidation. At a fast scan rate, an additional anodic peak was found to take place at more negative potential with a corresponding cathodic peak on the reverse sweep. This cathodic peak was attributed to a reduction of an unstable product ($BH_4^{\cdot}$). The $BH_4^{\cdot}$ was assumed to react rapidly with OH^- in a chemical reaction that accounts for the irreversibility of the process occurring at slow scan rate. The product of the chemical reaction (BH_3^-) undergoes further oxidation. Bard et al. concluded that the mechanism for this process follows the Electrochemical-Chemical-Electrochemical (ECE) sequence (Equations 1-9 to 1-11) and the products of these reactions (the decomposition of the BH_3) are oxidised at a different potential to eventually complete the 8-electron electrochemical oxidation process.

$BH_4^- \leftrightarrow BH_4^{\cdot} + e^-$ **(E)** Equation 1- 9

$BH_4^{\cdot} + OH^- \rightarrow BH_3^- + H_2O$ (very fast reaction) **(C)** Equation 1- 10

$BH_3^- \leftrightarrow BH_3 + e^-$ **(E)** Equation 1-11

The mechanism of the BH_4^- oxidation reaction has not yet been fully understood. However, some studies have suggested potential pathways for a number of catalyst materials. Most research in this regard has confirmed that there is a competition between the BH_4^- oxidation reaction and

the hydrolysis reaction, depending on the catalytic activity. Gyenge studied the BH_4^- oxidation in a solution containing 2 M of NaOH and 0.03 M of $NaBH_4$ using modern electroanalytical methods such as CV and chrono-techniques [39]. A comparative study, which involves an investigation of the catalytic activity of both Pt (with and without surfactants as a hydrogen inhibitor) and Au catalysts, has been conducted. In the case of Pt, Gyenge found that its catalytic behaviour is complex because it undergoes a number of oxidation processes resulting from the catalytic hydrolysis of borohydride that coincides with the direct BOR (Figure 1). It has been suggested that the electrode reaction mechanism of Pt follows a chemical-electrochemical (C-E) reaction mechanism. The chemical reaction is the hydrolysis reaction that yields products such as H_2 and the BH_3OH^- ion, which undergo further oxidisation. The H_2 is oxidised at a low potential (-0.7 to -0.9 *vs.* Ag/AgCl, KCl_{std}) and the BH_3OH^- is either oxidised or exposed to further hydrolysis. The author concluded that the direct BOR on Pt takes place at a more positive potential (between -0.2 and 0 V *vs.* Ag/AgCl, KCl_{std}) following a four-electron electrochemical oxidation reaction pathway.

The oxidation of BH_4^- on Au has been found to take place at a more negative potential (ca. -0.6 V *vs.* Ag/AgCl, KCl_{std}). The Au does not affect the hydrolysis, as is the case with Pt. As a result, it was suggested that Au follows the eight-electron electro-chemical oxidation pathway.

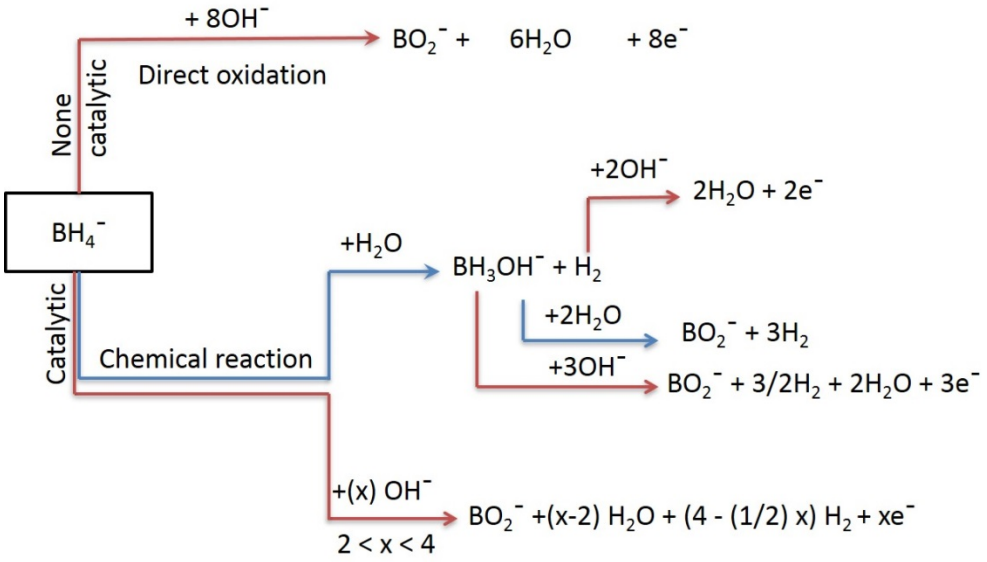

Figure 1: Potential reaction pathways of the BH_4^- oxidation occurring at the catalytic or non-catalytic electrode surfaces with respect to the borohydride hydrolysis. Adapted from [49].

Marian et al. conducted studies on both Au and Ag electrodes as bulk polycrystalline or nanoparticles for the direct oxidation of sodium borohydride reaction using a number of voltammetric methods[50]. An alkaline solution containing 0.1-1 M of NaOH and 0.01 M of $NaBH_4$ was used for the oxidation of the BH_4^-. The results of this study show that the oxidation of BH_4^- on both electrodes was found to take place at a low potential (-0.2 V and -0.3 V *vs.* NHE for Ag and

Ag/C, respectively). However, the oxidation of BH_4^- depended on the state of the Ag surface. The BH_4^- ion was found to be more active on Silver oxide (Ag_2O), while the pristine Ag surface exhibited poor activity. The formation of the oxide layer occurred at around ca. +0.2 V *vs.* NHE. In the case of the bulk Au electrode, the oxidation of BH_4^- was found to take place at -0.5 V *vs.* NHE, which is 0.3 more negative than that on Ag, while the oxidation of the BH_4^- on nanoparticles Au/C took place at a lower potential (-0.57 V *vs*. NHE) than that on bulk Au. The number of electrons transferred that are utilised per BH_4^- molecule was 7.5 electrons for both the Au and Ag electrodes.

1.3.3 Binary Alloy Catalysts for Direct BOR

Many researchers have used a number of materials as an alloy with Au or Pt to improve their performance. The direct oxidation reaction on Au remains kinetically slow, while the direct oxidation of BH_4^- on Pt is masked by the H_2 resulting from its catalytic hydrolysis. Attempts have been made to increase Au electrode kinetics for the direct oxidation as well as reduce the effects of the hydrolysis on Pt. Amendola and his co-workers studied the oxidation of the BH_4^- on an electrode-deposited on Au (97%)-Pt (3%)/C[51]. In this study, the reported number of electrons transferred was calculated. A closed electrochemical cell containing a basic solution of 5% $NaBH_4$ and 25% NaOH was employed, while applying a constant potential to the working electrode at fixed times. The volume of the H_2 formed during the BH_4^- ion oxidation was measured using an inverted burette filled with water. The coulombic efficiency was affected by the competing H_2 reaction and the total number of the electrons transferred obtained was close to seven.

Atwan et al. conducted a comparative study of the carbon supported colloidal Au alloyed with Pt or Pd (Au-Pt and Au-Pd, 1:1 atomic ratio) using conventional and modern analytical electrochemical methods along with fuel cell experiments[52]. They studied the catalytic activity of the Au and its proposed alloy towards the oxidation of BH_4^- using a solution containing 2 M of NaOH and 2 M of $NaBH_4$. They demonstrated that the Au-Pd alloy catalyst showed a complex voltammetry response, and also found that the Au-Pt displayed the highest catalytic activity followed by the Au-Pd and Au, respectively. The fuel cell experiments demonstrated that Au-Pt anode catalysts recorded substantial operating cell voltages (0.47 V at 100 mA Cm^{-2} and 333 K) compared to Au (0.17 V) preformed under the same conditions.

The above studies have reported that Au and Pt are the most active anode materials used in DBFCs compared to other materials. However, noble catalysts make DBFCs more expensive. For that reason, a number of researchers have focused their attention on finding less costly and highly efficient anode materials.

Pei et al. investigated the catalytic activity of Au-Co/C nanoparticles towards the BH_4^- ion[53]. The oxidation of borohydride in an alkaline media containing 0.1 M of $NaBH_4$ + 3.0 M NaOH, which has been studied using cyclic voltammetry and chrono-techniques. According to the cyclic voltammetry studies, the onset potential of the direct oxidation shifted towards more positive values as the concentration of the Co content increased in the Au-Co alloy. The current density reached its maximum on the Au_{45}-Co_{55}/C. In addition, at higher Co concentrations (Au_{70}-Co_{30}/C up to $Au_{30}Co_{70}$/C), the recorded voltammogram showed two additional peaks in the region of hydrogen evolution (between -1.2 V and -0.8 V vs. Ag/AgCl, KCl_{std}), which have been attributed to the oxidation of H_2 resulting from the catalytic hydrolysis. At pure Co/C, the hydrolysis reaction was found to be dominant and no signs of the direct oxidation of borohydride were recorded. It was pointed out that the Co/C promoted hydrolysis and was inactive towards the BH_4^- oxidation. The chronopotentiometry study illustrates that the BH_4^- oxidation on a number of different Au-Co/C alloy compositions (between $Au_{88}Co_{12}$/C and $Au_{30}Co_{70}$/C) at a current density of 8.5 mA cm^{-2} showed lower overpotential than that on Au/C. The results obtained by the chronoamperometry measurements showed that the Au-Co alloy in all its compositions showed higher current densities compared to the Au/C electrode controlled by the diffusion of BH_4^-. The authors concluded that the kinetics of the BH_4^- oxidation reaction on Au has been enhanced by alloying with Co and the most active catalyst was reported for the $Au_{45}Co_{55}$/C.

Lanhua et al. conducted electrochemical studies for the oxidation of borohydride on Au-Fe/C alloys using voltammetric methods and fuel cell experiments[54]. They found that the Au electrode's performance as an anode material for the DBFCs was improved after alloying it with Fe. Various compositions of the Au-Fe/C were investigated in a solution containing 0.01 M of $NaBH_4$ + 1.0 M NaOH. Based on the cyclic voltammetric studies carried out on Au/C, $Au_{67}F_{33}$/C $Au_{50}Fe_{50}$/C $Au_{33}Fe_{67}$/C and Fe/C electrodes, the peak current of the direct BOR recorded on the Au-Fe/C alloy was generally higher than that on Au/C. The highest catalytic activity was reported for the Au_{50}-Fe_{50}/C with a maximum current of 33.8 mA cm^{-2} compared to the Au/C electrode (17.6 mA cm^{-2}). The Fe/C electrode on its own was inactive towards the BH_4^- oxidation. In relation to the current-time curve, which was obtained using chronoamperometric responses, the rate of the current density on Au/C decayed more rapidly than that on the Au-Fe/C electrodes. The highest steady state current density was reported for the Au_{50}-Fe_{50}/C electrode. Furthermore, the catalytic performance of the Au-Fe/C has been investigated using the chronopotentiometry technique. The results showed that the anode performance of the Au/C electrode was improved when alloyed with Fe, as lower overpotentials were recorded for all the Au–Fe/C catalysts. According to the fuel cell experiments, the authors concluded that the $Au_{50}Fe_{50}$ is the most active anode material and can be a promising anode catalyst for the DBFCs.

Pei et al. used a number of non-noble nanoparticles materials supported on carbon including Zn, Fe, CO, Ni and Cu alloyed with Au as cost-effective alloys for the DBFCs[55]. The oxidation of BH_4^- (in various concentrations (from blank to 0.2 M) of $NaBH_4$ in 3 M NaOH) on the Au-M/C alloys has been studied using cyclic voltammetry measurements. The oxidation of BH_4^- on Au/C was found to take place between -0.8 V and +0.2 V *vs*. Ag/AgCl. The direct BOR on each of Au-Ni, Au-Co and Au-Cu showed a shift towards a more negative potential. On the other hand, the direct BOR for each of the Au/C and Au-M/C (M= Zn and Fe) showed no significant change in terms of the onset potential. In addition, high peak currents have been recorded for the Au-Ni, Au-Co/C and Au-Cu/C.

Table 1 summarizes the direct BOR on different catalysts. The HOR resulting from the catalytic hydrolysis reaction was also reported. Catalysts such as Au, Ag and Au-M alloys gave the highest number of electrons transferred (n= nearly 8), while other catalysts including Pt and Pd gave lower number of electrons transferred (n= 4) due to their high activity in weakening hydrogen bond to the boron atom[34, 56](loss of hydrogen). The activity trend shown by table 1 demonstrates that Au and all Au-M on the basis of the onset potential are very active for the direct BOR, while Cu and Ni (pure metals) require a large overpotential for the BOR due to the suppression by the readily formed oxide.

Table **1** Electrochemical characteristics of investigated catalysts carried out for the direct BOR under different conditions. Symbols: E is the onset potential for HOR (hydrolysis product)/ Direct BOR. T is the temperature in Kelvin and n is the number of electrons transferred in the direct BOR.

Catalyst	**$NaBH_4$(M)**	**Media**	**Reaction path**	**E_{op}/V_{SCE}**	**T/K**	**N**	**Ref.**
Au/micro-disk	0.01	1 M NOH	Direct BOR	-0.6	298	8	Bard et al.[48]
Pt/smooth	0.1	0.1 M KOH	H_2 + Direct BOR	N/A	298	4	Elder et al.[34]
Au-Pt/colloidal	0.03	2 M NaOH	H_2 Direct BOR	-0.95 -0.6	298	N/A	Atwan et al. [52]
Pt/macro-disk	0.001	2 M NaOH	H_2 Direct BOR	-0.91 -0.17	298	4	Gyenge[39]
Au/macro-disk	0.001	2 M NaOH	Direct BOR	-0.6	298	8	Gyenge[39]

Pd/zeolite	0.01-0.06	2 M NaOH	H_2 Direct BOR	-0.241 0.259	298	4-5	Raisa et. al [56]
Au-Pd/colloidal	0.03	2 M NaOH	Direct BOR	-0.2 and -0.001	298	N/A	Atwan et al.[52]
Dropping Mercury	0.01	0.1 NaOH	Direct BOR	-0.06	298	7.8	Gradiner et. al[41]
Ag/C	0.01	1 M NaOH	Direct BOR	-0.35	N/A	N/A	Ramirez et. al[57]
Ag/bulk	0.01	1 M NaOH	Direct BOR	-0.44	298	7.6	Marian et. al[50]
Ni/Zn-Ni	0.02	1 M NaOH	Direct BOR	+0.6	N/A	N/A	Hosseini et. al[58]
Au-Ni/C	0.05	3 M NaOH	Direct BOR	-0.8	293	6.8	Peiying et al. [59]
Cu/C	1	2 M NaOH	Direct BOR	+0.608	N/A	N/A	Moreno et. al[60]
Au-Cu/C	0.05	3 M NaOH	Direct BOR	-0.69	293	6.3	Peiying et al. [59]
Au-Fe/C	0.05	3 M NaOH	Direct BOR	-0.64	293	5.7	Peiying et al. [59]
Au-Co/C	0.05	3 M NaOH	Direct BOR	-0.74	293	6.5	Peiying et al. [59]

1.4 Objectives

The objective of this thesis is to develop and identify new anode electro-catalyst materials for DBFCs using combinatorial synthesis and electrochemical screening methods, and to understand their electrocatalytic activity for the direct BOR. The questions to be asked are (i) how can the activity towards the direct BOR be increased and (ii) how can the selectivity towards the catalytic spontaneous hydrolysis of the borohydride reaction be controlled to make full use of the eight-electron. Various metals have been evaluated in the literature and the most efficient anodic material recorded for the BOR is Au. However, a disadvantage of this is that the cost of Au limits its application in DBFCs. In order to answer the proposed research question, we will change the properties of Au by alloying it with the 3d metals Ni and Cu. Subsequently, H_2 generated at the alloy catalyst surface (due to the catalytic hydrolysis of the borohydride reaction) will be electrochemically detected using a hydrogen probe.

Consequently, we will broadly focus on the Au-Ni alloy (Chapter 4), Au-Cu alloy (Chapter 5) and Au-Pt alloy (Chapters 6 and 7). These chapters will present a detailed study of the binary alloy bulk/surface properties which will lead to understanding the alloying effect on the electrocatalysis of the direct BOR. The electrocatalytic activity of the alloy catalysts will be assessed by measuring the onset potential and the current of the direct BOR as a function of compositions. Chapter 2 will describe the studies related to the preparation and the characterisation methods that have been used to synthesis and examine the surface/bulk composition and the bulk structure of these alloy systems.

Chapter 2 Experimental Methods

2.1 Combinatorial Catalysts, Synthesis and High Throughput Electro-catalysis

2.1.1 Combinatorial Synthesis

Over the past years, combinatorial methods have become the focus of many researchers. This is because of the rapid rate of generating, screening and discovering novel effective materials. Combinatorial synthesis is used for creating materials libraries with various compositions. It was first invented by Merrifield[61] in 1963 who applied it to the synthesis of long chain peptides entitled “the solid phase peptide synthesis”. In 1970, Hanak developed a combinatorial approach called “the multiple sample concept” to search for effective super conductive materials. Hanak used co-deposition of binary or ternary materials using a single divided sputter-target and was able to obtain graded compositions [62]. The sputter-target was divided into A, B and C, allowing for the deposition of binary or ternary systems at the same time. In the early 1990s, the terms “combinatorial synthesis” and “high throughput screening” were introduced by Xiang et al[63], who made thin film materials using the combination of sequential depositions and a binary mask or quaternary mask. The used masks were rotated by 90° for each deposition. Subsequently, the deposited thin film materials were heat-treated to allow interdiffusion. As a result, the authors were able to deposit material libraries with a discrete composition gradient[64-65].

The combinatorial synthesis method has led to further developments in material science by incorporating innovative ways in an attempt to reach larger numbers of depositing materials libraries within a short period of time. Cooper et al. used a rotating carousel with 12 holes placed between the substrate and six sputtering targets. Multilayer thin films were obtained in a sequential deposition followed by post-deposition[66]. Applying an identical method to that introduced by Xiang et al., 256 library materials were deposited on 16×16 microelectrode arrays generated by the choice to change the computer programmed mask and target[66]. Moreover, Danielson et al. were able to deposit up to 25,000 different materials when searching for effective luminescent materials[67]. The deposition of the materials library was carried out using electron beam evaporation. A mask attached to a three-inch diameter silicon substrate was placed to segregate each library. The spatial distribution of the materials was produced through a movable or fixed mask. This allowed the screening of the deposited libraries to search for novel luminescent materials. As a result, new luminescent materials were detected and showed more efficient or comparable properties than those obtained by single sequential deposition.

2.1.2 High Throughput Electrochemical Screening Methods

High-throughput synthesis and screening are key to making and determining effective catalyst materials quickly. The conventional sequential synthesis in which a number of catalyst materials are individually tested takes time as well as physical effort. Investing companies are demanding a large production of efficient electro-catalyst materials in a short time[68]. Therefore, rapid screening is an integral part of the combinatorial synthesis.

The first high throughput screening study was carried out on electrocatalyst anode materials for the direct methanol fuel cells[69]. The catalysts consist of ternary arrays of Pt/Rh/Os, which were prepared by hand-pipetting or ink-jet printer on a paper carbon. As the oxidation of the methanol produces four hydrogen ions, the generated hydrogen ions were absorbed by quinine (a sensitive acid-based detector). This resulted in dark blue colour images displaying the active region of the electrocatalysts. However, this indirect screening method (where the current is not directly measured but only the fluorescence signals are detected) is only applied to electrolytes that are not highly concentrated.

Prochaska et al. used both fluorescence screening and Scanning Electrochemical Microscopy (SECM) methods[70] to screen Pt-Bi-Pb/Si ternary thin film materials. The thin film ternary materials were synthesised by co-sputtering to produce continuous compositions and the electro-catalytic activity of the Pt-Pb rich region was confirmed by fluorescence screening. The composition of the active region was estimated as $Pt_{0.50}$ $Bi_{0.16}$ $Pb_{0.35}$ catalysts. However, the fluorescence screening exhibited low spatial resolution because of the rapid diffusion of the protons generated from the oxidation of the methanol. In the meantime, SECM screening was used to check the active region detected by the optical screening. A selective catalyst of Sb towards the protons was used as a probe for monitoring the variation in the hydrogen concentration by recording either the current or the potential. The hydrogen concentrations resulting from the electro-oxidation of the methanol were detected through an increase in the tip potential. The researchers concluded that Pt-Pb rich active regions showed the highest electro-catalytic activity, which is consistent with the active region detected by the optical screening.

Simon et al. designed the first 64 multielectrode array searching for new sensor materials using high throughput screening impedance spectroscopy[71]. The high throughput screening was applied to a 64 printed-Pt electrodes array. It was noted that the investigation of new catalysts using the 64 microelectrodes array approach is also appropriate for other electrocatalytic applications.

Jiang et al. used a movable electrolyte probe for screening electrode arrays to investigate the impact of different electrolyte concentrations, along with various catalyst loadings, on the electro-oxidation of methanol[72]. They designed an electrochemical cell by linking the counter and

reference electrode to the moveable probe so that all working electrodes shared one counter electrode and one reference that are located separately. They also placed porous separators on each electrode surface of the electrode arrays. Different concentrations of the electrolyte were injected into each electrode via a flexible tube. The researchers were able to carry out an electrochemical experiment on an electrode array consisting of 144 working electrodes.

Sullivan et al. fabricated an automated electrochemical screening method to measure the electrochemical current of 64 electrodes directly as an attempt to detect any slight changes in the produced current that are undetectable by fluorescence screening[73]. Therefore, the Au electrodes array was modified with various alkenethiols to validate their approach. These electrodes were immersed in a single electrochemical cell and the current was measured sequentially via CV. The time taken to measure the current depends on the scan rate and the number of sweeps. They used a scan rate of 100 mV/s and 2-3 sweeps for each complete electrochemical array measurement. It took between 2 and 3 hours to collect the full data set of the electrode arrays.

Warren et al. studied the methanol oxidation on 64 Pt-Ru deposited by electrode deposition in various compositions on insulated substrates containing 64 Au individually addressable electrodes[74]. A patented study related to the high throughput electrochemical screening was applied and the researchers used a multi-channel potentiostat for the electrochemical screening. They tested different materials that were deposited via automated combinatorial electrode deposition onto non-conductive substrates. The researchers stated that the arrays consisting of 66 or 64 individually addressable electrodes, which could be measured in parallel using the multichannel potentiostat, or in serial order using a single channel potentiostat.

2.1.3 High Throughput Methodologies Applied Here

Our approach relies on high-throughput experimentation integrated with combinatorial synthesis in a laboratory containing a number of surface sensitive probe tools. These tools are specially designed for high throughput mapping of composite materials deposited by the Hayden Research Group. Materials libraries of binary alloys containing continuous or discrete thin films with a wide range of compositions such as Pd-Au[14], Pd-Cu[75] and Pd-Bi[76] alloy systems were synthesised for electrocatalysis studies using the High Throughput Physical Vapour Deposition method (HT-PVD), which has been described in detail[77]. This method allows co-deposition of a number of materials simultaneously in Ultra High Vacuum (UHV) chamber consisting of multisource molecular beam epitaxy (MBE).

The HT-PVD method also allows the deposition of solid solution materials under experimental conditions without the need for exposure prior to subsequent annealing. The latter results in formation of alloys with non-identical surface and bulk compositions, as well as

thermodynamically stable bulk phases better known as equilibrated solid solution materials. This phenomenon can be avoided by applying the HT-PVD method, which allows formation of metastable alloy materials with identical surface and bulk compositions as well as non-equilibrated bulk phases better known as non-equilibrium solid solution materials.

This is an advanced technique in combinatorial synthesis science in which not only can the deposition be controlled under low temperature but also the deposition profile of each material can be controlled without resorting to conventional methods (mask techniques). Therefore, our technique is of great importance for the discovery and development of innovative and functional materials.

The Hayden group applied pseudo-parallel methods of high-throughput electrochemical screening for novel electro-catalytic materials. Initial studies involved direct current measurements performed to study the oxidation of CO, oxygen reduction and methanol oxidation on various Pt loadings, and particle size deposited an array consisting of 64 individually addressable electrodes using cyclic voltammetry and steady state measurements[78]. A single electrochemical cell containing the same electrolytes with a common counter electrode and a common reference electrode was used. In addition, a combination of a single channel potentiostat and a pair of 64-channel current followers with programmable triangular wave generator were used to illustrate the feasibility of the high throughput electrochemical screening approach. The potential of all active electrodes was distributed evenly and therefore electrochemical processes taking place at each independent addressable electrode occurred simultaneously. The current followers converted the currents reverted from the electrode arrays into voltage to be digitalised by PCs incorporated into A to D cards. The data was collected in a fast-sequential way for rapid screening. Two Visual Basic software programmes written by the Hayden group (one for acquiring and the other for analysing data) were developed to control all parameters necessary to carry out electrochemical experiments and to visualise the recorded data of all 64 electrodes. This innovative method enabled those involved in this study to conduct rapid electrochemical screening and to monitor and analyse the recorded data of the 64-Pt /C electrodes within seconds.

Further methods have been carried out in subsequent studies for the pseudo-parallel methods of High Throughput Electrochemical Screening. The High Throughput Electrochemical Screening experiment was developed by incorporating a silicon micro-fabricated chip (electro-chemical array chip) and designing a special electrochemical cell that allows only the area of interest to be examined. This coincided with the development of the HT-PVD method, which was used to synthesis thin film materials with graded compositions of ternary metal alloys[79]. The compositional gradient thin film materials were deposited on the electrochemical array chip (e-

chem chip) consisting of 10x10 Au electrodes. The e-chem chip was connected to the electrochemical cell in such a way that the non-active area (Au contact pads at the edge of the e-chem chip) was not in contact with the electrolyte during electrochemical screening measurements and the potential was applied to the active electrodes using interconnector-insulated wires connecting each electrode with the contact pads. The application of voltage to the 10x10 array occurred at the same time by connecting the contact pads to an electronic board. By combining the two methods, the synthesis and screening led to the discovery of novel electro-catalysts in various studies carried out by the research group.

2.1.4 Outline of the Research Project Methodology

The experimental work of this project was conducted in two parts. The first part was the synthesis of the compositional gradients of Au-Ni, Au-Cu and Au-Pt thin film alloy materials. The second part aimed to characterise the prepared alloy materials. All alloy catalysts were synthesised by HT-PVD and characterised as detailed in Table 6 (Appendix A). The surface/bulk composition and bulk structure of the alloy catalysts were characterised using high throughput screening methods:

- Energy Dispersive X-ray Spectroscopy (EDX)
- X-ray Diffraction (XRD)
- X-ray Photoelectron Spectroscopy (XPS)

The electrochemical behaviour of the catalysts was investigated using the High-Throughput Electrochemical Screening Method (HT-ECS). The characterisation of the catalysts was electrochemically screened in both the presence and absence of borohydride in the alkaline media. To fully characterise the electrochemical reaction at the bimetallic arrays, hydrogen evolution generated at the catalyst surface was measured to gain a general understanding of how the catalytic spontaneous hydrolysis reaction affected the direct BOR. Thus, a high throughput hydrogen probe was developed (Chapter 7).

2.2 High Throughput Physical Vapour Deposition

Combinatorial synthesis of compositional gradient thin film libraries was carried out using the UHV system from DCA, Finland. The HT-PVD system consists of different interconnected chambers all under UHV and includes film synthesis chambers; synthesis chamber A (SCA), synthesis chamber B (SCB) and an RF-sputtering chamber. The system also includes a surface analysis chamber equipped with an XPS chamber (Figure 2).

These chambers are linked by buffer lines so that a sample on a trolley can easily be moved within the whole system under UHV vacuum conditions. To load/unload samples in the system, a connecting load lock allows transfer of substrates from atmospheric pressure. The samples are transferred into the system by a pick-up mechanism and transfer arms. Each chamber has a transfer arm to allow a sample to be transferred from the buffer chamber to a rotatable and heated manipulator in the synthesis chambers. The manipulator is designed to hold the sample and control the temperature of the sample up to 1000 °C. The analysis chambers were pumped by a cryo-pump (Helix Tech. Corp.), turbo-molecular pump and a titanium sublimation pump (Varian). The transfer line and the surface analysis chamber were pumped by an ion- pump (Varian) and titanium sublimation pumps. The load lock was pumped by an oil free rotary pump (Pfeiffer) and a turbo-molecular pump (Pfeiffer). The whole system is under UHV with an overall base pressure of about 6.66×10^{-8} mbar.

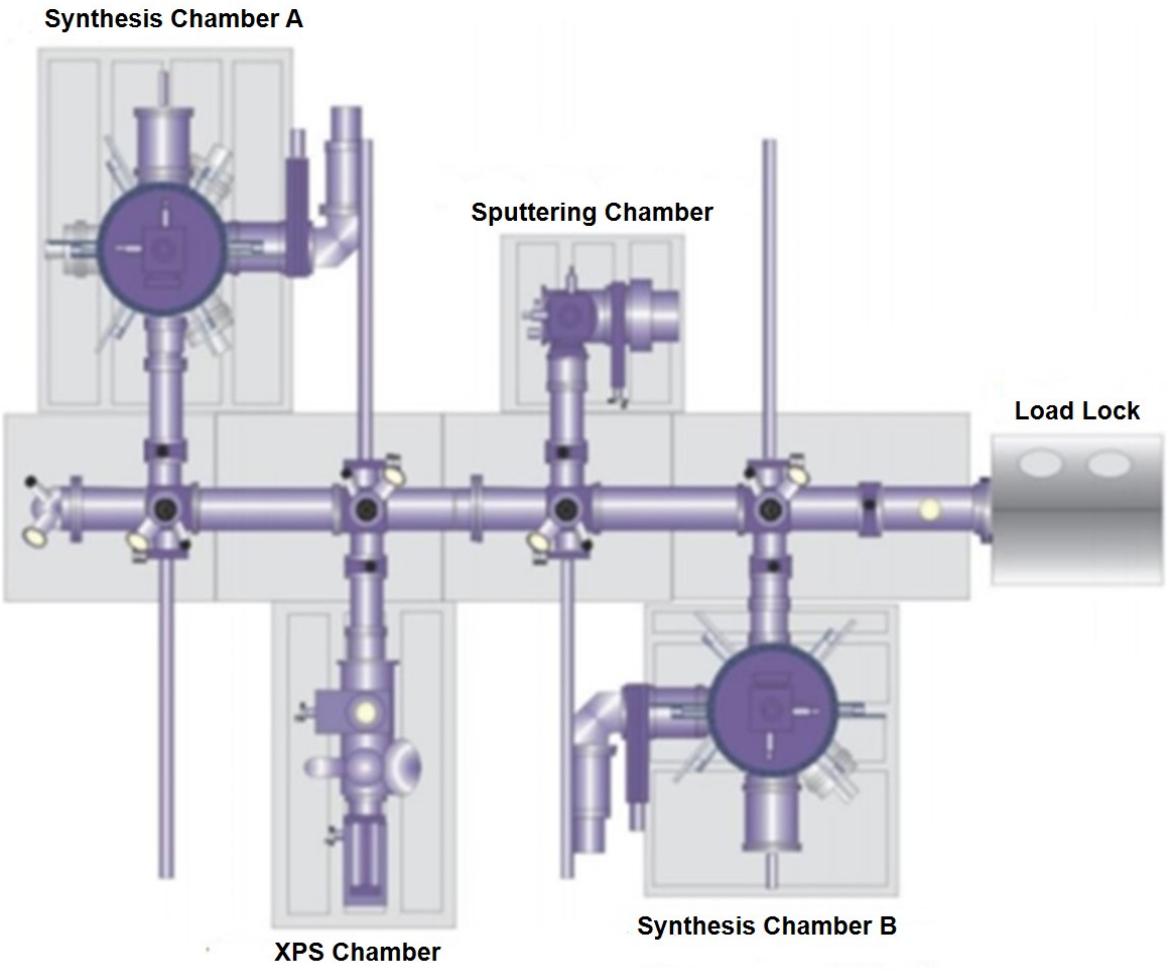

Figure 2: Schematic view of the HT-PVD system used for the thin film binary systems including multi-source combinatorial synthesis chambers A and B and the XPS chamber.

SCA, which consists of six off-axis sources, three Knudsen-cells (K-cells) sources and three electron beam (e-beam) sources, can be used for depositing thin film materials. As the maximum number

of sources is limited by the physical size of the vacuum chamber and the size of the sources (Figure 3), it is possible to carry out co-evaporation of materials with up to six pure elements. However, the number of evaporation sources used in this work is, as shown in the Figure, two; one was allocated for the Au and the other for the Ni, Cu or Pt. Each source material is combined with shutters (main and wedge shutters). When starting the deposition of a material, the main shutter can be opened fully to allow the flux of the evaporated material to deposit on the surface. The wedge shutter, which is positioned above the source, can be manually moved backward or forward to partially block the flux of the evaporated material creating a shadow-like effect across a sample. By using the wedge shutter at a calibrated position, the deposition profile of a material can be controlled as desired.

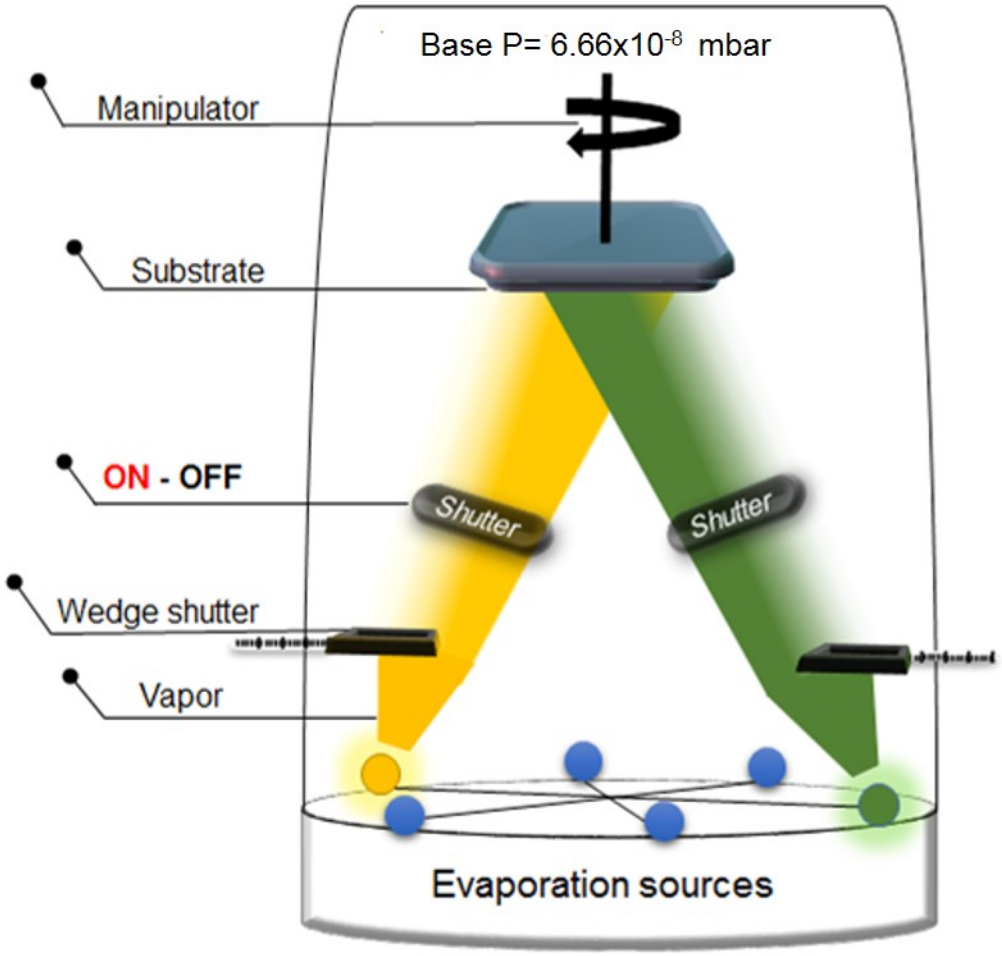

Figure 3: Schematic view of the PVD synthesis chamber (A) showing the six off-axis sources inside, three K-sources and three E-beam gun sources surrounding the substrate. Each source is provided with a shutter and a wedge shutter. The source sites used for deposition are displayed as shadows and gradients representing the evaporated materials.

In order to obtain a linear gradient of deposition for each element along a substrate, the wedge shutter of each source was calibrated by making subsequent depositions on a transparent glass substrate, through which the appropriate position for the wedge shutter relative to the deposited material was identified. Based on the position of the adjusted wedge shutters, not only can a large range of compositions of solid-state materials, varying from about 0 to 100 atomic percentages across a substrate be achieved, but also a gradual change in thickness of each element across the substrate can also be obtained. Figure 4 displays how the gradient of a material can be controlled as a function of the wedge shutter position.

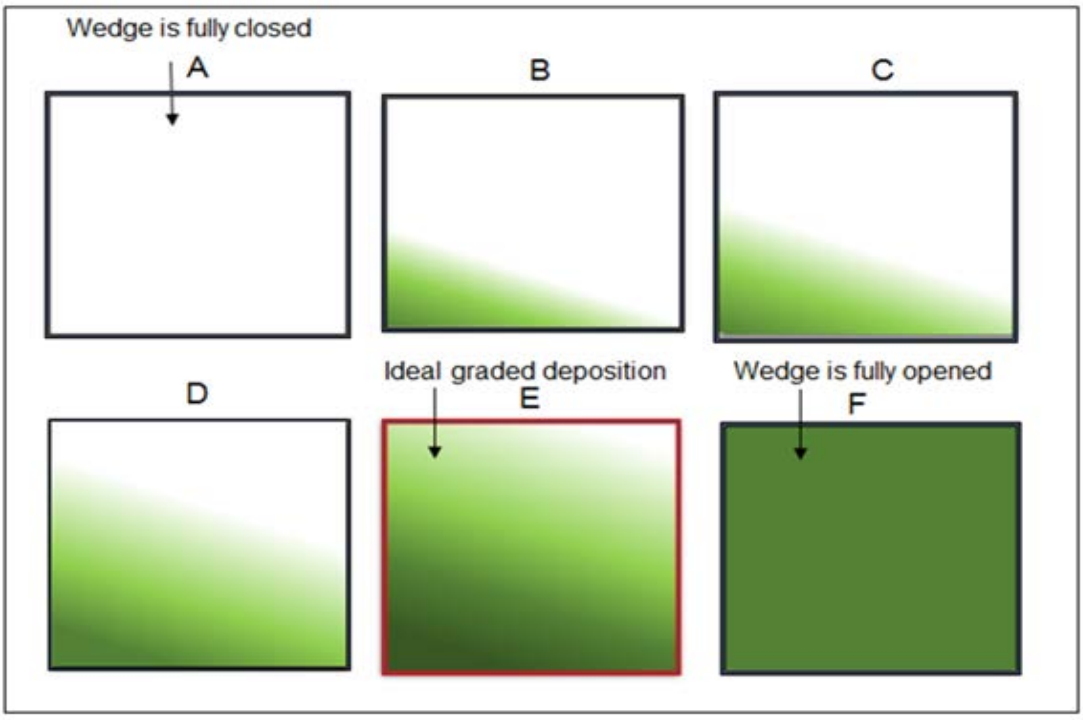

Figure 4: Simulation of serval deposition profiles describing how the gradient of a material deposited from a single evaporation source can be controlled as a function of a wedge shutter position.

When the evaporated material is intercepted by a fully closed wedge shutter, this results in no film deposition (Figure 4 A). If the evaporated material is partially blocked, a gradient deposition of the film will be created. When the wedge shutter is fully opened, the gradient of the deposited material is minimal. Between the two extremes of a fully closed and fully opened shutter, the wedge position can be adjusted to provide a range of graded depositions, as illustrated in Figure 4 (B to E). Our goal is that the magnitude of the gradient of a material to be deposited is similar to that indicated in Figure 4 E. Hence, when two materials (A and B) containing the same gradient across a substrate are combined, it is possible to obtain a wide range of compositional gradients, provided that the direction of the growth of the material (A) is opposite to the direction of the

growth of the other material (B) (Figure 5). The compositions of each material then vary as a function of substrate position but are almost equal along the 50/50 binary line. The variation of the composition depends on what is desired at the time. In the present study, it was intended that the range of the compositional gradient would vary from 5.0 to 95 (±5) at. % of each material along the substrate.

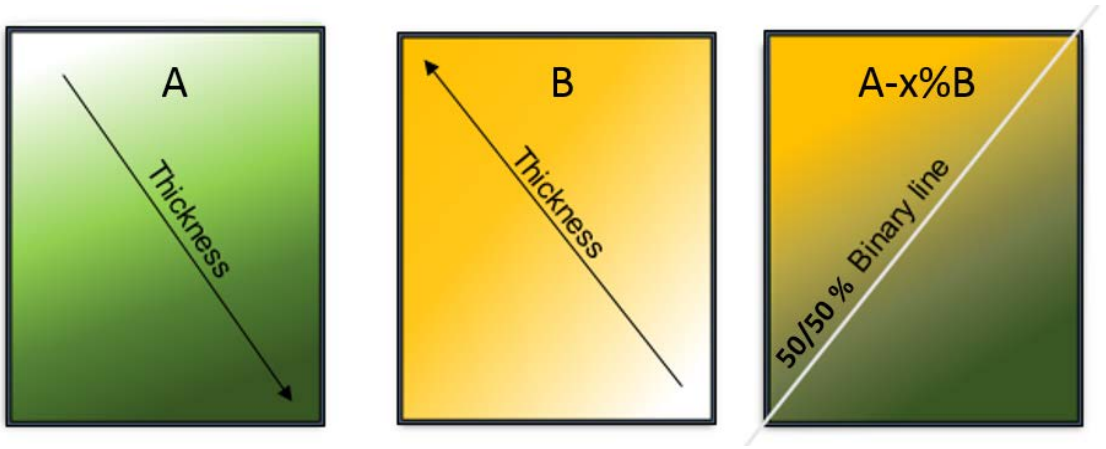

Figure 5: Images mimicking the stage at which both materials A and B are synthesised at the same time from opposite evaporation sources to produce combinatorial A-B alloy materials (A-x%B).

2.3 Materials and Deposition Conditions

The deposition of Au-Ni, Au-Cu and Au-Pt thin film materials as real samples is determined first by using calibrated samples. The calibration involves adjustments required for the desired deposition parameters, such as the deposition temperature, deposition rate, the deposition time, the film thickness and the composition gradient. Initial depositions of the thin film materials were carried out using glass and silicon substrates for calibration.

The Au-Ni, Au-Cu and Au-Pt thin film materials were prepared as follow:

1. Au evaporation source: the raw material was gold pellets (Goodfellow Cambridge Ltd) with a purity of 99.999%. A crucible of graphite was half-filled with the Au pellets and then inserted into a high temperature effusion cell (K-cell 1). The Au source was degassed by increasing the temperature of the K-cell 1 gradually by 50°C every 10 to 15 minutes to eliminate any source of contamination, such as water contents or air. The deposition temperature was observed at 1250°C.
2. Ni evaporation source: the raw material was a nickel block from Testbourne Ltd Materials with purity of 99.9999%. The nickel block featured a truncated tube with a dimension of top OD shape 43 mm and bottom OD shape 32.9 mm, with a height of 18.5 mm. A graphite crucible was used and placed into E-beam 2 in order to contain the nickel source.

To ensure that the material source was contaminant free, the source was degassed by increasing the e-beam power 0.5% every 10 to15 minutes. The start of the deposition was observed at a power of 8.5% with a rate of 0.3 Å/s to 0.6 A/s.

3. Cu evaporation source: the raw material was copper pieces 3-8 mm of the same length and diameter from Testbourne Ltd Materials with a purity of 99.999% mounted into a graphite crucible and loaded into E-beam 2. The source material was degassed by increasing the power up to 0.5% every 10 to 15 minutes. The start of deposition was observed at a power of 8.5% with a rate of 0.3 Å/s.
4. Pt evaporation source: the raw material was Pt pellets (Goodfellow Cambridge Ltd) with a purity of 99.999%. A graphite crucible was used and placed into E-beam 2. The source was degassed by increasing the e-beam power 0.5% every 10 to 15 minutes. The start of the deposition was observed at a power of 24.5% with a rate of 0.2 Å/s.

Table **2** Deposition parameters of the calibrated Au-Ni sample.

Element	Wedge Position	K-cell/e-beam	Temperature	Rate(Å/s)/power pwr%	Substrate temperature
Au	32 mm	K-cell 1	1430 ^{o}C	N/A	No external heating
Ni	43 mm	e-beam2	N/A	1.2 Å/s 11.5 pwr%	No external heating

Table **3** Deposition parameters of the calibrated Au-Cu alloy sample.

Element	Wedge Position	K-cell/e-beam	Temperature	Rate(Å/s)/power pwr%	Substrate temperature
Au	31 mm	K-cell 1	1450 ^{o}C	N/A	No external heating
Cu	43 mm	e-beam2	N/A	1.05 Å/s 18.9 pwr%	No external heating

Table **4** Deposition parameters of the calibrated Au-Pt alloy sample.

Element	Wedge Position	K-cell/e-beam	Temperature	Rate(Å/s)/power pwr%	Substrate temperature
Au	32 mm	K-cell 1	1490 ^{o}C	N/A	No external heating
Pt	45 mm	e-beam2	N/A	0.5 Å/s 32.0 pwr%	No external heating

2.4 Characterisation Methods

2.4.1 Energy Dispersive X-ray Spectroscopy (EDX)

EDX is an analytical tool used for elemental identification via "excitation-relaxation" processes. Almost all elements can be identified except for H, He, Li and Ba. The elements can be probed using a source of x-ray that excites core level electrons. When the core level electrons receive more energy, transition of the excited electrons to high energy levels occurs, resulting in vacancies. Higher energy level electrons lose energy to fill in these vacancies (relaxation process) and the difference in energy is released as X-rays. The energies of the emitted X-rays are then measured via an energy-dispersive spectrometer. Each element has its own unique energy value as a fingerprint among other elements.

The bulk compositions of the Au-Ni, Au-Cu and Au-Pt have been obtained using EDX. The instrument is equipped with a scanning electron microscope (SEM) (JEOL JSM5910) coupled to an EDX (Oxford instruments Inca 300). The sample was placed on the vacuumed SEM chamber, which contains a stage that can move in x-y and z directions. SEM was used to select the position of the electrode to be measured by the EDX using a working distance of 10 mm and spot size of 43 (proportional to the diameter of the beam). An accelerating voltage of 15 kV and acquisition time of 60 seconds per electrode sample were used for macro measurement programmed to measure 100 samples on a silicon substrate. The composition of the samples was specified as an atomic percentage and collected in a text file.

2.4.2 X-ray Diffraction (XRD)

XRD is used for phase identification of solid-state materials. Monochromatic X-ray is produced by an x-ray tube. A sample (crystalline material) is irradiated by the X-ray resulting in scattering of the x-ray wavelength. Scattering occurs as a result of the atoms' electrons being distributed in planes within the crystal lattice. The crystalline material consists of either a single phase or multiphase structure (single or random orientations of small crystallites). If subsequent

constructive interference of the scattered wavelengths takes place, according to Bragg's law (**n**λ=2**d** sin θ) (where n is an integer number of a wavelength λ, d is the inter-planer spacing and θ is the scattering angle), diffraction maxima of the X-rays occurs. A graph relating the diffraction angle to the diffracted intensity consists of diffraction patterns, which in turn characterise each individual phase as a fingerprint.

XRD was used for phase identification of the Au-Ni, Au-Cu and Au-Pt thin film materials. The instrument used is a Bruker D8 powder diffractometer with a C2 area detector. The source used is Cu Kα. To allow measurement of x-ray reflections at several two theta angles of a sample containing such combinatorial libraries, the general area detector diffraction system (GADDS) was used for high speed data collection. To identify the phase structure of the Au-Ni system, the X-ray source angle was set at 11° and the detector angle was set at 35°. The phase structure of the Au-Cu and the Au-Pt alloys was investigated by XRD (Ilika Technologies instruments) using a Bruker D8 equipped with an Incoatec microsource Cu Kα and GADDS detector. The angles of the X-ray source and the angle of the detector were set at 11° and 30°, respectively. This resulted in generation of 100 graphs that relate the diffraction angle to the diffracted intensity within a range of 2θ from 25° to 60°, 2θ from 25° to 55° for Au-Ni, Au-Cu and Au-Pt alloy systems, respectively. A macro was used for each sample using 180-second acquisition time per recorded point (the number of total points is 100). The diffraction patterns, which characterise each individual phase were analysed using the Paradise software as a function of the electrode composition. Paradise is a piece of software developed in-house by Ilika Technologies Ltd to analyse high throughput data.

2.4.3 X-ray Photon Spectroscopy (XPS)

XPS is a sensitive surface analytical tool. It is usually used to probe the uppermost atomic layer from a surface of a solid-state material to provide physical and chemical information. This information is obtained when the material of concern (under ultra-high vacuum conduction) is exposed to X-rays with a photon energy of 200-2000 eV (Figure 6). The core-level electrons of the atoms are ejected because their interaction with X-ray makes them emitted. Once the emitted photoelectrons are in a vacuum, they are collected by an electron analyser and measured as a function of their kinetic energies. The kinetic energy (E_k) depends on the photoelectron energy (hv), the work function and the binding energy (B_E) of the atomic orbital from which it originated (Equation 2-1). The data presented are expressed as an energy spectrum consisting of intensity on the y-axis versus electron bending energy on the x-axis. Each unique energy peak on the spectrum corresponds to a specific element and provides information about the element's chemical state. The intensity of the peak provides information about the concentration of the element concerned. The atomic percentage presented in the element can be calculated by integrating the peak area (I_A) and dividing it by the relative sensitivity factor (F_A)[80] (Equation 2-2).

$$E_B = h\nu - E_k - W$$ Equation 2-1

[A] atomic %= {I_A / F_A/ ∑(I / F) ×100% Equation 2-2

Where I_A is the area of the peak of the element A, F_A is the sensitivity factor for the element, and ∑ (I / F) is the all normalised intensities.

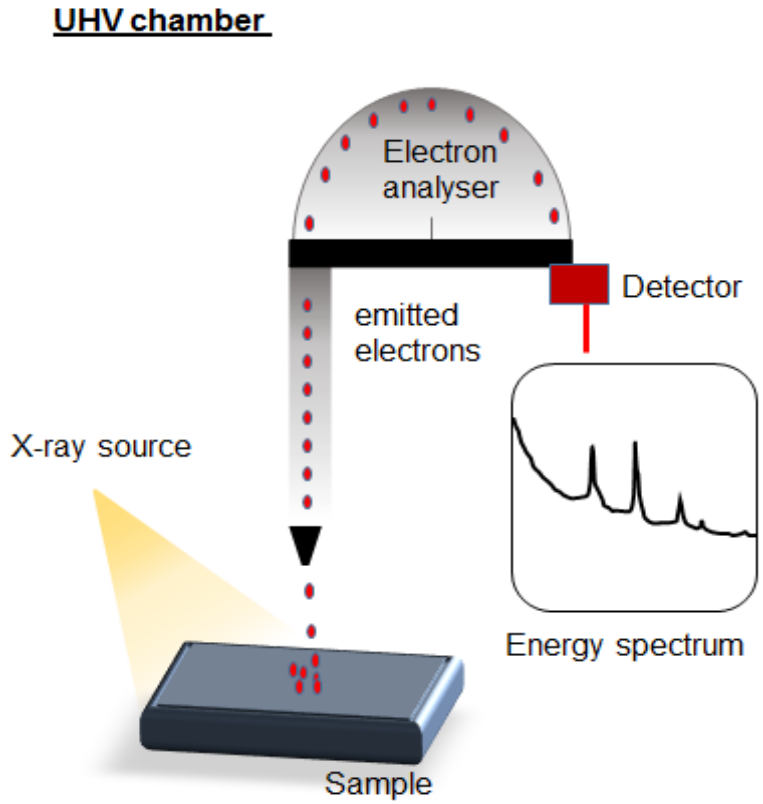

Figure 6: Schematic view describing a typical XPS experiment of a sample examined under ultra-high vacuum condition.

XPS measurements were carried out to determine the surface elemental composition of Au-Ni, Au-Cu and Au-Pt thin film materials. The samples were deposited as a continuous thin film on Si substrate with an area of 18 × 18 mm. Since the XPS chamber is connected to the UHV system, the samples were annealed and XPS measurements were carried out without exposure to air. The XPS features a twin anode X-ray source (Al K α and Mg K α) and hemispherical analyser (VG clam) at constant analyser energy (CAE). An analyser energy of 50 eV was used. The filament used in this work was the Al. In order to calibrate the peak position of the binding energy of the Au-Ni and Au-Cu systems, a sample containing a silver block was measured as a reference. The filament current was set at 4.41 A. The emission current was set at 10 mA. The measured area was determined

based on the slit size (a large round slit (⌀ 4mm) that covers an area of 2x2 mm of the thin film to be detected by the electron energy analyser. The number of points or places measured were five, which were distributed along the line between the rich Au and Ni rich or Cu rich or Pt rich (in case of Au-Cu and Au-Pt). The generated data of the XPS measurements were analysed using the CasaXPS software.

2.4.4 Atomic Force Microscopy (AFM)

AFM is a scanning probe microscopy technique that determines the topography of a sample surface by creating 3-dimensional images at high resolution within the nanometre scale. One of the most prominent features of this technique is that, unlike scanning tunnelling microscopy, investigation of the samples is not limited by their electrical conductivity as even those that are electrically insulated can be probed. The basic function of AFM depends on the atomic interaction forces (repulsion or attraction forces) between a tip and a sample. The tip works as a force sensor and it is located at the end of a spring-like cantilever made from a single crystal Si or Si-Ni. The forces of attraction or repulsion are formed depending on the distance between the tip and the surface (Figure 7). If the tip approaches the surface of a sample, a deflection of the cantilever occurs. The direction of this deflection is a function of the type of the force that is present. Vertical displacements are measured through a photodiode detector by monitoring the laser reflecting off the back of the cantilever and translates these deflections into an imaging signal.

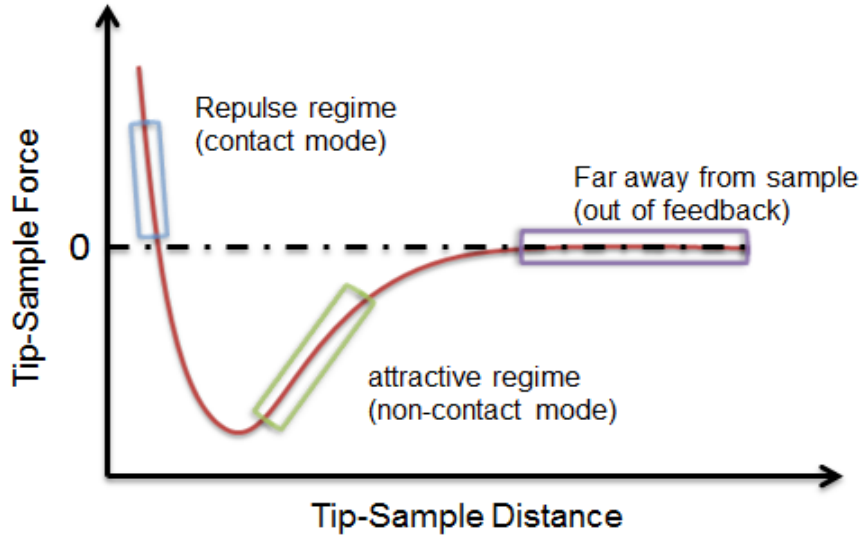

Figure 7: Force-distance relationship between a tip and a sample.

It should be noted that the distance between the tip and the sample determines the operation mode of the AFM, namely the contact mode and non-contact mode. In our study, the AFM was operated using the non-contact mode. In this mode, a feedback loop system is used to keep a constant oscillation amplitude of the tip whilst the tip oscillates above the sample at its resonance

frequency. When the vibrational frequency of the cantilever is reduced by the attraction force, a topographic image of the sample can be created by recording the distance between the tip-sample.

The AFM used in this work is the Keysight (formerly Agilent) Technologies 5600LS Atomic Force Microscope. The experiment was used to confirm the film thickness of the Au-Ni, Au-Cu thin film and Au-Pt samples. The tip used is a nano sensor product designed for the non-contact mode and the product number is PPP-NCLR-10. The type of tip is the Point Probe-Plus* n- doped Silicaon-SPM-Sensors. The tip thickness is 7.0 ± 10 µm with a length of 225 ± 10 µm and a width of 38 ± 7.5 µm. The resonance frequency of the tip is 146-236 KHz. The actual value of the resonance frequency was 169.059 (auto-tuned). The topography at the corner edges of the thin film was measured over a space of 50µm at a 0.7 line/s scan rate and a resolution of 256 points/lines.

2.5 Electrochemical Experiments

2.5.1 Conventional Electrochemical Method

Three electrochemical cell components were used for the cyclic voltammetry experiments (CVs) using a potentiosotat (PG580) provided by Uniscan instruments. Figure 8 displays a schematic picture of the electrochemical cell used. The tested working electrodes were 1 cm of Au (0.25 mm radii), Pt (0.25 mm radius), Ni (0.25 mm radius), Ag (0.25 mm radius) and Cu (0.25 mm radius). A commercial saturated calomel reference electrode (SCE), Fisher Scientific accumet, +0.241 V vs. SHE) was used. Prior to each electrochemical measurement, the electrolyte ($NaBH_4$ + NaOH alkaline solution) was purged with Ni for 15 minutes in order to avoid the presence of the air in the solution. The CV experiments were conducted both in the absence and the presence of $NaBH_4$ at room temperature.

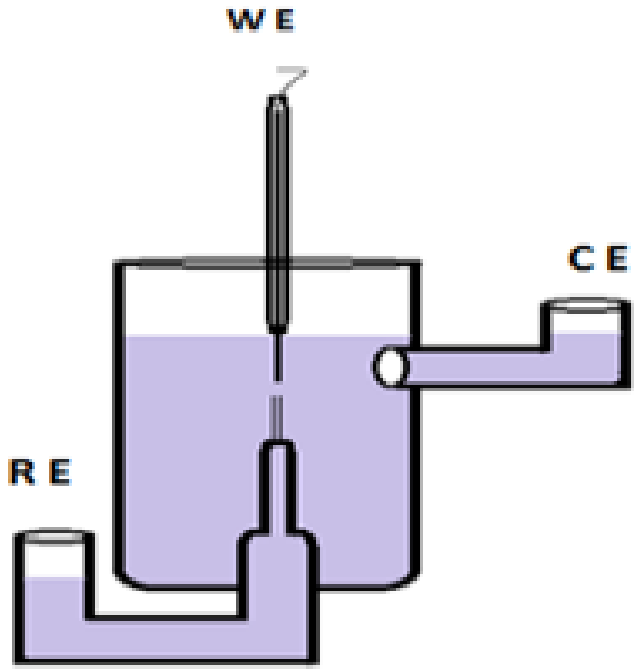

Figure 8: View illustrating the electrochemical cell used to study the oxidation of $NaBH_4$.

2.5.2 High Throughput Electrochemical Screening Method

High Throughput Electrochemical Screening Methods[78] were used to study the catalyst behaviour of each of Au-Ni, Au-Cu and Au-Pt binary systems. A silicon nitride (Si-N) substrate containing either (10x10) Indium Tin Oxide (ITO) pad arrays or (10x10) Au pad arrays discretely located in the centre were purposely used for the deposition of Au-Ni, Au-Cu and Au-Pt binary systems. An illustrative view of the 10 ×10 Au array (E-chem arrays) substrate is displayed in Figure 9. Each side of this substrate accommodates 25 Au contact pads connected individually to 25 working electrodes through Au tracks.

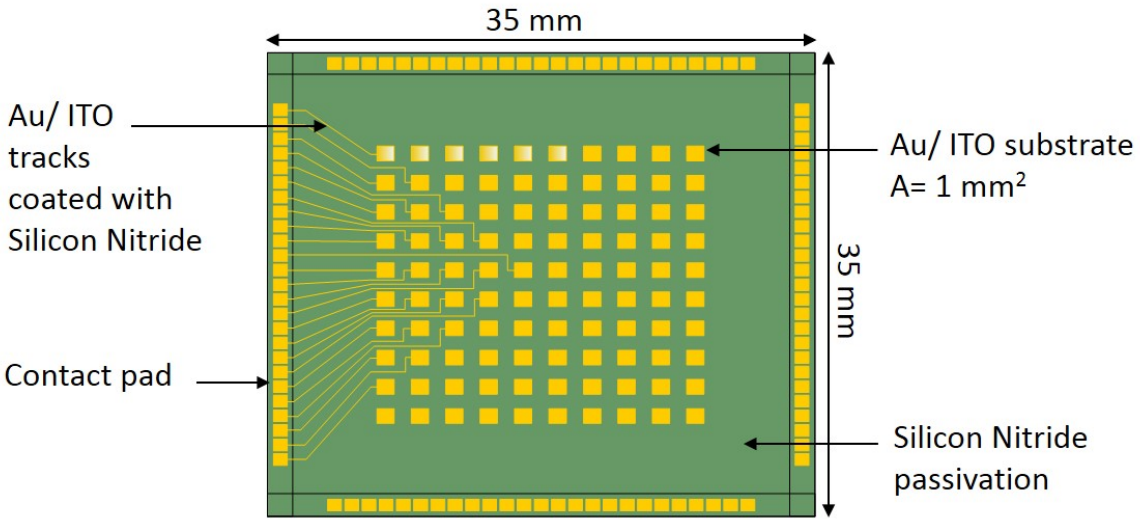

Figure 9: Schematic view showing the 10×10 E-chem arrays used in this experiment, which consists of individually addressable electrodes connected to the contact pads through Au or ITO tracks.

The High Throughput Electrochemical Screening experiment was carried out in the following steps (Figure 10). First a polytetrafluorethylene (PTFE) plate was placed, which works as an insulated base and holds the sample during the experiment. The sample was then mechanically (using screws) connected to a printed circuit board (PCB) for electrical connection. A gold ket, which is a rubber-shaped square wrapped around with fine bristles of gold, specifically designed to electrically link each contact pad on the sample with the PCB, was used. The PCB was connected to a custom-built single potentiostat with a pair of 100-channel current followers controlled by a computer. The current followers converted the returned current of 100 electrodes from the cell to voltage to be measured via PC A/D cards (PCI-DAS6402/16 data acquisition card (Talisman Electronic). The current follower sensitivity used in this experiment was 10 µA V^{-1}.

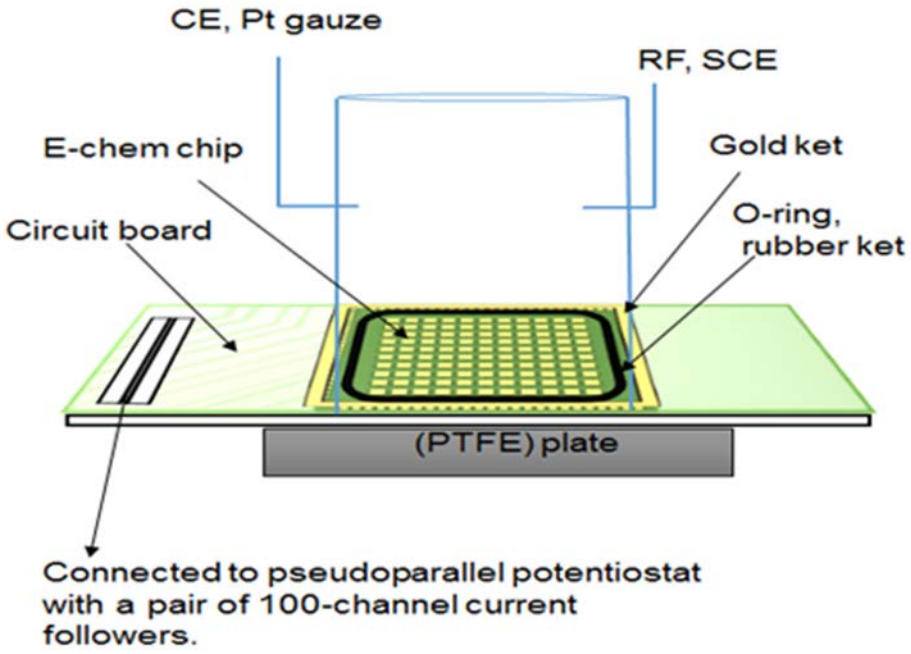

Figure 10: Schematic view of the electrochemical cell configurations which were used for screening the electrode arrays electrochemically.

Prior to each experiment, the electrochemical cells, which contain glass compartments, were rinsed with diluted ethanol (distilled water/ethanol mixture (50/50)) followed by distilled water to remove any contaminations. The electrochemical cell is specially designed to allow exposure of only electrode arrays to the electrolyte. An O-ring rubber ket was used to prevent the electrolyte from reaching any of the contact pads. The electrolyte was purged with Argon gas, which was connected through an inlet, for 15 min to evacuate air from the solution. SCE was used as a reference electrode, while a platinum mesh was used as a counter electrode.

Each binary alloy system was electrochemically screened in an alkaline solution of NaOH. Subsequently, the electrochemical cell was rinsed with distilled water and the used sample was replaced by a new one of the same deposited materials and tested in the presence of $NaBH_4$.

During the electrochemical screening experiment, the electrochemical reactions occurring at the surface of each electrode could be visualised using the High Throughput Data Analysis and Visualization for Electrochemistry (HT-DVAE) software made and developed by the Hayden research group. The HT-DVE enables the user to control all the experiment parameters necessary to carry out potentiostatic measurements. The software provides different options of setting the electrode potentials, the range of the measured current, the electrodes potential scan rate and provides close monitoring of the current-potential peaks for up to 5 electrodes simultaneously.

After conducting the electrochemical screening experiments, the data was analysed by the Paradise software developed by the Ilika group to allow different types of data analysis. Based on the acquired 10x10 CVs, the voltammogram of each electrode can be selected and presented

individually or an all in one voltammogram. In addition, the electrochemical data can be linked with the data of the electrode arrays' compositions. The software also enables identification of the onset potential of a defined current as a function of electrode position. Thus, the Paradise software was used to plot a number of combinatorial data to allow identification of general trends and active regions of the investigated Au-Ni, Au-Cu and Au-Pt thin film anode materials as a function of electrode composition.

2.6 Summary

This chapter has described the experimental methods, instruments, techniques and materials used in this project. The HT-PVD method was used to synthesise combinatorial libraries such as Au-Ni, Au-Cu and Au-Pt thin film materials. The electrochemical measurements were used to screen the combinatorial materials in a base electrolyte in the absence and the presence of the $NaBH_4$. The bulk composition of the Au-Ni, Au-Cu and Au-Pt thin films was confirmed by the EDX. Moreover, the phase structure of the thin film materials was identified by XRD using GADDS for fast data collection. The surface composition was determined by XPS using a sample containing a continuous film of the deposited materials. Furthermore, the thickness of the Au-Ni, Au-Cu and Au-Pt thin film materials were confirmed by the AFM measurements (results are shown in the Appendix).

Chapter 3 Catalytic Evaluation of Pure Catalysts for Direct BOR

3.1 Electrochemical Characterisation

Cyclic Voltammetry (CV) is regarded as a powerful technique that provides a rapid qualitative analysis, which is an electrochemical fingerprint of the sample under investigation. Although previous studies have characterised the electrochemical behaviour of the proposed pure metals towards the BOR under given experimental conditions using the CV technique, our initial goal was to establish a baseline of the potential range at which the anodic current peaks of the BOR on pure catalysts (Pt, Au, Ni, Ag, and Cu) can be well-defined and whether there are any distinct features that can possibly be studied before commencing our study for the BOR on the proposed binary alloy catalysts. After this basic information was recognized, we were able to continue with examining the alloy systems to determine the effect of the alloyed materials deposited in a wide range of compositions from voltammograms recorded using the high-throughput electrochemical screening method. Thus, a number of pure metals were studied in the absence and in the presence of the $NaBH_4$, with a view to preparing more efficient anode catalysts and demonstrating their activities with respect to the direct BOR.

The investigation of the direct BOR on pure metals using CV involves the immersion of the metal in a 1 M of NaOH solution containing 0.01 M of $NaBH_4$. CVs were recorded for Pt, Au, Ni, Ag and Cu at a scan rate of 25 mV s^{-1} at 25 ˚C to allow only diffusion-controlled electrode reactions.

3.1.1 The Electro-Oxidation of $NaBH_4$ on Pt

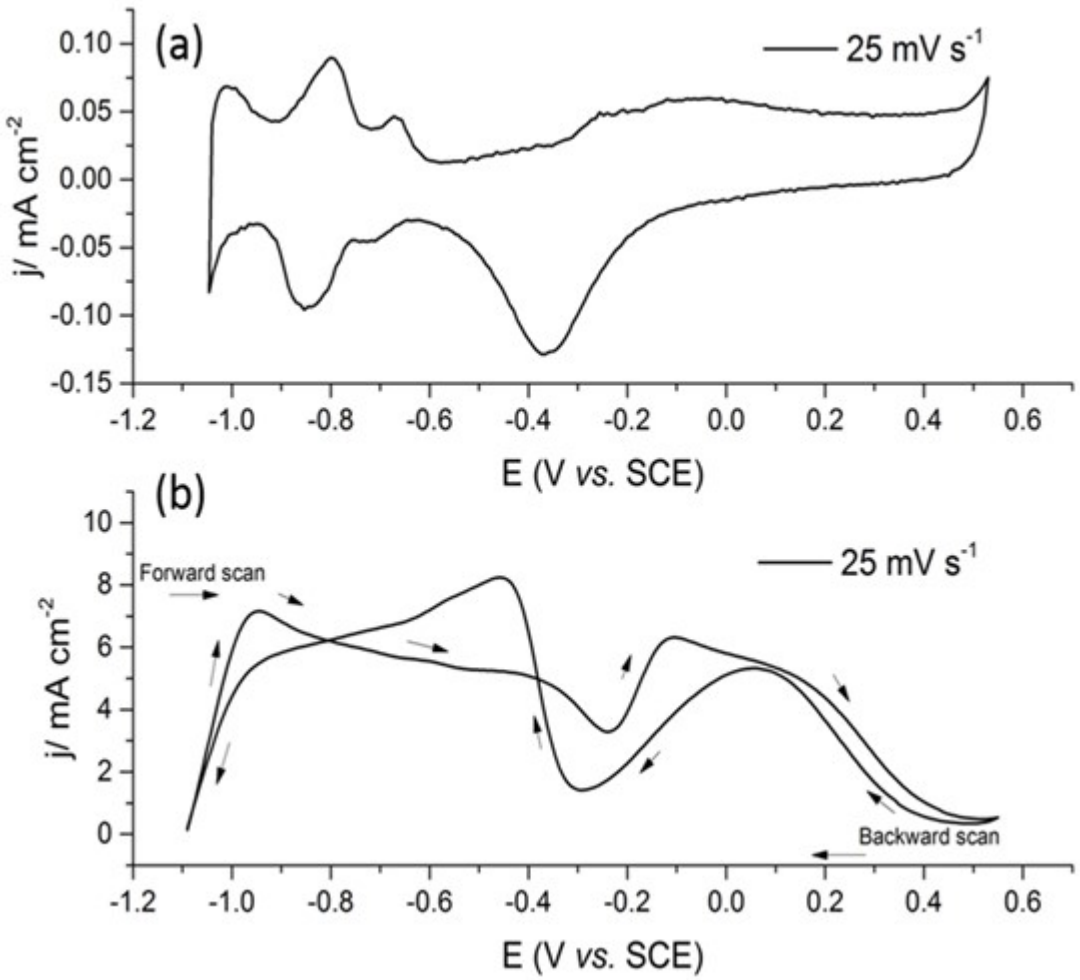

Figure 11: Cyclic voltammograms showing (a) a typical CV of Pt in 1 M of NaOH and (b) the electro-oxidation of 0.01 M $NaBH_4$ on Pt electrode (v =25 mV s^{-1}, N_2-saturated 1M NaOH electrolyte, T 293 K).

CV measurements were performed in both the absence and presence of $NaBH_4$ to study the electro-catalytic behaviour of Pt. As can be seen from Figure 11 (a), the typical CV curve of the Pt electrode recorded in 1 M of NaOH involves three distinct regions between -1.1 V_{SCE} and +0.55 V_{SEC} associated with the bulk hydrogen gaseous evolution/ oxidation and oxygen evolution reactions. The first region is in the potential range of -0.6 V_{SCE} to -0.9 $V_{SCE,}$ at which hydrogen adsorption and desorption processes are taking place at two pairs of cathodic and anodic peaks attributed to weakly and strongly bond hydrogen[81]. The second potential region is between -0.55 V_{SCE} and -0.6 V_{SCE}, at which non-Faradic processes are occurring, due to the double layer capacitance (charging and discharging). As the potential is proceeded to more positive values, oxidation processes associated with the oxide formation takes place due to subsequent adsorptions of OH species onto the Pt surface. Once the electrode potential is reversed, the formed oxide is reduced (stripped) and desorbed from the Pt surface.

The CV in the presence of the $NaBH_4$ displays a complicated CV shape. The typical CV of the borohydride on Pt involves four distinct oxidation peaks occurring at different potentials[39]. Figure 11 (b) shows the electro-oxidation of 0.01 M $NaBH_4$ in 1 M NaOH on the Pt electrode studied in the potential range between -1.1 V_{SCE} and +0.55 V_{SCE} at a scan rate of 25 mV s^{-1}. As can be seen in Figure 11 (b) on the forward scan, the first oxidation peak is taking place over a broad range between -1.0 V_{SCE} and -0.3 V_{SCE} with maximum of 7 mA cm^{-2}. Continuing the scan in the forward direction, a second oxidation peak at -0.1 V_{SCE} reaches a maximum of 6 mA cm^{-2}. As the potential is scanned further, the current of the second oxidation peak abruptly drops to its initial stage. During the backward scan, two cathodic peaks appear as oxidation processes where the current is maximum at +0.1 V_{SCE} and at -0.5 V_{SCE}.

Because of its natural ability to catalytically decompose the borohydride via the non-Faradaic process (the catalytic hydrolysis of the borohydride), the Pt is influenced by the oxidation of the evolved hydrogen. This indicates the complexity of the BOR process on the Pt surface. It can be observed that the oxidation potential of the first oxidation peak (Figure 11(b)) is in the region of the H_2 oxidation reaction generated from H_2O_{ad} between -1.0 V_{SCE} and -0.7 V_{SCE} (Figure 11(a)). This indicates that the first oxidation peak taking place in the presence of $NaBH_4$ is due to the H_2 oxidation produced by the catalytic hydrolysis chemical reaction and that the BH_{ad} is competing with the H_{ads} for the same catalytic site. A similar observation was reported by Gyenge et al. who found that after using a small concentration of hydrogen inhibitor (thiourea TU, $1.5x10^{-3}$), the BH_4^- CV was simplified, giving rise to one oxidation peak that was then assigned to the direct borohydride oxidation[39].

The catalytic hydrolysis reaction:

$BH_4^- + H_2O \rightarrow BH_3(OH^-) + H_2$ Equation 3-1

Electro-oxidation of the products: H_2 and BH_3OH^-

$½\ H_2 + OH^- \rightarrow H_2O + e^-$ Equation 3-2

and

$BH_3OH^- + 3OH^- \rightarrow BO_2^- + 3/2H_2 + H_2O + 3e^-$

The direct electro-oxidation of BH_4^-:

$BH_4^- + 4OH^- \rightarrow BO_2^- + 2H_2 + 2H_2O + 4e^-$ Equation 3-3

The detailed mechanism of the borohydride reaction on Pt remains uncertain. However, studies suggest that both the hydrolysis reaction and the direct oxidation of the borohydride via a 4-e^- process take place on the Pt surface (Equations from 3-1 to 3-3)[36, 39, 3]. This indicates that the

oxidation reaction taking place at -0.1 V_{SCE} can be assigned to the direct oxidation of BH_4^-, which is in agreement with[39,3].

It is interesting to note that the current of the direct BOR abruptly drops at about +0.1 V_{SCE} due to the adsorbed OH/O species on the Pt surface. As more oxide species are formed at the Pt surface, a significant current drop develops in the potential range immediately after the direct borohydride oxidation. The BOR remains inhibited on the Pt surface until the Pt becomes active, due to the partial Pt-OH reduction taking place on the reverse scan, and then increases sharply. The oxidation reaction occurring on the reverse scan is associated with the intermediate products of the direct oxidation of the borohydride (also has been reported in[39,82]). This reaction decreases when the electrode potential proceeds towards a more negative potential and possibly competes with the hydrogen adsorption resulting in a decrease in the current density.

3.1.2 The Electro-Oxidation of $NaBH_4$ on Au

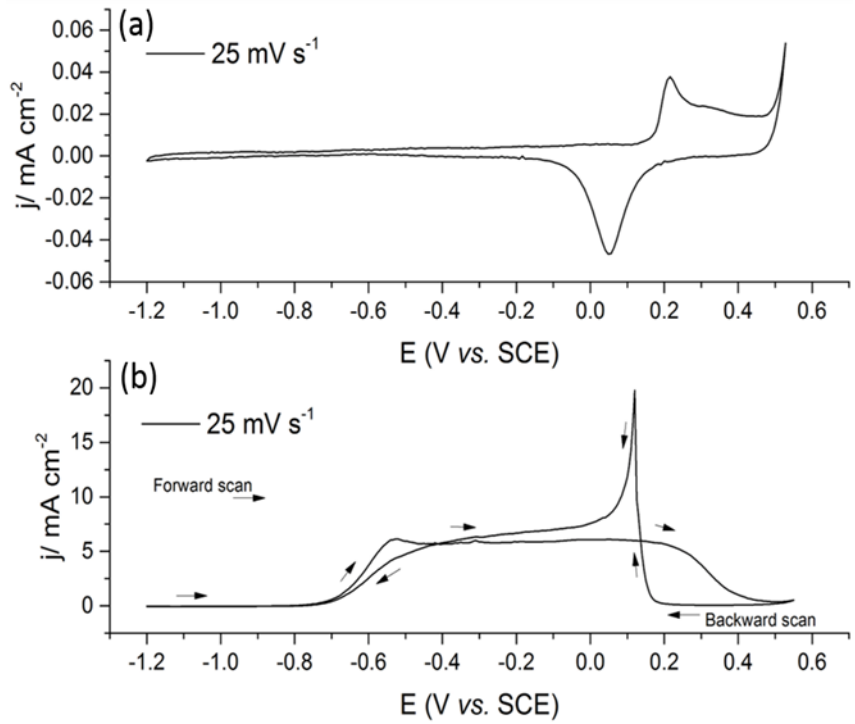

Figure 12: Voltammograms showing (a) a typical CV of the oxidation of 1M of NaOH and (b) the electro-oxidation of 0.01M of the $NaBH_4$ on Au wire electrode along with (v = 25 mV s^{-1}, N_2-saturated 1M NaOH electrolyte, T 293 K).

In order to study the behaviour of the Au electrode towards the BH_4^- ion, CV measurements were applied in both the absence and in the presence of $NaBH_4$. Figure 12 (a) shows a typical CV of the Au in 1 M of NaOH along with (b) the electro-oxidation of 0.01 M of $NaBH_4$ in 1 M of NaOH. In both cases, the electrode potential was cycled in the range between -1.2 V_{SCE} and +0.55 V_{SCE} at 25 mV s^{-1} for comparison. The electrochemical behaviour of Au in 1 M of NaOH involves a simple CV

shape consisting of a double-layer charging/discharging followed by the formation/ removal of Au oxide species taking place at high potential (-0.1 V_{SCE} to +0.4 V_{SCE}) and oxygen evolution starting at +0.5 V_{SCE}.

The shape of the voltammogram in the presence of the borohydride (Figure 12(b)) is also complicated by the irreversible behaviour of the oxidation of the borohydride and the oxidation of the intermediates. During the forward scan, a broad anodic peak occurs over a wide range of negative and positive potentials that was not seen in the absence of the $NaBH_4$. This anodic peak reaches a maximum of ca. 7 mA cm^{-2} at -0.55 V_{SCE} and extends until +0.3 V_{SCE}. As the potential was scanned further towards more positive (> +0.35 V_{SCE}), the current showed a significant drop. When the potential was scanned back, a sharp oxidation peak appeared as a cathodic peak is taking place at +0.15 V_{SCE}. This peak can be characterised not only by its sharpness but also by its long tail that extends until -0.6 V_{SCE}.

Au is regarded as being non-catalytic with respect to the hydrolysis of the BH_4^-, which indicates that the electro-oxidation reaction taking place on the forward scan at -0.68 V_{SCE} (j, threshold= 1 mA cm^{-2}) is attributed to the direct oxidation of the BH_4^- via 8-electron electrochemical process (Equation 3-4)[39].

The direct oxidation of BH_4^-:

$$BH_4^- + 8OH^- \rightarrow BO_2^- + 6H_2O + 8e^- \qquad \text{Equation 3-4}$$

It is difficult to identify the oxidation reactions taking place at high potential. However, the reaction mechanism of the BH_4^- oxidation occurring on the Au electrode, as suggested by Bard et al.[48] can be employed and compared with our results. Bard et al. found that the oxidation of BH_4^- on Au is an 8-electron process and follows electrochemical-chemical-electrochemical (ECE) reaction mechanism type [48] (Equations from 3-5 to 3-7).

BH_4^- Oxidation reaction mechanism (ECE):

$$BH_4^- \leftrightarrow BH_4^{\cdot} + e^- \quad \textbf{(E)} \qquad \text{Equation 3-5}$$

$$BH_4^{\cdot} + OH^- \rightarrow BH_3^- + H_2O \text{ (very fast reaction)} \quad \textbf{(C)} \qquad \text{Equation 3-6}$$

$$BH_3^- \leftrightarrow BH_3 + e^- \quad \textbf{(E)} \qquad \text{Equation 3-7}$$

This can be explained as follows: (1) an adsorption step accompanied by electron transfer reaction followed by (2) a chemical reaction in which the adsorbed $BH_4^{\cdot}$ reacts with a hydroxyl ion to break a B-H bond and forms BH_3^-. (3) The product of this electrochemical reaction (intermediates) is expected to undergo further oxidation and complete the total $8e^-$ process (equation 3.8 see below)[82]. This indicates that the oxidation reaction occurring at +0.3 V_{SCE} may

correspond to the final oxidation as suggested by the proposed reaction mechanism. However, this oxidation reaction is possibly supressed because of the oxide layer formed between +0.35 V_{SCE} and +0.6 V_{SCE}. When the Au surface is renewed, the remaining BH_3OH^- is oxidised, proceeding on the reverse scan at +0.2 V_{SCE} to complete the BH_4^- oxidation process. This explains why the potential at which the oxidation of the intermediate reaction (BH_3OH^-) appears at different potentials on the forward and reverse scans.

The oxidation of BH_3OH^- (intermediates products)

$$BH_3OH^- + 3OH^- \rightarrow BO_2^- + 3/2H_2 + 2H_2O + 3e^- \qquad \text{Equation 3-8}$$

3.1.3 The Electro-Oxidation of $NaBH_4$ on Ni

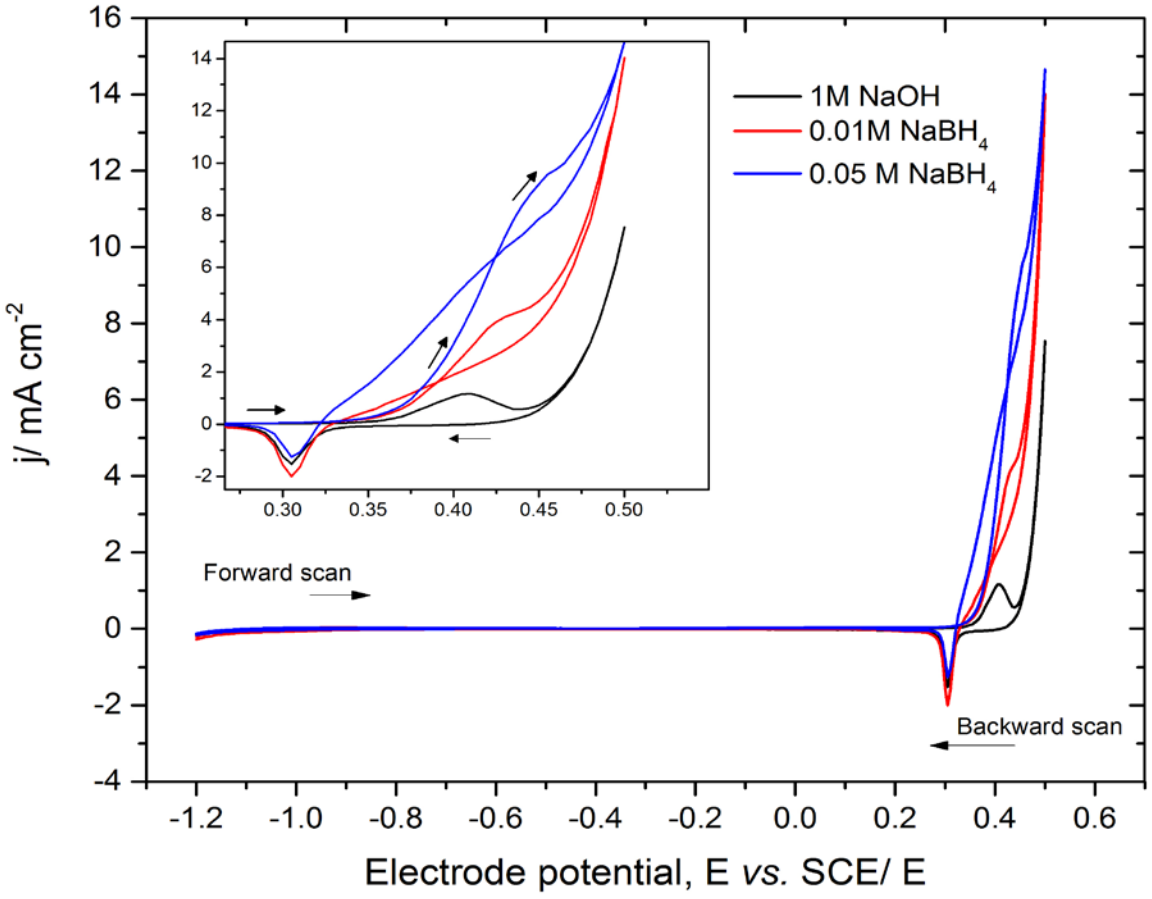

Figure 13: Voltammograms showing the electro-oxidation of BH_4^- on the Ni wire electrode displayed as 1 M of NaOH, 0.01 M and 0.05 M of $NaBH_4$, and an inset graph showing an enlarged area of the redox reactions (v =25 mV s^{-1}, N_2-saturated 1M NaOH electrolyte, T 293 K).

To assess the catalytic behaviour of the Ni electrode towards the BH_4^- ion, CV experiments were carried out in the absence and in the presence of $NaBH_4$. For the purpose of clarity, Figure 13 shows the electro-oxidation of 1 M of NaOH as well as different concentrations of $NaBH_4$,

including 0.01 M and 0.05 M, which are presented on the same voltammogram. The electrode potential was studied in the range between -1.2 V_{SCE} and +0.55 V_{SCE} at a scan rate of 25 mV s^{-1}. On the forward scan, one can see three distinctive anodic peaks with maximum of 1 mA cm^{-2}, 4 mA cm^{-2} and 10 mA cm^{-2} in 1 M of NaOH as well as 0.01 M and 0.05 M of $NaBH_4$ respectively, at +0.4 V_{SCE}. The oxidation peaks are difficult to distinguish from the oxygen evolution current at more positive potentials. However, the inset graph clearly shows the oxidation currents produced at +0.4 V_{SCE}. When the electrolyte contains only 1 M of NaOH, the anodic peak is small compared to that of the $NaBH_4$ electrolytes. However, in the presence of 0.01 M and 0.05 M of the $NaBH_4$, the produced current increases as the concentration of the $NaBH_4$ increases. On the reverse scan, the cathodic peaks showed no significant change in terms of the current density indicating that the oxide removal is the only feature in the CV. This suggests that the changes in the electrochemical behaviour are directly linked to the electrolyte, and that the presence of the borohydride, may have a promoting effect in increasing the anodic peak.

The CV data for Ni (Figure 13) 1M of NaOH showed that after the formation of the $Ni(OH)_2$ took place at negative potentials on the Ni surface, the $Ni(OH)_2$ is oxidised to NiOOH at a positive potential (+0.4 V_{SCE}) according to the following reactions:

$$Ni + 2OH^- \rightarrow Ni(OH)_2 + 2e^- \qquad \text{Equation 3-9}$$

$$Ni(OH)_2 + OH^- \rightarrow NiOOH + H_2O + e^- \qquad \text{Equation 3-10}$$

This may lead to the conclusion that the BH_4^- is supressed by the formation of the oxide layer at negative potentials, but catalytic turnover appears as the NiOOH phase is present on the surface, resulting in an increase in the activity of the BH_4^- oxidation reaction. Therefore, the anodic current peak observed in the presence of the $NaBH_4$ at +0.38 V_{SCE} (j, threshold= 1 mA cm^{-2}) can be attributed to the BOR (Figure 13) and this is in line with the findings in the literature[58]. The electro-oxidation of the $NaBH_4$ on the Ni electrode is covered in the literature within a small area. Most studies, in this regard, deal with studying the electro-catalyst behaviour of Ni-bimetallic, including Au-Ni [83], Pt-Ni [3] and Ni-Ru/C [84]. The studies, including [85] and [58], have investigated the oxidation of $NaBH_4$ on Ni/C and Ni/Zn-Ni, respectively. It has been reported that the electro-oxidation of the $NaBH_4$ occurs at more positive potentials. The electro-oxidation of $NaBH_4$ is suggested to occur as described in [85] and [58] :

$$NiOOH + NaBH_4 \rightarrow Ni(OH)_2 + \text{oxidation products of } NaBH_4 \qquad \text{Equation 3-11}$$

3.1.4 The Electro-Oxidation of $NaBH_4$ on Ag

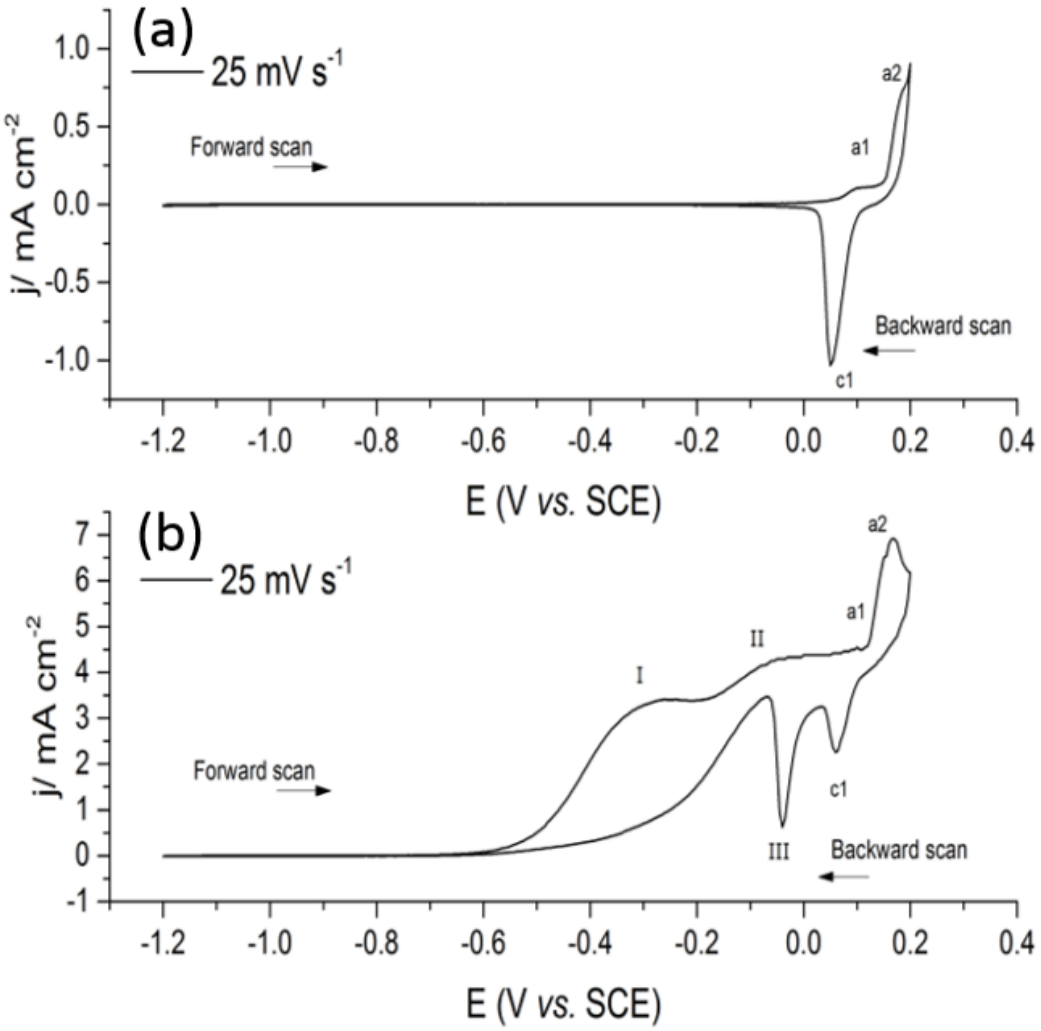

Figure 14: Voltammograms showing (a) the electro-oxidation of 1 M of NaOH and (b) 0.01 M of $NaBH_4$ on Ag electrode (v =25 mV s^{-1}, N_2-saturated 1M NaOH electrolyte, T 293 K).

CV measurements were performed to investigate the electro-catalyst behaviour of Ag towards the electro-oxidation reaction of the $NaBH_4$. Figure 14 (a) displays the electrochemical behaviour of Ag in 1 M of NaOH and (b) in 0.01 M of $NaBH_4$. As can be seen, in the absence of $NaBH_4$, at low potentials, there are no clear peaks. As the potential is further increased, two oxidation peaks associated with Ag_2-O and Ag-O take place on the forward scan at +0.1 V_{SCE} and +0.2 V_{SCE}, albeit with a reduction peak taking place on the backward scan at +0.1 V_{SCE} (in agreement with [57]). In the presence of the $NaBH_4$, the CV curve shows that the oxidation peaks appeared in the absence of $NaBH_4$ but there is appreciable difference in the plotted CV shaped curve. A well-defined anodic peak became apparent with a maximum of 3.5 mA cm^{-2} at a more negative potential (-0.35 V_{SCE}) than those that appeared for the Ag_2-O. As the potential increases, the current is much greater than that of peak I due to the oxidation peak appearing as a cathodic peak on the reverse sweep at -0.1 V_{SCE}.

The electrode behaviour of the Ag has been considered as noncatalytic with respect to the hydrolysis reaction [86] . This indicates that the appearance of the anodic peak (I) at a more negative potential (-0.45 $V_{SCE,}$ at j, threshold= 1 mA cm^{-2}) after the addition of the borohydride could be due to the direct oxidation of the BH_4^-. This is in partial agreement with [57], which reported that the direct oxidation took place at -0.3 V_{SCE}. It is possible that the oxidation of BH_4^- on Ag may follow similar electrode behaviour as Au, meaning that the 8-electron oxidation process on Ag follows a similar reaction mechanism as Au. This explains that the oxidation reaction occurring on the backward scan at -0.1 V_{SCE} could be due to the electrochemical oxidation reaction of the intermediate (BH_3OH^-).

3.1.5 The Electro-Oxidation of $NaBH_4$ on Cu

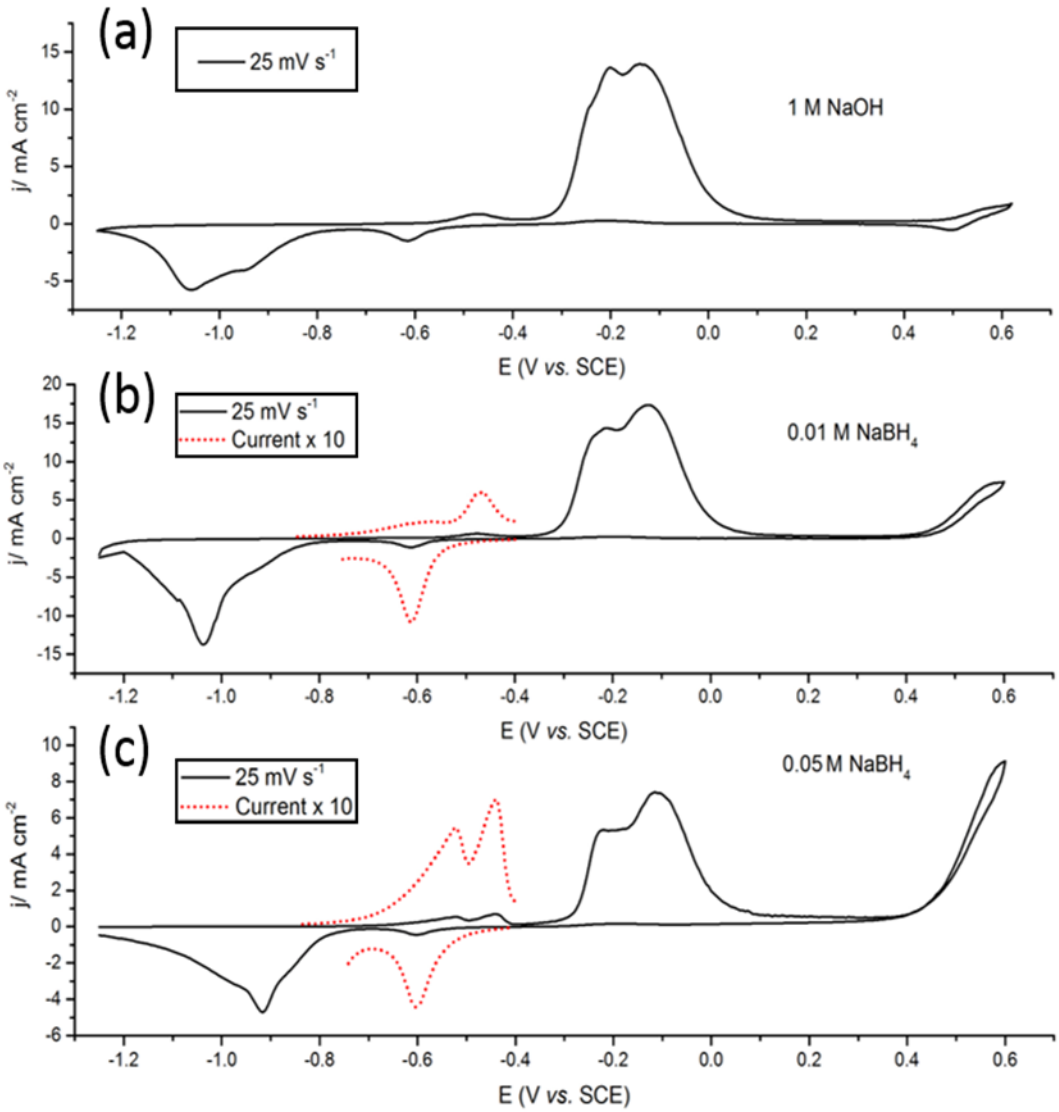

Figure 15: Cyclic voltammograms showing (a) the oxidation of 1 M of NaOH and ((b) and (c)) different $NaBH_4$ concentrations (0.01 M and 0.05 M) on the Cu wire electrode (v =25 mV s^{-1}, N_2-saturated 1M NaOH electrolyte, T 293 K).

In order to investigate the electro-catalyst behaviour of the Cu electrode towards the oxidation of BH_4^-, CV measurements were carried out. The electrode potential was cycled in the range between -1.25 V_{SCE} and +0.6 V_{SCE} at 25 mV s^{-1}. Figure 15 (a) shows the CVs of the Cu electrode in 1M of NaOH as well as in the presence of $NaBH_4$ 0.01 M (b) and 0.05 M (c), respectively.

On the forward scan, three separate anodic peaks can be seen during the oxidation of 1M of NaOH on the Cu electrode (Figure 15 (a)). These peaks occurred at different potentials and correspond to the formation of different forms of oxides[87]. The first anodic peak, starting at -0.45 V_{SCE}, corresponds to the formation of the cuprous oxide (Cu_2O), while the second anodic peak between -0.3 V_{SCE} and +0.1 V_{SCE} is due to the oxidation of the Cu_2O to either CuO or $Cu(OH)_2$ or both[87]. The anodic peak appearing at high potential between +0.5 V_{SCE} and +0.55 V_{SCE} (a3) corresponds to the oxidation of the copper sesquioxide (Cu_2O_3)[87].

It can be seen from Figure 15 that the electrode behaviour showed different trends with varying concentrations of $NaBH_4$ at negative and positive potentials. The most prominent trend was the increase in current density that can be clearly observed in the current near the oxygen evolution at +0.45 V_{SCE} (j, threshold= 1 mA cm^{-2}). This can be attributed to the borohydride oxidation. Similarly, the BOR was also observed at +0.45 V_{SCE}[88]. At a negative potential, the oxidation of 0.01 M of the $NaBH_4$ shows no apparent difference along the potential window from -1.25 V_{SCE} to -0.3 V_{SCE} (Figure 15 (b)). However, when the 0.05 M concentration was added (Figure 15 (c)), an anodic peak appeared at a more negative potential between -0.6 V_{SCE} and -0.5 V_{SCE}. This anodic peak has been reported for the oxidation of the hydrolysis products[45], indicating that the Cu catalyst can be affected by the adsorption of the oxide species and the hydrolysis reaction that leads to the suppression of the BOR to be oxidised at a low onset potential. Therefore, bimetallic catalysts may explain this process by reducing the adsorption of O_2 to allow for better catalytic activity.

3.2 Conclusion

The catalytic activity of the electrode materials including Pt, Au, Ni, Ag and Cu have been evaluated by CV. There is a significant difference between the examined metals in terms of the onset potentials for the direct BOR. The results show that the direct BOR on Au and Ag wire electrodes occurred more at negative potentials compared to Pt, Ni and Cu. Figure 16 shows the equilibrium potential of the direct BOR versus SHE. The direct BOR of the 8-e^- BH_4^- process takes place at -1.24 V_{SHE}, whilst on Au, Ag, Pt, Ni and Cu electrodes take place at -0.43 V_{SHE}, -0.21 V_{SHE}, +0.04 V_{SHE}, +0.62 V_{SHE} and +0.69 V_{SHE}, respectively. The electro-catalyst behaviour of the Pt towards the BH_4^- oxidation reaction produced a complicated CV shape compared to other metals. The BOR was influenced by the catalytic spontaneous hydrolysis reaction. Therefore, the onset potential of the BOR was forced to more positive potentials. Moreover, the adsorption of OH/O

occurred more readily on Ni and Cu producing oxide layer, which sharply supressed the oxidation of the BH_4^- ion.

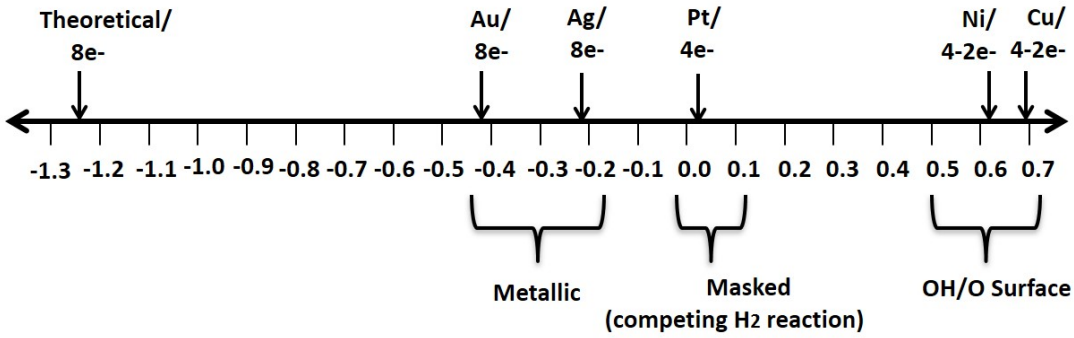

Figure 16: Diagram showing the difference between the onset potential of the direct BOR (at j, threshold= 1 mA cm^{-2}, except for Pt due to H_2 oxidation) vs. SHE taking place on different catalyst materials (Au, Ag, Pt, Ni, and Cu) and the theoretical equilibrium potential.

The CVs investigated in this study for the pure catalysts are of great importance both fundamentally and practically to verify the effects of alloying. The main factor affecting the catalytic activity is the key to tuning a catalyst. The question is what factor can be used to turn off the hydrolysis reaction pathway and reduce the accumulation of the oxide formation to oxidise the borohydride ion at much lower overpotentials. The catalytic activity and selectivity can be affected by ligand and ensemble effects or by the bifunctional nature on the alloy catalyst. Isolating these effects is difficult. However, to understand how these factors affect catalytic activity and selectivity, a model was proposed for the studied single-metals by the free energy of adsorption of OH_{ads} (ΔG_{OH}) as well as the free energy of adsorption of H_{ads} (ΔG_H). This allowed us to consider the consequences of alloying with Au on catalytic properties for the direct BOR.

Figures 17 and 18 show the relationship between ΔG_{OH} and ΔG_H , respectively, (calculated theoretically by Norskov et al.[13] on metal surfaces) and the overpotential of the direct BOR for the examined metals. The results displayed in Figure 17 show a correlation between the ΔG_{OH} and the catalytic activity for BOR, indicating that metals with higher ΔG_{OH} values (such as Au, Ag and Pt) showed better catalytic activity for BOR than those with low ΔG_{OH} values (Ni and Cu). In the case of H_{ads} (Figure 18), the trend for the ΔG_H is much lower on Ni and Pt compared to Au, Ag and Cu. Therefore, it can be predicated that alloying Au with Pt or Ni or Cu could be very effective for altering its adsorption energy to allow catalysing the direct BOR at a lower overpotential. This will be explored in depth later in this thesis.

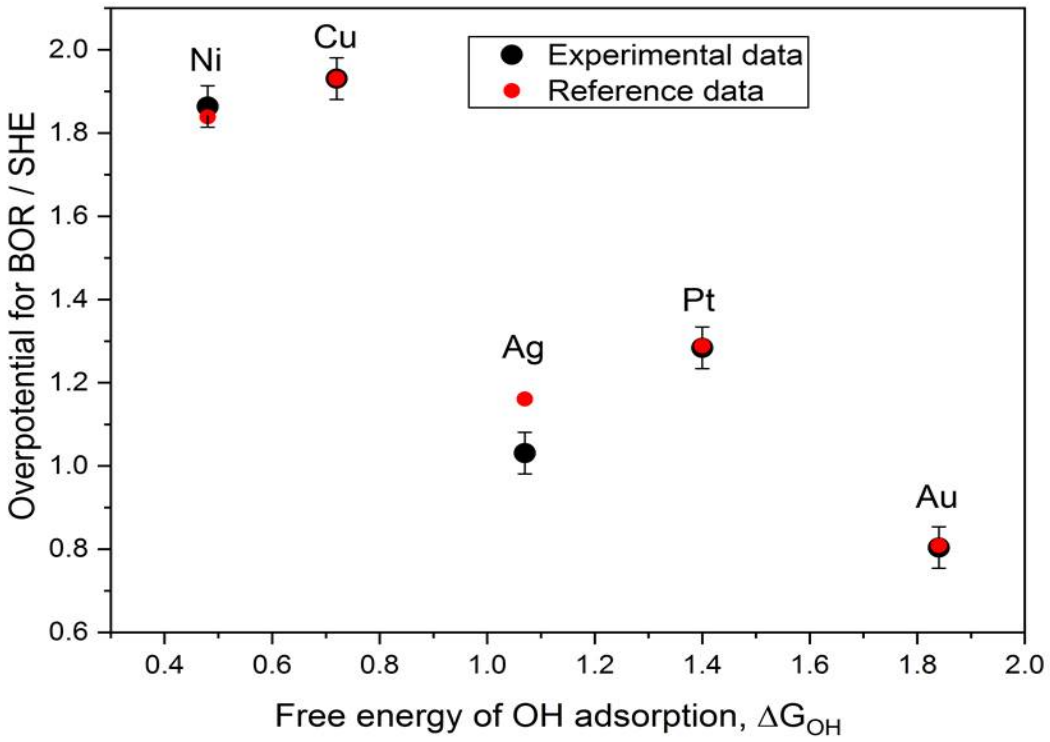

Figure 17: Relationship between the BOR and the free energy of OH adsorption on Au[39], Pt[39], Ag[57], Ni[85] and Cu[88].

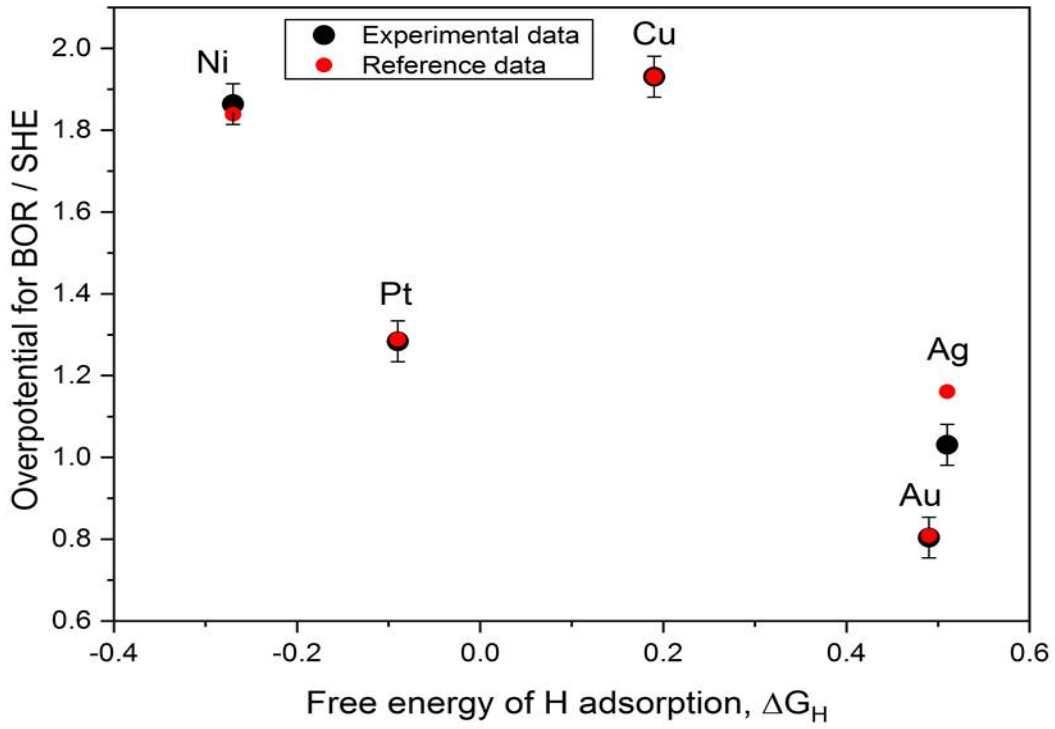

Figure 18: Relationship between the BOR and the free energy of H adsorption on Au[39], Pt[39], Ag[57], Ni[85] and Cu[88].

Chapter 4 Au-Ni Alloy Catalysts for Direct BOR

4.1 The Au-Ni Alloy System

4.1.1 Surface Science Studies of the Au-Ni Alloy System

Nickel has been extensively used in heterogeneous catalysis and increasingly as an electro-catalyst. It is often alloyed with other metals in order to optimise its catalytic activity and selectivity. A literature review is included in this chapter to provide background information related to the Au-Ni surfaces and specifically their role in catalysis for the direct BOR. Thus, the purpose of this chapter is three-fold: First, to highlight the literature by reviewing state of the art surface studies and catalysis of the Au-Ni alloy system. Second, to provide information of the bulk/ surface composition and the phase structure of the Au-Ni alloy samples characterised by high throughput methods including SEM/EDX, XRD and XPS. Third, to evaluate the Au-Ni alloy electrochemically, discuss its catalytic behaviour towards the direct BOR reaction, and identify the optimal catalyst in the Au-Ni alloy library for the DBFCs.

Surface chemistry is important in understanding the properties that appear from bimetallic systems in terms of the structural and the electronic properties. The properties of a single metal may differ when it is alloyed with another metal[89]. It is important to recognise these properties through the fundamentals, synthesis and characterisations of the surface, since this will help in understanding the factors affecting the catalyst. The following section will discuss studies that have previously synthesised and characterised the Au-Ni alloy system.

The bulk equilibrium phase diagram of the Au-Ni alloy consists of two phases: liquid and face-centred cubic (FCC), with a large miscibility gap (Figure 19[90])[91]. At higher temperatures (above the miscibility gap), a complete solubility at which a homogenous phase of the random (short-range-order) Au-Ni solid solution exists[92], while at lower temperatures (below the miscibility gap), there is a tendency towards a phase separation, resulting in the coexistence of a two-phase mixture of the ordered (clustering of like atoms) Au-Ni alloy system[93].

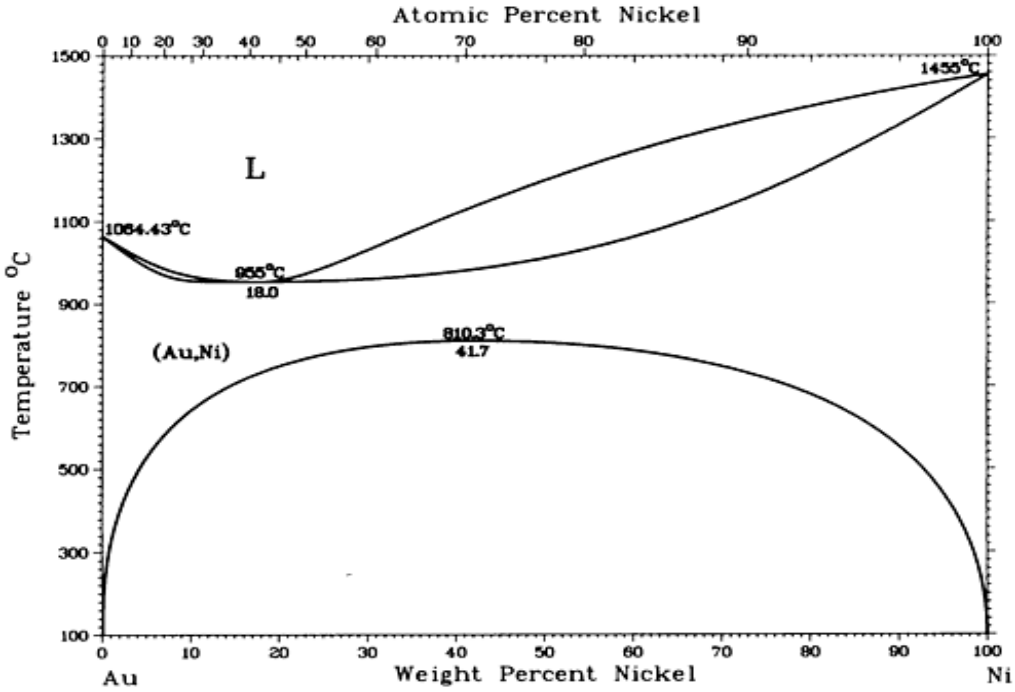

Figure 19: Phase equilibrium diagram of the Au-Ni alloy system showing the region of stability of different phases from-100 at %Ni to Au-0 at %Ni over a range of temperatures[90].

Non-equilibrated Au-Ni solid solutions have been synthesised via different methods, including quenching, ion sputtering and evaporative PVD. Quenching has been carried out through the rapid annealing from higher temperatures to lower temperatures[94], resulting in Au-Ni solid solutions for the entire composition of the Au-Ni alloy system.

Recently, Au-Ni alloys have been examined using other methods, including ion-beam sputter deposition and MBE[95-96]. A homogenous phase of the random Au-Ni solid solution, deposited at room temperature, in the range of Au-20 at % Ni has been confirmed by X-Ray Diffraction (XRD) using the sputter method. The XRD diffractograms for the random Au-Ni alloy were compared with the ordered Au-Ni alloy system. Apart from the Au (111) diffraction peaks, there was no appearance of the Ni (111) or the Ni (200) diffraction peaks for the deposited Au-Ni alloy. In order to obtain the two-phase mixtures, such as equilibrated Au-20 at % Ni alloy, heat treatment was applied at 600°C for 30 seconds. As a result, Ni (111) along with the Ni (200) diffraction peaks were reported.

Simultaneous synthesis of different coverage of Au-Ni ultrathin film via MBE has been characterised using surface analytical probes[97]. This includes X-ray and UV photoemissions spectroscopy (UPS and XPS) and temperature programmed desorption. The investigation involved a comparison of the co-deposited Au/Ni thin film (at room temperature and after annealing) once with Au and then with Ni pure metals. The intensity of the Au (4f) core level spectra remained the same for all samples, even after heat treatment, while there was a noticeable change in the intensity of the Ni (2p) core level. A reduction of 30% in the intensity of the Ni (2p) core level

spectra was reported for the co-deposited Au/Ni. After annealing, at 570K for 10 min, another decrease of 30% of the same peak intensity was reported. A shift in 0.2 eV towards lower binding energy values of the Au (4f) core level was also reported. This shift has been found at a small atomic ratio of the Au/Ni thin film, while no shift has been reported for higher atomic ratios of the Au/Ni thin film.

The Au/Ni thin film layers (10ML Ni/ 10ML Au/ Ru (0001)) deposited by evaporation were investigated at different annealing temperatures, ranging between 400 to 800K[98]. It was found that Au segregates at the surface after applying heat treatment to the unannealed Au/Ni thin film layers. X-ray photoelectron spectroscopy (XPS) measurements were used to study the interaction of Au and Ni atoms at the surface as a function of annealing. A gradual increase in the intensity of the Au (4f) core level was reported when increasing the temperature. On the other hand, a relative decrease in the intensity of the Ni (2p) core level was detected. Furthermore, a shift towards lower binding energy for both Au ($4f_{7/2}$) and Ni ($2p_{3/2}$) was observed. These binding energies shifted from 83.8 eV at 400 K to 83.7 eV at 800 k, and from 852.2 eV (at 400 K) to 851.6 eV (at 800 K) of the Au ($4f_{7/2}$) Au and the Ni ($2p_{3/2}$) core levels, respectively.

4.1.2 Au-Ni Alloy Anode Electro-catalysis in the DBFC

The performance (activity and selectivity) of the catalyst of a metal can be enhanced by alloying it with a second metal. Alloying Au with Ni, for instance, has been used in many applications since they have shown better performance, such as in the steam reforming of the hydrocarbons[99], hydro-dechlorination[100] and low temperature CO oxidation[101-102]. Recently, the Au-Ni alloy system was tested as a potential catalyst for the DBFCs, and the catalytic behaviour of the Au-Ni in catalysing the BH_4^- oxidation is reviewed below.

Peiying et al. prepared different compositions of carbon supported Au-Ni nanoparticles alloy materials to verify their catalytic activities with respect to the BH_4^- oxidation[83]. The electro-oxidation of 0.05 M $NaBH_4$ in 3 M of NaOH on each of $Au_{80}Ni_{20}$, $Au_{58}Ni_{42}$ and $Au_{41}Ni_{59}$ was measured by CV at a scan rate of 20 mV s^{-1}. An offset by 0.15 V towards a negative potential was recorded for the direct BOR on the Au_x-Ni_{x-1} compared to the Au/C. In addition, an increase in the peak current density for the Au-Ni alloy (as a function of the atomic ratio) compared to the peak current density for the Au/C was observed. The highest peak current density was recorded for the $Au_{41}Ni_{59}$/C electrode. The current density of this catalyst was more than double that for that of pure gold. The results obtained from the electrochemical measurements indicate that the Au-Ni alloy exhibits better performance than the non-alloyed Au.

In another study, the oxidation of 0.05 M $NaBH_4$ on nano-structured Au-Ni/Ti[103] was investigated by CV. The electrode kinetics and the catalytic activity of the Au-Ni electro-catalyst in relation to

different Au loadings were compared. The onset potential of the direct BOR was reported at -0.7 V *vs*. Ag/AgCl/KCl_{sat}. At a lower Au loading (0.91 μg_{Au} cm^{-2}) a shift towards a positive potential was occurring. However, at a higher Au loading (8.42 μg_{Au} cm^{-2}), there was a small shift towards negative potential. The authors concluded that the nano-Au (Ni)/Ti exhibited a higher electro-catalytic activity toward BH_4^- oxidation as compared to that on pure Au.

The composition and structure of a catalyst plays a key role in determining its performance. In the present study, since the electrochemical reactions occur on the surface of the Au-Ni alloy catalysts, the primary analysis aimed to define their bulk/ surface composition and structure respectively. Each of these will be characterised separately. Subsequently, the electrochemical behaviour of the Au-Ni catalysts towards the BOR will be analysed and discussed.

4.2 High Throughput Characterisation of the Au-Ni Alloy Catalysts

4.2.1 Bulk Composition Analysis of the Au-Ni Alloys

The bulk composition of the Au-Ni alloys was measured using SEM-EDX. The goal was to deposit a wide range of composition along the substrate. The presence of the wedge shutter during the HT-PVD deposition resulted in achievement of a compositional gradient. Figure 20 shows the atomic percentage of Au and Ni with respect to the position (x, y) in the ITO electrochemical array illustrated by composition maps.

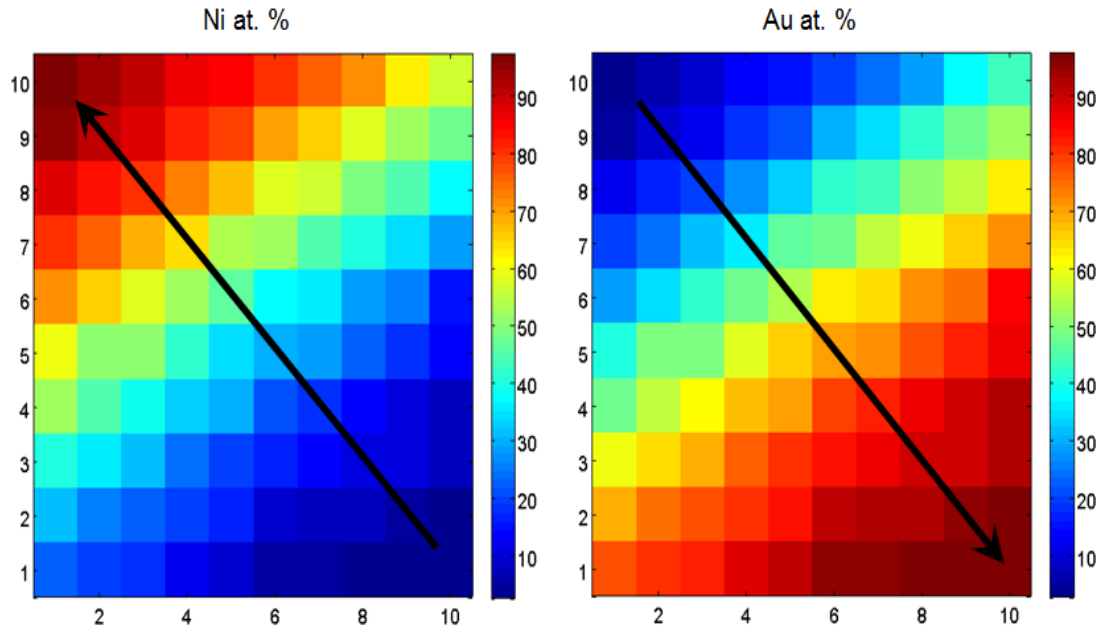

Figure 20: Composition map of Au and Ni contents in a sample of Au-Ni alloys deposited on the ITO electrochemical array. The arrows define the growth direction of each metal.

As shown, there are 100 samples with a different composition for each catalyst. It can be clearly seen from the gold composition map that there is a large change in the concentration of the Au material extending from the top left corner at the coordinate x_1, y_{10}, representing 2.7 at. % of Au content in Ni as a minimum to the bottom right corner at the coordinate x_{10}, y_1 representing 97.4 at. % of Au content in Ni as a maximum. On the other hand, the direction of nickel growth from low to high concentrations is the opposite of the Au, gradually increasing from the bottom right corner to the top left corner. The Ni concentration (with respect to Au concentration) at its highest level (97.3 at. %) can be found at the coordinate x_1, y_{10}, while at the coordinate x_{10}, y_1, the Ni concentration ((with respect to Au concentration) is at its lowest level (2.6 at. %). It can be concluded that there is a wide range of compositional gradient of the Au-Ni alloy as the results demonstrate that the bulk composition is varied across the substrate as ca. $98 \geq x$ at. % ≥ 2. This proves that the deposition profile along the substrate was successfully controlled during the period in which the solid-state materials were deposited using the HT-PVD method.

4.2.2 XRD Analysis of the Au-Ni Alloys

X-ray diffraction (XRD) was used to obtain information about the crystallinity, crystal structure and preferred crystal orientation in the Au-Ni alloy materials. The bulk structure of the Au-Ni alloy materials is interesting. The Au and Ni are immiscible in the bulk phase due to a strong tendency for phase separation at low temperatures. However, a complete solubility of the two components exists at high temperatures under equilibrated condition. The method we used for depositing the Au-Ni materials (HT-PVD) allowed us to obtain solid solution materials across a wide range of composition under non-equilibrated conditions. Therefore, high throughput XRD measurements were carried out to determine the structures and involved phases of the Au-Ni alloy library materials.

The X-ray diffraction patterns obtained from an array sample of the as-synthesised Au-Ni thin film alloy materials (at room temperature) are displayed in Figure 21. The Au-Ni (111) reflection is located between the (111) Bragg peaks of the pure elements Au and Ni, marked in red and black colour with vertical lines positioned at 38.2° and 44.5°, respectively. In addition to the (111) reflection, a minor (200) reflection occurred with a lower intensity than the (111) reflection between the (200) Bragg peaks marked in red and black colour positioned with vertical lines at 44.4° and 51.8°, respectively. Both the Au-Ni (111) and the minor (200) reflections shifted gradually to higher 2θ values with increasing concentrations of Ni, which reveals the variation of the alloy degree. This suggests that the produced (unannealed) Au-Ni alloy sample is a substitutional solid solution where Au atoms are replaced by Ni atoms.

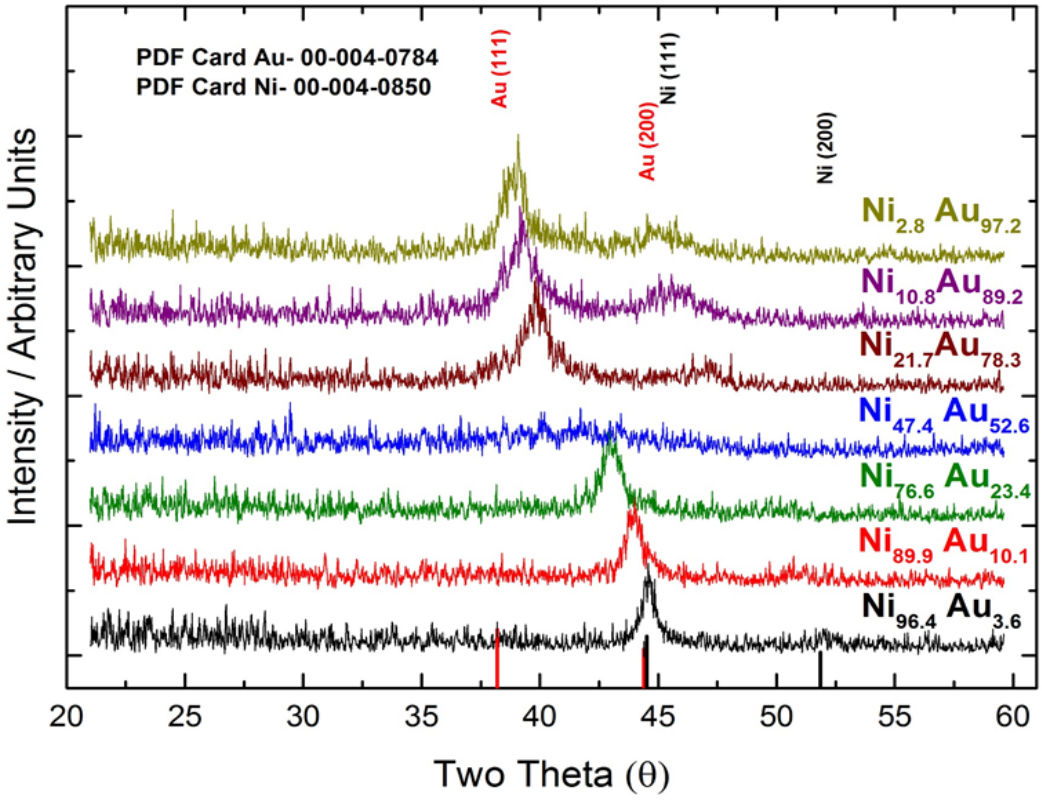

Figure 21: XRD patterns for a number of Au-Ni alloys deposited at RT (unannealed). The vertical red and black lines indicate the pure Au and Ni diffraction positions.

It should be noted that the XRD patterns exhibited clear crystal diffraction peaks with a strong (111) orientation except for the diffraction patterns recorded for the Au-Ni alloy at intermediate compositions ($Ni_{47.4}$-$Au_{52.6}$) (specified in blue colour) as it displays a significant broad reflection between 38.5° and 44.8°. This could have resulted from the distribution and arrangement of the atoms upon synthesis, forming an alloy which is likely amorphous.

This phenomenon was exploited to demonstrate the broadening of the (111) peaks of the Au-Ni alloy at intermediate compositions, where 40 ≤ x at. % ≤ 60 (Figure 22). As displayed, most of the XRD patterns observed in intermediate compositions exhibited extremely broad peaks and is difficult to determine if the Au-Ni is single-phase. As the (111) Bragg peaks are at a composition of ca. Au_{70}-Ni_{30}, the peaks exhibited splitting due to peak broadening. There is also a clear difference in the peak positions observed in the XRD spectra between the Au_{70}-Ni_{30} and Au_{30}-Ni_{70}. This is estimated to be single-phase due to the systemic shift in the peaks' position observed in the XRD pattern as Ni was added to the alloy. Suggesting that the Au-Ni solid solutions had formed. It is also possible that at the intermediate compositions, where 40 ≤ x at. % ≤ 60, amorphous or partly alloyed crystallites had formed.

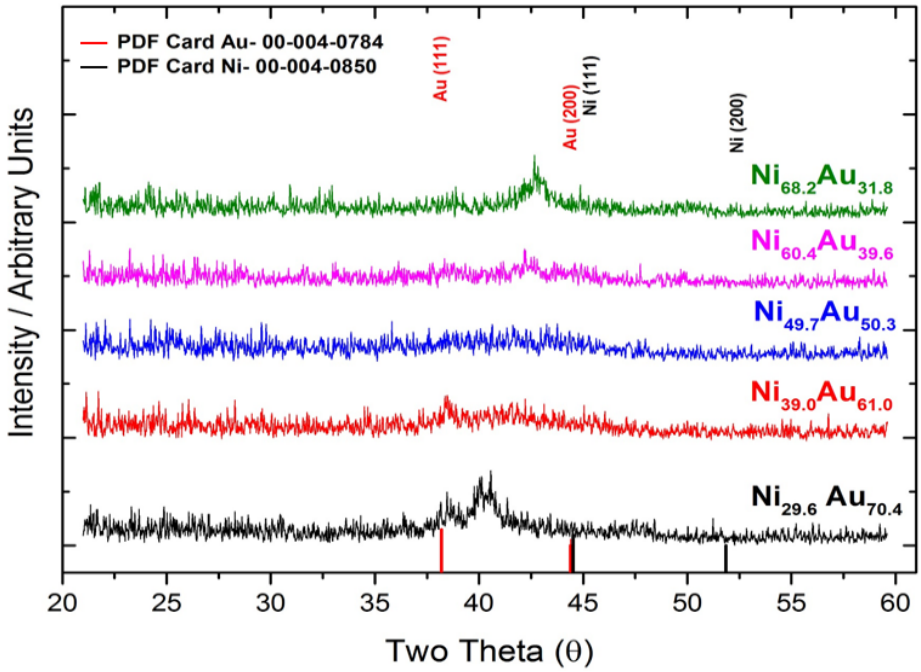

Figure 22: XRD patterns for a number of the unannealed Au-Ni alloys close to intermediate compositions showing the developed broad diffraction profiles. The vertical red and black lines indicate the pure Au and Ni diffraction positions.

The crystallisation of the alloy could be identified through the rise in peak intensity. Therefore, the maximum peak intensity was plotted as a function of Au composition and Ni composition in the Au-Ni alloy materials (Figure 23) to explain the trend observed in Figure 22 using the obtained XRD patterns and the corresponding compositions of the (111) Bragg peaks. To produce intensity profiles for the (111) Bragg peaks observed in the XRD analysis, the variation of the maximum peak intensity was extracted from single peak fitting using the Ilika Technology Informatics Paradise software.

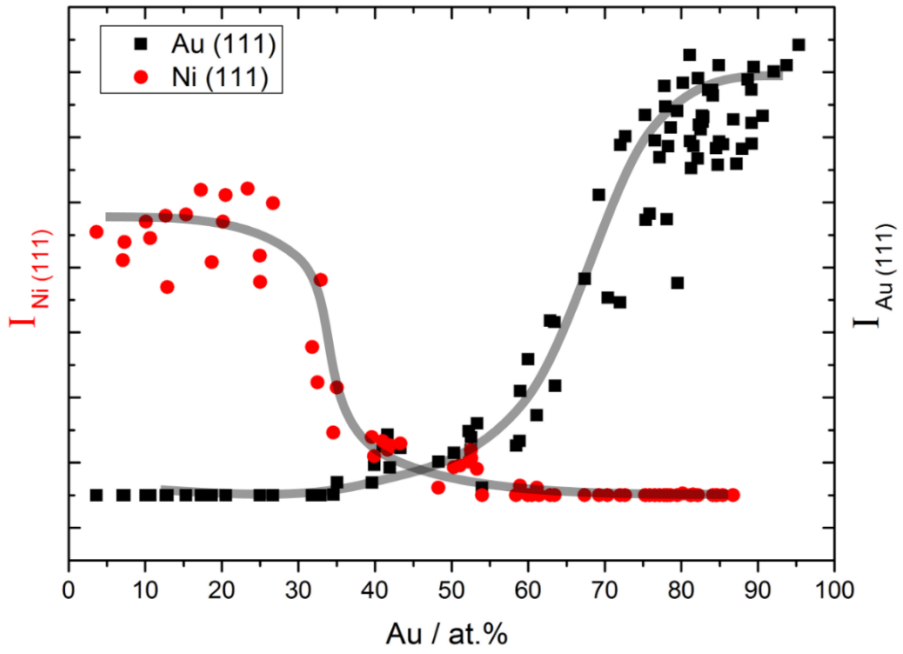

Figure 23: The maximum peak intensity of the Au (111) and Ni (111) versus Au content. The transparent line is a visual guide.

As can be seen, this trend is in line with the variation of the peak intensity of the (111) Bragg diffractions observed in the XRD pattern (Figure 21). For instance, the maximum peak intensity for the (111) non-equilibrated phases in the Au-rich is more intense than that in the Ni-rich. At an intermediate composition, much fewer intense peaks were observed compared to Au-rich and Ni-rich composition. It is possible that the crystallite size at an intermediate composition is too small for some peaks to be detected by XRD or too amorphous for quantification.

According to Vegard's law, a linear relationship between the lattice parameter (a) and the bulk composition is an indication of a miscible binary alloy forming solid solution. The lattice parameter for the Au-Ni was determined by combining the Bragg law with the plane spacing for cubic system using the following equations[104]:

$$2d \sin\theta = \lambda$$

Where λ is the wavelength of X-ray photon (λ = 1.5418 Å), d is the interplanar spacing, and 2 θ is the diffraction angle.

$$\frac{1}{2d^2} = \frac{(h^2 + k^2 + l^2)}{a^2}$$

Where a is defined as the lattice parameter and hkl refer to Miller indices.

$$a = \frac{\lambda}{2 \sin\theta} \times \sqrt{h^2 + k^2 + l^2}$$

The lattice parameters a_{fcc} of the Au-Ni were calculated from the (111) peak positions. The results are displayed in Figure 24. The dashed line connecting the lattice parameter of the Au to Ni (fcc) represents Vegard's law. The lattice parameter of the Au and Ni pure elements at room temperature are 4.061 Å[105] and 3.499 Å[106], respectively, displayed in the Figure as crossed circles. The Au-Ni compositions are based on the EDX analysis. As can be seen in Figure 24, increasing the Au content values in the Au-Ni alloy led to expansion of the lattice parameter, while increasing the Ni content values has the impact of compressing the lattice parameter of the fcc phase. This could be due to the difference in the atomic radius of the Au (2.884 Å) and Ni (1.62 Å). A linear relationship can be observed between the two ends of the alloying elements (Au, Ni). As is evident from the Figure, the effective lattice parameter shows a linear variation with the bulk composition of the Au-Ni alloy obeying Vegard's law. This is a strong indication of the formation of a continuous solid solution for all compositions ranging from $Au_{97.2}$-$Ni_{2.8}$ to $Au_{3.6}$-$Ni_{96.4}$ at. %.

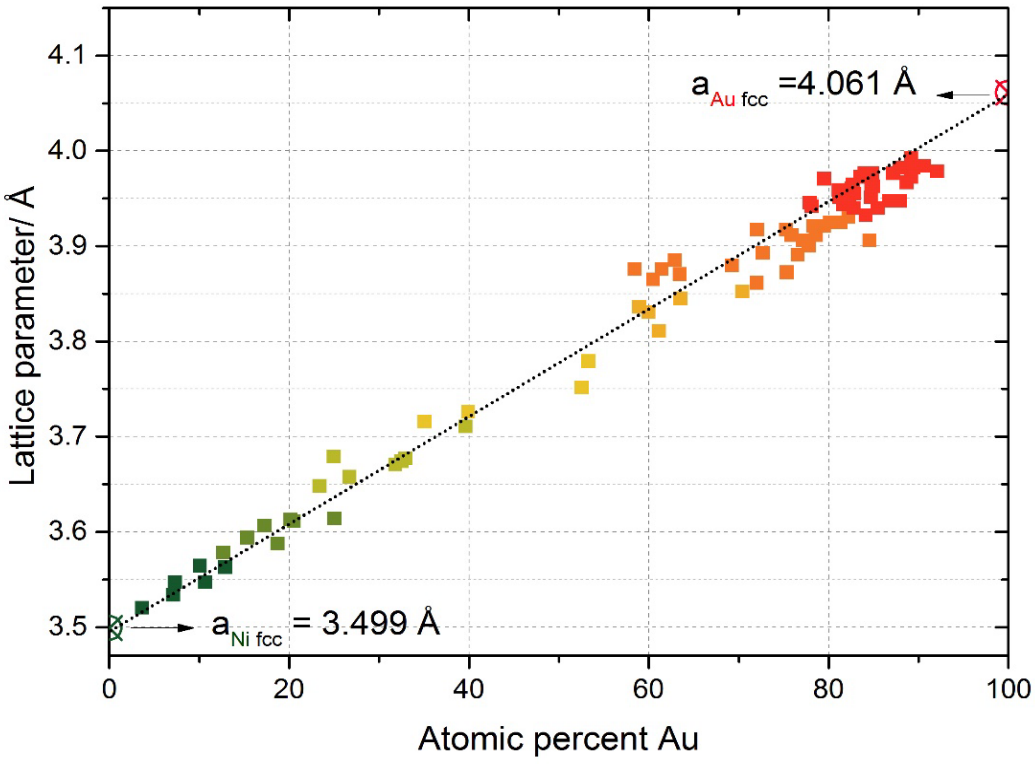

Figure 24: The lattice parameters a (in Å) of the unannealed (RT) Au-Ni alloy (calculated from the (111) peak positions) versus Au composition. The black crossed circles are the lattice parameters of pure Au and Ni elements[106, 105]. The dashed line represents the best linear fit of the plotted data.

The effects of the temperature on the phase stability of the unannealed Au-Ni sample were studied. Two sets of thermal annealing experiments were performed. Firstly, the Au-Ni sample was exposed to thermal treatment in the HT-PVD chamber in a 6.66×10^{-8} mbar vacuum for

annealing to 300 ˚C for a period of 15 min. The diffraction patterns of the annealed Au-Ni sample showed a distinct change after annealing the sample to 300 °C (under UHV). This is illustrated by Figure 25, which shows phase separation in the Au-Ni alloys. At $Ni_{21.7}$-$Au_{78.3}$ alloy the (111) reflection assigned to the Au (111) Bragg peak showed no shifts irrespective of the increasing Au content values. This could be a clear sign of the phase separation occurring in the unannealed Au-Ni sample after annealing.

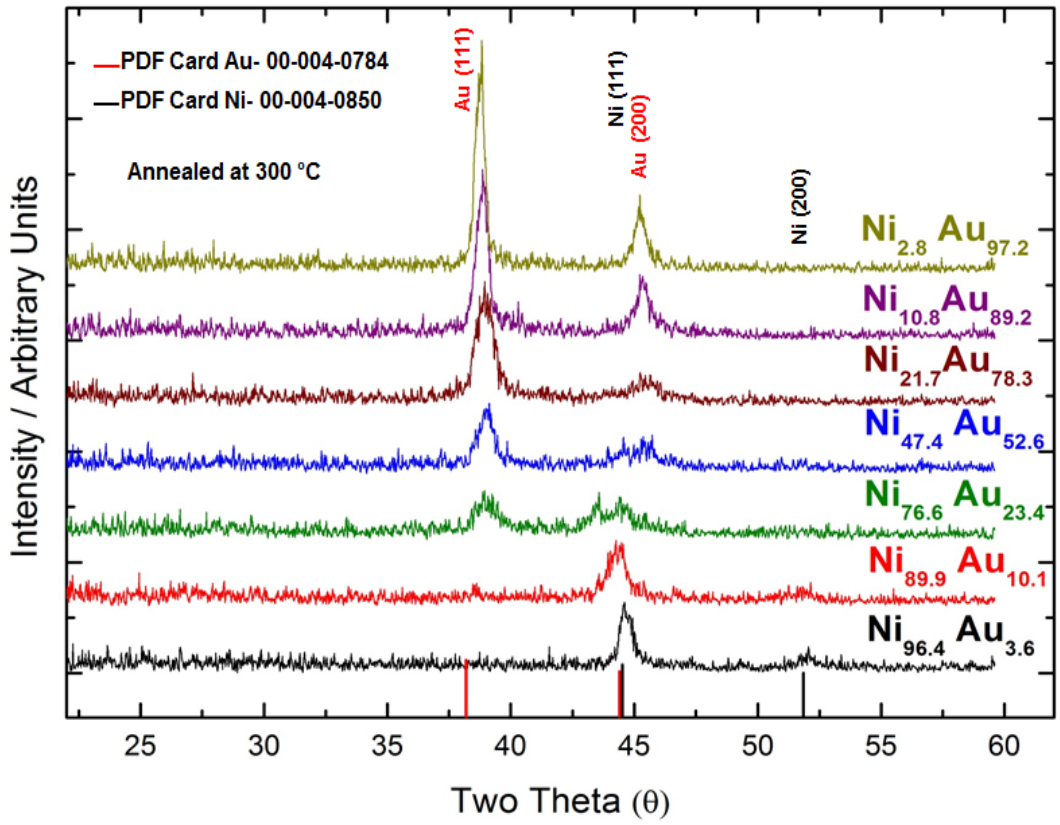

Figure 25: XRD patterns for a number of different compositions of the Au-Ni alloys after annealing at 300 °C for 15 min under UHV.

Comparing the XRD results with the equilibrium phase diagram of the Au-Ni alloy may explain the phase transformation of the Au-Ni alloy determined by the temperature. Although annealing at 300 ˚C is sufficient to form equilibrated phases, the XRD data showed that high-temperature annealing is necessary to verify the phase transformation of the non-equilibrated phases into a thermodynamically stable two-phase mixture. With the annealing temperature at 600 °C (Figure 26), the diffraction patterns of the $Ni_{89.9}$-$Au_{10.1}$, $Ni_{76.6}$-$Au_{23.4}$, and $Ni_{47.4}$-$Au_{52.6}$ alloys recorded with good crystallinity showed complete phase separation and the Au (111), Au (200), Ni (111) and Ni (200) Bragg peaks for the fcc phase could be clearly identified. However, the Bragg peaks position of the rich-Ni-Au and rich-Au-Ni alloys changed with the atomic composition and this is an indication of the formation of a one-phase solid solution. This is in agreement with the phase structure of the Au-Ni alloy system in the thermal equilibrium state diagram, which shows that at

600 °C, over ≈ 90 at. % of Au content and over ≈ 87 at. % of Ni content are expected to appear as a one-phase solid solution, while other compositions appear as a two-phase mixture.

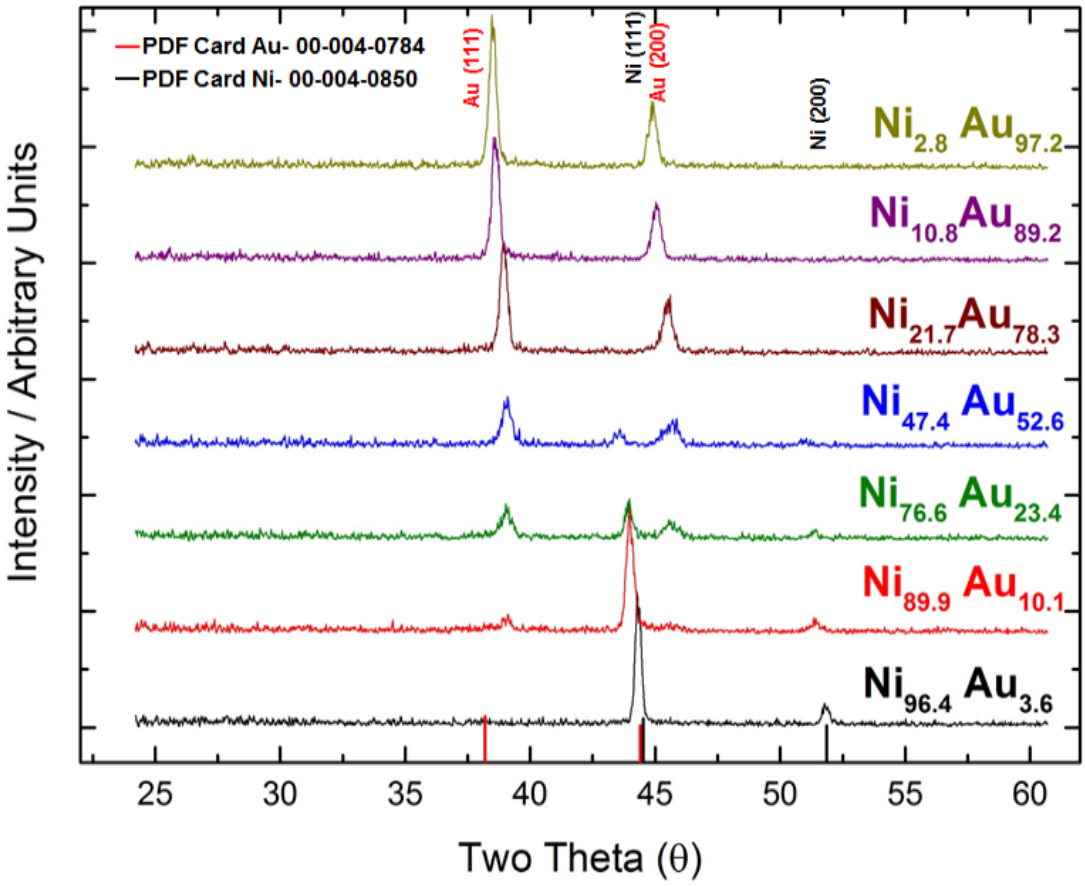

Figure 26: XRD patterns for a number of Au-Ni alloys after annealing at 600 °C for 15 min.

Figure 27 shows the lattice parameter of the Au-Ni sample (annealed at 600 °C for 15 min) calculated from the diffraction angle of the (111) Bragg peaks as a function of Au composition. As shown, the lattice parameter of the Au-Ni alloy material does not vary linearly, as is the case in the unannealed Au-Ni alloy film. In addition, the position of the (111) Bragg peak of the fcc phase as a function of the Au composition before and after the thermal annealing at 600 °C is displayed in Figure 28 for comparison. As is apparent from Figure 28, the peak position of the (111) Bragg diffraction in the annealed Au-Ni alloy varied linearly with the Au content. On the contrary, the annealed Au-Ni sample (600 °C for 15 min) exhibited separation for the position of the (111) Bragg peaks.

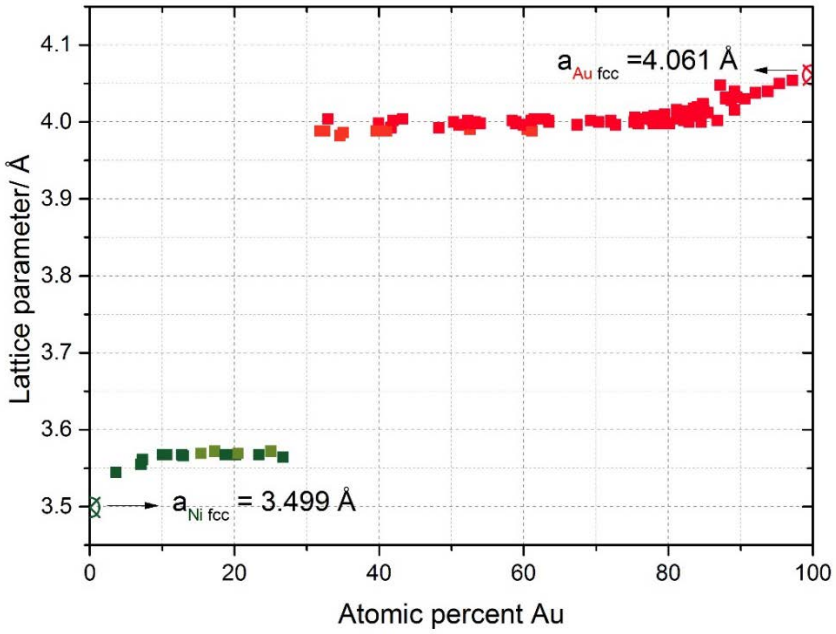

Figure 27: The lattice parameters a (in Å) of the Au-Ni alloy annealed at 600 °C versus the Au composition. The crossed circles are the lattice parameters of pure elements [106, 105].

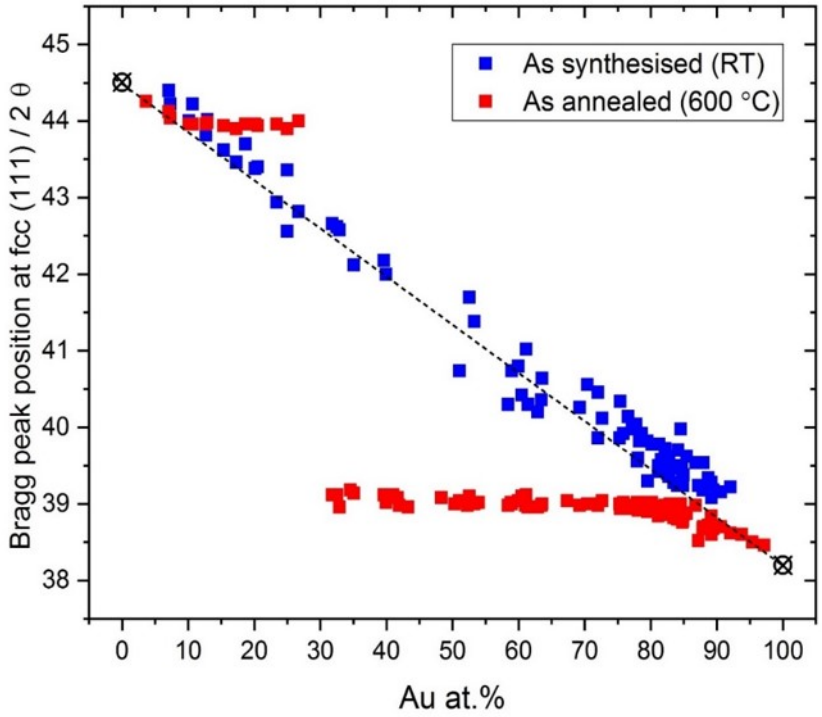

Figure 28: Comparison between the (111) Bragg peak position of the Au-Ni alloy as a function of the Au content before and after annealing at 600 °C. The characteristic diffraction peaks of pure Au (PDF card Au-00-004-0784) and Ni elements (PDF card Ni-00-004-0850) are given at the two extreme ends as black crossed spheres.

4.2.3 Surface Composition of Au-Ni Alloys

Surface sensitive studies conducted using XPS experiments were used to identify and determine the elemental composition, chemical and electronic state of the Au-Ni alloy sample at a number of specific areas. The measured area on the sample's surface is equivalent to four electrodes on the electrochemical array that corresponds to ca. 3 mm^2 (Figure 29). The areas, which were detected by the XPS, were selected to match the growth of Au in the Au-Ni alloy materials present on the sample's surface. The direction of the arrow line in Figure 29 represents the increase of the Au atomic ratio in the Au-Ni alloy sample determined by the EDX while the red-like squares, which cover the four electrodes, represent the surface composition determined by the XPS measurements. Consequently, quantitative analysis of the Au-Ni alloy as a function of alloy composition was carried out by deconvoluting the XPS spectra (using CASAXPS (commercially available) software) to verify the effect of chemical interaction between Ni and Au on the alloy surface through their core level binding energies. This was followed by studying the impact of the thermal annealing on the Au-Ni surface composition to confirm which element is rich on the surface.

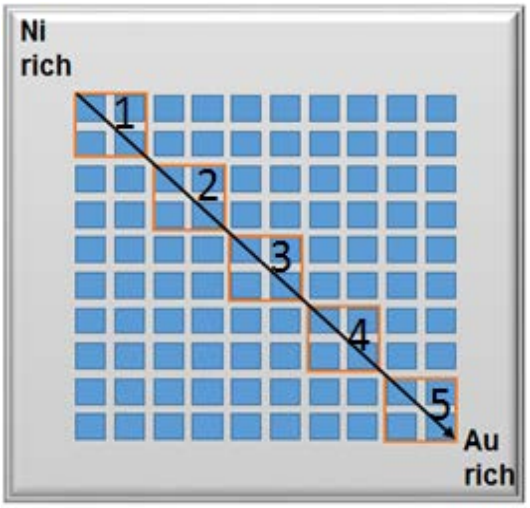

Figure 29: View of the sample area of each site detected during the XPS measurements. Each measured site corresponds to four electrodes on the array.

The main Au and Ni photoemission spectral features are summarised in Tables 7 and 8 (Appendix B). According to the XPS analysis of the Figure 30 (a), showed that the Au (4f) peak intensities gradually increased as the concentration of Au increases, while the Ni (2p) peak intensities decreased proportionally Figure 30 (b). Similarly, the Au ($4f_{7/2}$) peak for the highest content of Au in the unannealed Au-Ni alloy shifted to lower binding energy as the Au content decreased, while the Ni ($2p_{3/2}$) shifted to higher binding energy, which is a clear indicator of electron transfer from Ni to Au due to the formation of the bimetallic alloy.

The binding energy of the electron emitted from the Au ($4f_{7/2}$) and Ni ($2p_{3/2}$) core levels of the bimetallic Au-Ni alloy were analysed and compared with the Au and Ni pure elements, as shown in Figures 31 and 32. The values given in the literature for binding energy of the bulk Au ($4f_{7/2}$) and the bulk Ni ($2p_{3/2}$) were measured as 84.07 eV [107] and 852.00 [108], respectively. The binding energy the Au ($4f_{7/2}$) core level was plotted versus Au concentration (Figure 31). It can be observed that there is a clear effect on the peak position of the $4f_{7/2}$ associated with the concentration of Au on the surface of the Au-Ni alloy. Conversely, the peak position of the Ni ($2p_{3/2}$) (Figure 32) at high Ni content shifts from 851.45 eV up to 852.73 eV, providing evidence that modification of the electronic structure on the surface of the Au-Ni alloy occurred.

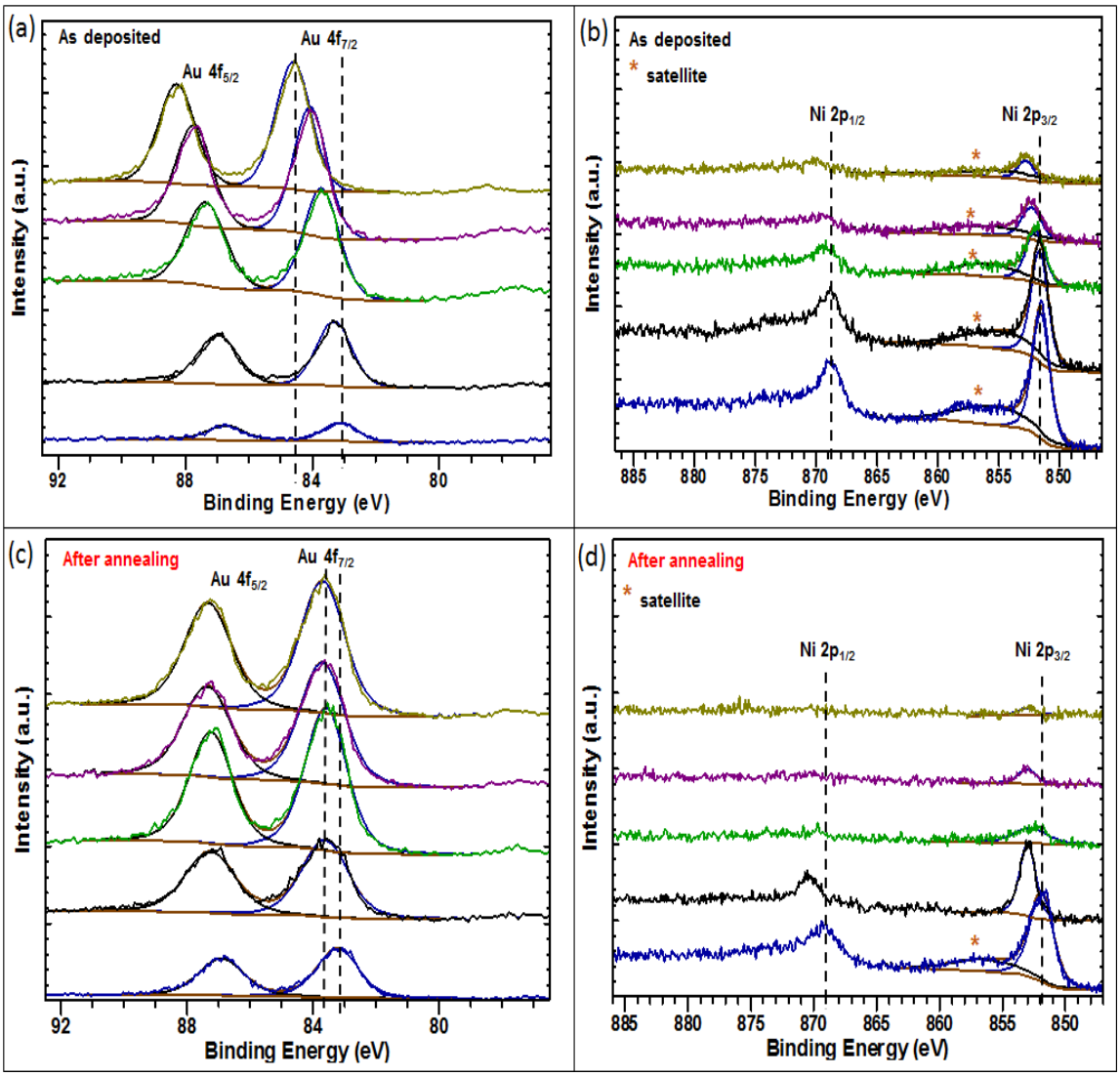

Figure 30: XPS spectra of (a) Au (4f) and (b) Ni (2p) regions of the unannealed Au-Ni alloy sample and (c) the Au (4f) and (d) Ni (2p) regions of the Au-Ni alloy sample after annealing at 300 °C for 15 min.

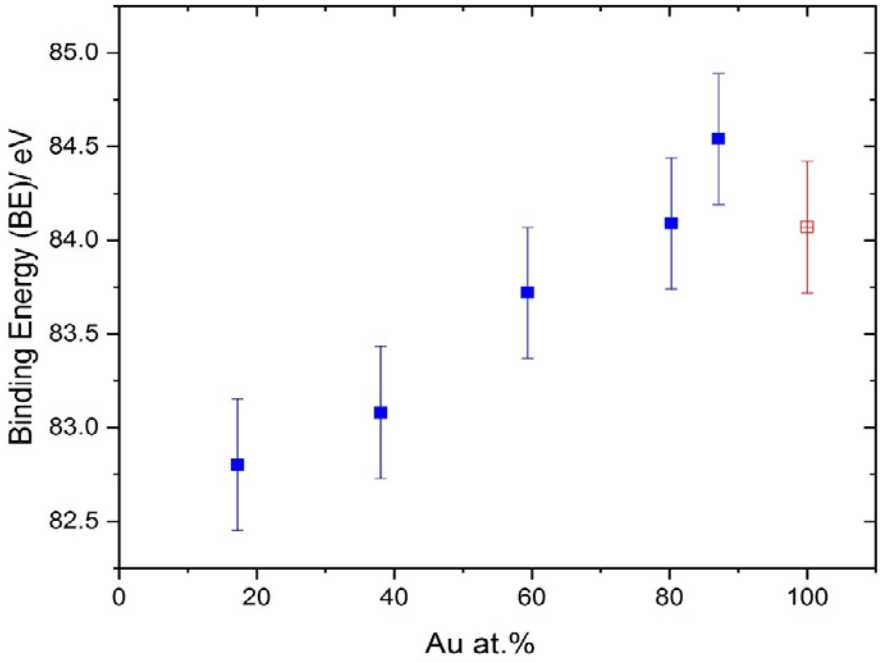

Figure 31: The peak positions of Au ($4f_{7/2}$) as a function of Au content. The red crossed square represents the peak position of the pure Au ($4f_{7/2}$) (with electron binding energy of 84.07 eV)[107].

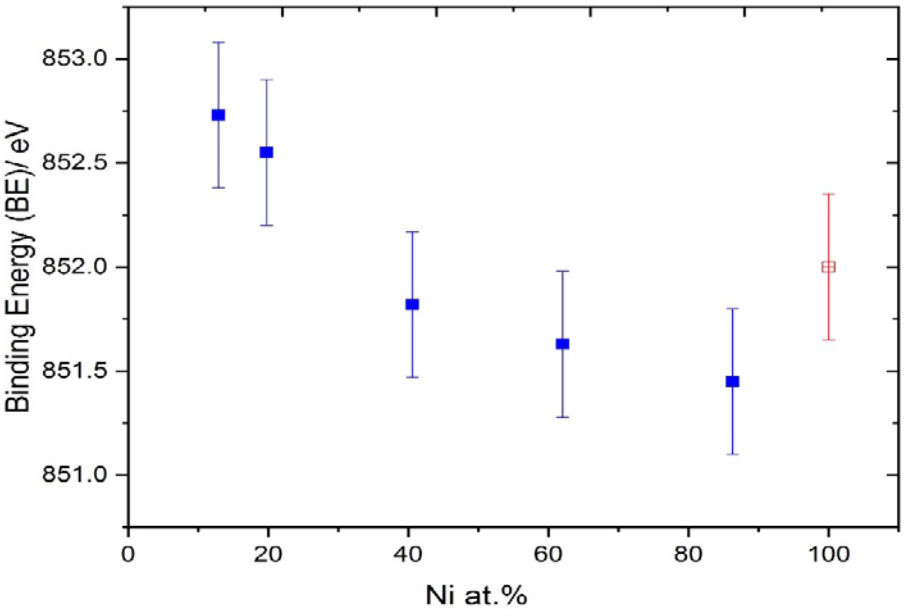

Figure 32: The peak positions of the Ni ($2p_{3/2}$) as a function of Ni content. The red crossed square represents the peak position of the pure Ni ($2p_{3/2}$) (with electron binding energy of 852.00)[108].

In order to identify the effect of the annealing temperature on the surface composition of the Au-Ni alloy, the sample was annealed at 300 ˚C for 15 minutes under UHV. Evident changes in the XPS spectra (Figures 30 c and 30 d) were observed regarding the position, shape and area of the peaks in comparison with the unannealed Au-Ni alloy. The XPS peak position of the Au ($4f_{7/2}$) core level

binding energies showed a negligible shift along the Au growth line compared to the unannealed alloy (Figure 30 (c)) (Table 8 Appendix B). Moreover, the peak area of the Au (4f) showed a significant increase and vice versa for the area of the Ni (2p) peaks. This indicates a strong tendency of Au to segregate to the surface upon thermal annealing due to the low surface energy of Au atoms.

The surface atomic percentage of Au in the Au-Ni alloy sample was calculated from XPS data before and after annealing and compared to the bulk composition determined by EDX to verify this statement (Figure 33). The amount of Au on the surface of the annealed Au-Ni sample shows a significant increase in concentration compared to the unannealed sample. It can thus be concluded that controlled synthesis (kinetically) of the (unannealed) Au-Ni alloy sample with surface compositions identical to bulk compositions were successfully achieved. However, the surface composition of the unannealed Au-Ni alloy was appreciably different from the bulk after annealing due to Au enrichment at the surface.

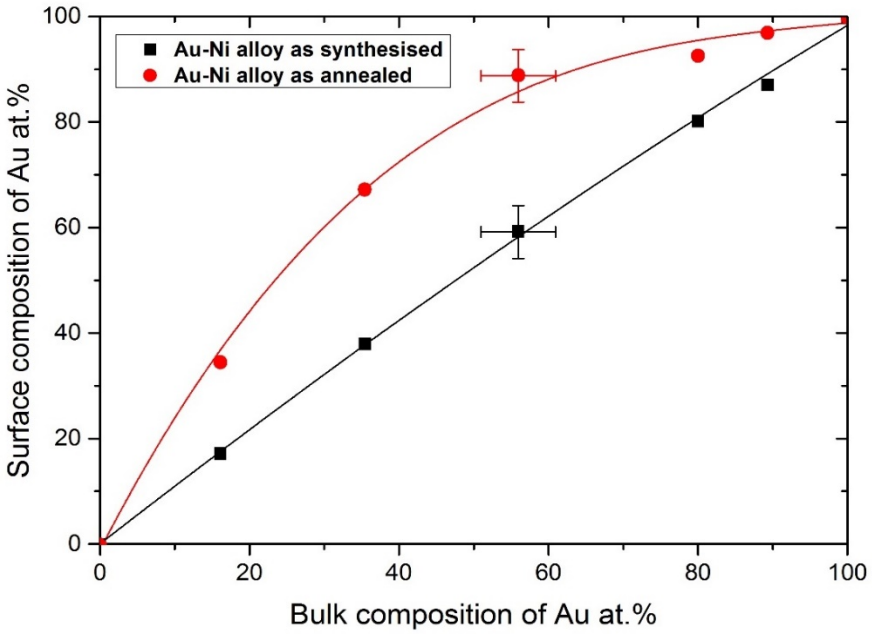

Figure 33: Surface composition of Au measured by XPS versus the bulk composition that were determined by EDX. Black diamond dots represent identical ratios for the surface and bulk compositions (no segregation). Red circles represent unequal surface and bulk compositions (segregation) of the annealed Au-Ni alloy for 15 minutes at 300 ˚C.

4.3 The Catalytic Activity of the Au-Ni Alloy Catalysts

The Au-Ni alloy catalysts (before and after annealing) were characterised electrochemically in the absence and in the presence of sodium borohydride using the high throughput electrochemical screening method to explore the optimal catalyst with respect to the direct BOR. Direct current measurement for the 10x10 Au-Ni electrodes in an array of ITO surfaces that are individually addressed were carried out. Simultaneous potential was applied to all working electrodes using a single potentiostat and a pair of 100 current followers. Comparing such a large number of catalysts requires high throughput electrochemical data analysis for fast determination of the electrode activity. Hence, the CV response of all electrodes was analysed using the Ilika Technology Informatics Paradise software. The bulk composition of each catalyst was linked with its response to the applied CV. The potential that defined the onset potential of an oxidation/ a reduction process for all catalysts can automatically be calculated through the Paradise software using the intercept of two straight lines at a defined I-threshold. The peak current density of an oxidation/ a reduction process at a defined voltage can also be calculated as a function of electrode composition. This is important in studying the combinatorial array to facilitate the tracking of electrode activity.

4.3.1 The Electro-catalytic Activity of the Unannealed Au-Ni Alloys for Direct BOR

The electrochemical behaviour of the Au-Ni alloy catalysts was studied in 0.1 M of NaOH. Since $NaBH_4$ can be decomposed at pH ≤ 12[48], a 0.1 M of NaOH (pH 13) was used to stabilise the $NaBH_4$ and prevent a potential chemical hydrolysis reaction whereby hydrogen is released. The potential range was scanned from -1.2 V_{SCE} to +0.01 V_{SCE} at a sweep rate of 50 mV/s. Figure 34 shows CVs of selected electrodes with different compositions of the unannealed Au-Ni alloy catalysts recorded in the absence of the $NaBH_4$. The arrows are illustrative of the direction of the scanned potential to record CVs.

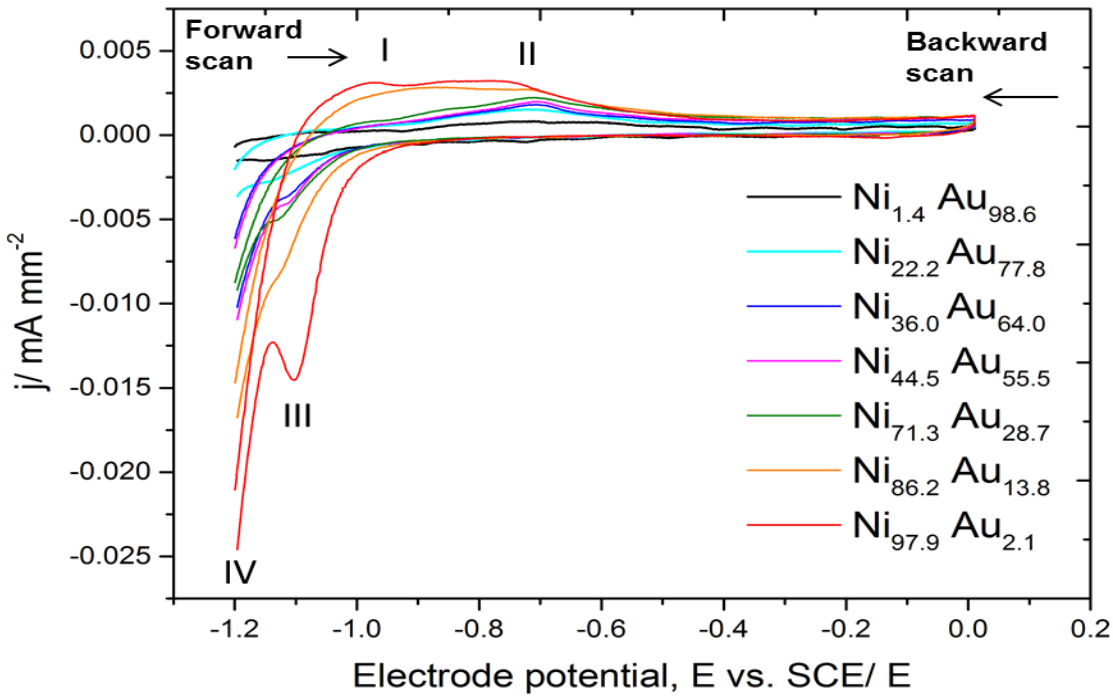

Figure 34: The electrochemical activity of the unannealed (RT) Au-Ni alloy materials in the absence of the $NaBH_4$ as a function of electrode composition at sweep rate: v =50 mV s^{-1}, Ar-saturated 0.1 M NaOH electrolyte, T 293.

The voltammogram can be divided into three distinct potential regions for the anodic and cathodic sweeps and include electrochemical processes at -1.00 V_{SCE}, -0.75 V_{SCE} and at -1.03 V_{SCE} corresponding to the oxidation of H_2 (I), oxide formation (II) and oxide removal (III), respectively[109]. One may also notice a distinct potential region on the cathodic sweeps at potential near -1.2 V_{SCE} referred to (IV) as the hydrogen evolution reaction HER[110].

The HER current density was affected by the presence of the Ni on the unannealed Au-Ni alloy surface and a significant increase in the HER activity was observed. In order to assess the hydrogen evolution activity, the current density (in the cathodic sweep of the voltammogram) at -1.18 V_{SCE} was extracted, and plotted in a false colour over the array, and as a function of bulk composition, in Figure 35. As the Ni content of the alloy increased, almost no current was observed in the limit of high Au alloy composition. The increase in hydrogen evolution activity did not take place linearly as Ni content in the bulk (and in the surface) increases. Three regions of behaviour can be identified. An initial increase in activity (region 1), near constant activity (region 2) and a further increase in activity (region 3).

The increase in hydrogen evolution activity is also reflected in the ignition potential for evolution (Figure 36). The ignition potential obtained for a threshold current density of -1.26 µA mm^{-2} was extracted and plotted in a false colour over the array, and as a function of bulk composition. A shift was observed between pure gold (> -1.2 V_{SCE} to pure Ni (-1.11 V_{SCE}) exists between the higher

content of Au and the higher content of Ni in the Au-Ni electrode arrays. This indicates that the HER activity on the unannealed Au-Ni alloy catalysts was due to either Ni acting as a more effective catalyst or to geometric effect associated with the ensemble effects or electronic effects.

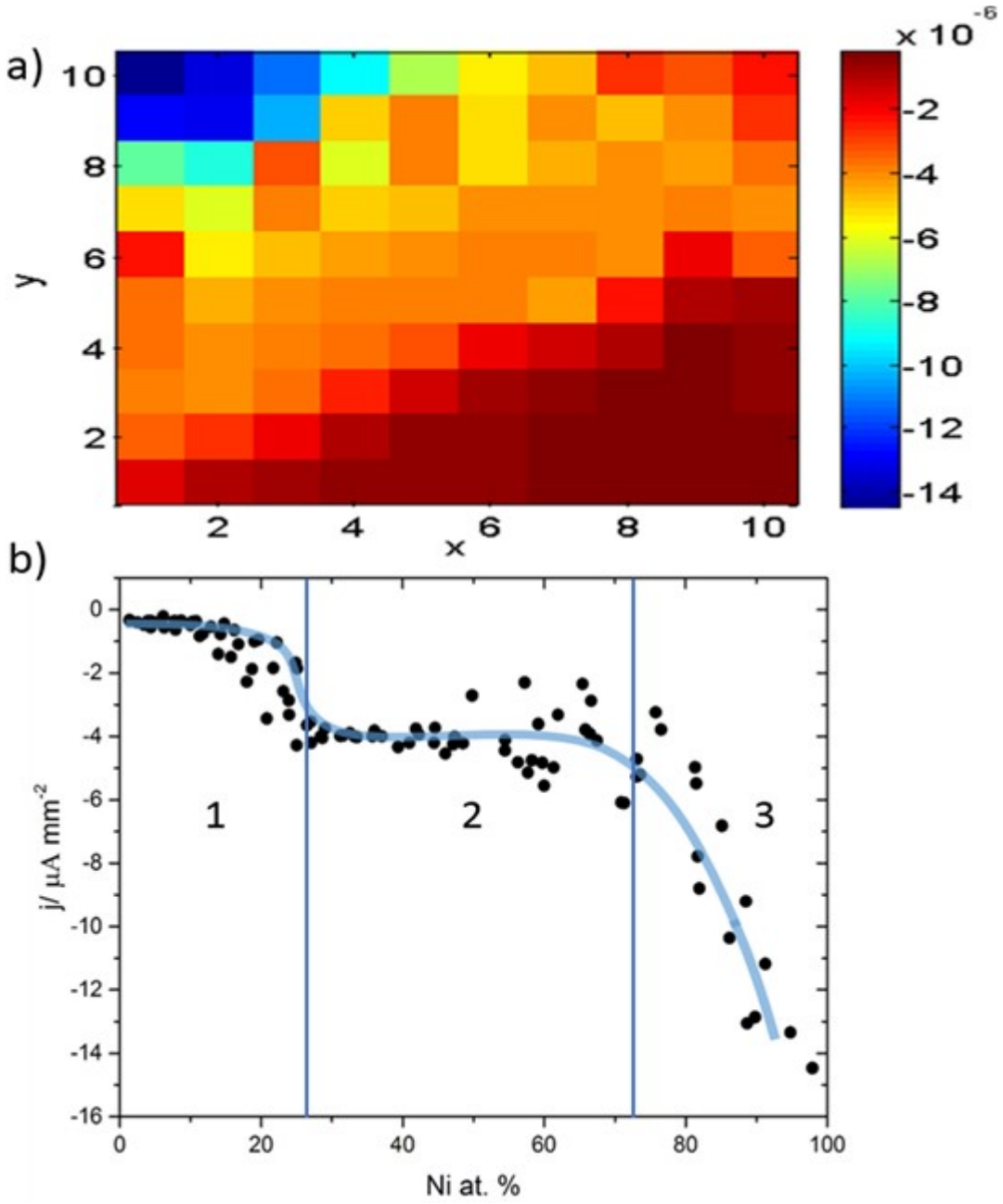

Figure 35: High throughput screening analysis of the metal catalysts by current versus composition showing the electrode activity toward the hydrogen evolution reaction extracted from CVs recorded on the Au-Ni alloy at E= -1.18 V_{SCE}. The line is a visual guide.

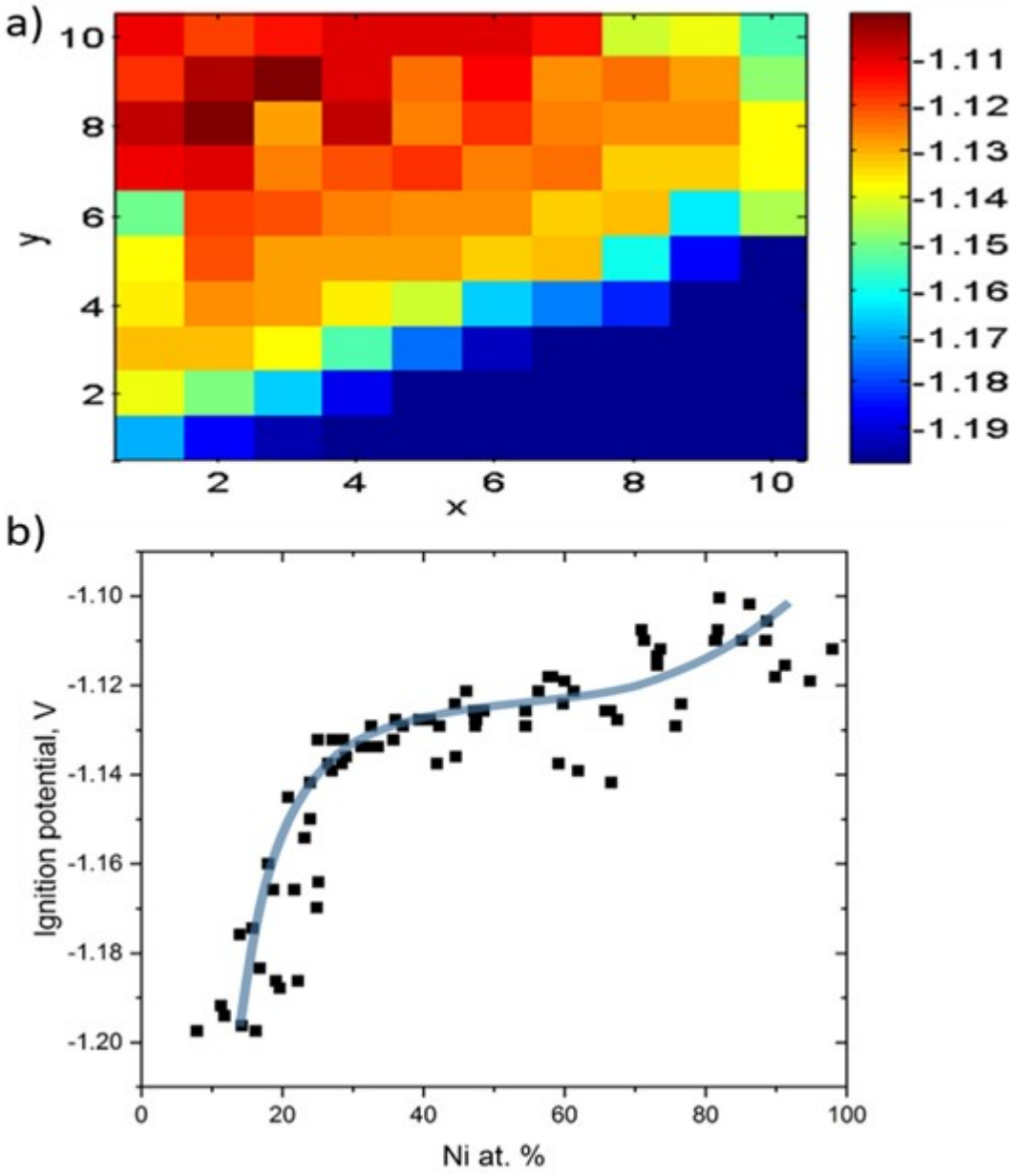

Figure 36: High throughput electrochemical screening analysis showing the activity of the electrode arrays through the onset potentials of HER reaction (at I threshold= -1.26 μA mm^{-2}) versus Ni at. %. The transparent line is a visual guide.

The voltammetric characteristics in the hydroxide formation (region II)/ removal (region III) also change with different alloy compositions. As can be seen from the voltammogram in Figure 34, there is an increase in the anodic current around -0.75 V_{SCE} in the anodic scan with increasing Ni content. At the same time, there is an increase in the cathodic peak at ca. -1.1 V_{SCE}. These currents are associated with the formation and reduction of α-$Ni(OH)_2$.

Electrochemical examinations were carried out on Ni wire electrode to rationalise this observation. Figure 37 shows a typical CV of a Ni electrode studied in 0.1 M of NaOH at a scan rate of 50 mV/s. A typical CV profile for the Ni electrode, when cycling the potential within the full range to the oxygen evolution region (-1.2 to +0.55 V_{SCE}), shows the following anodic features:

(1) the oxidation of metallic Ni to α-Ni $(OH)_2$ at - 0.75 V_{SCE}; (2) The conversion of the surface oxide α-$Ni(OH)_2$ to β-$Ni(OH)_2$ between -0.5 V_{SCE} to +0.15 V_{SCE} followed by the oxidation of the β-$Ni(OH)_2$ to β,*γ*-NiOOH at +0.35 V_{SCE} and +0.4 V_{SCE} respectively[111-114]. It has been reported that the formation of β-$Ni(OH)_2$ is an irreversible process causing passivation to the Ni electrode. To understand the changes occurring to the metallic Ni, subsequent potential sweeps were applied (Figure 38). The initial cycle was studied by starting the potential sweep at a potential up to -0.45 V *vs.* SCE where it is expected to observe the formed oxide layer before its conversion to β-$Ni(OH)_2$.

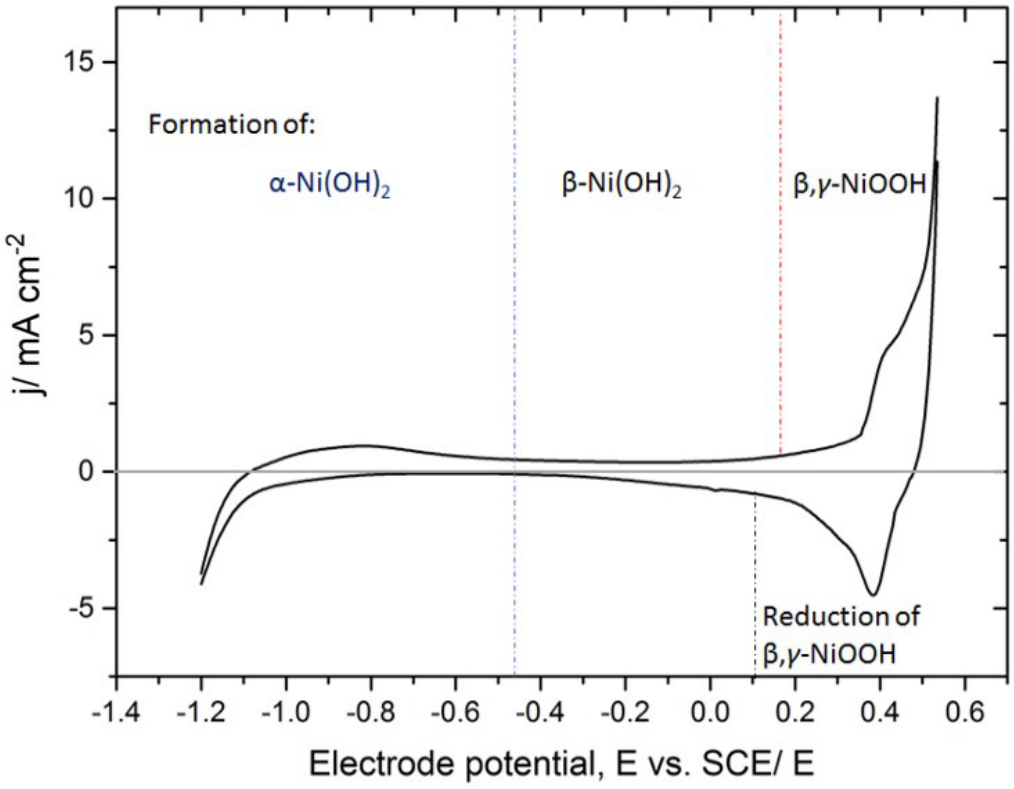

Figure 37: Typical CV of the Ni electrode in 0.1 M of NaOH at a scan rate of 50 mV/s showing different regions of oxide formations.

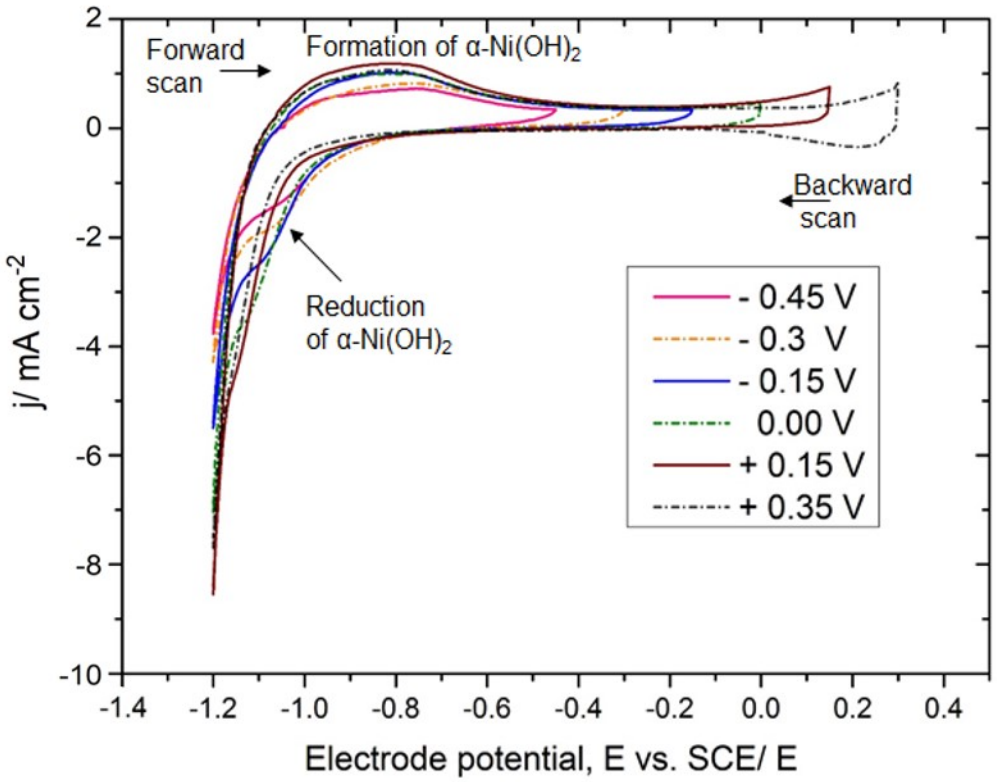

Figure 38: CVs of Ni electrode in 0.1 M of NaOH at 50 mV/s with increasing the potential window towards more positive potentials.

It can be seen that the conversion of the formed oxide to β-$Ni(OH)_2$ on the Ni electrode depends largely on the selected potential scans. According to the CV profiles, the current density of the α-$Ni(OH)_2$ oxidation reaction increased with increasing potential limits of the anodic scan. Interestingly, when the sweeping potential is extended into the region of the β,γ-NiOOH at +0.35 V_{SCE}, the formation of the hydroxide layer shows a decrease in the current density accompanied with increases in the HER current density when scanning the potential backward. As displayed in Figure 38, the cathodic peak of the α-$Ni(OH)_2$ is reduced when the applied voltage exceeds more positive anodic potential > 0.00 V_{SCE}. If the forward scan is continued to more positive anodic potentials (> +0.35 V_{SCE}) and back, this cathodic peak is indistinguishable suggesting that there is a concurrent change in the formation of $Ni(OH)_2$ and the converted formed oxide β-$Ni(OH)_2$ is more difficult to reduce. It can be concluded that the electrochemical behaviour of the Ni electrode can be affected by the passivation and occurs as a result of the chemical conversion of the α-$Ni(OH)_2$ to β-$Ni(OH)_2$ and the activity of the HER on the surface is determined by the structure of the $Ni(OH)_2$.

The anodic peaks of the α-$Ni(OH)_2$ oxidation reaction on the unannealed Au-Ni alloy catalysts, which take place at -0.75 V_{SEC} changes with the alloy composition (Figure 40) . As the Ni content increases in the Au-Ni alloy catalyst, the current density also increases. The current density of -0.70 V_{SCE} (the maximum of $Ni(OH)_2$ oxidation peak) was plotted as a function of alloy composition

in Figure 39. As shown in the Figure, the current density increases before it reaches intermediate compositions Ni_{30}-Au_{70} with a maximum of ca. 1.25 µA mm^{-2}. However, at intermediate compositions, the activity of the α-$Ni(OH)_2$ formation reaction shows a decrease in the current density value until a current maximum of 1.00 µA mm^{-2} is reached. With increasing Ni content (Ni ≥ 80 at. %), the α-$Ni(OH)_2$ oxidation reaction becomes more active and the current density showed a maximum of ca. 2.75 µA mm^{-2}. This indicates that the presence of the Au in the Au-Ni alloy supresses the formation of the α-$Ni(OH)_2$ and the existence of the Ni in the alloy promotes the oxidation reaction of the α-$Ni(OH)_2$ to occur.

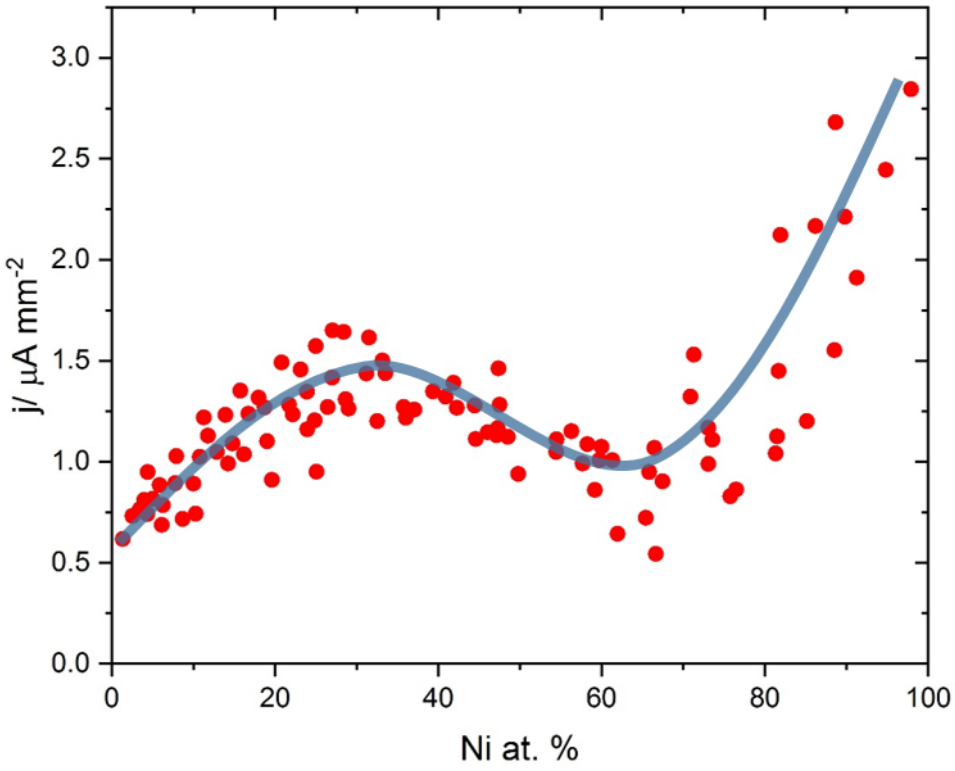

Figure 39: Currant densities (at -0.75 V_{SCE}) versus Ni composition showing the activity of the Au-Ni towards the hydroxide formation (α-$Ni(OH)_2$) on Au-Ni alloy materials. The transparent line is a visual guide.

The behaviour of the unannealed Au-Ni alloy catalysts in the presence of the $NaBH_4$ has been electrochemically investigated as a function of electrode composition. Figure 40 shows (a) selected forwards sweeps of the screened alloy catalysts along with (b) Au and (c) Ni pure metals in the potential range between -1.2 V_{SCE} and +0.15 V_{SCE} at a scan rate of 25 mV/s. The electrolyte was a 0.01 M $NaBH_4$ + 0.1 M of NaOH solution. The maximum in the anodic potential of +0.15 V_{SCE} was chosen in order to avoid oxidation dissolution or irreversible oxidation processes (see above).

During the forward anodic scan (Figure 40 a), one can observe two overlapping anodic peaks, the first is between -1. V and -0.7 V_{SCE}, while the second is between -0.7 V and -0.2 V_{SCE}. These anodic peaks can be attributed to the direct BOR taking place at different potentials depending on the

catalyst composition. As can be observed from Figure 40 (a), the selected CVs reveal that the activity of the Au-Ni alloy catalysts towards the BOR is correlated with the catalyst composition. Moreover, as displayed in Figure 40 (a and b), catalysts that are Au rich and pure Au show remarkable activity towards the direct BOR compared to Ni rich alloys and pure Ni (Figure 40 c). The catalysts' behaviour at intermediate compositions shows limited activity depending on the amount of Ni present at the surface, as the Au-Ni alloy catalysts that are Ni rich appear to be inactive towards the BOR with a continued increase in the electrode potential (Figure 40 c). It can also be seen from Figure 40 (a) that the first anodic peak occurred in the $Ni_{33.2}$-$Au_{66.8}$ alloy catalysts (-0.9 V_{SCE}), showing a shift of 0.3 V as compared with the metallic Au (-0.6 V_{SCE}) (Figure 40 b). This indicates the higher catalytic activity of the Au-Ni alloy catalyst towards direct BOR. This enhanced catalytic activity can be attributed to the ensemble / the electronic effects of Ni on Au. As a result, any activity towards the direct BOR over the unannealed Au-Ni alloy catalysts is due to the incorporation of Ni and that also confirms the Au-Ni alloy formation with the controlled gradient compositions using our HT-PVD method.

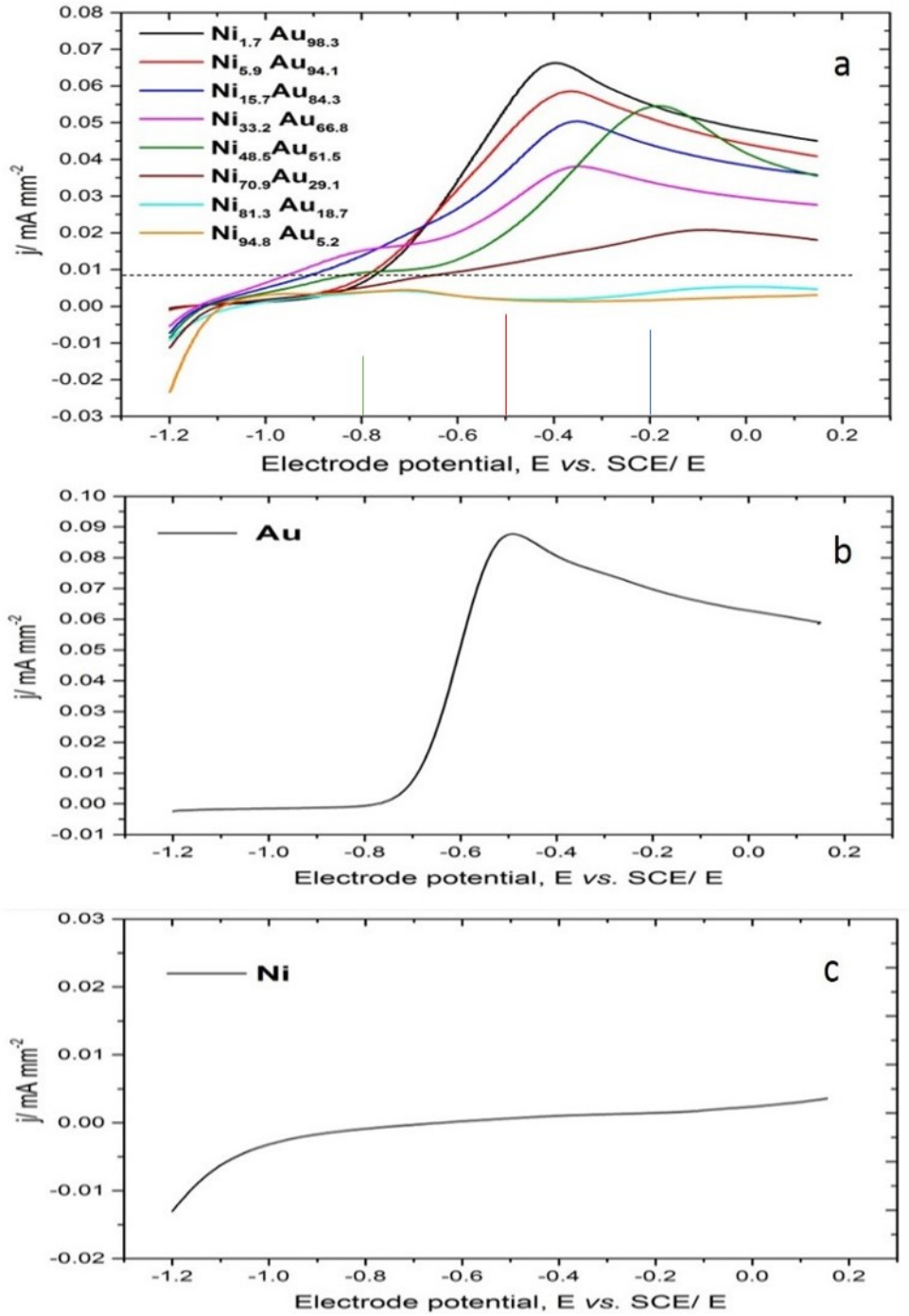

Figure 40: Forward sweep voltammograms showing the anodic peaks attributable to the direct BOR on (a) the unannealed Au-Ni alloy as a function of electrode composition, (b) pure Au (disc electrode (0.75 radii)) and pure Ni (disc electrode (0.25 radii)) recorded for 0.01 M of $NaBH_4$ in 0.1 M of NaOH at sweep rate of 25 mV s^{-1}.

To validate this observation, high throughput electrochemical analysis was carried out and is displayed as trend for the activity of the Au-Ni alloy catalysts. The catalytic activity in terms of the lower onset for the direct BOR was studied as a function of composition. The trends in catalytic activity revealed that a small amount of Ni indeed contributed to a higher activity for BOR due to a negative shift in the onset potential. This may have suggested that the improvement in activity

of the Au-Ni alloy catalysts is due to the HOR associated with the HER. However, upon annealing, the HER disappeared (Figure 43) but the enhance activity was retained. The enhancement in activity can be attributed to a modification of the electronic/ensemble in the Au-Ni alloy catalysts. This, in turn, changed the adsorption energy and the bonding strength contributing to active sites for the BH_4^- ion by means of alloying compared to pure Au. Figure 41 demonstrates the onset potentials (ignition potential), extracted from CV data at I-threshold= 0.0085 mA mm^{-2} vs. Ni composition, presented as an activity trend for the BOR reaction. By comparing the onset potential of the BOR to the rich Au catalysts, it can be observed that there is a negative shift in the onset potential of 0.2 V of the direct BOR due to the incorporation of small amount of Ni (ca. 10-40 at.%) in the Au-Ni alloy. This illustrates that the catalyst activity was enhanced by the small addition of Ni. However, excessive addition (50-95 at. % Ni) resulted in decreasing onset potentials of the direct BOR towards more positive potential values. This indicates that the direct BOR is sensitive to surface active sites of Au that are modified by the addition of Ni in the Au-Ni alloy catalysts. Perhaps the presence of an ensemble of more Ni atoms increases the passivation layer (OH_{ads}) on which the alloy surface favours removal of the OH_{ads}.

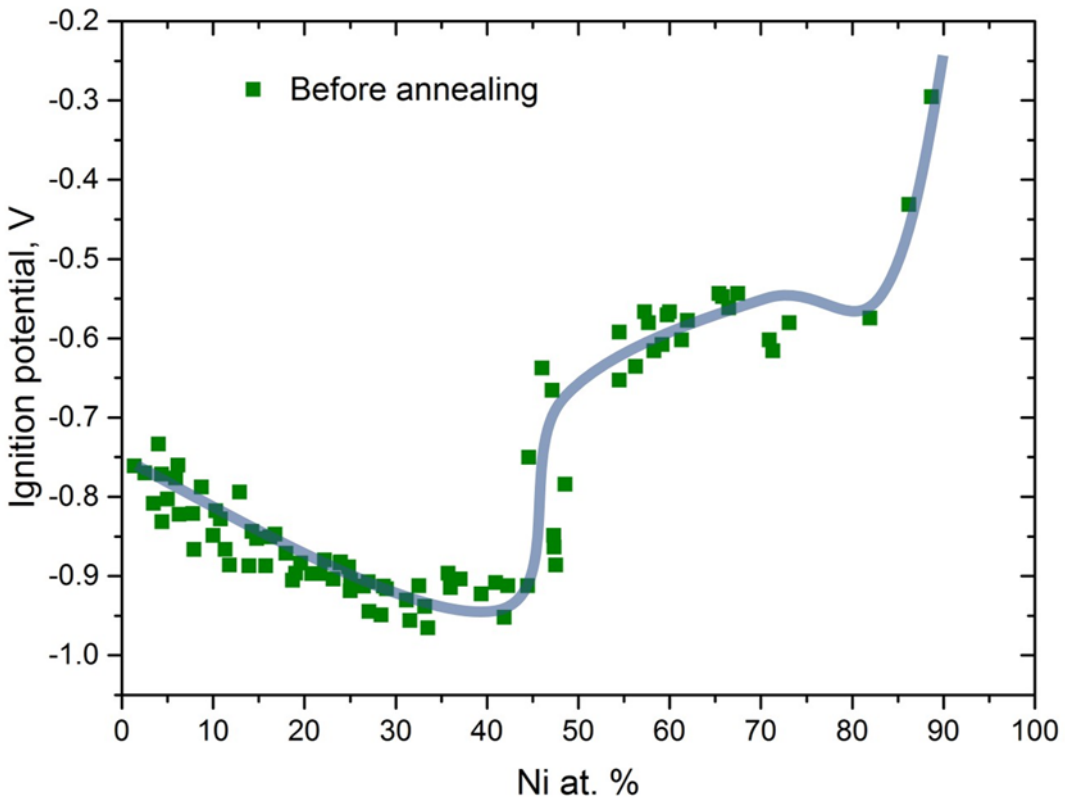

Figure 41: Onset potentials (at I threshold = 0.0085 mA mm^{-2}) of the BOR versus Ni composition for unannealed Au-Ni alloy sample. The transparent line is a visual guide.

In order to assess the activity for the direct BOR, plots of the current density as a function of compositions at potentials of -0.8 V_{SCE}, -0.5 V_{SCE} and -0.2 V_{SCE} (Figure 42) were chosen according to the followings:

- E= -0.8 V_{SCE} (low current V_{onset}): Most sensitive region to the surface kinetics of the reaction (activity of the catalyst) and is weighted (most sensitive) to the most active sites (ensembles) on the surface.
- E= -0.5 V_{SCE} (medium current V_{onset}): The reaction is being driven harder. Some mass transports may limit the measured current, but the current is still reflecting the surface reaction kinetics (activity of the catalyst). However, this will now be additionally influenced by the larger ensembles particularly when the main component (eg. Au) is also active in the catalysis, i.e., the majority sites which have not necessarily the highest activity.
- E= -0.2 V_{SCE} (maximum current V_{onst}): Strong contribution of mass transport limiting the measured current, and this will overlay any catalytic activity. Note that at this strong oxidation potential, many additional oxidation processes may be driven which are not catalysed at lower potentials.

The current densities at -0.8 V_{SCE} recorded on the unannealed Au-Ni alloy catalysts exhibited optimal activity at 30 % Ni (Figure 42). The current densities on the Au-richest region (Ni ≤ 10 at. %) is lower than that for Ni concentration between ca. 10 to 45 at. % (ca. 10 and 18 μA mm^{-2}). This composition region corresponds to those dominated by larger ensembles of Au and a small ensemble of Ni and this appeared to be promoting the direct BOR reaction. On the other hand, the current density of the direct BOR at -0.5 V_{SCE} on the unannealed catalysts varies linearly with the catalyst composition: High Au content being related to high current density towards the oxidation of BH_4^- and vice versa. This means that additional activity from regions of larger Au ensembles seems to dominate (no maximum seen anymore) and activity reduces linearly with Ni substitution (losing pure Au sites). This indicates that Ni is now an inert diluent to the catalysis and any additional activity is attributed to the addition of Au. The reason for Ni not helping to promote is that it is now at a potential where it is oxidizing, blocking the reaction.

The current density at -0.2 V_{SCE} is same as above underlining decrease in activity of catalyst and a surface morphological effect (small crystallite increasing surface area and hence current at 50 %) supported by XRD (Figure 21 and 23).

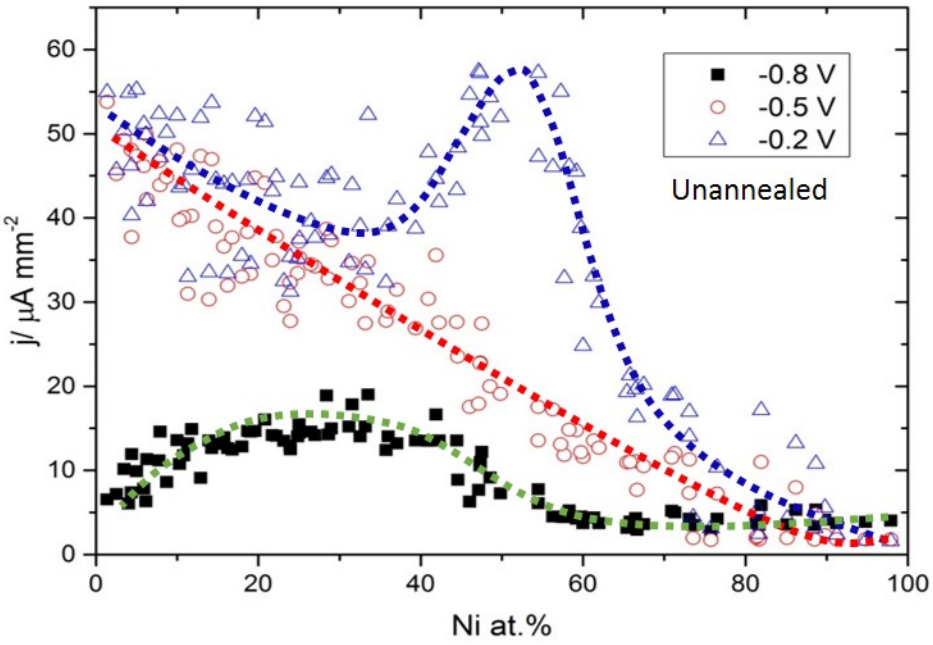

Figure 42: Borohydride activity trends analysis on the (unannealed) Au-Ni electrode arrays through current density extracted from the CVs at -0.8 V_{SCE}, -0.5 V_{SCE} and -0.2 V_{SCE} correlated with Ni composition. The dashed line is a visual guide.

Based on the above electrochemical screening results, it can be concluded that the Ni_{34}-Au_{66} alloy catalyst can be an optimal catalyst for DBFCs as it offers high activity for the direct BOR among other Au-Ni alloy catalysts. It should also be noted that it is difficult to compare the results obtained with those of other studies, not only because of the various compositions, but also the different methods of preparation used.

4.3.2 The Electro-catalytic Activity of the Annealed Au-Ni Alloys for Direct BOR

As shown in the previous section, the electrochemical behaviour of the Au-Ni alloy is strongly governed by the alloy composition. The variation in composition showed a noticeable difference in the catalytic activity towards the direct BOR reaction. Therefore, it is crucial to study the composition-catalytic activity for selecting the optimal alloy composition for DBFCs. The Au-Ni alloy sample (a new sample under the same conditions of deposition) was equilibrated by annealing at 300 °C for 15 min and then cooled to room temperature. The sample was then removed from the UHV chamber for electrochemical screening in the absence and presence of the alkaline sodium borohydride solution. This is part of the electrochemical characterisation for the process of materials discovery and optimisation and was used to determine the activity of the alloy materials at an alloy surface that is Au-rich, the catalytic behaviour of which can be significantly different from the unannealed Au-Ni sample.

The electrocatalytic behaviour of the annealed Au-Ni alloy in alkaline solutions was studied using the high throughput electrochemical screening method. Figure 43 show CVs obtained in 0.1 M of NaOH for the Au-Ni sample annealed at 300 °C for 15 min. The CV was performed in an argon-saturated electrolyte. The potential scan started at -1.2 V_{SCE} and was scanned positively at a rate of 50 mV/s up to the switching potential of +0.01 V_{SCE}. The cycle was then completed by scanning the electrode potential from +0.01 V_{SCE} back to -1.2 V_{SCE}.

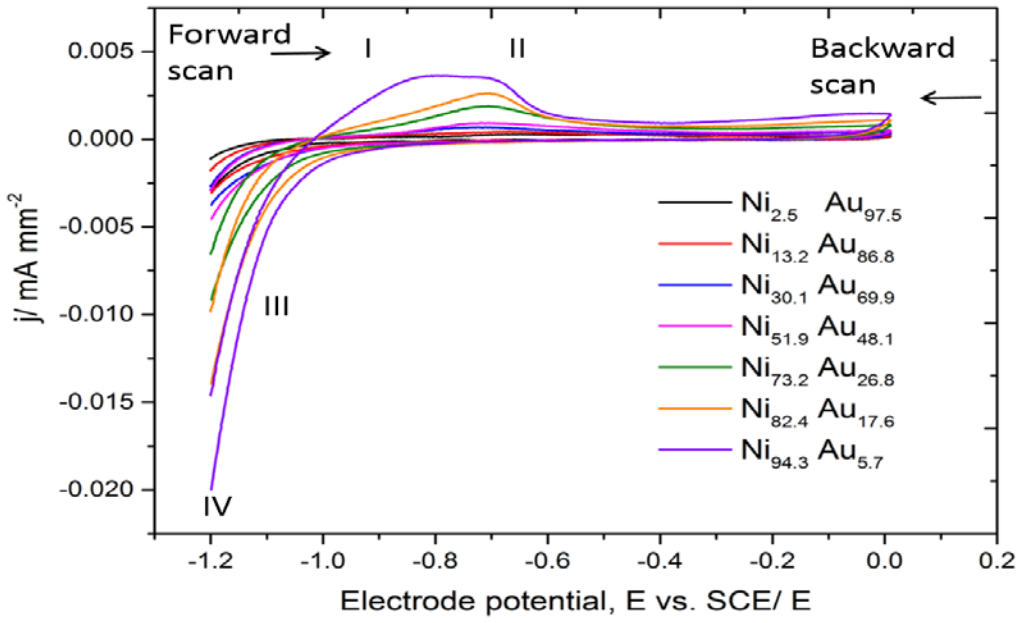

Figure 43: Selected voltammograms showing the electrochemical behaviour of the Au-Ni sample (annealed at 300 °C for 15 min) for different electrode compositions in borohydride free alkaline solution containing 0.1 M of NaOH. CVs are recorded at a scan rate of 50 mV/s at RT.

The CVs for the annealed Au-Ni sample at the selected catalysts show that the HER activity and the oxide formation layer was decreased by the annealing treatment. Modification of the electronic properties and/or structure of the Au-Ni alloy sample (as observed from the XPS and XRD measurements) can play a key role in reducing the HER activity and oxide formation layer. The current density associated with the HER versus the Au-Ni bulk composition is displayed in Figure 44 and is plotted in a false colour over the array for direct comparison. The HER trend can be divided into two groups: (a) where $x \leq 60$ Ni at. % and less activity for HER can be seen and (b) where $x \geq 60$ Ni at. % and significant increase in HER activity can be observed. The general trends show that the hydrogen evolution is associated more with higher Ni content compared to the unannealed sample. This can be seen from the displayed figure where the activity of HER at catalyst composition between 40 and 60 at. % of Ni is almost equal to that of the richest Au region. In contrast, the HER activity on the unannealed sample showed an increase at catalyst composition of Au_{80}-Ni_{20}. It is highly likely that the decrease in HER activity is due to the change of

surface composition after annealing the Au-Ni alloy sample that enriched the alloy surface with Au.

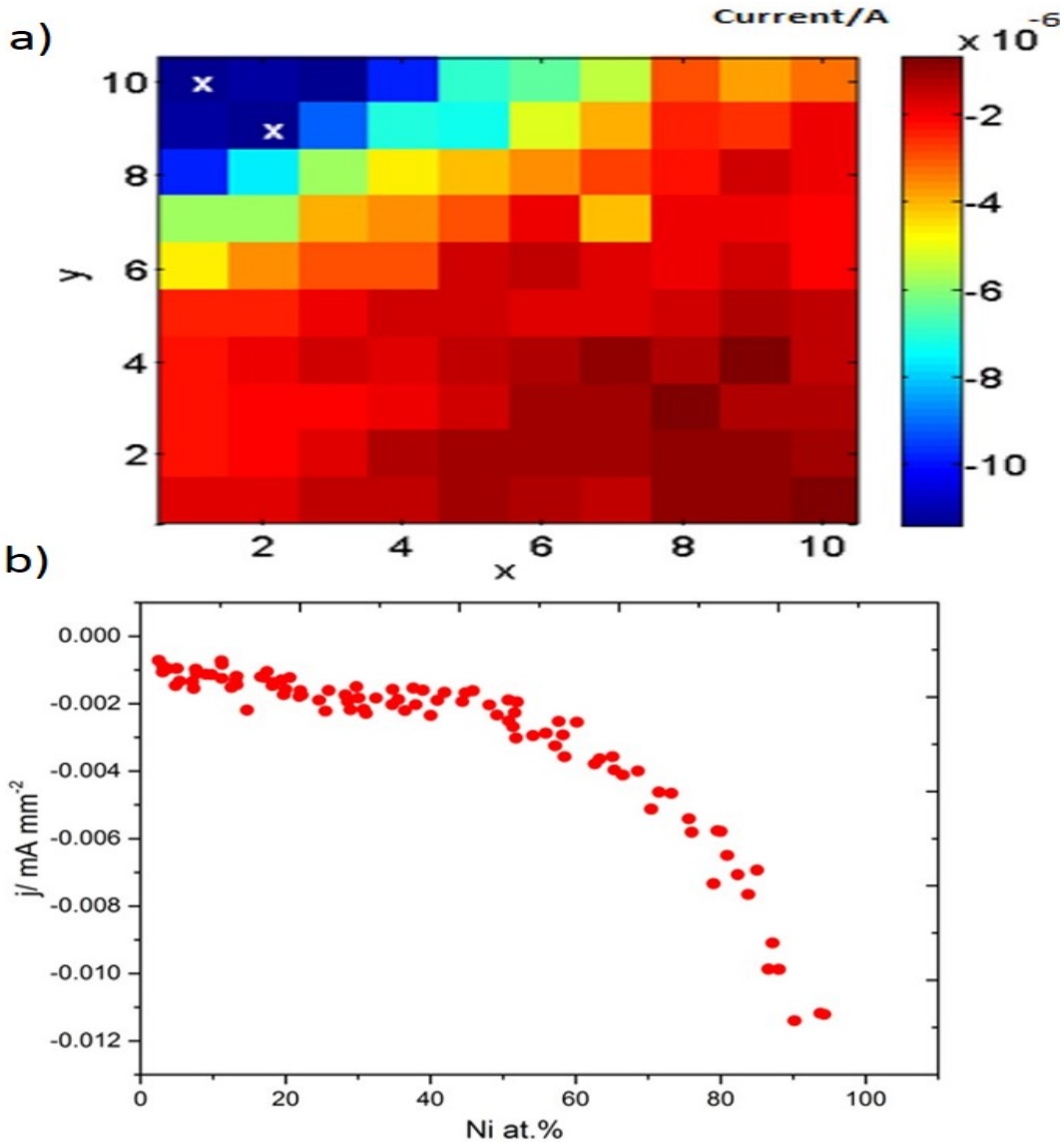

Figure 44: The current of the HER versus Ni compositions of the Au-Ni alloy sample annealed at 300 °C for 15 min. The current is extracted at E= -1.18 V *vs.* SCE.

The HER activity at the annealed Au-Ni alloy catalyst was evaluated as a function of electrode composition using the HER onset potentials. Catalyst regions that exhibited high/low HER activity was identified. Hydrogen evolution over rich Ni takes place near -1.06 V_{SCE}, while over rich Au it is near -1.2 V_{SCE}. Figure 45 shows the onset potential of the HER on the (annealed) Au-Ni alloy catalyst versus the Ni composition. The onset potential for the HER at Ni rich region is approximately 40 mV higher over the annealed Au-Ni alloy than over the unannealed Au-Ni alloy. At intermediate compositions between 40 ≤ x ≤ 60 of Ni at. %, the onset potential for the HER on the annealed Au-Ni alloy sample is approximately 50 mV lower than the unannealed Au-Ni alloy. On the other hand, the onset potential of the HER over the Au rich region at the unannealed Au-Ni alloy sample begins near -1.2 V_{SCE} for the high Au contents. When the Au composition on the

unannealed alloy catalysts is between 10 and 20 at. %, the onset potential increases significantly towards more positive potential values up to -1.16 V_{SCE}, while the onset potential of the HER at the annealed Au-Ni sample remained almost the same. This indicates that after annealing, the Au-Ni sample at the affected region, where Au is the dominant component at the alloy surface, is promoting lower activity towards the HER: it is not only decreases its onset potential but also reduces its current density, as shown in Figures 44 and 45.

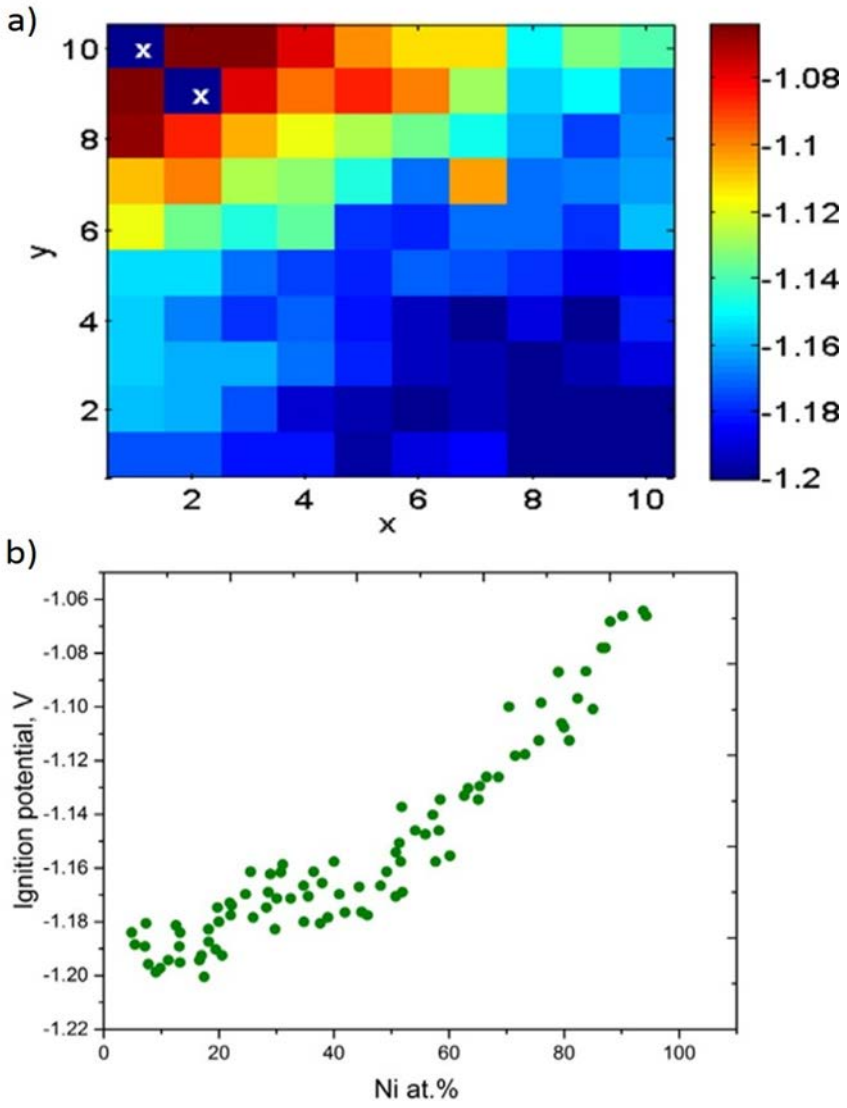

Figure 45: Onset potentials (at I threshold = -1.26 µA mm^{-2}) of the HER versus Ni composition for the annealed Au-Ni alloy sample.

The voltammetric behaviour of the electrochemically formed oxides on the annealed Au-Ni alloy sample was studied and compared with the unannealed Au-Ni alloy sample. The behaviour of the $\alpha(NaOH)_2$ oxidation/ reduction reaction occurring on the surface of the annealed Au-Ni alloy was quite different from the unannealed Au-Ni sample. The differences in the anodic/cathodic peaks for $\alpha(NaOH)_2$ oxidation/ reduction reaction was not only governed by the electrode composition but also by the phase structure of the alloys.

In the case of the as annealed Au-Ni sample, the catalyst arrays showed much less catalytic activity towards the $\alpha(NaOH)_2$ oxidation reaction with increasing the Ni content values (Figure 46). This may indicate that a weak hydroxide bond occurred after the annealing process due to surface compositional/ structural changes that in turn reduced the hydroxide coverage at the annealed Au-Ni alloy sample. Furthermore, the cathodic peak associated with the reduction of the $\alpha(NaOH)_2$ observed at the CVs of the unannealed Au-Ni alloy at around -1.03 V_{SCE} was not seen on the CVs of the annealed Au-Ni alloy sample. It appears that the annealed Au-Ni surface (enriched surface with Au) exhibits irreversible behaviour for the oxidation/ reduction hydroxide processes occurring on the annealed surface of the richest Ni region in comparison with the unannealed Au-Ni sample. This can be supported by the observed fading of the cathodic shoulder in the CV profile (see Figure 38) taking place when increasing scanning potential limits. This could imply that the transition from reversible to irreversible behaviour for the oxidation/ reduction processes of the $Ni(OH)_2$ reaction during an anodic sweep may start at low scanning potential limits for the annealed Au-Ni alloy sample.

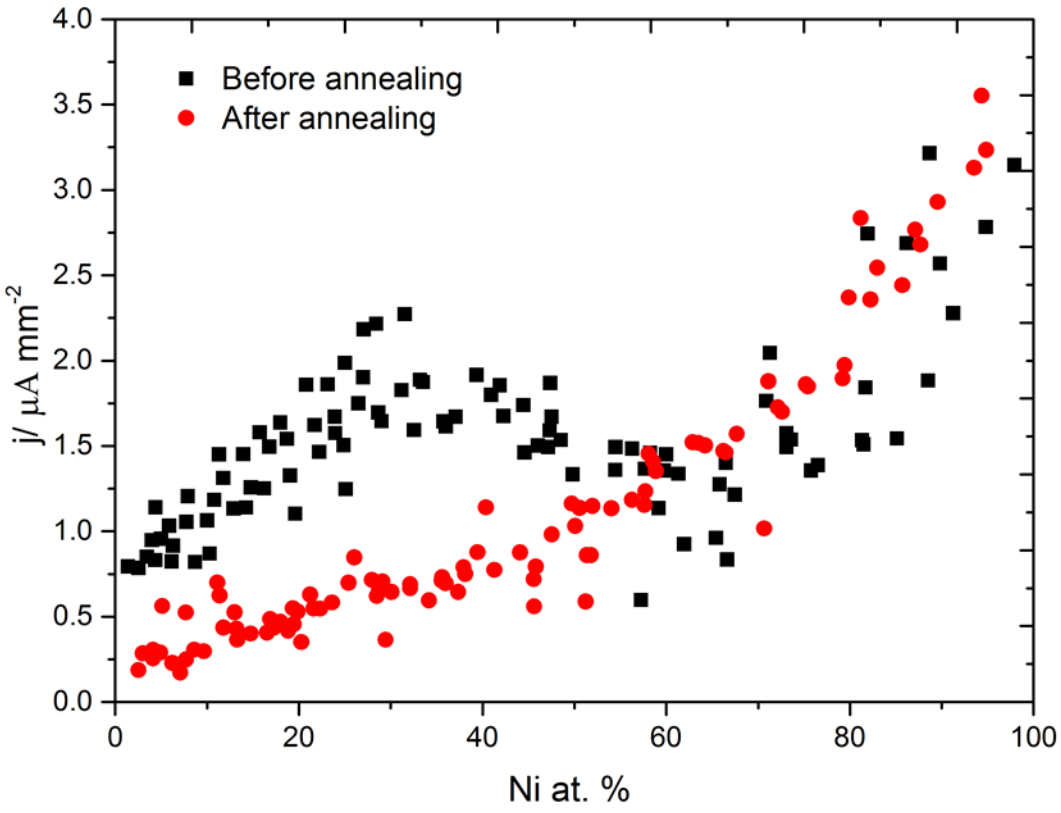

Figure 46: Comparison of the current density of the α-$Ni(OH)_2$ oxidation reaction before and after annealing the Au-Ni alloys.

High throughput electrochemical screening measurements were carried out on the Au-Ni alloy after annealing to 300 ^{o}C for 15 min. The CV responses of the catalysts arrays were investigated in the potential range between -1.2 V_{SCE} and +0.15 V_{SCE} at a scan rate of 25 mV/s. Figure 47 shows selected forward sweeps of (a) the annealed Au-Ni alloy catalysts in an alkaline solution

(containing 0.01 M and $NaBH_4$ 0.1 M NaOH) recorded for the electrode arrays as a function of composition along with (b) Au and (c) Ni pure metals. Apart from the onset potential shift of the direct BOR, the anodic peaks of Au-Ni alloy catalysts before and after annealing exhibited electrochemical behaviour with similar qualitative responses. However, the Au-Ni activity of the electrode arrays towards the direct BOR exhibits noticeable changes.

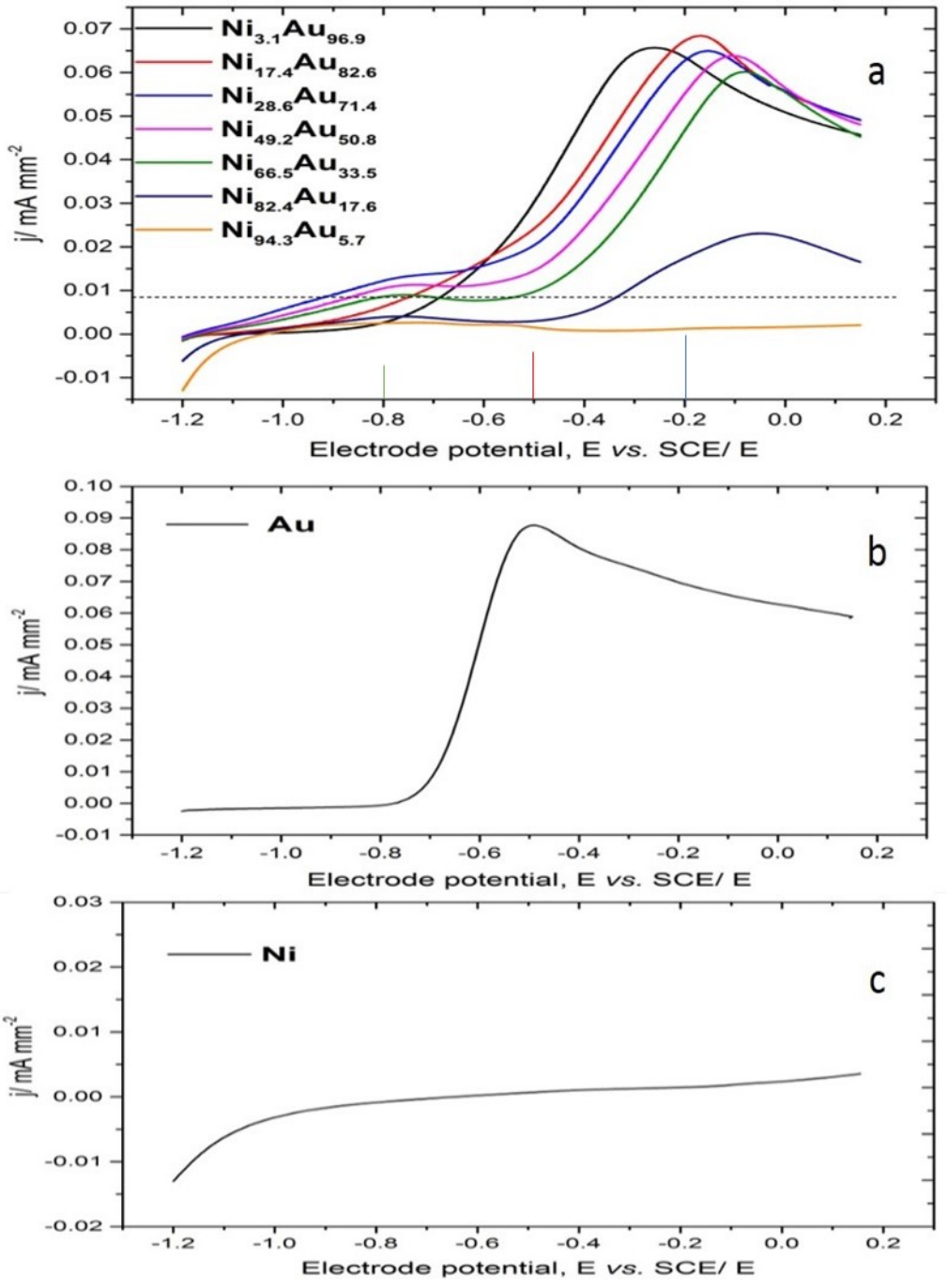

Figure 47: Forward sweep voltammograms showing the anodic peaks attributable to the direct BOR on (a) the annealed Au-Ni alloy as a function of electrode composition, (b) pure Au (disc electrode (0.75 radii)) and pure Ni (disc electrode (0.25 radii)) recorded for 0.01 M of $NaBH_4$ in 0.1 M of NaOH at sweep rate of 25 mV s^{-1}.

The onset potential and the current density were extracted from the CV data to assess the performance of the Au-Ni alloy catalysts before and after annealing. A shift towards more positive potential values occurred for most of the alloy catalysts to that recorded for the unannealed Au-Ni alloy catalysts. The results of this comparison are given below in Figure 48. It can be seen in this figure that the electrode composition influences the behaviour toward the direct BOR on both samples (annealed and unannealed). The value of the onset potential difference between the unannealed and annealed Au-Ni alloy varies with the alloy compositions. As compared with the high Au concentration, both samples showed negative shifts for alloy catalysts with Ni concentration between ca. 10 and 40 at. %, indicating that the addition of the Ni in the Au-Ni shows improved activity for the direct BOR. However, with the increase of more Ni content, the onset potential of the BOR moves further positive potential values. For the annealed Au-Ni alloy sample, the most negative potential of the BOR was recorded for the Au_{72}-Ni_{28} at around -0.9 V_{SCE}. However, the direct BOR onset potential for the Au_{72}-Ni_{28} catalyst is 0.05 V_{SCE} higher than the unannealed Ni_{35}-Au_{65} (optimal) catalyst (-0.95 V_{SCE}). A possible reason for the shift in the onset potential of the direct BOR is that the Au-Ni alloy surface was enriched with Au after annealing, which could have reduced the degree of alloying at the alloy surface and give higher onset potential values. It is also possible that the Au ensemble is associated with lower ensembles of Ni atoms that give rise to the activity reduction.

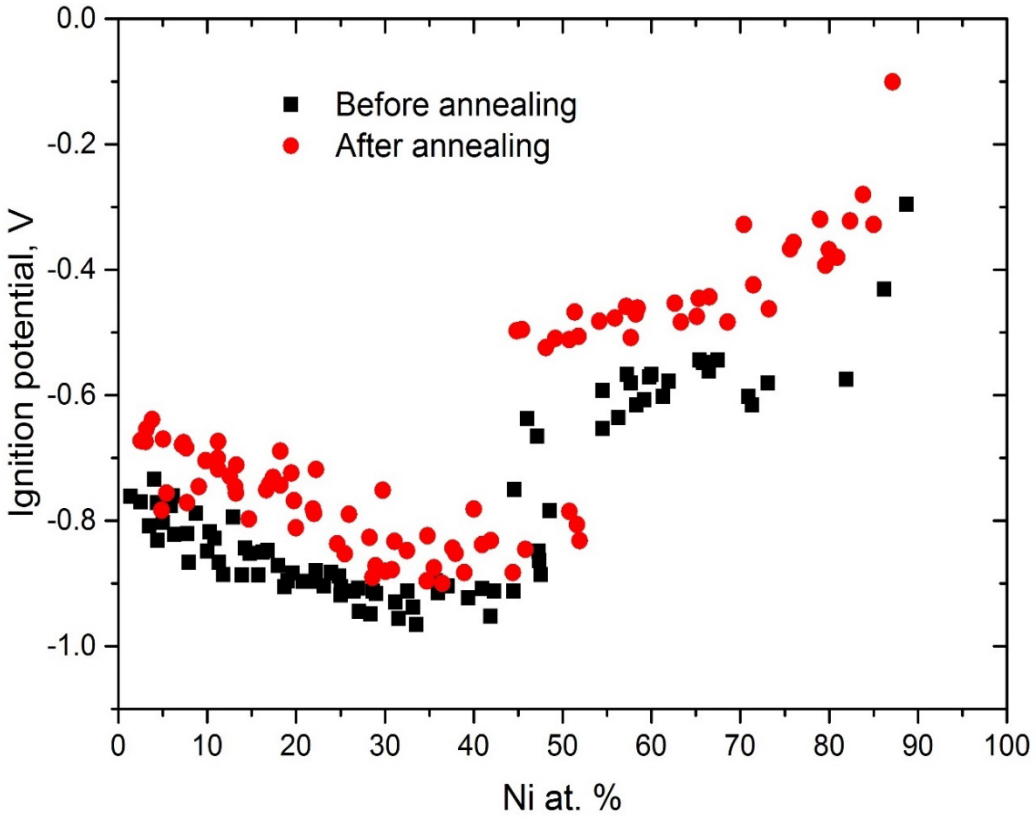

Figure 48: The onset potential of the BOR as a function of electrode composition for the Au-Ni alloy before and after annealing extracted from the recorded CVs at I threshold= 0.0085 mA mm^{-2}.

The activity of the Au-Ni alloy catalysts after annealing was determined based on the current density of the direct BOR extracted at the same oxidation potentials (-0.8 V_{SCE}, -0.5 V_{SCE} and -0.2 V_{SCE}) (Figure 49). Annealing the Au-Ni alloy catalysts increased the number of active sites in the Ni-rich region, and hence, the catalysis of the BOR. As can be seen, the current density at -0.8 V_{SCE}, in both unannealed and annealed cases, is sensitive to the incorporation of Ni. However, the activity in the annealed Au-Ni alloy is now broader over composition due to Au segregation. This indicates that more active centres were produced over a larger region on the annealed surface.

Active sites are delayed on the annealed Au-Ni alloy surface due to Au segregation. The highest current density at -0.5 V_{SCE}, before and after annealing, was recorded for the high Au contents. However, the BOR at the annealed Au-Ni alloy showed a maximum current density of ca. 35 µA mm^{-2} (Figure 49), while the unannealed Au-Ni alloy showed a maximum current density of ca. 55 µA mm^{-2} (Figure 42). Note that this also coincides with the shift of the onset potential to more positive values and, thus, the effect of mass transport at -0.5 V_{SCE} is lower on the annealed catalysts compared to the unannealed Au-Ni alloy. The reason for this is that Ni in the unannealed sample provides adsorption sites at low oxidation potentials (more negative) adjacent to active Au sites and, therefore, the reaction is being driven harder at -0.5 V_{SCE}, while a delayed formation of these active sites was occurring after annealing.

The shape of the current trend at -0.2 V_{SCE} reflects low coverage of formed oxide on the annealed alloy surface due to Au segregation. The relationship between the current density and the surface composition at -0.2 V_{SCE} in the annealed Au-Ni alloy is not linear anymore as it was in the case of the unannealed Au-Ni alloy catalysts. This indicates that the effect of the inert Ni blocking the BOR was reduced after annealing the Au-Ni alloy catalysts.

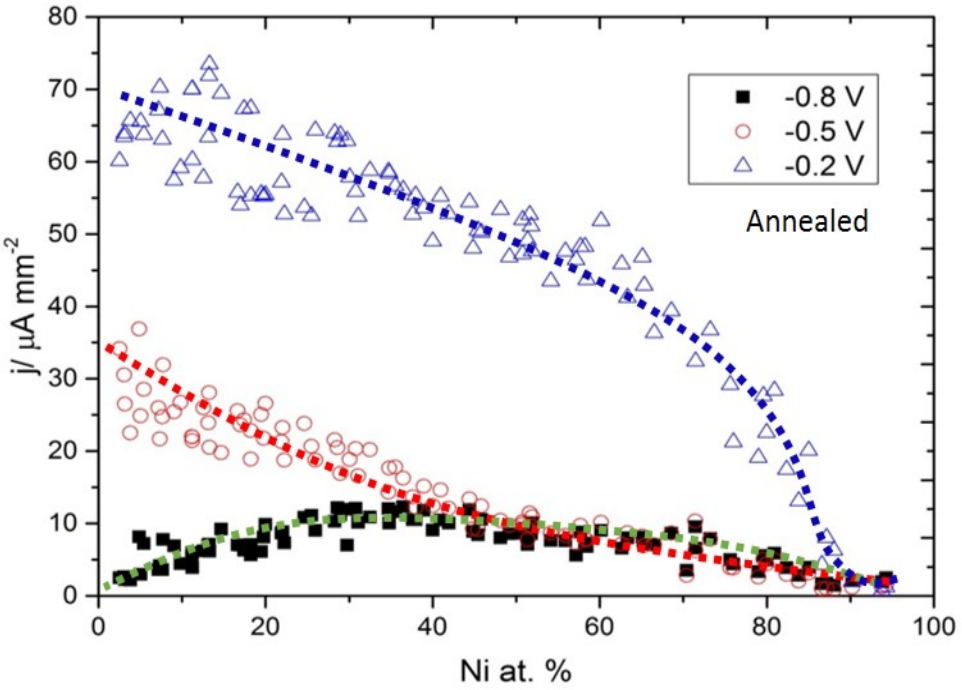

Figure 49: Borohydride activity trends analysis on the (annealed) Au-Ni electrode arrays through current density from the CVs at -0.8 V_{SCE}, -0.5 V_{SCE} and -0.2 V_{SCE} correlated with Ni composition. The dashed line is a visual guide.

4.4 Conclusion

The main goal of this chapter was to understand the relationship between the bulk/ surface of the alloy Au-Ni alloys and their catalytic activities as catalysts for the direct BOR. Therefore, HT-PVD method was used to deposit non-equilibrium and equilibrium Au-Ni alloy catalysts with a wide range of compositions. EDX/SEM measurements demonstrated that a linear gradient in the range of $5 \leq x \leq 95$ was achieved. Non-equilibrated phases exhibited solid solution alloy materials in the unannealed (RT) Au-Ni alloy materials. The thermal annealing performed at 300 ˚C and 600 ˚C for 15 min was carried out under vacuum conditions. The (111) diffraction region was presented with respect to the Au content to illustrate the change after the thermal annealing. It was noticed that the (111) Bragg peak positions of the annealed Au-Ni alloy showed phase separation. The XPS analysis of the surface composition with respect to the bulk composition before and after annealing showed evidence of segregation of Au to the alloy surface.

The catalytic activity of the Au-Ni alloy catalysts for the direct BOR was evaluated using the high throughput electrochemical screening technique. The addition of a small Ni concentration (ca. 10-40 at. %) in the Au-Ni alloy sample increased the activity for the direct BOR. As seen, the typical CV curves shifted towards more negative potential values as small amount of Ni contents added to the Au-Ni alloy catalysts. The results of the ignition potential analysis of the direct BOR showed that among all the catalysts, the unannealed Au_{65}-Ni_{35} catalyst was the most active catalyst recorded at -0.95 V_{SCE}. Moreover, the composition-ignition potential trend of the direct BOR on the annealed Au-Ni alloy catalysts showed a potential shift to higher potential values when small amount of Ni was present on the Au-Ni alloy surface compared to unannealed Au-Ni alloy catalysts. The maximum negative potential of the direct BOR on the annealed Au-Ni alloy catalysts was recorded for the Au_{72}-Ni_{28} at around -0.9 V_{SCE}. This alloy catalyst can be an optimal catalyst for low cost DBFCs as it offers high activity for the direct BOR compared to the pure Au.

Generally, several surface catalytic properties may influence the performance of the Au-Ni alloy catalysts due to structural or electronic/ ensemble effects. It was proven that an addition of a small concentration of Ni (ca. 30 %) into Au catalyst enhanced the activity for the BOR. The appearance of the current density of the BOR on the annealed Au-Ni alloy in the Ni-rich (up to 70 %) region also reflects the small coverage of oxide layer on the annealed alloy surfaces due to Au segregation.

Chapter 5 Au-Cu Alloy Catalysts for Direct BOR

5.1 The Au-Cu Alloy System

The aim of this chapter is to understand the relationship between the catalytic activities of Au-Cu thin film alloys as catalysts for the direct BOR. The composition and structure of a catalyst plays a key role in determining its performance. Since the electrochemical reactions take place on the surface of the Au-Cu alloy catalysts, the initial analysis was conducted to define their bulk/ surface composition and structure, respectively. Each of these will be characterised separately. Subsequently, the electrochemical behaviour of the Au-Cu catalysts towards the direct BOR will be analysed and discussed.

5.1.1 Surface Science Studies of the Au-Cu Alloy System

The Au-Cu alloy system is a model of the order-disorder phase transformation. Figure 50 shows the bulk equilibrium phase diagram that contains two stable phases depending on the temperature[115]. Below the solidus, at high temperature, a continuous solid solution with a face centred cubic (fcc) structure is formed all over the alloy composition. At this stage, the lattice sites are randomly occupied by the Au and Cu atoms creating a short-range order (disordered phase). At low temperatures, super lattice structures, named as Au_3Cu, AuCuI and $AuCu_3I$, are formed depending on the composition. These three structures are identified at room temperature at compositions $Cu_{25}Au_{75}$, $Cu_{50}Au_{50}$ and $Au_{25}Cu_{75}$, respectively. During this transformation, the atoms rearrange themselves into specific lattice sites in a long-range order creating ordered phase.

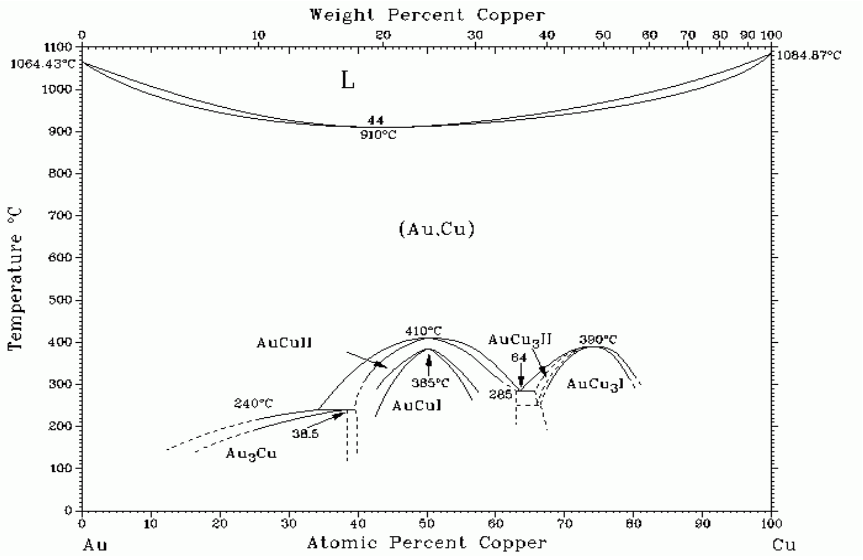

Figure 50: The phase equilibrium diagram of Au-Cu alloy system illustrates the order-disorder phase transformation over a range of temperatures[115].

Disorder-order Au-Cu alloys were synthesised and characterised using different methods. Silva et al. used two different preparation methods; quenching of the bulk Au-Cu alloy and co-deposition by magnetron sputtering[116]. The composition of the bulk Au-Cu alloy was $Au_{50.5}$-$Ni_{49.5}$ atomic percentage, while the Au-Cu thin films (as deposited and annealed) compositions were $Au_{50.6}$ - $Cu_{49.4}$ at. %. The diffraction peak (220) of the Au-Cu for the as deposited sample indicated that the sample corresponded to the disordered fcc phase structure. The annealed sample showed a characteristic of the Au-CuI super lattice structure due to the separation of the 220 peaks into (220) fct (face centred tetragonal) and (022) fct.

Tynkova et al. used DC magnetron sputtering to prepare Au/Cu nanocrystalline thin films with different bilayer thicknesses[117]. Different annealing times were applied on the bilayer thin film samples and the formation of homogenous layer was studied. The samples were annealed under vacuum with a different set of temperatures ranging from 160 to 330 °C. For the Au (25 nm)/Cu (50 nm) thin film sample, they found that the diffusion ratio of the Au to the Cu layer was less intensive than the Cu diffusion into the Au layer. However, when studying a lower thickness of the bilayer Au (10 nm)/ Cu (25 nm) (under the same conduction), the diffusion developed more rapidly. When applying 180 ˚C on samples Au (25nm)/Cu (25nm) and Au (25nm)/Cu (12nm), a homogeneous layer was formed after 5 h with 50/50 composition in the uppermost layer. The depth profile measurements revealed an increase (up to about 10%) of the Au composition in the centre of the Cu layer. This increase in the Au composition was also found to be greater after increasing both the annealing time (20 h) and the temperature (200 °C).

Losch et al. studied the effect of temperature on the surface composition of polycrystalline Au-Cu alloys by means of Auger electron spectroscopy (AES) measurements[118]. The composition of the surface was in the range of Au 7.5 to 65.3 at. %. Enrichment of Au at the Au-Cu alloy surface occurred at temperatures ranging from 200 to 550 °C. The segregation was found to linearly decrease as the temperature increases. In addition, an inverse enrichment on the surface when the surface contained impurities such as S or O at 600 °C was also seen.

Edgar et al. also conducted a study on various compositions of the polycrystalline Au-Cu alloy[119]. They prepared the Au-Cu alloy using pure Au and Cu metals, which were heated via a tube furnace up to 1100 °C for 6 h and then left to cool down to room temperature. The surface compositions of the Au-Cu alloy before and after O_2 exposure at room temperature were examined by angle resolved XPS. The authors found that Au was segregated to the Au-Cu alloy surface before exposing to O_2. However, after O_2 exposure, the Au-Cu alloy surface showed Cu enrichment.

Dennis et al. used combinatorial synthesis to make Au-Cu binary alloys[120]. The co-deposition was carried out using sputter targets. The sputter targets of both elements were fixed in an opposite

direction at an angle of 28° with respect to the substrate in order to make materials libraries of Au-Cu binary alloy nanoparticles with a range of compositions. Gradient compositions of Au-Cu binary alloys ranging from Au_{15}-Cu_{85} to Au_{77}-Cu_{23} atomic percentage were determined by EDX. The small concentration of the Au-Cu nanoparticles affected the XRD patterns and showed unsatisfactory XRD results.

5.1.2 Au-Cu Alloy as Catalysts for DBFC

Au-Cu alloy has been used in catalysis for several applications in various fields. The Au-Cu alloy is a selective catalyst for low temperature CO oxidation[121-123]. Au was found to be a good low temperature oxidation catalyst for CO when a nanoparticle. However, the incorporation of Cu to Au nanoparticles was found to produce much more stable nanoparticles in applications such as automobile emission in high temperature environment. Similarly, the Au-Cu alloy exhibits high activity for the oxidation of alcohol to aldehydes used for the manufacture of cosmetics and food[124-125]. In the following section, studies that examined the catalytic activity of the Au-Cu alloy for the direct BOR will be reviewed.

Lanhua et al. examined the catalytic activity of Au-Cu/C bimetallic catalysts using electrochemical measurements and the fuel cell experiment[126]. The Au-Cu/C where prepared by a reduction of $NaBH_4$ to $HAuCl_4$ in aqueous solution. Their investigations were carried out on Au_{75}-Cu_{25}/C, Au_{67}-Cu_{33}/C and Au_{50}-Cu_{50}/C in a basic solution containing 0.1 M of $NaBH_4$ and 3 M of NaOH. Among the Au-Cu alloy catalysts, the $Au_{67}Cu_{33}$ catalyst showed high catalytic activity for the direct BOR. This was attributed to the non-catalytic nature of the Au/C and the Au-Cu/C towards the hydrolysis reaction of the BH_4^-.

The oxidation of BH_4^- on a nanostructured Au-Cu/ Ti surface with various loading of Au including 5.6, 9.8, and 19.8 μg cm^{-2} was studied using CV and chronoamperometry (CA)[127]. The oxidation of the BH_4^- was performed in an alkaline solution containing 1 M of NaOH and 0.05 M of $NaBH_4$. The catalyst behaviour of both Au and Cu pure catalysts in the absence and in the presence of $NaBH_4$ was studied. It was found that the pure Cu was inactive as the oxidation of BH_4^- occurs at a surface that is already covered by an oxide layer of OH_{ads}. Unlike the Cu, the catalytic activity of the pure Au was found to be more active towards the BH_4^- ion. The anodic peak assigned for the direct oxidation of the BH_4^- on alloy compositions of $Au_{1.77}Cu_{95.49}$, $Au_{2.73}Cu_{94.67}$ and $Au_{6.87}Cu_{91.14}$ catalysts shifted towards more positive potential values compared to the pure Au. This indicated a higher overpotential on the alloy, and hence a lower electro-catalytic activity. The highest activity recorded by chronoamperometry (CA) was found to be for the catalysts that have less Au loading. The current density of BOR peak was found to be seven times higher than that of the pure Au.

Wang et al. carried out a comparative study of Au-Cu nanotube alloy catalysts for the oxidation of the BH_4^- ion[128]. The catalytic behaviour of the noble alloys towards the direct BOR was investigated in a basic solution containing 3 M of NaOH using CV. It was found that the Au-Cu alloy exhibited higher catalytic activity than that of Au particles.

5.2 High Throughput Characterisation of the Au-Cu alloy Catalysts

5.2.1 Bulk Composition Analysis of the Au-Cu Alloys

SEM/ EDX measurements were carried out for high throughput analysis of the bulk composition of the Au-Cu alloy thin film catalysts. Measurements made in the discrete 10 x 10 fields of an electrochemical chip with ITO substrate to determine the precise composition at each electrode that is defined by x and y coordinates. Figure 51 shows two composition plots of the normalized atomic ratio of the Cu content and the Au content useful in determining electrode compositions. Each composition plot represents visually observable electrodes with graded compositions as a function of position. The composition gradient was chosen such that it includes a wide range of composition across the substrate. The composition of the $Au_{1-x}Cu_x$ alloy catalysts synthesised correspond to the range $10 \leq x$ at. % ≤ 96.

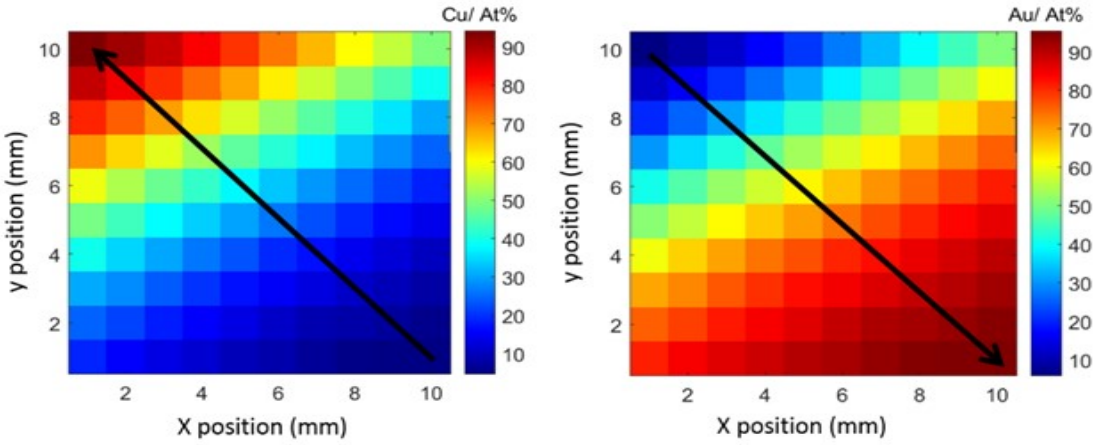

Figure 51: Composition plots of the relative Au and Cu concentration on the 10x10 (ITO-e-chem) electrode arrays determined by EDX measurements showing distinguishable regions of the pure-components with false colour in which the composition of each electrode can be identified in terms of visual analysis.

5.2.2 XRD Analysis of the Au-Cu Alloys

XRD measurements were carried out to determine the bulk crystal structure of the Au-Cu alloy sample synthesised under non-equilibrium conditions. The XRD patterns of the unannealed Au-Cu

alloy shown in Figure 52 are regarded as the best representation for the crystal structure across all compositions on a thin film of thickness ca. 150-180 nm. As is evident in the XRD patterns, the diffraction peaks at 38.10°, 43°, 45.00° and 51° Bragg angles are assigned to the alloy phases Au-Cu (111) and Au-Cu (200) (PDF Card-01-077-6964). Both Bragg peaks shift to higher Bragg angles with increasing Cu content. This indicates that solid solution alloy phases were formed. In addition, orthorhombic Au-Cu structures were distinguished by a low intensity peak observed at intermediate composition. The diffraction peaks observed in the XRD spectrum of the intermediate composition ($Cu_{51.3}Au_{48.7}$) at 2θ= 23.45° correspond to Au-Cu orthorhombic (013) (PDF Card-01-072-5239).

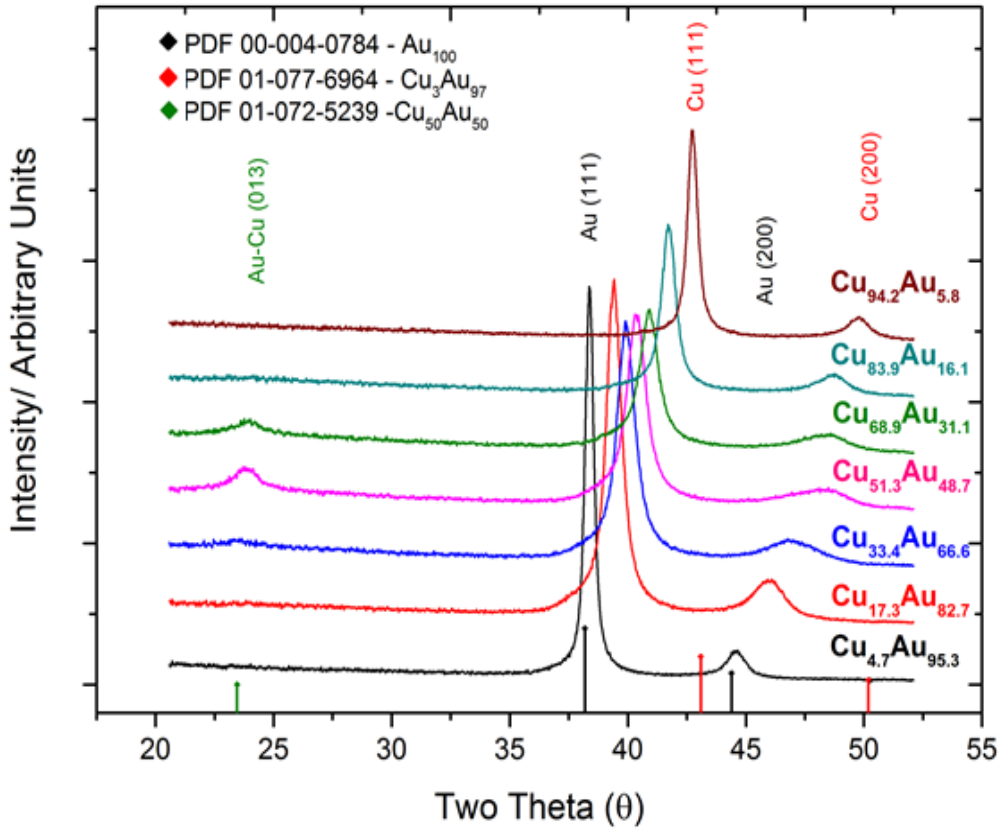

Figure 52: XRD diffraction patterns for the unannealed Au-Cu alloy (RT) covering different compositional regions where 5 ≤ x at. % ≤ 95.

The XRD spectra from 21° to 53° Bragg angles demonstrate that the (111) reflection that corresponds to the Au-Cu (111) fcc structure is the most intense peak. The strong reflection at 38.4°, corresponding to the (111) (Cu deficient), shows a clear shift to higher 2θ values with increasing the Cu content. The peak position of the (111) Bragg peaks was used to experimentally determine the relationship between the lattice constant and composition in the Au-Cu alloys. The lattice constant of the unannealed Au-Cu alloy sample was calculated using Vegard's law to obtain a linear relationship between the lattice parameter of the Au-Cu solid solution alloy and the bulk composition of the Au-Cu alloy. The lattice constants of the pure elements, Au and Cu, are a =4.06

Å[105] and a Cu= 3.615 Å[129], respectively. Comparing the lattice constant with the Cu composition suggests that Au and Cu are alloyed in a single crystalline phase with no phase separation for alloy compositions less than Cu-60 at. % (Figure 53). A small deviation can be seen for alloy compositions of Cu higher than 60 at. % which could indicate that an intermetallic phase of Au-Cu is beginning to form.

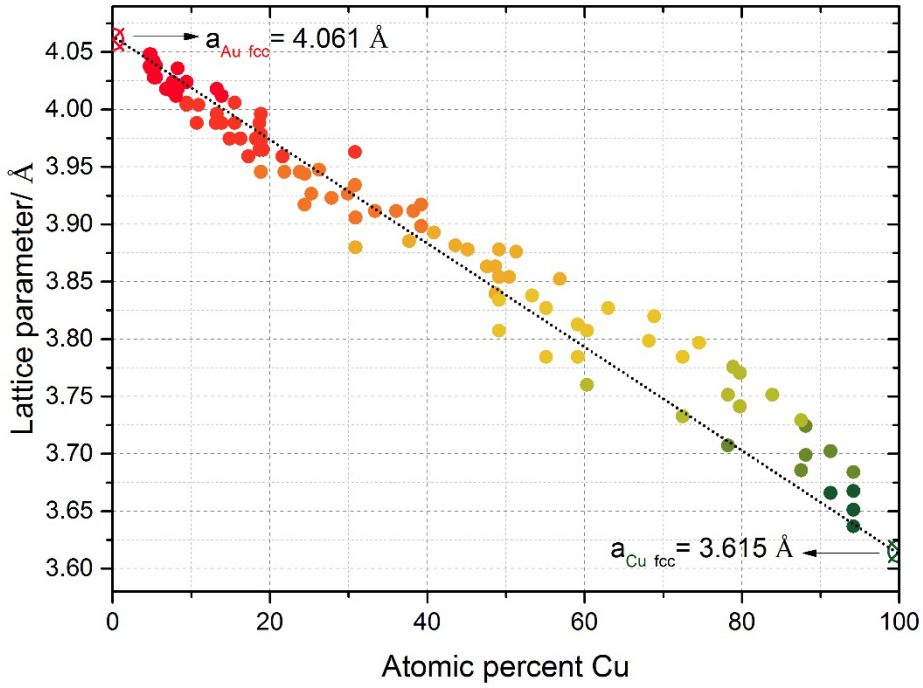

Figure 53: The lattice parameter (a) fcc of the unannealed Au-Cu unit cell versus Cu composition. The red and the green crossed circles at the extreme ends are the lattice parameters of pure Au[105] and Cu[129] pure elements. The dashed line represents Vegard's law.

XRD measurements were performed on the Au-Cu alloy sample annealed at 300 °C for 15 min under UHV (Figure 54). The diffraction patterns of the annealed Au-Cu exhibits neither indication for phase separation nor extra reflections in the regions shown when compared to the unannealed Au-Cu alloy sample (Figure 52). As can be seen, the (111) peak and (200) Bragg peaks shifts to higher 2θ with increasing Cu content with the same peak position as the unannealed Au-Cu alloy sample. Figure 55 shows the lattice constant of the annealed Au-Cu alloy as a function of Cu composition. It can be observed that the lattice constant of the Au-Cu alloy between the pure elements shows no difference when compared with lattice constant variations in the unannealed Au-Cu (Figure 53).

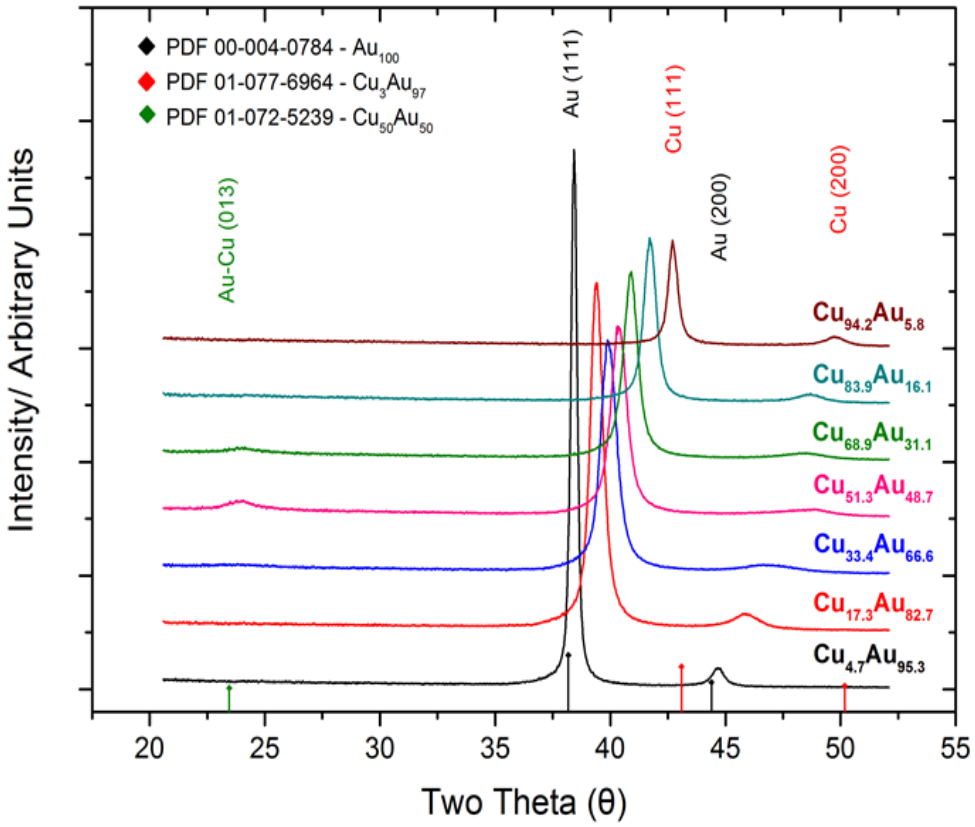

Figure 54: XRD diffraction patterns for the annealed Au-Cu alloy (300 ^{o}C for 15 min) covering different compositional regions where 5 ≤ x at. % ≤ 95.

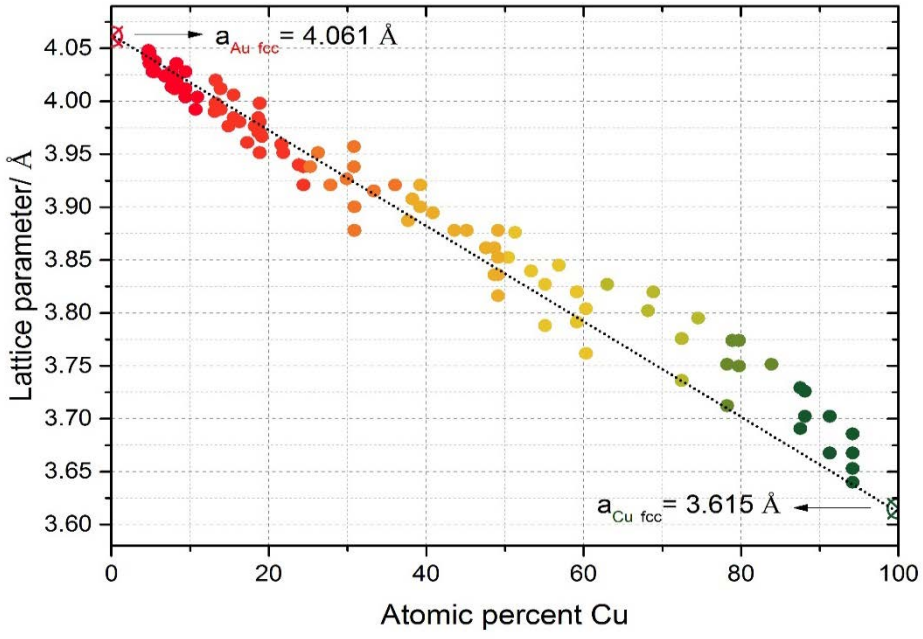

Figure 55: The lattice parameter (a) fcc of the as annealed Au-Cu unit cell versus Cu composition. The red and the green crossed circles at the extreme ends are the lattice parameters of Au[105] and Cu[129] pure elements. The dashed line represents Vegard's law.

In order to distinguish the contribution of the thermal annealing on the Au-Cu alloy, the maximum peak intensity and the full width at half maximum (FWHM) of the (111) Bragg peak was plotted as a function of Cu content (Figure 56 and 57). The maximum peak intensity of the (111) Bragg peak of the annealed Au-Cu alloys show a significant increase, noticeably, the intensity of the (111) Au-rich Bragg peaks compared to the unannealed alloys. Moreover, the FWHF of the (111) Bragg peaks showed a decrease. This indicates that the crystallite size of the Au-Cu alloy increased after the thermal annealing.

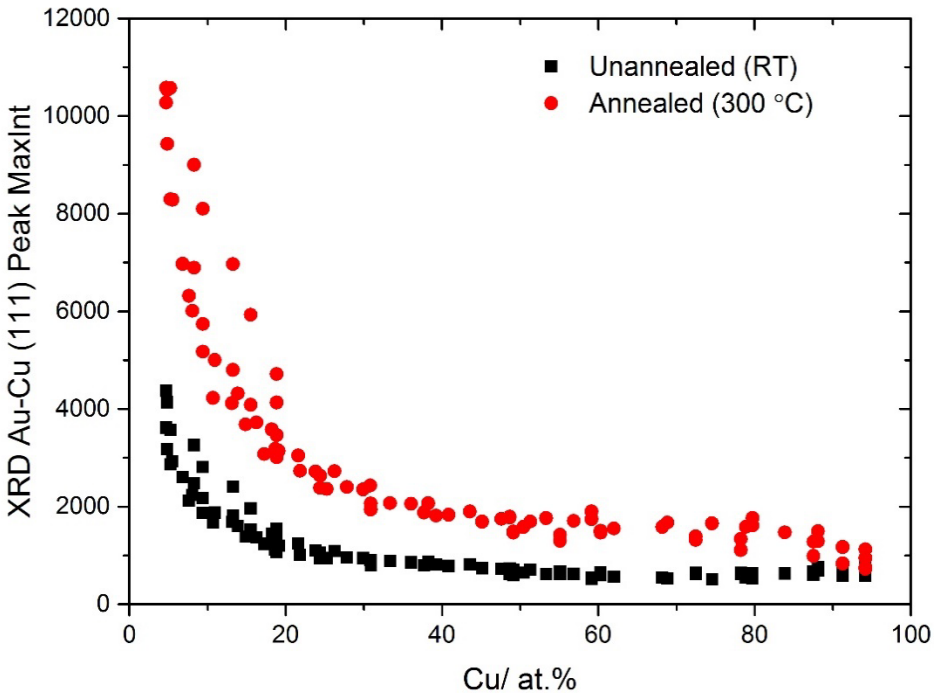

Figure 56: Maximum peak intensity of the (111) Bragg peak in the Au-Cu alloy (a) unannealed and (b) annealed at 300 °C versus Au bulk composition.

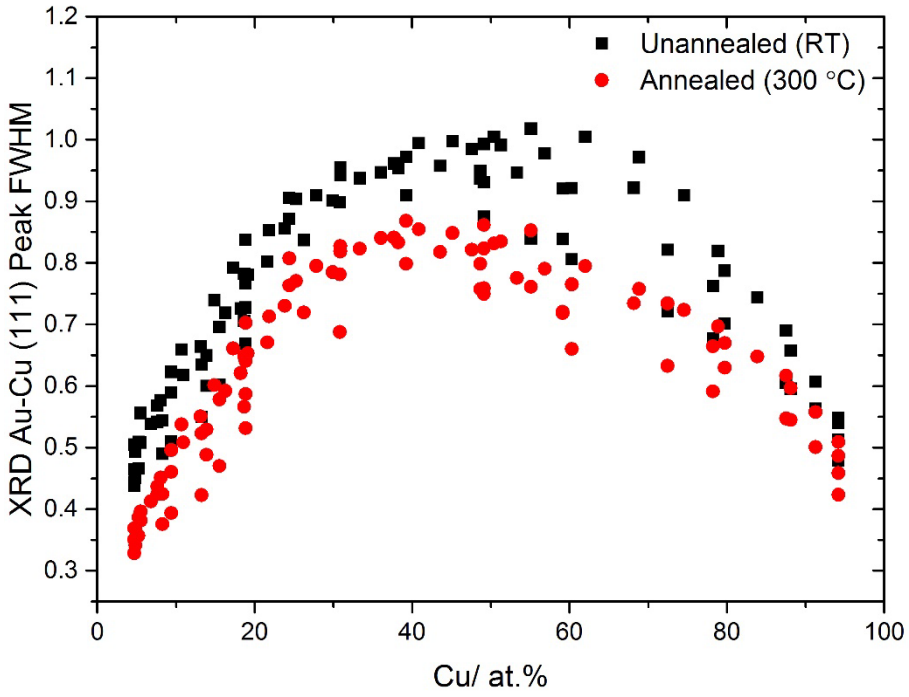

Figure 57: Full width at Half-maximum intensity (FWHM) of the (111) Bragg peaks for the unannealed (RT) and the annealed (300 ^{o}C) Au-Cu alloys based on Gaussian fitted (111) peaks.

5.2.3 Surface Composition of Au-Cu Alloys

XPS experiments were carried out to determine the surface composition of the Au-Cu alloy before and after annealing. The sample was transferred to the XPS chamber with a base pressure of 4.266 10^{-9} mBar after deposition without breaking the UHV. The XPS results of the Au-Cu alloy sample are given in Figure 58. The XPS spectra display the Au 4f and the Cu 2p core levels measured at different bulk composition. The Au 4f and the Cu 2p spectra show that the ratio of the two elements varies as a function of surface composition. As the concentration of the Cu increases in the unannealed Au-Cu alloy, the Au 4f XPS peaks become less intense than the Cu 2p XPS peaks and vice versa.

The results displayed in Figure 59 show features of binding energy shifts for the Au $4f_{7/2}$ and Cu $2p_{3/2}$ core levels of the unannealed Au-Cu alloy sample. When decreasing the Au concentration in the Au-Cu alloy, the Au ($4f_{7/2}$) peak shifts towards a lower binding energy. However, when decreasing the Cu concentration in the Au-Cu alloy, the Cu ($2p_{3/2}$) shifts towards higher binding energy. The increase/decrease in binding energy with increasing/decreasing composition is indicative of the effect of the electron transfer, which confirms the alloying of Au with Cu.

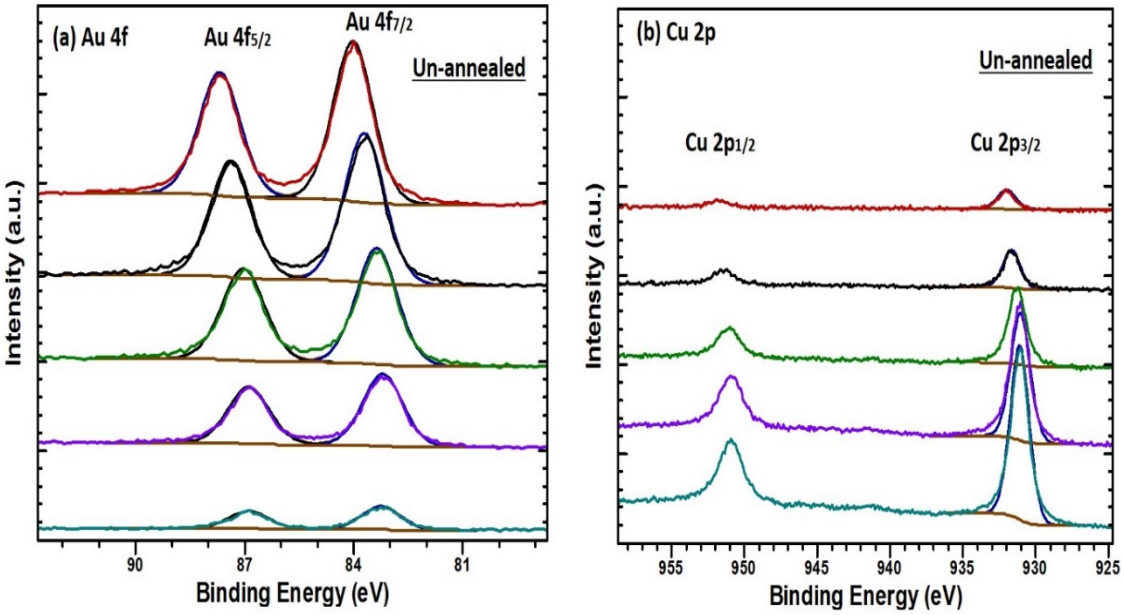

Figure 58: XPS spectra of the (a) Au 4f and (b) Cu 2p valance bands for various bulk (Unannealed) Au-Cu alloy compositions including ($Au_{92.61}$-$Cu_{7.39}$, $Au_{79.99}$-$Cu_{20.01}$, $Au_{58.51}$-$Cu_{41.49}$, $Au_{6.9}$-$Cu_{93.1}$).

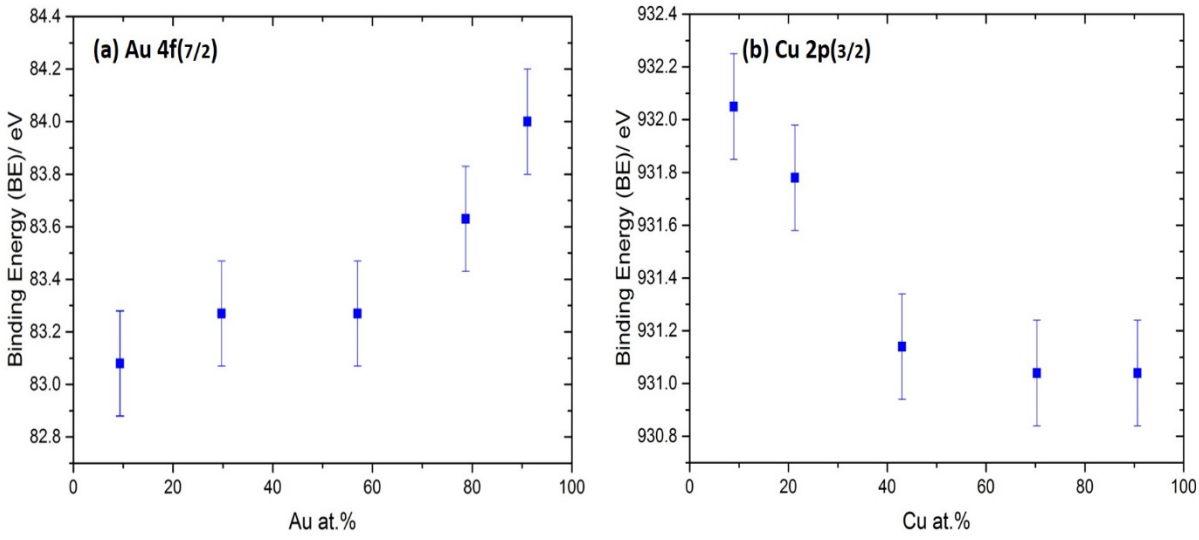

Figure 59: The peak positions of the unannealed Au-Cu alloy (a) Au ($4f_{7/2}$) and (b) Cu ($2p_{3/2}$) core levels as a function of composition.

The Au-Cu alloy sample was exposed to post-annealing at 300 ^{o}C for 15 min to determine the surface segregation of Au to the top-most surface layer. Figure 60 shows the XPS spectra of the Au 4f and Cu 2p core levels. The Au 4f doublet peaks show a slight shift in the Au ($4f_{7/2}$) peak position towards higher binding energy as the Au decreases in the Au-Cu alloy. The observed binding energies were slightly higher than those of the Au-rich alloy possibly due to a slight enrichment that can be observed at low Au composition. The atomic concentration was calculated from the XPS peak areas. Figure 61 shows a comparison of the Au surface compositions

before and after post annealing relative to the bulk composition of Au determined by EDX. The results show (within experimental error) no evidence of segregation of either element at any composition on the equilibrated Au-Cu alloy, in contradiction with other experimental observation where the occurrence of the Au segregation to the surface in the absence of impurities (O_2) was reported[118, 120].

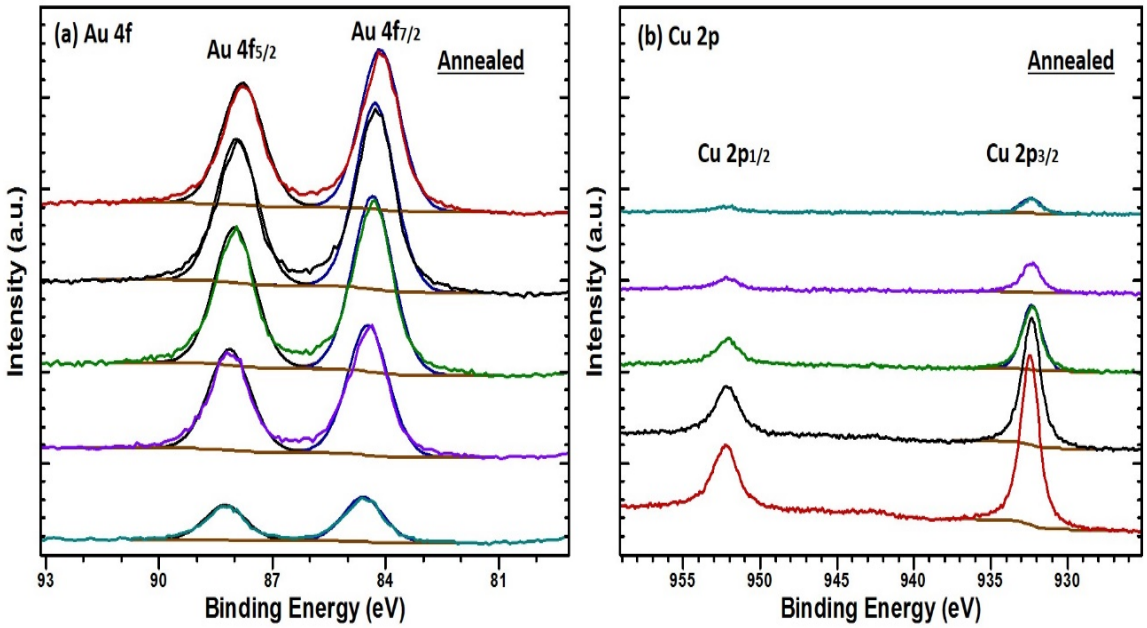

Figure 60: XPS spectra of the (a) Au 4f and (b) Cu 2p valance bands for various Au and Cu compositions ($Au_{92.61}$-$Cu_{7.39}$, $Au_{79.99}$-$Cu_{20.01}$, $Au_{58.51}$-$Cu_{41.49}$, $Au_{6.9}$-$Cu_{93.1}$) after annealing to 300 °C for 15 min.

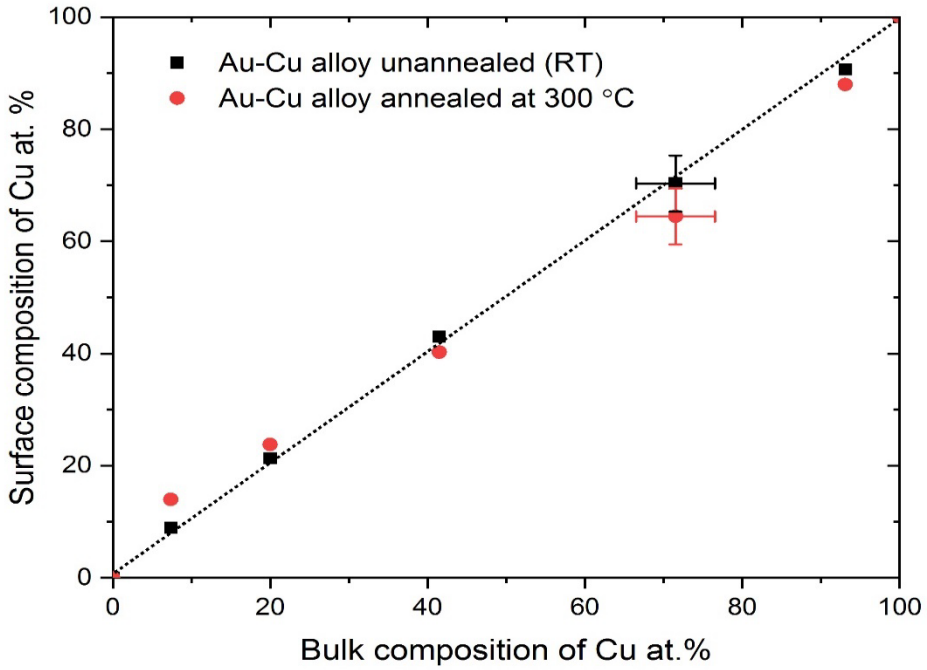

Figure 61: Surface composition of Au-Cu alloy before and after annealing to 300 °C measured by XPS versus the bulk composition determined by EDX.

5.3 The Catalytic Activity of the Au-Cu Alloy Catalysts

High Throughput Electrochemical Screening was used to evaluate the catalytic activity of the Au-Cu alloy catalysts as a function of composition. Efforts were made to lower the cost as well as to increase the activity of the direct BOR. The formation of oxide on the pure Cu was shown to block the surface sites for the BH_4^- (see Chapter 3). Unlike Cu, the direct BOR is active on pure Au. Alloying Au with Cu has been reported to improve the catalytic activity of Au for the BOR[127,128] although a distinction of the catalytic activity for a wide range of Au-Cu alloy compositions was not explored. The combinatorial method for achieving solid solution alloys could lead to a better understanding of the reasons for the increase in the BOR activity on Au-Cu alloy catalysts. It could also offer interesting insight into the reaction mechanism. Therefore, Au-Cu alloy catalysts were synthesised with a wide range of compositions to study the effects of the alloy formation on the catalytic properties in the presence and in the absence of the borohydride.

5.3.1 The Electro-catalytic Activity of the Unannealed Au-Cu Alloys for Direct BOR

In order to understand the role of the electronic/ ensemble effects on the electrochemical oxidation of the borohydride, the possible redox reactions occurring on the unannealed Au-Cu alloy catalysts in the 0.1 M NaOH were studied in the potential range between -1.3 V_{SCE} and +0.1 V_{SCE} at a scan rate of 50 mV/s. The CVs displayed in Figure 62 show (1) the hydrogen evolution reaction and (2) surface oxide formation/ reduction on the Au-Cu alloy catalysts for various compositions taking place at different potentials. The large peak observed in the cathodic scan at -1.05 V_{SCE} for the Cu 89.7 at. % alloy catalysts correspond to the hydrogen evolution which increases with increasing Cu content, shifting the onset potential to positive values.

The CVs also show that the surface oxide formation/ reduction increases as the Cu content increases in the Au-Cu alloy. The peaks corresponding to the oxide formation have a close relationship with the peaks of the oxide removal. It can be seen that three anodic peaks in the forward scan at -0.4 V_{SCE}, -0.2 V_{SCE} and 0.0 V_{SCE} are associated with three cathodic peaks in the backward scan that was also observed on Cu pure metal catalysts assigned for Cu_2O, CuO and Cu_2O_3 respectively (see Chapter 3). These anodic peaks are very pronounced on the alloy catalysts of Cu 89.7 at. %. This indicates that the increase of Cu concentrations in the Au-Cu alloy catalyst increased the activity for the oxide formation.

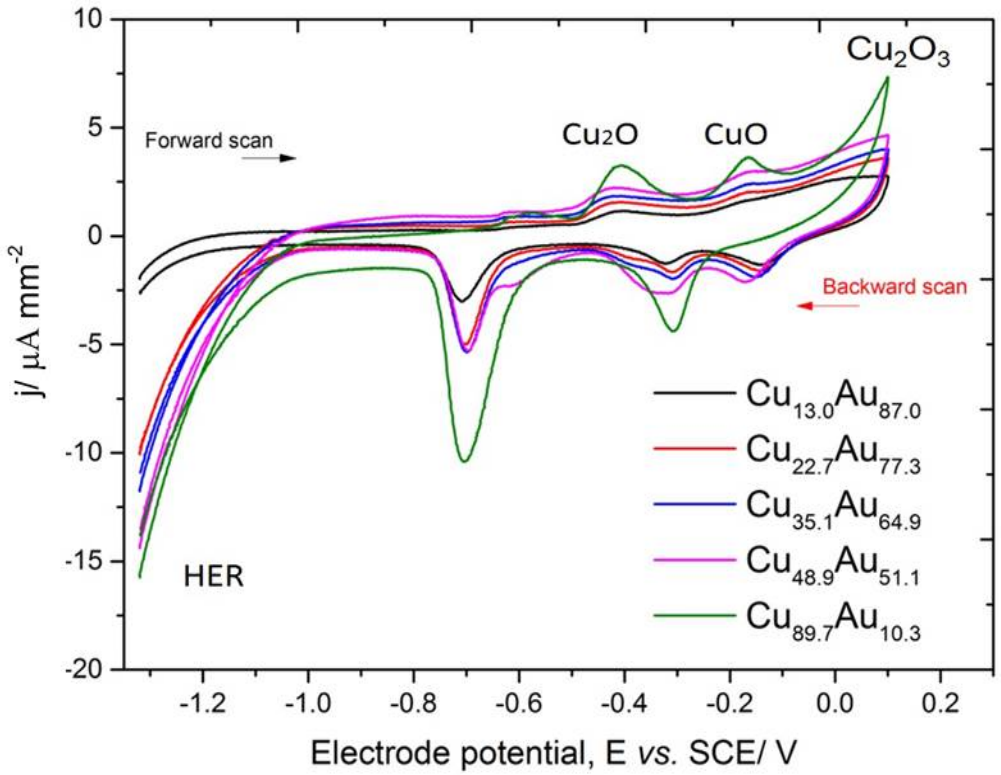

Figure 62: CVs showing the electrochemical activity of the (unannealed) Au-Cu alloy catalyst in 0.1 M of NaOH at a potential scan rate of 50 mV/s from -1.3 V_{SCE} to +0.1 V_{SCE} as a function of electrode composition.

The catalysts activity of the unannealed Au-Cu alloys towards the BOR was examined over a wide range of compositions. For comparison, Figure 63 shows forward scans of selected Au-Cu alloy catalyst compositions in the presence of 0.01 M $NaBH_4$ recorded in between the potential range -1.2 V_{SCE} and 0.0 V_{SCE} at a scan rate of 25 mV/s. Initially, it is important to observe the appearance of new anodic peaks, the shape of these peaks and their current peaks on the voltammogram in the presence of the borohydride, under these conditions, as a function of Au-Cu catalyst compositions. The second step is to evaluate the activity of the alloy catalysts as a function of composition because there is a clear difference in the onset potential values of the BOR.

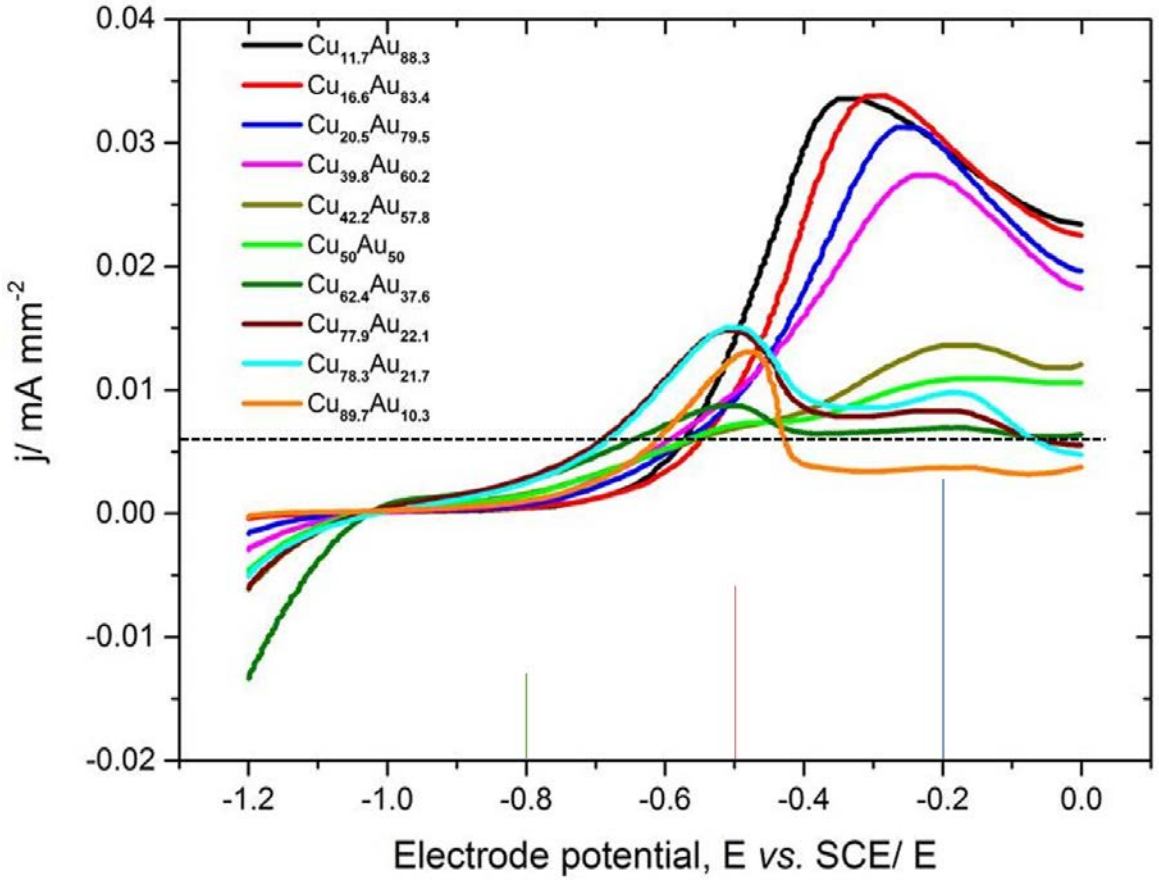

Figure 63: A forward scan of CVs showing the unannealed Au-Cu alloy catalysts over a wide range of compositions in 0.01 M $NaBH_4$ at scan rate of 25 mV/s from -1.2 V_{SCE} to 0.0 V_{SCE}.

It should be noted that the BOR observed during the evaluation of the catalytic activity of Cu pure metal was reported to take place at a very positive potential +0.5 V_{SCE} (Figure 15 Chapter 3), while in the case of pure Au, the BOR was taking place at more negative potential (-0.6 V_{SCE}). The anodic peak of the BOR on pure Au has a similar shape to the anodic peak observed on the Au-rich alloy catalysts. The onset potential of this anodic peak is shifted as the composition of the Au-Cu alloy catalyst is changing which is a clear indication of the dependence of the BOR activity on the catalyst composition.

Figure 64 shows comparison of the onset potential of the BOR as a function of Au-Cu alloy composition. The onset potential of the BOR starts on the Au-rich alloy catalysts at an onset potential around -0.5 V_{SCE}, while for Cu-rich catalysts the onset potential starts at about -0.67 V_{SCE}. The presence of Cu in the Au alloy catalysts shifts the onset potential of the BOR to more negative potentials.

Clearly, the activity of the Au-Cu alloys for the direct BOR depends on the composition. Among the Au-Cu alloy catalysts, the $Au_{22.1}$-$Cu_{79.9}$ composition oxidised the BOR at more negative onset potential (ca. -0.71 V_{SCE}) offering high catalytic activity. It seems that the presence of a small ensemble of Au atom surrounded by more Cu atoms plays a major role in which it activates the

direct BOR. When the concentration of Au at the surface is largely decreased (nearly pure Cu), the catalytic activity becomes very low and the onset potential of BOR shifts from a very negative to a very positive onset potential. These two characteristics are a clear indication of the role of the electronic and ensemble effects in modifying the catalytic activity of the Au-Cu alloy catalysts for electro-oxidation reaction of the borohydride.

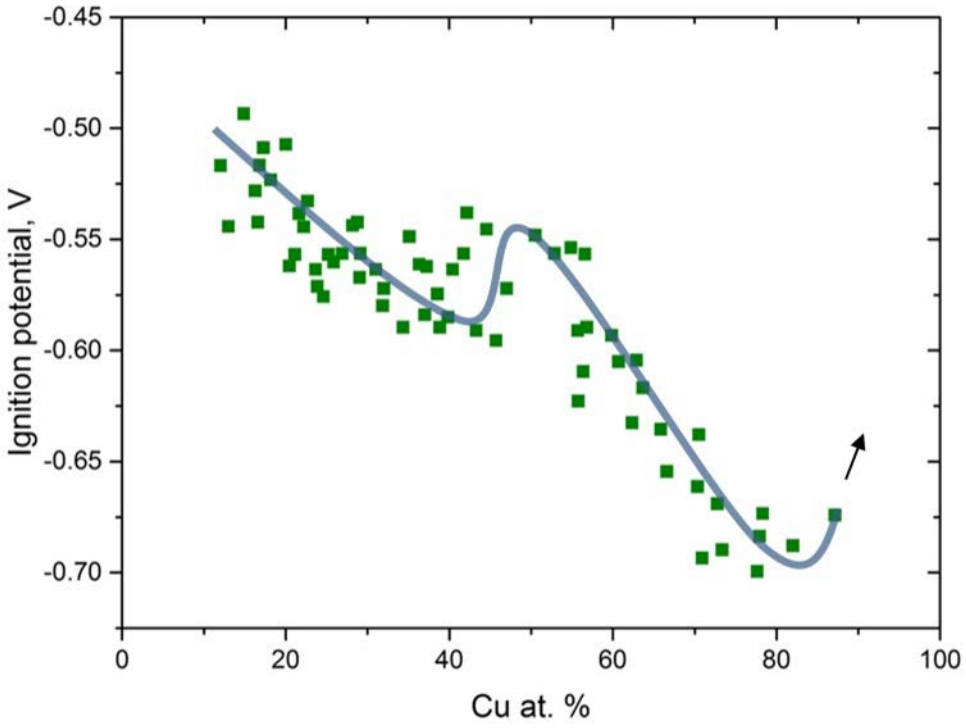

Figure 64: Onset potentials (at I threshold = 6.3 x10^{-06} A mm^{-2}) of the BOR versus Cu composition for the as unannealed Au-Cu alloy sample. The pure Cu has an onset potential is much higher. The transparent line is a guide to the eye.

The next step is to determine the activity of the direct BOR in terms of the measured current as a function of Au-Cu alloy composition. Figure 65 shows the current density of the direct BOR at -0.8 V_{SCE}, -0.5 V_{SCE} and -0.2 V_{SCE}. The highest current density at -0.8 V_{SCE} can be assigned to the catalyst composition between Cu-70 and Cu-87 at. % in the Au-Cu alloy increasing from 1 µA mm^{-2} to 3 µA mm^{-2}. This indicates that the catalysis is occurring on a surface containing small Au ensembles embodied in larger Cu ensembles.

The increase of the measured current at -0.5 V_{SCE} in the Cu-rich region indicates the presence of two processes on the Au-Cu alloy surfaces for the same oxidation reaction process. The first process, the catalysed BOR, is occurring earlier and therefore it is being driven harder at -0.5 V_{SCE}. On the other hand, the second process is due to the additional activity in which Au is the active component. At a potential of -0.2 V_{SCE}, the latter seems to be dominant, and therefore it is now influenced by the addition of Cu due to the suppression caused by oxidation of the Cu sites.

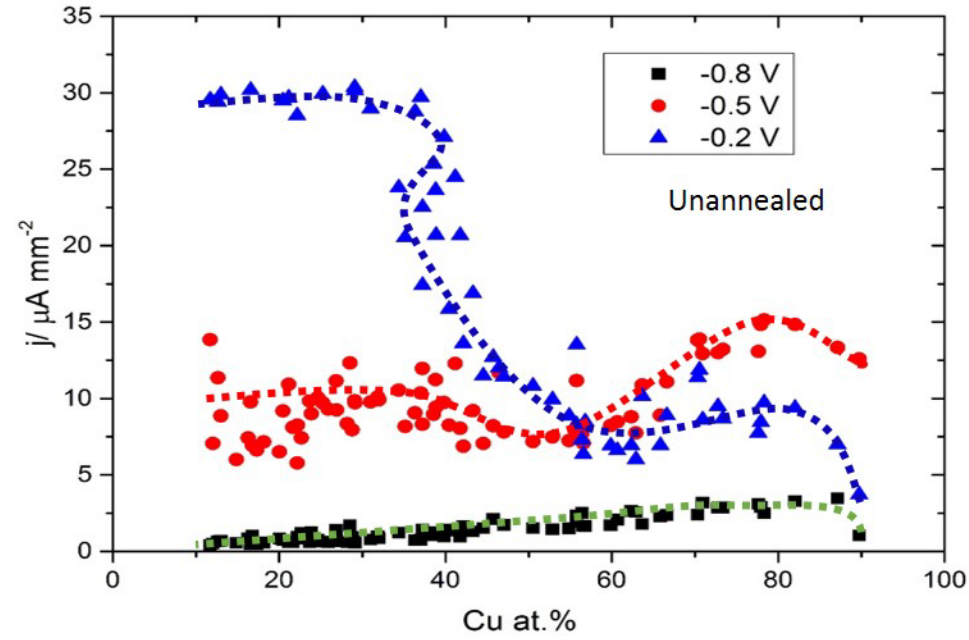

Figure 65: Comparison of the current density of the direct BOR extracted from the CVs data of unannealed Au-Cu alloy catalysts at -0.8 V_{SCE}, -0.5 V_{SCE} and -0.2 V_{SCE}.

.

5.3.2 The Electro-catalytic Activity of the Annealed Au-Cu Alloys for Direct BOR

The Au-Cu alloy catalysts (after annealing to 300 ^{o}C for 15 min) were electrochemically screened in 0.1 M NaOH to determine their activities in the absence of the borohydride (Figure 66). The CVs of the alloy catalysts were investigated at the same potential range as the unannealed Au-Cu alloys (between -1.3 V_{SCE} and +0.1 V_{SCE}) at a scan rate of 50 mV/s.

The CVs of the annealed Au-Cu alloy for the oxide formation/removal and the hydrogen evolution is quite different when compared with the unannealed Au-Cu alloy sample. During the anodic scan, the oxide layer on the Cu-rich catalyst is started to form at ca. -0.65 V_{SCE}, while on the unannealed sample the oxide formation started at ca. -0.45. This shift indicates higher activity of the annealed Au-Cu alloy catalysts towards the formation of the OH_{ads}. As the potential increases to more positive potential (to -0.1 V_{SCE}), the current density of the oxide formation increased. The largest current density of the oxide formation at -0.1 V_{SCE} can be observed for the $Cu_{86.4}$ $Au_{13.6}$ alloy catalyst. This demonstrates that the oxide formation is strongly dependent on the Cu content. Furthermore, on the cathodic scan, as can be seen, the annealed Au-Cu alloy catalyst show no activity for the hydrogen evolution compared to the unannealed Au-Cu alloys. It is possible that an arrangement transformation of the Au/Cu atoms at the surface occurred after annealing that

increased the formation of the oxide and reduced the HER activity on the annealed Au-Cu alloy catalysts.

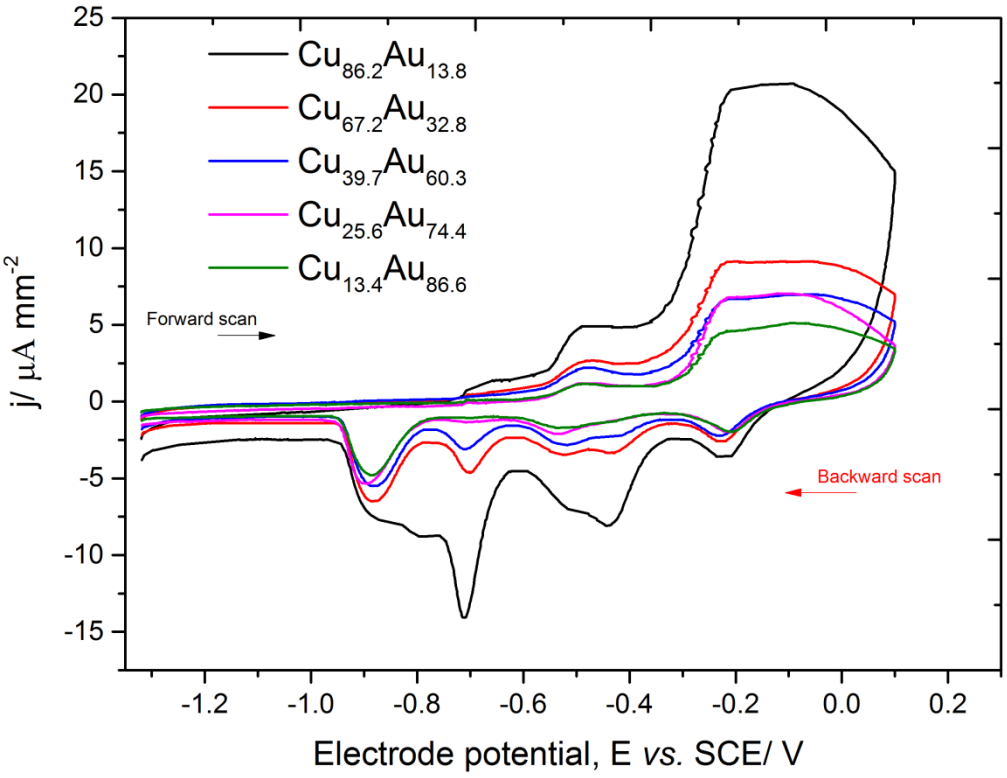

Figure 66: Cyclic voltammograms showing the electrochemical activity of the annealed Au-Cu alloy catalyts (at 300 ˚C for 15 min) in 0.1 M of NaOH at a potential scan rate of 50 mV/s as a funtion of electrode composition.

A large change occoured in the the catalytic activity of the Au-Cu alloy catlyts towards the direct BOR after annealing the sample to 300 for 15 min. Figure 67 shows the forward scan of selected CVs of 0.01 M $NaBH_4$ in the potential range between -1.2 V_{SEC} and 0.0 V_{SCE} at a scan rate of 25 mV/s. It can be seen that the annealed Au-Cu alloy sample exhibits better catalytic activity for BOR when compared to the unannealed Au-Cu alloy catalysts. A shift of the onset potential of the BOR to more negative potential (ca. 0.15) can be observed for the annealed Au-rich alloy catalysts. For alloy catalysts with higher Cu content, the anodic peak of the BOR occurs at two discrete potentials at -0.7 V_{SCE} and -0.3 V_{SCE}. Similarly, the BOR on the unannealed $Cu_{78.3}$-$Au_{21.7}$ catalysts were also separated (CVs results in Figure 63) but the oxidation peak of the second peak was smaller and absent for catalysts with higher Cu content compared to the annealed Au-Cu alloys.

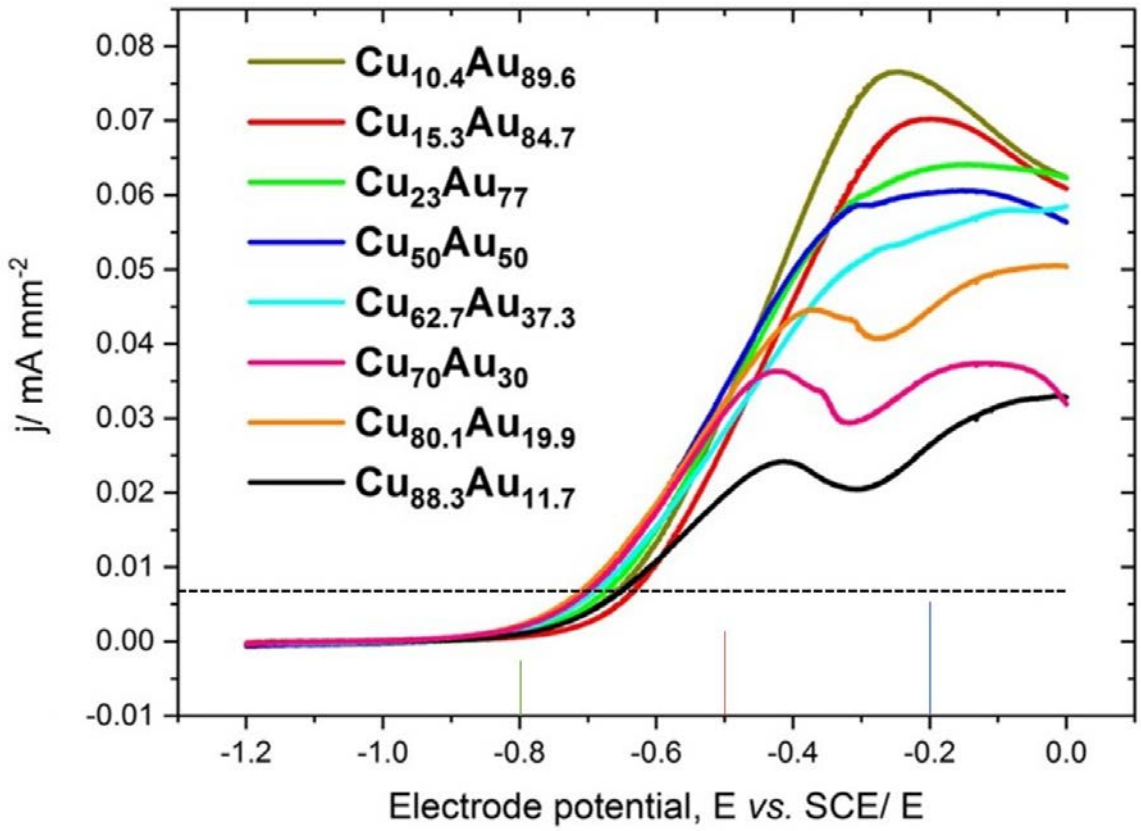

Figure 67: CVs of the annealed at 300 ˚C Au-Cu alloy catalysts over a wide range of compositions in 0.01 M $NaBH_4$ at scan rate of 25 mV/s from -1.2 V_{SCE} to 0.0 V_{SCE}.

The onset potentials of the BOR on the annealed Au-Cu alloy catalysts was evaluated and compared with the unannealed Au-Cu alloys (Figure 68). As can be seen, the annealed Au-Cu alloy catalysts show a shift in the onset potential of the direct BOR to more negative values indicating enhanced activity. It can also be observed that there is a general upward trend in the onset of the BOR activity on the annealed sample as the Cu content increases from 70-90 at. %, while there is a downward trend in the onset potential of the alloy catalysts with composition of between ca. Cu40-55 at.%. This showed that atoms present on the alloy surface were affected by the thermal annealing that modified the active sites (adjacent active sites), a possible reason to account for why the onset potential of the direct BOR shifted to more negative potentials on the annealed Au-Cu alloy when compared with the unannealed Au-Pt alloy sample. Thus, the thermal annealing appears to have a beneficial effect on the activity of the Au-Cu catalysts.

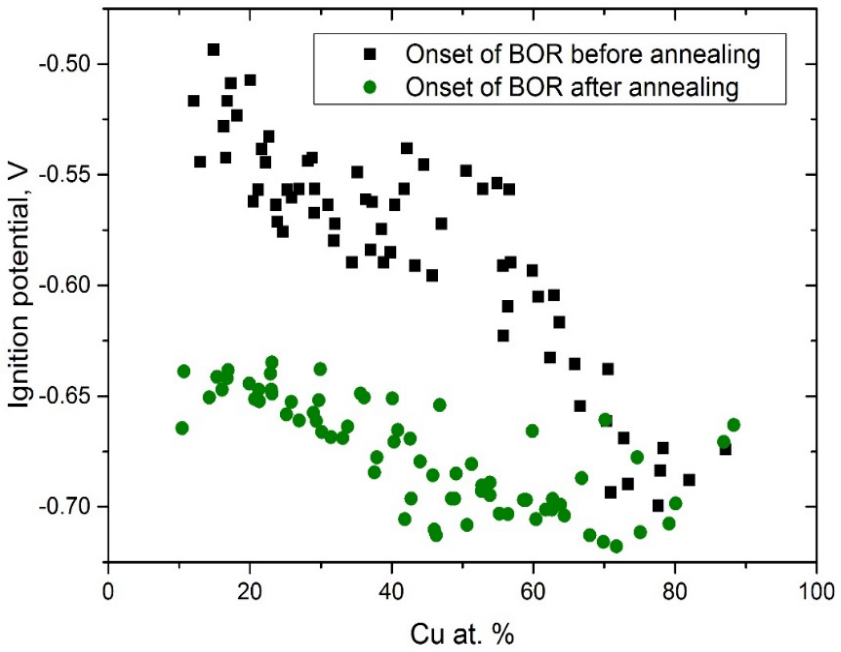

Figure 68: Onset potentials (at I threshold = 6.3 x 10^{-06} A mm^{-2}) of the BOR versus Cu composition for the unannealed Au-Cu alloy and the annealed Au-Cu alloy catalysts. The transparent line is a guide to the eye.

The current densities of the BOR on the annealed Au-Cu alloys were extracted from the CV data at the same potentials (-0.8 V_{SCE}, -0.5 V_{SCE} and -0.2 V_{SCE}) as before annealing. The current was plotted as a function of Cu compositions (Figure 69). As can be seen, there is almost no measured current at -0.8 V_{SCE} across all alloy compositions compared to the unannealed Au-Cu alloy sample. This could mean that a modification of the electronic/ensemble on the annealed Au-Cu alloy surfaces may have developed after the annealing process, and thus affected the overall active sites. This, in turn, accounts for the constant current density observed at -0.5 V_{SCE}. On the other hand, there is a linear decrease in the current densities at -0.2 V_{SCE} as the Cu content on the annealed alloy surfaces increases compared to the measured current densities extracted at -0.8 V_{SCE} and -0.5 V_{SCE}. This demonstrates how the addition of Cu atoms in the alloy surface are responsible for adsorbing O_2 (blocking the BOR) compared to Au atoms at higher oxidation potentials (-0.2 V_{SCE}).

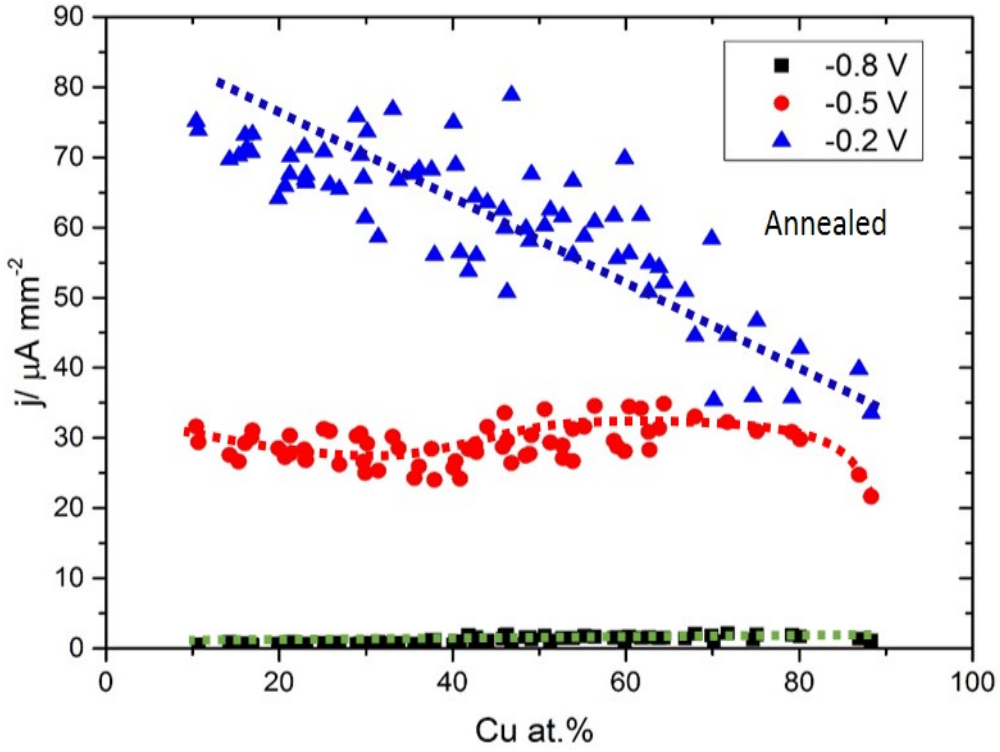

Figure 69: Comparison of the current density of the direct BOR extracted from the CVs data of annealed Au-Cu alloy catalysts at -0.8 V_{SCE}, -0.5 V_{SCE} and -0.2 V_{SCE}.

5.4 Conclusion

HT-PVD method was used to deposit non-equilibrium and equilibrium Au-Cu alloy catalysts with a wide range of compositions. EDX/SEM measurements demonstrated that a linear gradient in the range of $5 \leq x \leq 90$ was obtained. The XRD results of the unannealed Au-Cu alloy showed single-phase alloys. Moreover, XRD analysis showed a shift in the Bragg peak diffractions due to incorporation of Cu to the Au. With an annealing temperature of 300 ^{o}C, a clear difference in the peak intensity of the (111) Bragg peak was observed. The increase in the peak intensities was more noticeable in the region of Au-rich compositions. This was attributed to the increase in the crystal size. The XPS analysis showed that the binding energy of the Au 4f and Cu 2p core levels was influenced by the electronic interaction between the Au and Cu atoms showing binding energy shifts as the concentrations of the two elements change in the Au-Cu alloy. The XPS analysis of the surface composition relative to the bulk composition before and after annealing showed no evidence of segregation of either element at any composition.

The high-throughput electrochemical screening results, in the absence of the borohydride, showed that the addition of Cu in the unannealed Au-Cu alloy catalysts increased the activity of the HER as well as the surface oxide formation/ removal reactions. Conversely, a large decrease in the HER was found on annealed Au-Cu alloy catalysts. When the Au-Cu alloy catalyst was

examined in the presence of the borohydride, the activity of Au-rich catalyst for the BOR was increasing by the addition of Cu. Moreover, the presence of a small amount of Au contents (20-30 at. %) in the Cu-rich catalysts enhanced the activity for the direct BOR compared to the other alloy catalysts. This assumption is perhaps best explained using a representation of a single Au atom embedded in Cu atoms (Figure 70). This suggests that BH_4^- adsorbs preferentially on an ensemble of small Au atoms surrounded by a large ensembles of Cu atoms and that may be the catalytic site that exhibited high activity for the direct BOR. Based on the evaluation of the onset potential of the direct BOR on the annealed Au-Cu alloy catalysts, the Cu_{72}-Au_{28} catalyst can be a promising catalyst for the DBFCs.

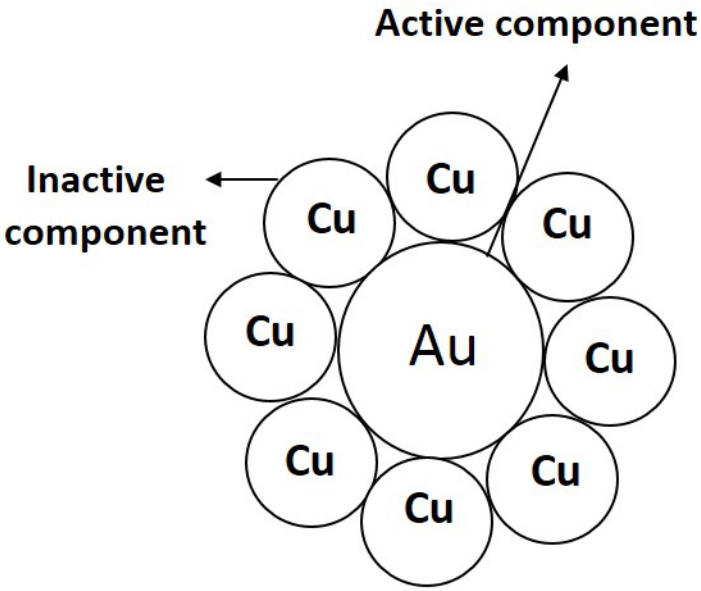

Figure 70: Au-Cu alloy ensemble corresponding to a small ensemble of Au with Cu atoms around it, which can be the catalytic site that offered high catalytic activity for the direct BOR.

Chapter 6 Au-Pt Alloy Catalysts for BOR

6.1 The Au-Pt Alloy System

6.1.1 Introduction

This chapter discusses the catalytic behaviour of the Au-Pt alloys for the direct BOR reaction. It begins with a brief introduction to the Au-Pt alloy binary system including surface properties and catalysis followed by characterisations of the surface/ bulk composition and phase structure on Au_{1-x}-Pt_x ($1 \leq x \leq 99$) thin films grown on Si, ITO and e-chem-Au arrays substrates. Post-annealing was carried out on the non-equilibrated Au-Pt alloy and was characterised as a function of atomic composition to elucidate further correlations between the non-equilibrated and equilibrated phases of the Au-Pt alloy materials. Moreover, the electrochemical activity of the (unannealed and annealed) Au-Pt alloy catalysts results in the absence and in the presence of the $NaBH_4$ will be presented and discussed. Therefore, the goal of this chapter is as follows: to obtain an understanding of the phase structure of the Au-Pt bulk material alloys along with the surface alloy properties, to synthesis Au-Pt alloy catalysts using HT-PVD and to verify their activity for DBFCs.

6.1.2 Literature Review of Au-Pt Alloy System

Over the last years, the Au-Pt alloy systems have shown much interest in catalysis for fuel cells reactions. The Au-Pt alloys bulk are thermodynamically not miscible, and at below 1260 ^{o}C, the critical temperature, they exhibit a large immiscibility gap extending to higher temperatures over a wide range of composition[130]. According to the phase diagram (Figure 71), at 400 ^{o}C, the face-centred cubic Au-Pt alloy shows bulk materials made of two separate phases to achieve Pt concentrations greater than 15 at. %, while single-phase Au-Pt alloys exist for Pt concentrations less than 15 at. %.

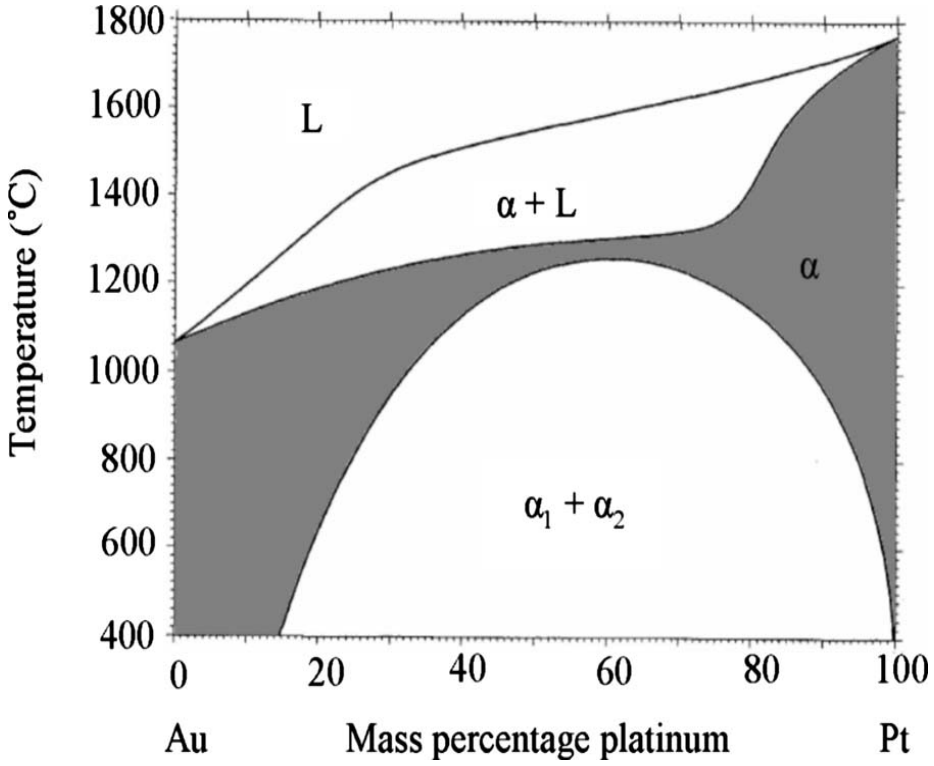

Figure 71: The phase diagram for the Au-Pt binary alloy as a function of both the system temperature and composition[131].

The surface properties of the Au-Pt alloys can have a profound impact on the catalytic activity. The preparation method for the synthesis of homogeneous bulk Au-Pt alloys (one phase mixture) with a wide range of compositions is challenging and the literature on this topic is limited. The deposition method of the Au-Pt alloy has a strong effect on its bulk structure and compositions, and therefore careful control is needed during synthesis due to the large miscibility. For example, Mihut et al.[132] studied Au-Pt/C nanoparticles prepared by impregnation with Pt and Au precursors and found that alloy catalysts exhibited an activity similar to the pure Pt catalyst. The addition of the Au showed no improvement in the catalysts due to phase separation.

Mott et al.[133] synthesised bimetallic Au-Pt nanoparticles (NPs) in a composition range of Au10-90 at. %. They demonstrated evidence of transformation of the Au-Pt NPs from non-equilibrated to equilibrated phase structure materials. They also found that by increasing the temperature of the Au-Pt alloys to 650 ^{o}C, the fcc alloy phase structures were subjected to phase separation. A similar strategy was employed by Wanjala et al.[134] and his co-workers to different supported materials for Au_n-Pt_{100-n} nanoparticles prepared by co-reduction of $HAuCl_4$ and H_2PtCl_6. The study showed XRD comparisons for various compositions of the Au-Pt catalysts as deposited and annealed at high temperatures including 300 ^{o}C, 400 ^{o}C, 500 ^{o}C, 600 ^{o}C and 800 ^{o}C. The structure of the Au-Pt homogenous alloys identified by the XRD at 300 ^{o}C, 400 ^{o}C and 500 ^{o}C exhibited alloyed and partially alloyed materials, while intermetallic materials were also reported for the Au-Pt alloys ($Au_{89}Pt_{11}$/C and $Au_{56}Pt_{44}$/C alloys) that were treated at 600 ^{o}C and 800 ^{o}C, respectively. Post-

annealing on the surface of the Au-Pt alloy resulted in surface atom arrangements different from the bulk materials (surface enrichment). For the Au-Pt bimetallic alloy, surface segregation was reported for the equilibrated Au-Pt alloys at 800 ^{o}C resulting in surface alloys rich in gold due to the lower surface energy of Au (1.41 J cm^{-2}) compared to Pt (2.34 J cm^{-2})[133, 135].

Although many researchers have been continually studying the bulk and surface properties of Au-Pt alloy on nanoparticle materials, few have demonstrated the effects on thin film materials for Au-Pt alloys with controllable compositions and structures that exhibit a single-phase structure. For example, Irissou and co-workers [136] synthesised Au-Pt thin films by Crossed-Beam Pulsed Laser deposition. They achieved a non-equilibrated thin film alloy deposited at room temperature with various compositions ranging between Pt-0 to 100 at.%. The formation of the as deposited Au-Pt alloy was studied by XRD. The diffraction patterns showed a shift in the (111) Bragg peaks to higher Bragg angles that confirmed the formation of single-phase alloy structure.

Brown et al.[131] deposited non-equilibrated Au-Pt thin film alloys by co-sputtering. The process for preparing the Au-Pt alloys was interesting in its control of the elemental ratios, which were controlled by adjusting the power supplied to each source target. Despite the existence of the large miscibility gap, they proved that, as a result of the structural and compositional characterisations of the Au-Pt solid solutions, single phase alloys were formed over the compositions between Pt0-100 at%. To ensure that the surface and the bulk Au-Pt alloys had not segregated, Brown et al. determined the surface composition by XPS as a function of bulk composition. The atomic ratio of the surface was compared with the atomic ratio of the bulk by fitting them to lattice constant values. The straight line of the solid solution alloys, which consists of determining the phase structure along with the surface/bulk compositions, showed that the variations of the surface atomic ratio relative to the bulk were less than 4 to 10 percent for most of the alloys. Based on this, it was assumed that surface segregation across the entire surface had not occurred.

6.1.3 Catalysis by Au-Pt Alloys

Extensive research has been carried out by many scientists to identify the catalytic activity and the stability of the Au-Pt alloys for various electrochemical reactions including the oxygen reduction reaction (ORR)[134, 137-138], methanol oxidation reaction[139-140] and ethanol oxidation reaction (EOR)[141-143] operated under acidic or alkaline conditions. In addition, the Au-Pt catalysts were designed to selectively increase the activity of the BOR for DBFCs[144-146 147]. The presence of the Pt in the Au-Pt alloy may have a substantial influence on the direct BOR due to its catalytic nature towards the borohydride hydrolysis reaction affecting the complete oxidation of the eight electrons. This requires synthesising Au-Pt alloy catalyst that has a low catalytic selectivity towards the

borohydride hydrolysis reaction to reduce the production of H_2[148]. Hence, the discussion will need to include both the BOR and the catalytic hydrolysis reactions.

Based on the mechanism of the BOR, the rate of the hydrolysis of the BH_4^- varies according to the type of the metal catalysts (see Chapter 3). When comparing the catalytic behaviour of Pt to Au metal catalysts, the hydrogen evolution on Au was increasingly low[147]. Recently, Geng and co-workers [147] reported high activity over two kinds of carbon-supported Au-Pt bimetallic alloys for the BOR with a maximum number of electron-transfers, 6.4 for 1 M $NaBH_4$ and 7.2 for 0.5 M $NaBH_4$. They found that the onset potential was reduced by 0.2 V in comparison with pure Au. They concluded that rate of the hydrolysis on the Au-Pt/C catalyst was higher than Au. Amendola and his co-workers studied the oxidation of the BH_4^- on an electrode-deposited (Au (97%)-Pt (3%)[51]. The Coulombic efficiency was affected by the H_2 competing reaction and the reported number of the electrons transferred was close to seven.

The Pt-Au alloy has been investigated by other researchers to study the BOR and gain information about the reaction mechanism through kinetic parameters. However, there is a need to synthesise Au-Pt alloy catalysts with controlled composition and structure in order to find which alloy catalyst have lower overpotential and evolve no H_2. Based on the above studies, the surface atom arrangement and the electronic structure for various compositions of the Au-Pt alloy catalysts should be optimised to investigate their effects on both BOR and hydrolysis reactions. In the present study, deposition of the Au-Pt alloy with a wide range of compositions was synthesised in an effort to electrochemically screen and determine the electrocatalytic activity of BOR as a function of catalyst compositions.

6.2 High Throughput Characterisations of the Au-Pt Alloy Catalysts

6.2.1 Bulk Composition Analysis of the Au-Pt Alloys

The SEM/EDX was used to quantitively determine the bulk composition of the deposited Au-Pt alloy catalysts. The EDX maps show that the composition-spread of both Au and Pt are gradually distributed across the substrate. The composition-spread for the alloy catalysts are displayed in Figure 72 as a function of electrode position. As displayed, the elemental concentration (in atomic percentage) for each element across the substrate shows a wide range of compositional gradient. The concentration range for the Au is in the range between $1 \leq x$ at. % ≤ 99. This is also the same for Pt. At the centre of the substrate, the region of the 50//50 binary line, the change in composition shows the targeted concentration (Au/Pt =1). This region is located along the line parallel to the directional growth of the deposited material. Therefore, a wide range of the Au and Pt contents across the sample were successfully achieved.

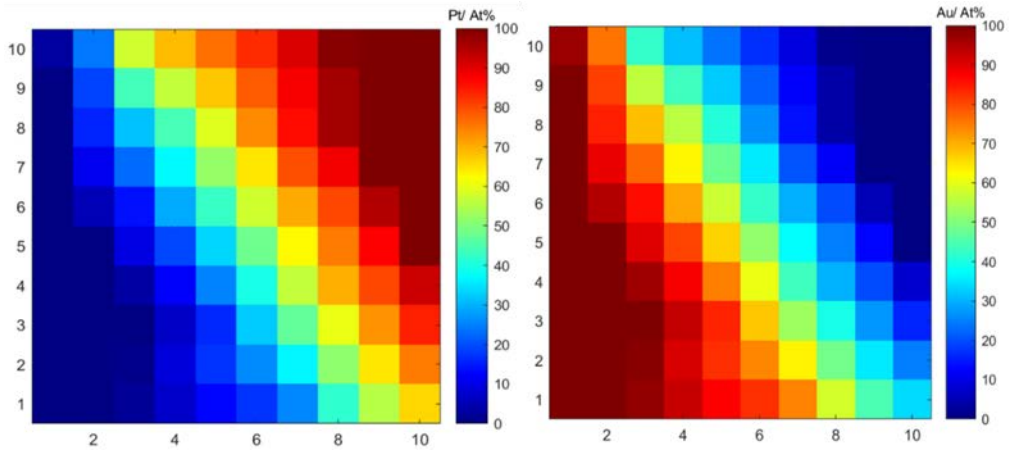

Figure 72: Composition plots comparing the Pt and Au content determined by EDX for the Au-Pt alloy sample deposited by HT-PVD. The EDX data show that the two elements are deposited across the sample with a wide range of compositional gradient.

6.2.2 XRD Analysis of the Au-Pt Alloys

The crystalline structure for the unannealed Au-Pt alloy (RT) samples were determined by XRD. Figure 73 shows the XRD patterns of single-phase fcc alloys with selected samples covering a wide range of compositions across the surface. The XRD patterns were recorded in the 2θ range of 21^{o} to 52^{o}. The Au and Pt have the same crystal structure (fcc) and their peak positions are close to each other. The sharp Bragg diffraction peaks observed between 38.2^{o} and 40^{o} exhibit reflections of the (111) plane, while the small Bragg diffraction peaks observed between 44.5^{o} and 47^{o} exhibit reflections of the (200) plane. As greater concentrations of the Pt are added to the Au-Pt sample, the peaks clearly shift towards higher Bragg angles. This indicates that the Pt atoms are present in the fcc structure as the (111) peaks of the selected samples shifted from 38.2^{o} to 40.4^{o}. Furthermore, when the Pt concentration increases, the peak intensity of the (111) the Au-Pt alloys decreases and become broader. This is also an indication of changes in the lattice because of the addition of a smaller atomic radii into the Au lattice. From the XRD data, it can be seen that there is no observable phase-separation of the bulk Au-Pt alloy materials, which confirms that the unannealed (non-equilibrated) samples are alloyed across all compositions.

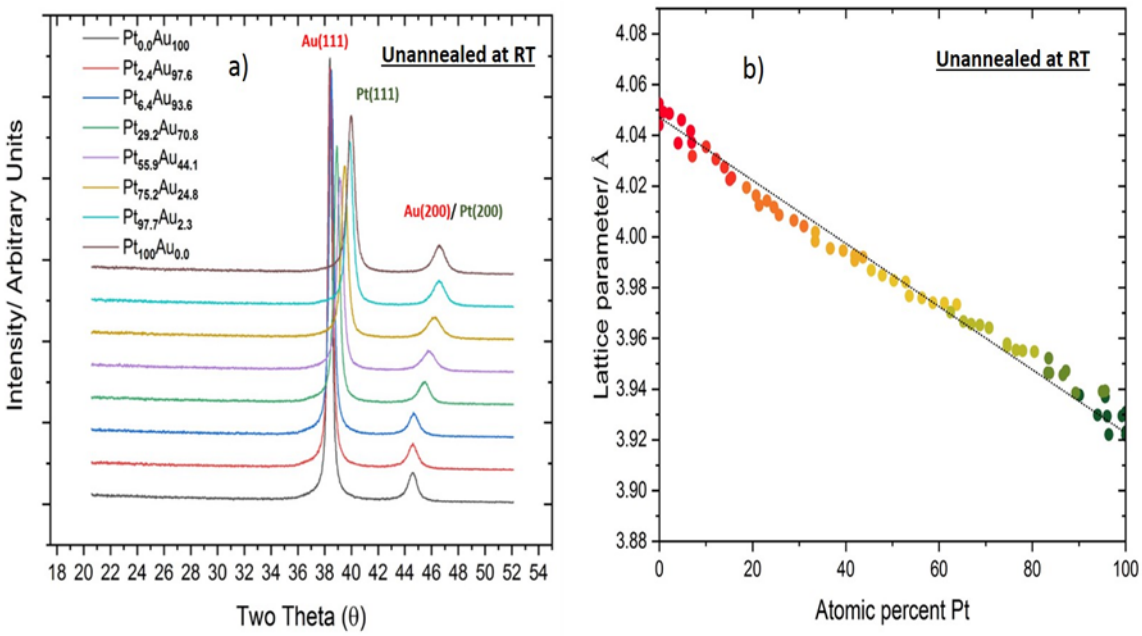

Figure 73: XRD data analysis of (a) the XRD patterns of the unannealed Au-Pt (RT) alloy sample with various compositions synthesised by HT-PVD at room temperature and (b) the cell parameter of the (111) Bragg diffraction as a function of composition. The film thickness is in the range between 180-200 nm.

The correlation between the crystal lattice and the composition of the Au-Pt alloy was studied to confirm the formation of single-phase Au-Pt solid solution alloys. The lattice parameter was obtained from XRD analysis and was calculated using Vegard's law. The lattice parameter for Pt and Au pure elements was calculated to be 3.91 Å[105] and 4.07 Å[105], which corresponds to composition values of 100 at. %. The XRD data of the (111) Bragg peak positions were combined with bulk composition obtained from the EDX and then compared with the calculated lattice parameters. The lattice parameter of the Au-Pt alloy sample was plotted against Pt compositions (Figure 73 b). It is clear that the lattice parameter, which is between the pure Au and Pt, forms a straight line over the entire range, indicating full degree of alloying.

The Au-Pt alloy samples underwent different temperature thermal annealing (300 ^{o}C and 600 ^{o}C for 15 min under UHV) and their phase structures were determined by XRD after cooling down to room temperature. The method of annealing was carried out using the manipulator in the HT-PVD chamber. From Au-Pt/RT ^{o}C to Au-Pt/300 ^{o}C, the phase structure of the Au-Pt alloys showed no phase separation (Figure 74 (a,b)). The XRD patterns of the annealed Au-Pt/300 ^{o}C sample showed higher and sharper peak intensities which indicates that further crystallisation (more ordered structure) was occurring.

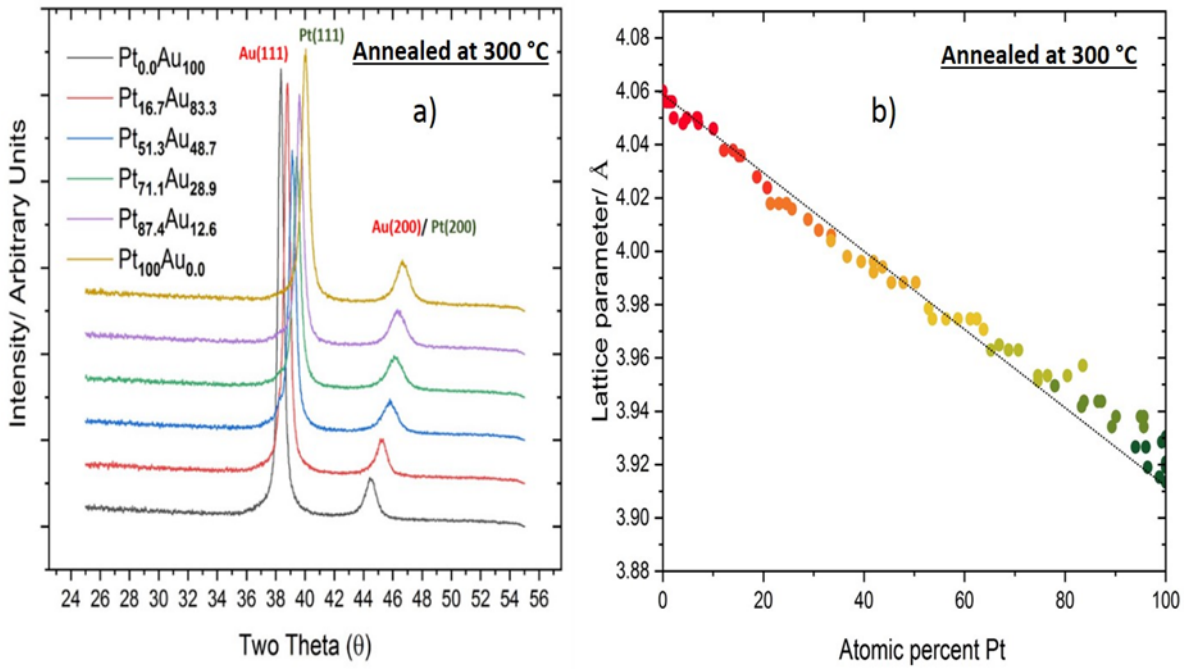

Figure 74: Plots of XRD analysis showing (a) comparison of XRD patterns of the Au-Pt alloys annealed for 15 min at 300 °C of selected samples covering the entire compositions and (b) lattice parameters curve determined experimentally for the entire composition. The film thickness is in the range between 180-200 nm.

As the thermal annealing temperature increased from 300 °C to 600 °C, the phase structure showed fcc Au-Pt solid solutions up to 20 atomic % of Pt and a two-phase region of Au and Pt beyond 70 atomic % of Pt. From the XRD patterns displayed in Figure 75 a, the (111) Au-Pt Bragg peaks that are in between the Au (111) and Pt (111) peak positions showed a shoulder peak evolving at 39° for the sample with composition of $Pt_{62.5}Au_{37.5}$. As the Pt concentration decreased, the (111) Bragg peak split into two peaks observed at 39° and 38.2°, which can be seen from the XRD pattern at both composition $Pt_{35.5}Au_{66.5}$ and $Pt_{25.7}Au_{74.3}$. The split of the (111) Bragg diffraction for a Pt concentration lower than 20 was observed at 39° then shrank and disappeared and the (111) Bragg diffraction peaks observed at 38.2° showed no shifts in the positions. The results of the lattice parameter calculation suggest that the Au-Pt/600 ◦C sample contained unalloyed Pt, as indicated by the non-linearity displayed from the lattice parameter curve (Figure 75 b).

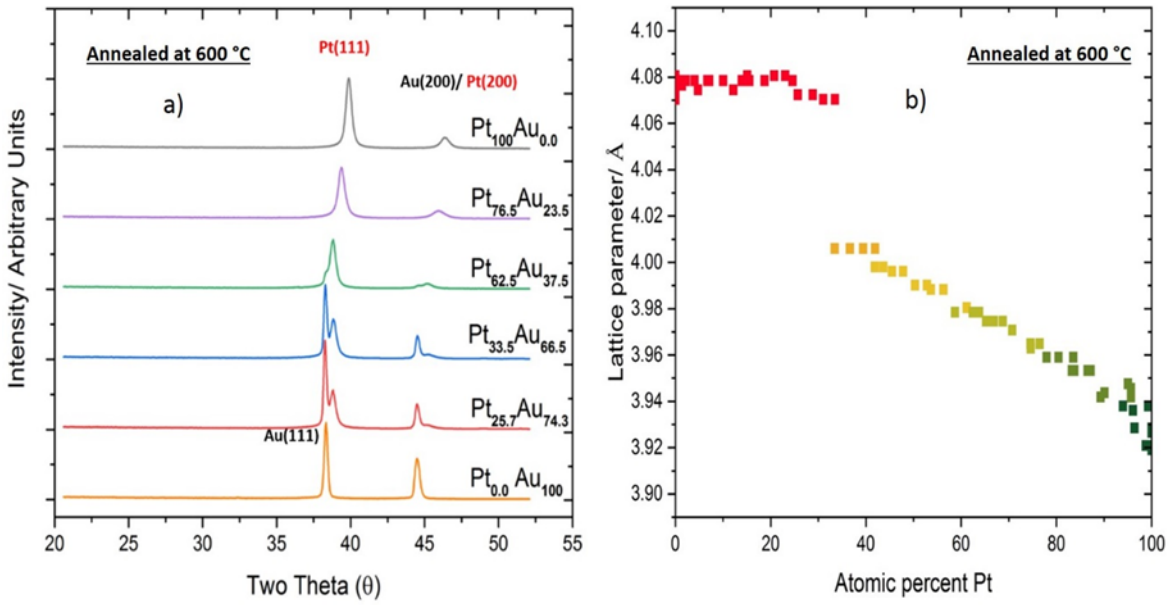

Figure 75: Plots of XRD analysis showing (a) comparison of XRD patterns of the Au-Pt alloys annealed for 15 min at 600 °C of selected samples covering the entire compositions and (b) lattice parameters curve determined experimentally for the entire composition. The film thickness is in the range between 180-200 nm.

6.2.3 Surface Composition of Au-Pt Alloys

XPS experiments were carried out to measure the binding energy of electrons in the core levels and determine the surface composition of the Au-Pt alloy materials (before and after annealing) as well as their oxidation states. A set of XPS spectra were measured on different surface positions along the Au-Pt binary line where the composition of Au varies linearly with the Pt. A surface area of 3 mm^2 used for each XPS measurement. The XPS spectra of Au 4f and Pt 4f regions were analysed using their peak areas, positions and intensities. The XPS data were processed using the CasaXPS software.

Figure (76) shows the XPS spectrum containing doublets with high and low binding energies of $4f_{5/2}$ and $4f_{7/2}$ signals for (a) Au and (b) Pt in the Au-Pt alloy sample. As can be seen, there is a positive shift of ca. 1.4 for the Au ($4f_{7/2}$) signal, whereas a negative shift of ca. 1.11 occurred for the Pt ($4f_{7/2}$) signal in the unannealed Au-Pt alloy. Figure 77 shows (a) the peak position of the Au ($4f_{7/2}$) and (b) the Pt ($4f_{7/2}$) binding energies as a function of Au and Pt concentration. It can be observed that the Au ($4f_{7/2}$) binding energy decreases as the Au content increases. Conversely, the Pt ($4f_{7/2}$) binding energy increases as the Pt content decreases. This is a clear indication of the electronic interaction between Au and Pt atomic orbits of the surface atoms in the (unannealed) Au-Pt alloy sample as a result of the alloy formation.

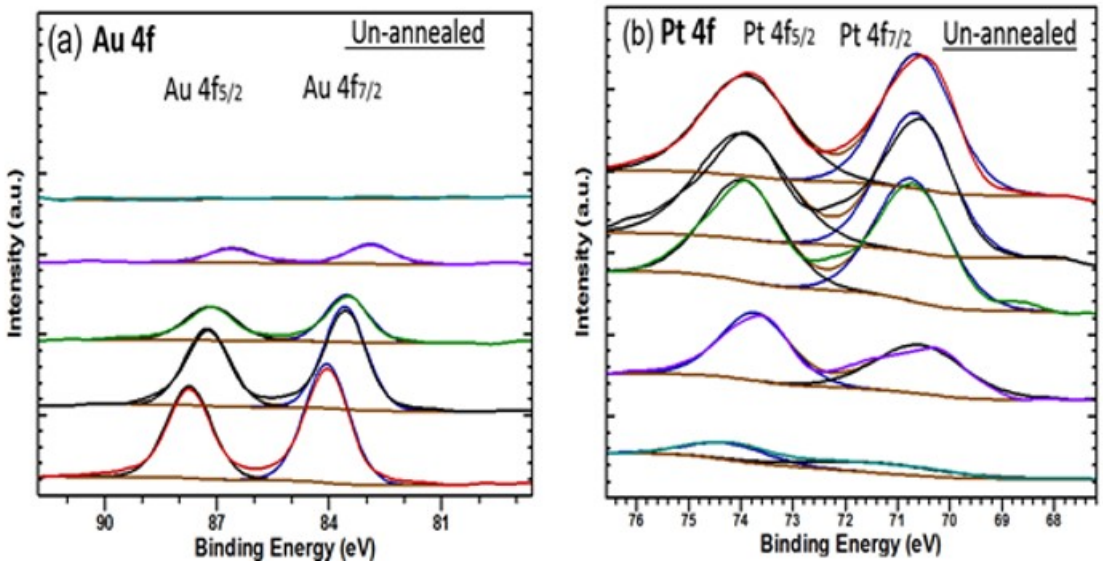

Figure 76: XPS analysis of the binding energy of (a) the Au(4f) and the (b) Pt (4f) core levels in Au-Pt alloy as a function of compositions before annealing. The film thickness is in the range between 180-200 nm.

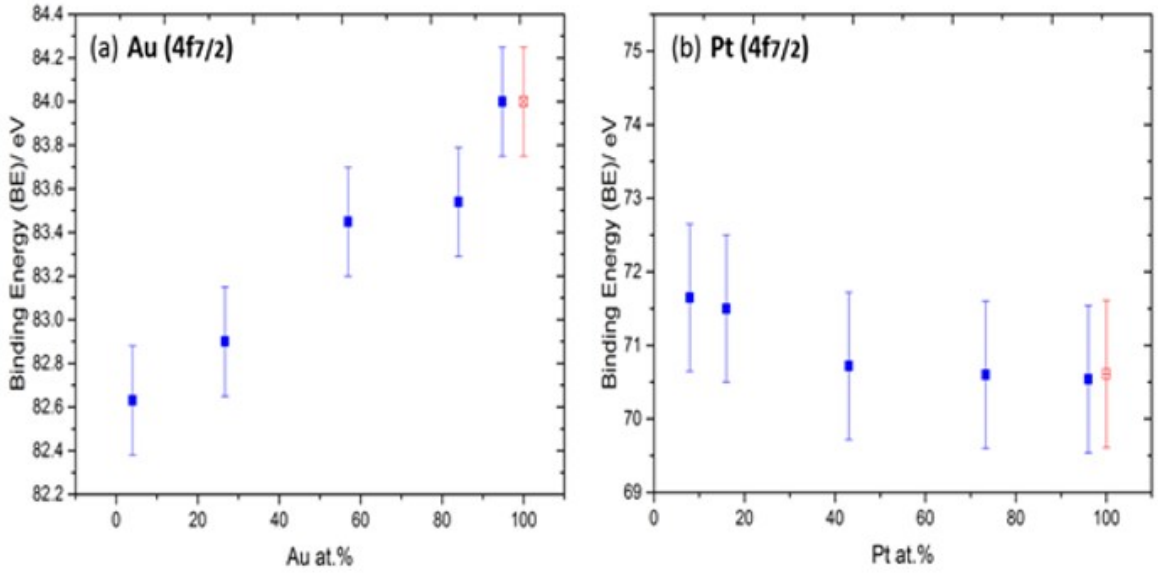

Figure 77: The peak positions of the (a) Au ($4f_{7/2}$) and (b) Pt ($4f_{7/2}$) core levels as a function of compositions. The red crossed squares represent the peak position of the pure Au ($4f_{7/2}$) and Pt ($4f_{7/2}$) (with electron binding energy of 84.00[149] and 70.61[150]).

The annealed Au-Pt alloy sample was also analysed by XPS to verify surface enrichment of Au on the top-most surface layer as reported experimentally[133, 135]. The XPS spectra of the Au-Pt alloys (annealed at 300 for 15 ^{o}C) shown in Figure 78 shows (a) the binding energy of the Au 4f core levels and (b) the binding energy of the Pt 4f core levels as a function of composition. The bending energies of the Au $4f_{7/2}$ are centred at 83.90 eV for a surface composition lower than 70 at. %. Moreover, the doublet of the Au 4f peaks of the annealed shows no apparent change in terms of

peak areas when compared with the doublet of the unannealed Au 4f peaks. However, it was difficult to obtain definitive XPS spectra for the Pt 4f as the doublets overlaps with the Au ($5p_{1/2}$) signal between those binding energies especially at low Pt concentration (Figure 78(b)).

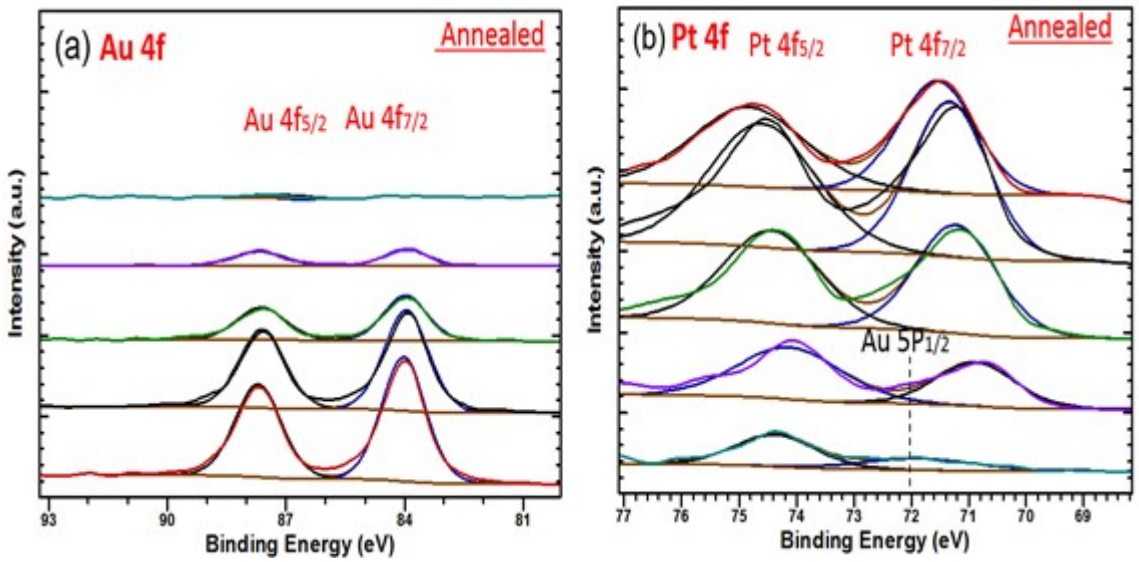

Figure 78: XPS analysis of the binding energy of (a) the Au (4f) and (b) the Pt (4f) core levels in Au-Pt alloy as a function of compositions after annealing to 300 ^{o}C. The film thickness is in the range of 180-200 nm.

The surface composition of the Au-Pt alloy before and after annealing was evaluated. Figure 79 shows the surface compositional analysis of the Au-Pt alloy (before and after annealing) relative to the bulk composition determined by the EDX. The surface composition of the (annealed) Au-Pt alloy showed a small percent of Pt segregation on the surface compared with the unannealed Au-Pt alloy.

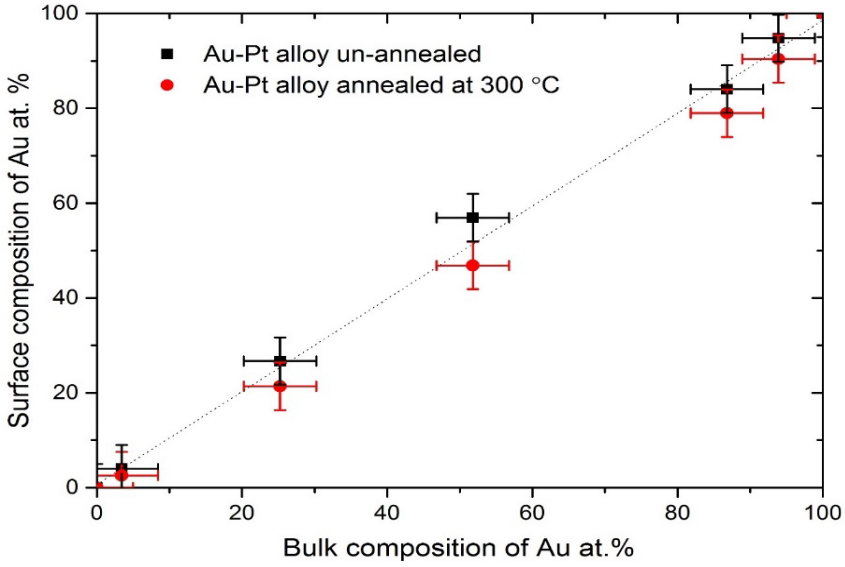

Figure 79: Surface composition of Au-Pt alloy before and after annealing to 300 ^{o}C for 15 min measured by XPS versus the bulk composition determined by EDX.

6.3 The Catalytic Activity of the Au-Pt Alloy Catalysts

The development of Au-Pt electro-catalysts for BOR has been the subject of extensive research in DBFCs. The drive for this effort is to improve the catalytic activity for the BOR and allow a complete oxidation of eight-electrons by hindering the catalytic spontaneous hydrolysis reaction. Our literature review demonstrates that alloying Au with Pt increases the catalytic activity for the direct BOR [144-146] [147]. In the present study, the catalytic activity of the Au-Pt alloy catalysts before and after annealing in alkaline borohydride solutions, on the biases of the electronic effect and the ensemble effect, will be examined. The formation of a wide range of Au-Pt alloy compositions is one of the strategies for identifying optimal catalysts. However, searching for a catalyst with higher activity towards the borohydride requires also monitoring H_2 evolution produced by the catalytic spontaneous hydrolysis reaction. Therefore, an electrochemical method was developed to improve the utilisation of electrocatalytic screening by monitoring the H_2 at the Au-Pt alloys as a function of electrode composition. Thus, in this study, the following questions will be addressed:

- What is the impact of Pt addition on the Au-Pt alloy catalysts for the direct BOR and its consequences on the hydrolysis reaction?
- What is the optimal ratio of the Pt to Au to increase/ decrease the catalytic BOR activity?
- Which surface compositions are active sites for H adsorption that mostly contribute to the hydrolysis of the borohydride ion?

6.3.1 The Electro-catalytic Activity of the Unannealed Au-Pt Alloys for Direct BOR

The Au-Pt alloy catalysts were electrochemically screened in the absence and in the presence of the sodium borohydride using the High Throughput Electrochemical methods. Figure 80 shows selected CVs of the unannealed Au-Pt alloy catalysts for various compositions across an array of 100 electrodes deposited on e-chem gold arrays substrate. The potential range was scanned between the hydrogen evolution reaction and oxygen oxidation/ reduction regions, (negative) -1.05 V_{SCE} and (positive) +0.15 V_{SCE} at a scan rate of 100 mV/s. The electrolyte was purged by Ar gas to remove O_2. The electrochemical screening was carried out at room temperature.

The electrochemical behaviour of the Au-Pt alloy catalysts in 0.1 M NaOH demonstrates Faradic processes of hydrogen oxidation/evolution and oxygen adsorption/desorption reactions that vary with the catalyst's composition. In addition, non-Faradic processes also occurred between the hydrogen and oxygen region, the double layer charging.

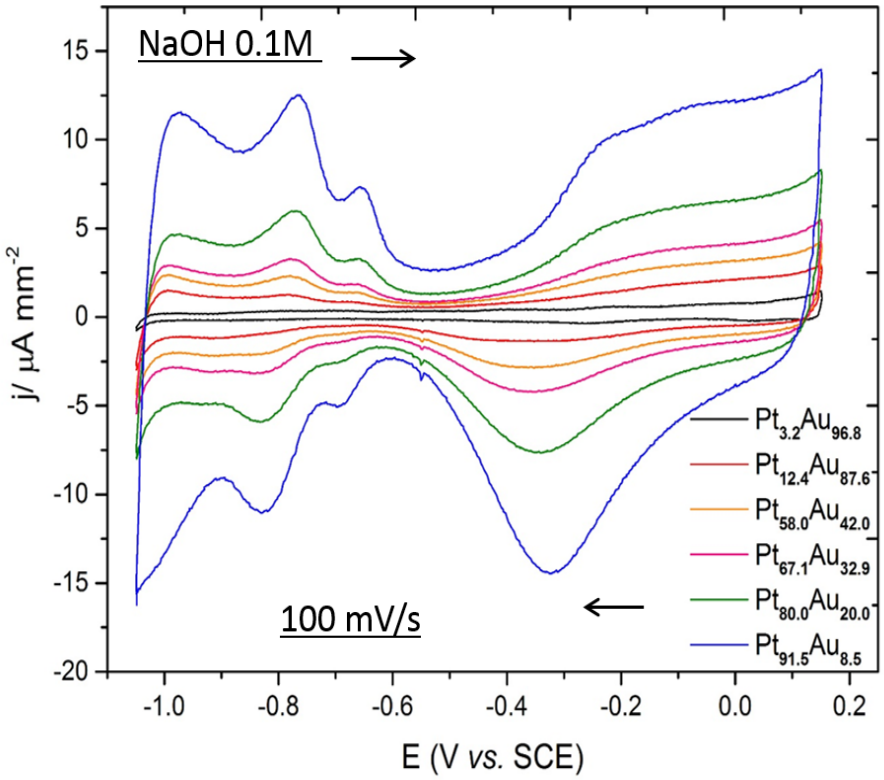

Figure 80: Cyclic voltammograms showing the electrochemical activity of the unannealed Au-Pt alloy catalysts in 0.1 M of NaOH at a potential scan rate of 100 mV/s as a function of electrode composition.

On the forward and reverse scans, the observed anodic/ cathodic peaks for Pt-rich alloy catalysts exhibits Pt-surface activity, while no activity can be observed for the formation of Au-O and $Au(OH)_2$ due to capping the potential range at +0.15 V_{SCE} to prevent possible dissolution of the binary film when cycling to more positive potentials (in the potential range between +0.2 and +0.5 V_{SCE}) . Figure 81 a, b, and c show electrochemical stability tests for each of $Pt_{6.1}$-$Au_{93.9}$, $Pt_{55.7}$-$Au_{44.3}$ and $Pt_{97.9}$-$Au_{2.1}$ alloy to evaluate the stability of the alloy films as the potential is scanned at more positive values. For the purpose of quantification, the current of the oxygen evolution reaction (OER) at +0.5 V_{SCE} versus the number of cycles was determined. Significant changes can be noticed in the OER activity at the Au-Pt alloy catalyst after carrying out 100 sweep scans without stopping or allowing any convection. As the number of sweep scans increase, the peak current of the OER continually decreases. Among the Pt-Au alloy samples, the $Pt_{55.7}$-$Au_{44.3}$ catalyst show the highest reduction current. The reduction of the OER peak current can be attributed to subsequent dissolution of Pt. Thus, the range of the potential scan when investigating the catalytic activity was capped to +0.15 V_{SCE}.

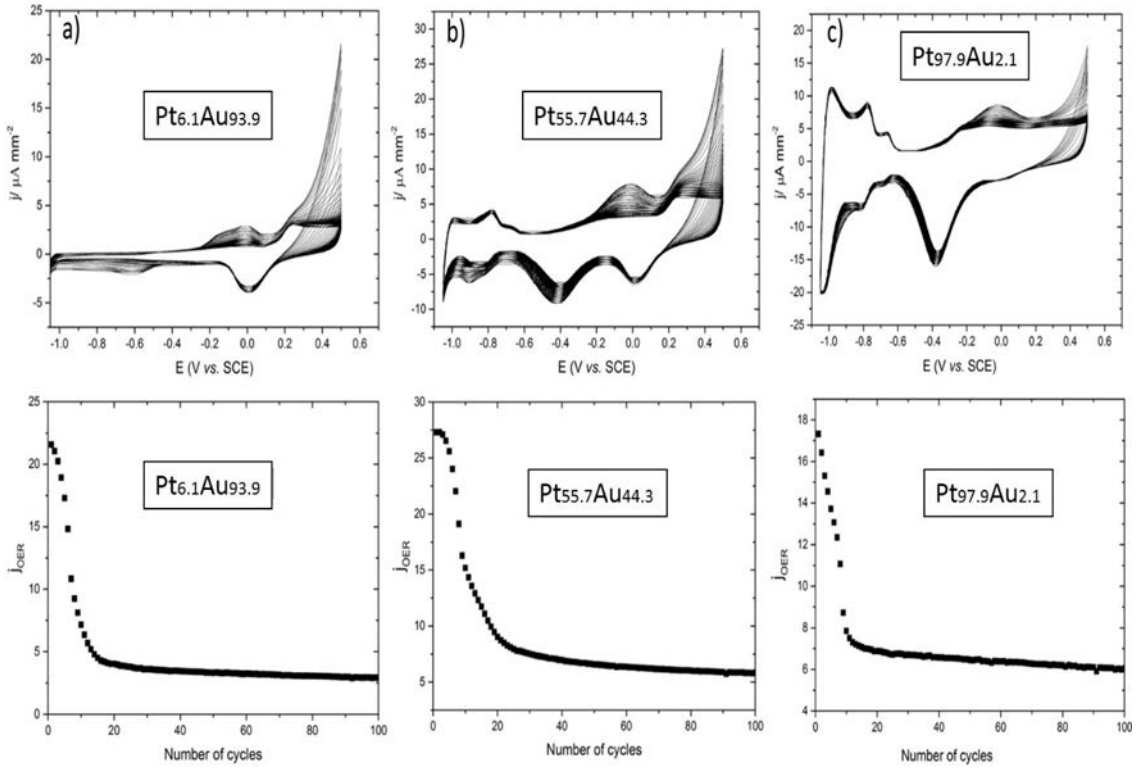

Figure 81: CVs of (a) ($Pt_{6.1}$-$Au_{93.9}$, (b) $Pt_{55.7}$-$Au_{44.3}$, (c) $Pt_{97.9}Au_{2.1}$ recorded for 100 sweep scans at a scan rate of 100 mV/s in which the upper potential limits is reaching the oxygen evolution reaction (OER) range. OER is plotted as a function of the number of cycles showing a continuous decrease in the peak currents indicating loss of surface area.

The key purpose of comparing the catalytic activity of the Au-Pt alloy catalysts was to study the hydrogen adsorption/desorption over different composition, as their peak current is clearly dependent on Au-Pt alloy concentrations. As the Pt concentration increases in the Au-Pt alloy catalysts, the current density of the hydrogen adsorption/ desorption becomes more pronounced (Figure 80). The incorporation of Au alters the surface ability to adsorb/desorb the hydrogen, suggesting low surface activities in the alloy catalysts within the potential range and therefore lower current density. As can be seen, the peak current of the hydrogen adsorption/desorption is maximum for the Pt-rich alloy catalysts, while the peak current for the Au-rich alloy catalysts shows a substantial drop. Moreover, the double layer charging of the Pt-rich is much higher compared to the Au-rich alloy catalysts. This indicates that the presence of Au in the Au-Pt alloy catalysts could modify the electronic structure and reduce the hydrolysis of borohydride on the alloy catalysts. The question to be asked is how the BH_{ads} species associated with catalytic hydrolysis and the direct BOR would respond to the Au-Pt alloy surface over various compositions.

When 0.01 M $NaBH_4$ was added to the 0.1 M NaOH solution, two characteristic oxidation peaks were observed. Figure (82) shows CVs of various compositions of the Au-Pt alloys recorded on the anodic scan between -1.1 V_{SCE} and -0.2 V_{SCE}. The shape of the CVs in the displayed Figure show irreversible anodic peaks, which indicates very complex electrochemical reactions. The forward

scan of the Pt-99 at. % alloy shows a large anodic peak taking place at -1.03 V_{SCE}. As the concentration of the Pt in the Au-Pt alloy decreases, this anodic peak shifts to more positive potentials. As the potential is scanned further positive, another process starts to appear on Au-Pt alloy catalysts with Pt composition ≤ 80 at. %. Note that the appearance of this process is absent of the anodic peak observed on the Pt-99 at. % alloy catalyst.

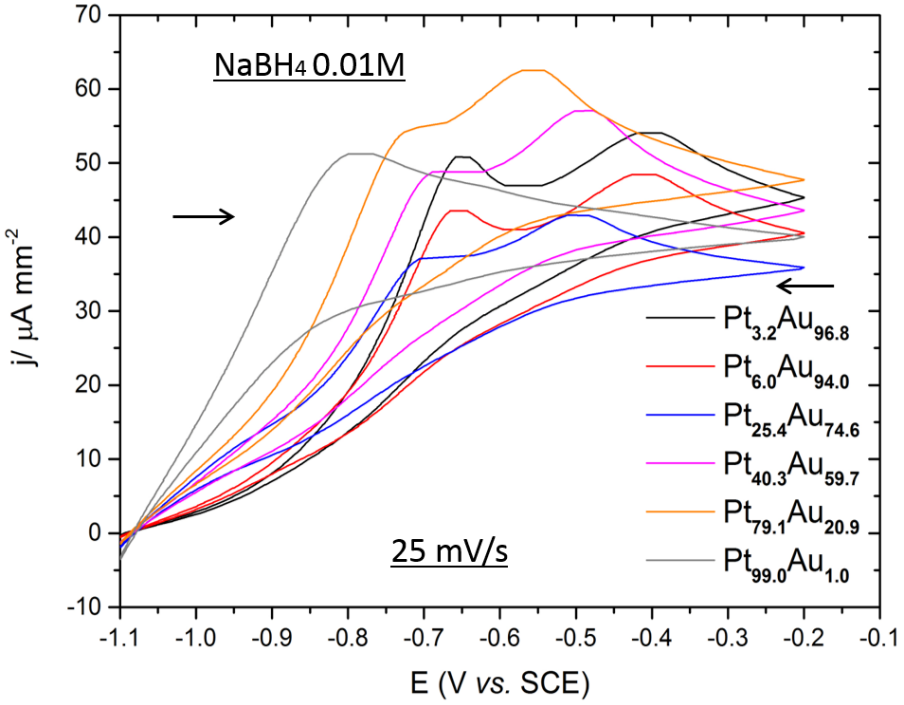

Figure 82: CVs showing the electrochemical behaviour of the unannealed Au-Pt alloy catalysts in alkaline solution containing 0.01 M $NaBH_4$ and 0.1 M NaOH at scan rate of 25 mV/s from -1.1 V_{SCE} to -0.2 V_{SCE}.

The mechanism of the BOR on pure Pt[39] suggests that H_{ads} produced by the hydrolysis of borohydride reaction competes with the BH_4^- for sites on the electrode surface, and considering the literature, the anodic peak taking place on the Pt-99 at. % catalyst at -1.03 V_{SCE} is attributed to the H_2 oxidation reaction. This indicates that the second process (on the $Pt_{79.1}Au_{20.9}$ catalyst) which starts on that at more positive potential is due to BOR. The onset potential of these oxidation reactions for the Au-96 % and Pt-99 % alloys is in line with the oxidation peaks observed in the case of Pt and Au pure metals (see Chapter 3). Therefore, alloying Pt with Au could provide more interesting interpretations into the mechanism of the BOR.

One can see the dependence of these onset potential values of both oxidation reactions (HOR and BOR) on the alloy catalyst composition. As displayed in Figure (82), the HOR peaks on the Pt-rich and the Au-rich shifts between -1.03 V_{SCE} and -0.88 V_{SCE}. As the Pt concentration increases in the Au-Pt alloys, the onset potential of the HOR shifts towards more negative potential and vice versa. In the same range as the increase in the Pt content, the onset potential of the BOR shifts towards

more negative potentials from -0.5 V_{SCE} to -0.63 V_{SCE}. This suggests that the addition of Pt on the Au-Pt alloys causes the BOR to occur at a more negative potential. Among the Au-Pt alloy catalysts, the $Pt_{79.1}$-$Au_{20.9}$ alloy catalyst shows high activity for the BOR. The observed phenomena of shifting the potential value of both reactions (HOR and the BOR) is a clear indication of the adjusted electronic/ ensemble properties.

The BH_4^- on the alloy catalysts follows both the BOR and the spontaneous catalytic hydrolysis pathways. Providing sites on the alloy surface that facilitate the catalytic hydrolysis reaction of the BH_4^- gave rise to H_{ads}. The measured current at -0.8 V_{SCE} increases with increasing the Pt content in the alloys due to its high kinetics for HOR (Figure 83). In the case of Pt-rich catalysts, the sites preferably favour adsorption of H_{ads} as observed by the linear increase in the measured current densities of HOR at -0.8 V_{SCE}. This illustrates that the pathway for the catalytic hydrolysis reaction of the BH_4^- largely affected the catalysis for the direct BOR when Pt is present on the Au-Pt alloy surface. On the other hand, the measured currents at both -0.5 V_{SCE} and -0.2 V_{SCE} indicate that the BOR is more rapid for Pt > 30%. As can be seen, there is a slight increase in the measured current relative to areas where the number of the Pt atoms decreases on the Au-Pt alloy surface. When more addition of Pt (≥ 80 %) is present on the alloy surface, the current drops to the same as in the Au-rich alloy surfaces. This suggests that when the BH_4^- reaches the Au-Pt alloy surface, it undergoes a spontaneous catalytic hydrolysis followed by the production of the hydrogen and therefore leading to reducing the full utilization of the BOR. This means that the pathway for the BOR reaction in the presence of Pt on the Au-Pt alloy surface may proceed through less than the 8-electron route at a potential higher than -0.8 V_{SCE}.

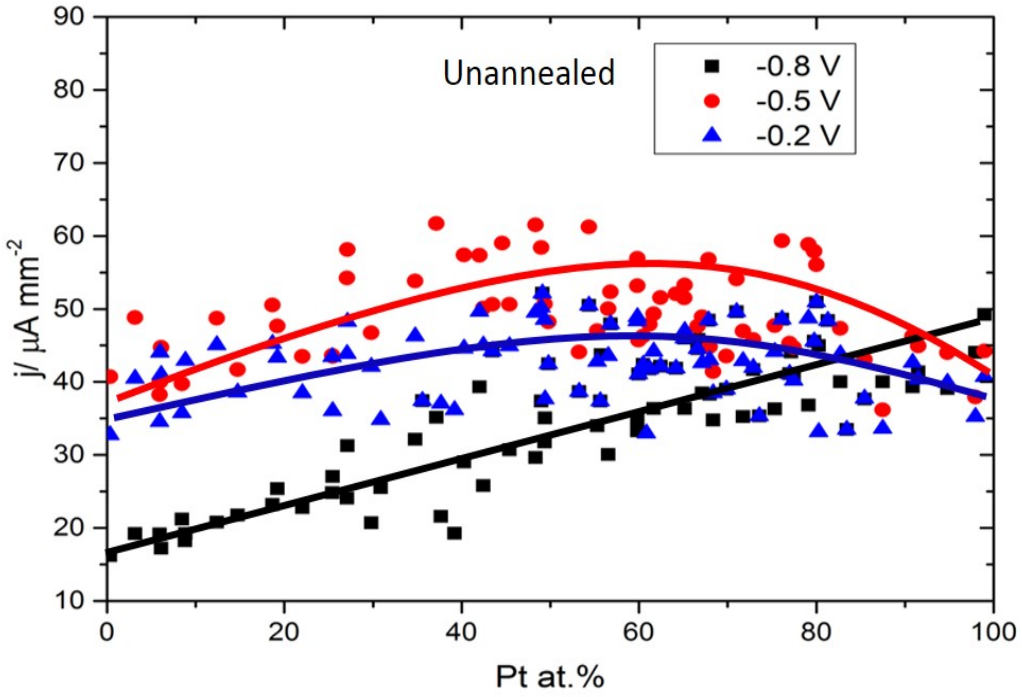

Figure 83: Comparison of the current density of the direct BOR extracted from the CVs data of the unannealed Au-Pt alloy catalysts at -0.8 V_{SCE}, -0.5 V_{SCE} and -0.2 V_{SCE}.

It should be noted that it is difficult to make high throughput electrochemical analysis using I-threshold to extract the ignition potential of the BOR as a function of composition and give an indication of the high/ low catalytic activity due to interference from the HOR. It appears that the presence of an ensemble of a single Pt atom surrounded by ensembles of Au atoms still offer active sites on the Au-Pt alloy surface for H_{ads} produced by the hydrolysis of the borohydride. Therefore, an electrochemical technique is required that can be used to determine the catalytic activity of the Au-Pt alloy catalyst via monitoring the hydrogen produced by the catalytic spontaneous hydrolysis of the borohydride that will be revealed in Chapter 7.

6.3.2 The Electro-catalytic Activity of the Annealed Au-Pt Alloys for Direct BOR

Further electrochemical screening experiments were carried out to examine the activity of the Au-Pt alloy (annealed at 300 ^{o}C for 15 min) in the absence and in the presence of $NaBH_4$. Figure 84 shows a comparison of selected CVs of the Au-Pt alloy catalysts with different compositions. The CVs were recorded in in 0.1 M NaOH under same conditions and at the same potential range as the unannealed Au-Pt alloy catalysts (between -1.05 V_{SCE} and + 0.15 V_{SCE}) at a sweep rate of 100 mVs^{-1}.

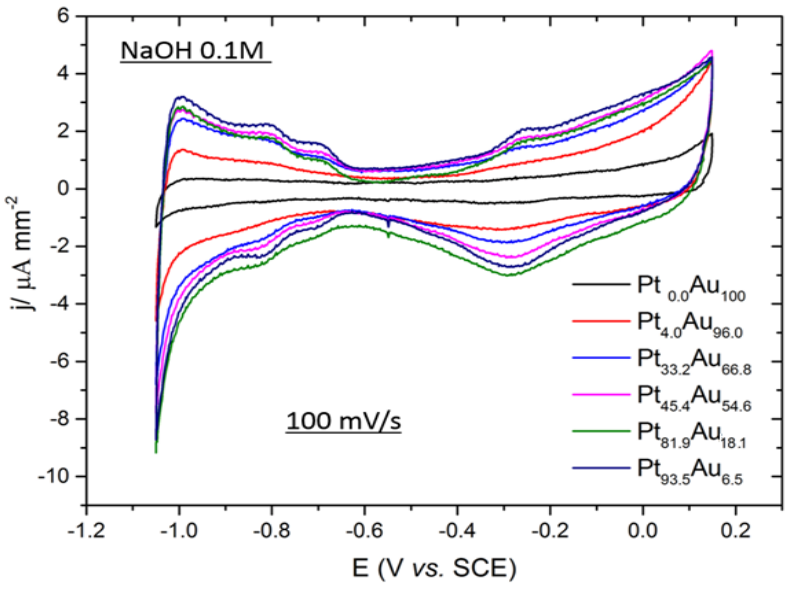

Figure 84: Cyclic voltammograms showing the electrochemical activity of the annealed Au-Pt alloy catalysts in 0.1 M of NaOH at a potential scan rate of 100 mV/s as a function of electrode composition.

The CVs carried out on the annealed Au-Pt alloy catalysts show similar surface redox processes to the unannealed Au-Pt alloy. For both alloy samples (annealed and unannealed), increasing the composition of Pt in the alloys results in increasing the current density of the surface redox reactions. However, the annealed Au-Pt alloy sample exhibits much lower peak currents. In comparison with the CVs of the unannealed Au-Pt alloy catalysts, the two pairs of the hydrogen desorption peak are less pronounced. The maximum current density of the HOR reaction at -0.7 V_{SCE} can be extracted to understand the effect of Pt addition on the annealed Au-Pt alloy catalysts after annealing. The peak current of the hydrogen desorption for the (annealed) $Pt_{93.5}$ $Au_{6.5}$ catalyst is maximum at ca. 1.8 µA mm^{-2}, whereas that for the (unannealed) $Pt_{91.5}Au_{8.5}$ catalyst is maximum at 7.5 µA mm^{-2}. This indicates that the Au-Pt alloy catalysts after annealing exhibited a change in the surface area, which leads to a decrease in the current density of the HOR on the annealed alloy catalysts.

The CVs shown in Figure 85 are representative of the activity and catalytic behaviour of the annealed Au-Pt alloy catalysts in 0.01 $NaBH_4$. The voltammogram shows no foreign peaks as compared with the unannealed Au-Pt alloy catalysts. The anodic peak assigned for the HOR (produced by the catalytic hydrolysis) has a similar shape to those discussed above for the HOR on the unannealed Au-Pt alloy in the presence of the borohydride. However, based on the CVs data, the HOR on the annealed Au-Pt alloy exhibits a shift towards more negative potential values compared to the unannealed Au-Pt alloy sample. As can be seen, the onset potential of the first anodic peak corresponding to the HOR on the Pt-rich (97 at. %) alloy catalyst starts at ca. -1.07 V_{SCE} (extracted at I-threshold= 10 µA mm^{-2}) with a current density maximum at ca. 60 µA mm^{-2},

while on the unannealed Pt-rich (99 at. %) alloy catalyst, the HOR occurs around -1.03 V_{SCE}. The anodic peak of the HOR on the annealed the $Pt_{78.4}$-$Au_{21.6}$ alloy catalyst starts at ca. -1.05 V_{SCE} reaching a maximum current density at ca. 59 µA mm^{-2}. Moreover, the onset potential of the HOR on the annealed $Pt_{51.7}$-$Au_{48.3.}$, $Pt_{39.2}Au_{60.8}$, and $Pt_{11.5}Au_{88.5}$ alloy catalysts starts almost at the same onset potential, -1.04 V_{SCE} and -1.03 V_{SCE} respectively. Furthermore, the onset potential of the HOR on the $Pt_{1.6}Au_{98.4}$ alloy catalyst is at ca. -1.1 V_{SCE}, while on the unannealed $Pt_{3.2}$-$Au_{96.8}$ alloy catalyst, the HOR onset potential was at ca. -0.88 V_{SCE}. It could be possible that a beginning of a phase separation in the Au-Pt alloy bulk structure (or perhaps alight enrichment of Pt on the alloy surface) were formed after annealing which may account for the shifts of the HOR to more negative potential on the annealed Au-Pt catalysts.

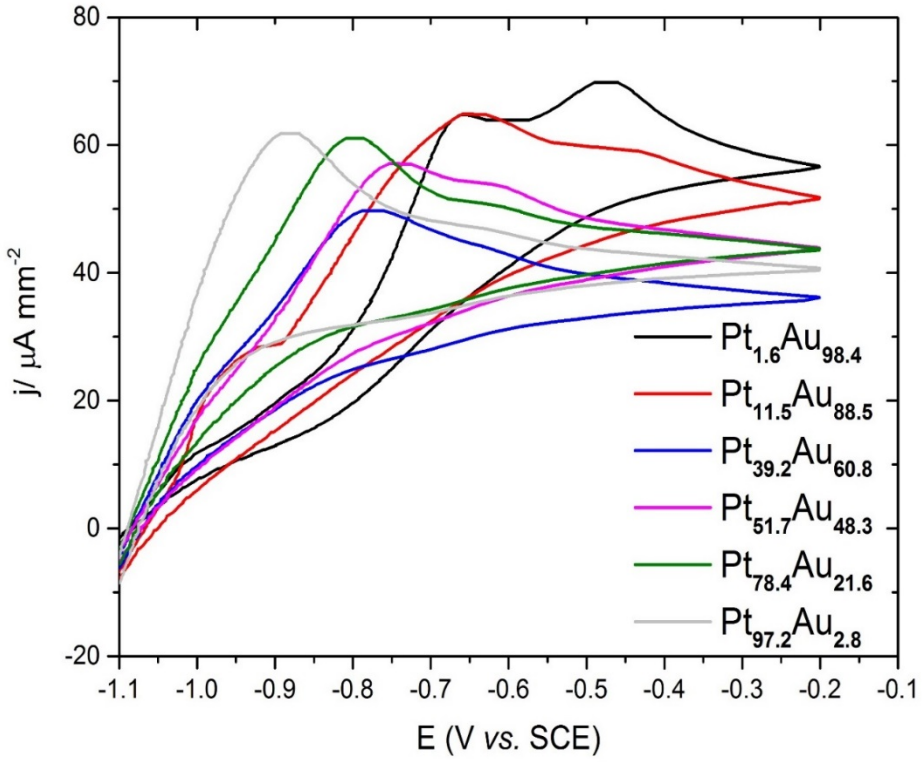

Figure 85: CVs showing the electrochemical behaviour of the annealed Au-Pt alloy sample with various compositions in 0.01 M $NaBH_4$ and 0.1 M NaOH at scan rate of 25 mV/s from -1.1 V_{SCE} to -0.2 V_{SCE}.

The anodic peaks of the HOR overlaps with the BOR for alloy catalysts of Au concentration ≥ 10 at. %. This indicates that a mixed oxidation reaction is occurring in this potential region. As can be seen from the CV of the catalyst composition of $Pt_{97.2}$-$Au_{2.8}$ that as the potential is forward scanned from -1.0 V_{SCE} to more positive potentials, an anodic peak current starts to increase. This anodic peak can be seen on the Au-rich (Pt ≤ 10 at. %) alloy catalysts at -0.5 V_{SCE}. This can be attributed to the BOR exhibiting the same anodic peak shape observed on the unannealed Au-rich

alloy catalysts. Note that the BOR on the unannealed Au-Pt alloy was clearly observed at higher Pt concentrations (Pt-79.1 at. %). It seems that the high catalytic activity towards the borohydride hydrolysis at more negative potentials block the active sites for the BH_4^- and that reduces the effective oxidation of the borohydride on the annealed Au-Pt alloy compared to the unannealed Au-Pt alloy.

The increase in the HOR current for the annealed Au-Pt alloy compared to the unannealed alloy sample can be related to increasing Pt atoms on the alloy surface (Figure 86). The HOR current density at -0.8 V_{SCE} increases almost the double compared to the unannealed alloy sample. This may indicate that a formation of a Pt-like structure as well as a change in Pt composition on the Au-Pt alloy surface (Pt segregation) may have occurred after annealing the Au-Pt alloy sample as was apparent from the XRD and XPS results. For this reason, a high amount of H_{ads} on the alloy surface was produced by the catalytic hydrolysis of BH_4^-.

The current density at -0.5 V_{SCE} and -0.2 V_{SCE} is following almost the same trend for Pt > 30 at. %, whereas at lower than 30 at. % of Pt, there is a deviation to a higher current density compared to the unannealed Au-Pt alloy sample. The increase in the current densities of the HOR associated with the overlap of the BOR current densities as well as the shift of the HOR towards lower onset potentials could mean that a higher rate of HOR oxidation was produced. Thus, it can be concluded that although the formation of H_{ads} or H_2 (bubbles) at the surface can be oxidized by Pt at a lower onset potential, the two processes (BOR and the spontaneous catalytic hydrolysis) proceeding simultaneously can be a challenge on the Au-Pt alloy catalysts and therefore it should be further investigated.

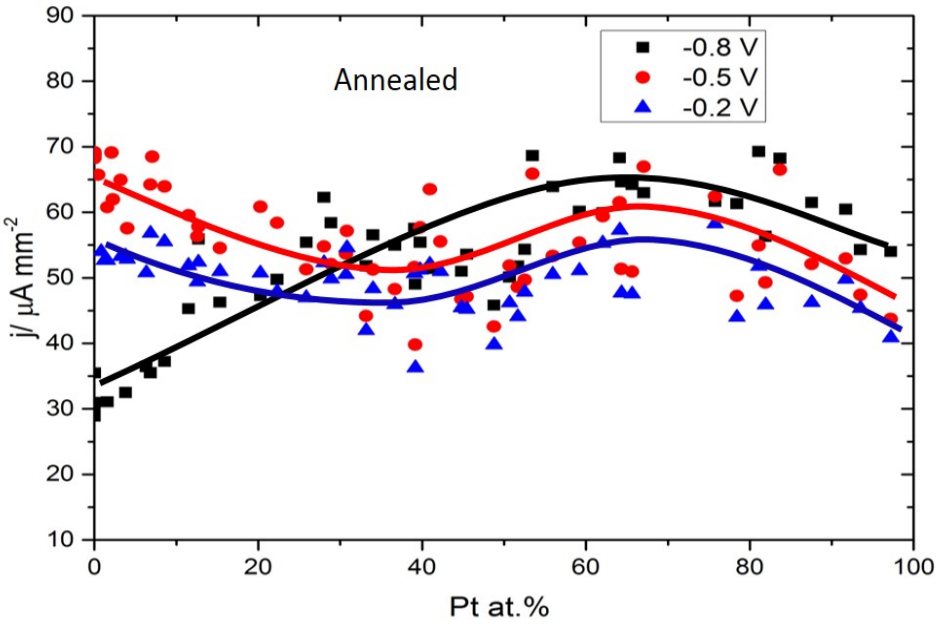

Figure 86: Comparison of the current density of the direct BOR extracted from the CVs data of the annealed Au-Pt alloy catalysts at -0.8 V_{SCE}, -0.5 V_{SCE} and -0.2 V_{SCE}.

6.4 Conclusion

The HT-PVD method was used to synthesise non-equilibrated and equilibrated Au-Pt binary alloys as a function of compositions. The synthesised Au-Pt alloys were then characterised using SEM/EDX, XRD and XPS respectively. The EDX results showed that the composition of Pt in the Au-Pt alloys varied linearly across the surface in the range between $1 \leq x$ at. % ≤ 99.

The XRD patterns of the Au-Pt alloy were characterized. Different annealing temperatures (300 ^{o}C and 600 ^{o}C) were performed on the Au-Pt alloys. It was found that the Au and the Pt of the Au-Pt alloy samples (RT and annealed at 300 ^{o}C) formed a single crystalline phase over the complete composition, while two-phase mixture in the annealed Au-Pt alloy sample (600 ^{o}C) appeared in the composition range between ca. 10 and 40 Pt at. %.

The XPS analysis showed binding energy shifts in the unannealed Au-Pt alloy sample. The surface compositions present on the Au-Pt alloy, quantified by XPS, were compared with the EDX bulk composition before and after annealing at 300 ^{o}C for 15 min. The surface composition of the Au-Pt alloy showed minimal segregation of Pt atoms on the alloy surface.

While focused on the direct BOR on the unannealed and annealed Au-Pt alloy catalysts, this study highlighted electrochemical stability of the Au-Pt alloy film to explain some of the effects on Au-Pt alloy film. This experiment was carried out by repeatedly cycling the potential (without stopping)

in the range between -1.05 V_{SCE} and +0.5 V_{SCE}. After performing 100 cycles, it was found that the peak current of the OER continually decreased. This was ascribed to the subsequent dissolution of Pt on the Au-Pt surface and suggested that lower potentials are required when studying the direct BOR on the surface of the Au-Pt alloy catalysts.

The electrochemical behavior of the unannealed and annealed Au-Pt alloy catalysts was screened in the absence and in the presence of the borohydride. Observations made from the CVs data for the Au-Pt alloy catalysts in 0.1 M NaOH showed Pt-surface redox reactions. The Au surface oxide redox reactions in the voltammetry were absent and were not observed because of the much lower potential scan. However, from the CVs, it was possible to observe the effect of the Pt addition on the HER and HOR. The cathodic and the anodic peaks on Pt-rich catalysts showed high current density compared to the Au-rich catalysts. The activity of the HOR and HER decreased on the annealed Au-Pt alloy compared to the unannealed Au-Pt alloy.

The catalytic assessment of the Au-Pt alloy catalysts in the presence of the 0.01 $NaBH_4$ showed interesting results. The voltammograms of the annealed and unannealed Au-Pt alloy catalysts are complicated due to anodic overlapping peaks. The characteristics of the Au-Pt alloy oxidation reactions were found to be affected by changing the catalyst composition. The presence of Pt in the Au-Pt alloy catalyst showed strong influence on promoting the borohydride hydrolysis reaction. This led to producing large amount of H_2 oxidized at more negative potential than the BOR. This suggested that the presence of a very small Pt in the Au-Pt alloy catalysts increasingly modified their catalytic properties. Thus, an electrochemical technique is essential for monitoring the H_{ads} oxidation reaction produced by the catalytic hydrolysis of the borohydride to determine the catalytic activity, and that will be discussed in the following chapter. It can be concluded that the Au-Pt alloy system may not be suitable for DBFCs due the issue of high catalytic activity towards the borohydride hydrolysis reaction.

Chapter 7 High Throughput Hydrogen Probe Technique

In this chapter, a novel electrochemical method for detecting H_2 produced by the catalytic borohydride hydrolysis at an array of 100 solid surface electrodes will be revealed. This method is adapted from the SECM technique invented by Professor Alan J. Bard, in which electrochemically oxidizable or reducible species generated at an electrode surface are detected through an electrochemical reaction at a tip (ultra-micro-electrode (UME) with a diameter of 10μm)[151] (The so-called Surface Generation/ Tip Collection mode). Our method uses the High Throughput Hydrogen Probe technique (Ni, diameter of 0.5 mm) that works as an indicator of hydrogen oxidation. The probe is specially designed to measure the electrochemical current of hydrogen evolution produced by the hydrolysis of the borohydride across the substrate as a function of electrode composition (a 1 mm^2 solid surface).

Limited studies have used methods for characterising the hydrogen evolution. Most of these studies measured the borohydride hydrolysis indirectly by determining the hydrogen volume. For example, Amendola and his co-workers studied the oxidation of the BH_4^- on an electrode-deposited (Au (97%)-Pt (3%)[51]. A closed electrochemical cell containing a basic solution of 5% $NaBH_4$ and 25% NaOH was used, while applying a constant potential to the working electrode at fixed times. The volume of the H_2 formed during the BH_4^- ion oxidation was measured using an inverted burette that was filled with water. From the gas volume, they found that the calculated number of electrons was less than eight. Geng and his co-workers[147] measured the hydrogen produced by the hydrolysis using a flow metre during the operation with DBFCs. They concluded that the rate of hydrolysis on the Au-Pt/C catalyst is higher than Au.

Allen J. Bard and his co-workers[48] used direct current measurements to study the intermediates of the BOR on Au. They used the SECM technique for detecting the intermediates reaction at an ultra-micro tip (10 μA) of Au electrode generated by Au substrate by holding the substrate potential in the region of the BOR. They found that the intermediates generated at the Au surface due to the oxidation of the borohydride gave a reduction current at the tip. Our method, however, provides direct current measurements for the hydrogen oxidation reaction at the Ni probe, which at negative potentials does not interfere with the BOR or intermediate reactions. In addition, it is fast and easy for screening combinatorial materials combined with the high-throughput electrochemical screening method to monitor active catalysts and detect which catalyst has the higher hydrogen oxidation current.

$$BH_4^- + H_2O \rightarrow BH_3(OH^-) + H_2 \qquad \text{(Equation 7-1)}$$

The hydrogen evolution rate is equivalent to the borohydride hydrolysis rate. According to Equation 7-1, for each BH_4^- ion produced by the catalytic hydrolysis, one molecule of H_2 is

evolved. Therefore, as the concentration of the borohydride increases, the hydrogen evolution rate increases[2]. In addition, the selectivity to the hydrolysis reaction varies with surface composition. Thus, this chapter outlines analytical and detailed studies on monitoring H_2 for the Au-Pt alloy catalysts over a wide range of compositions.

7.1 Experimental

To validate the approach, hydrogen evolution was first monitored on a Pt arrays sample (Figure 87). This approach was used to make sure that no other products on the Pt surface are produced apart from H_2 while the detection is taking place at the tip, $H_2 \rightarrow 2H^+ + e$. The Pt arrays sample was placed on a stage that is mounted onto two linear stages (Zaber, T-LS28-M) to allow the substrate to move in the x,y directions. A piezoelectric motor from Burleigh instruments was used to alter the tip-substrate separation in the z direction. The high throughput electrochemical cell contained a solution of 0.1 M NaOH. A Ni macro electrode (0.5 mm in diameter and 1 mm length) was used as a working electrode probe, SCE was used as a reference electrode and Au mesh was used as a counter electrode. The H_2 was generated at the Pt arrays by applying a fixed potential using a single potentiostat that was connected separately to a different PC. Prior to any detecting measurement of H_2 oxidation at the tip, the area surrounding the substrate-tip separation was purged by Ar gas using glass pasteur pipettes (FisherBrand), Inner-Ø at the tip approx. 1.0 mm to prevent hydrogen saturation. The substrate area of the Pt surface is 1 mm^2.

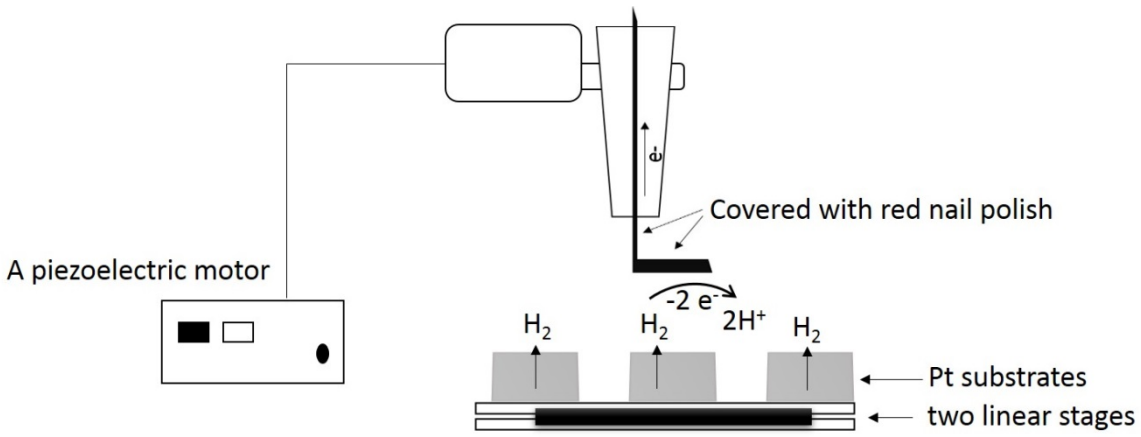

Figure 87: Schematic view of H_2 detection using Ni macro electrode to probe H_2 over the surface of Pt.

It should be noted that H_2 bubbles generated at the catalyst and interacting on the probe did not allow a stable screening. To overcome this issue, as the probe moves to the passivated substrate (the area between each Au-Pt surface), the separation between the probe and the substrate was adjusted to a sufficient distance in order to prevent accumulation of bubbles at the probe and subsequently brought back again when detecting at the rest catalyst field.

7.1.1 Calibration of the Hydrogen Generation from the Pt Surface and Hydrogen Oxidation at Ni Probe

To generate H_2 at the surface (via water reduction), the potential of the Pt substrate subsequently was alternated between -0.85 V_{SCE} and a range of potentials, -1.05 V_{SCE} and -1.1 V_{SCE}, -1.2 V_{SCE}, -1.3 V_{SCE} and -1.4 V_{SCE} (Figure 88). When the Pt substrate potential was at -1.4 V_{SCE}, hydrogen was vigorously evolved into the bulk solution. The time taken for H_2 generation was limited to 20-30 seconds to prevent H_2 saturation. As the potential is switched to -0.85 V_{SCE}, no hydrogen bubbles were observed. Figure 89 shows the H_2 oxidation current recorded at the Ni macro electrode during H_2 generation and H_2 elimination. As can be seen, the oxidation current at the Ni electrode increases as the hydrogen generation increases. The oxidation current remains at zero during H_2 elimination. This indicates that the amount of hydrogen evolution at the Pt surface is reflected in the increase/ decrease of the oxidation currents at the Ni probe.

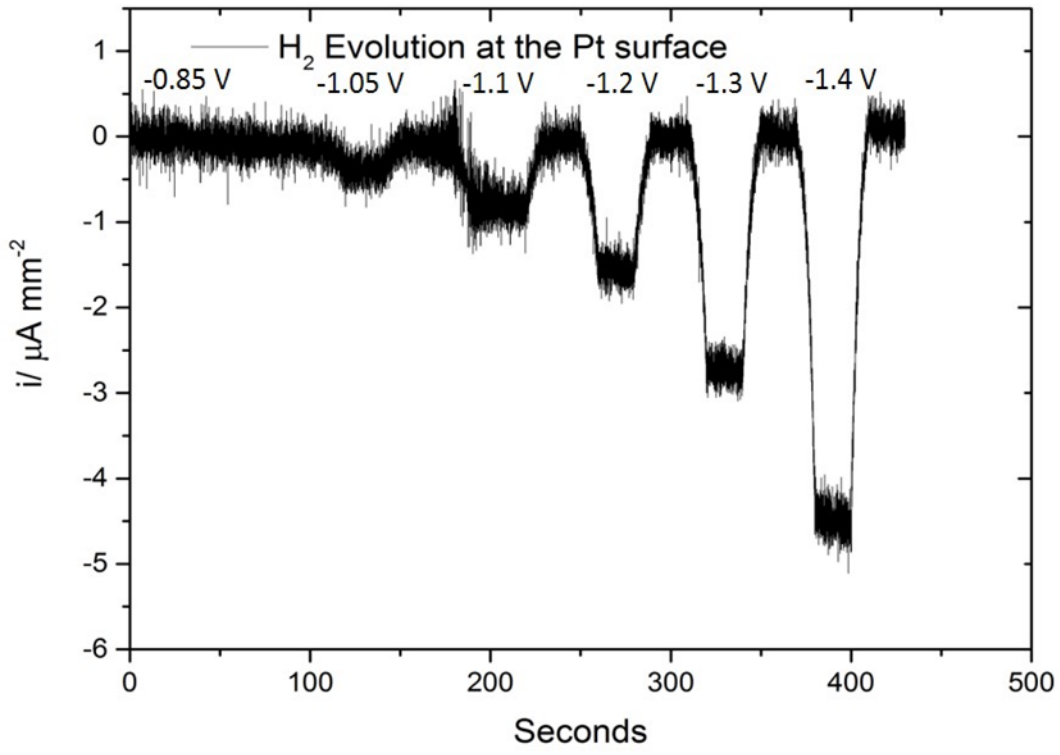

Figure 88: Chronoamperometric approach showing the hydrogen evolution on the Pt surface generated by alternating the potential between -1.00 V_{SCE} at a range of potentials including -1.05 V_{SCE}, -1.1 V_{SCE}, -1.2 V_{SCE}, -1.3 V_{SCE}, and -1.4 V_{SCE}.

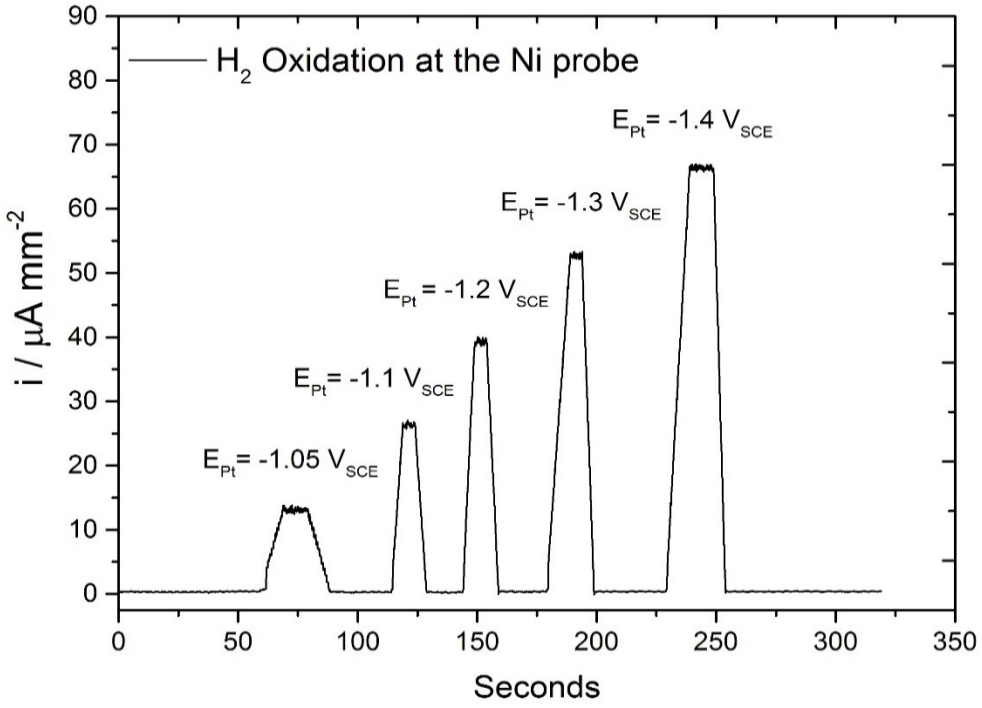

Figure 89: Chronoamperometric approach showing the response of the Ni probe to the hydrogen generated from Pt surface while the Ni probe was fixed at -1.0 V_{SCE}.

A further experiment was carried out to measure the oxidation of H_2 through the hydrolysis of the borohydride over the Pt substrate using concentrations of $NaBH_4$ 0.005 M and 0.01 M. Small concentrations of borohydride were used to reduce saturation of H_2 from surrounding areas (hydrogen generation from adjacent Pt substrates) while H_2 probing (Figure 90).

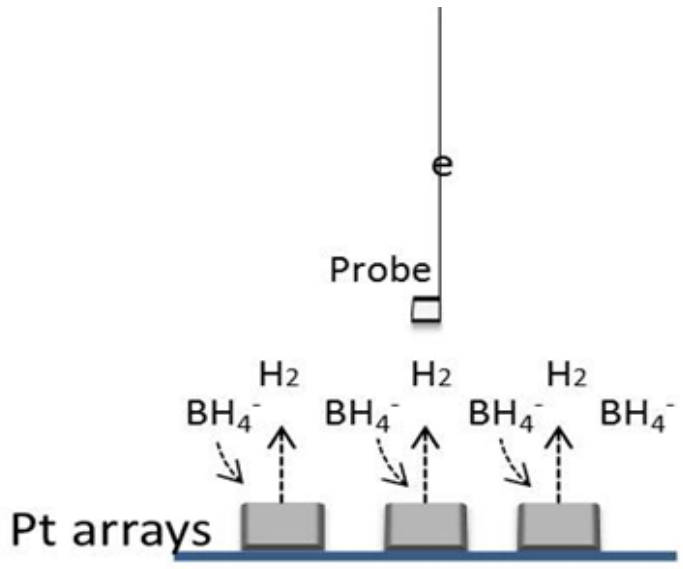

Figure 90: Schematic view showing H_2 generation by the borohydride hydrolysis from the surrounding Pt array as well as the area of detection while probing H_2 between two Pt substrates.

The Pt substrate was fixed at -1.0 V_{SCE} at which neither hydrogen generation from water reduction nor hydrogen oxidation occurs. The potential of the Ni electrode probe was fixed at -1.0 V_{SCE} to oxidise H_2. More positive potentials were avoided to prevent possible interference of oxygen reduction with the hydrogen oxidation at the Ni. The probe was brought into close proximity with the Pt substrate (50 µm). When the probe was in position to effectively probe H_2, $NaBH_4$ (0.005 M) was added to the electrolyte (0.1 M NaOH). This was followed by adding more borohydride (0.01 M) after about a minute. Figure 91 shows the influence of the borohydride hydrolysis reflected on the oxidation of H_2 at the Ni (noise is due to bubbles). As was expected, the H_2 oxidation current increased as more borohydride was added due to an increase in the surface coverage by borohydride at the Pt substrate. This illustrates that our approach can be used for determining the hydrolysis of the borohydride, whereby the probe can move across the whole arrays sample to monitor H_2 as a function of electrode composition.

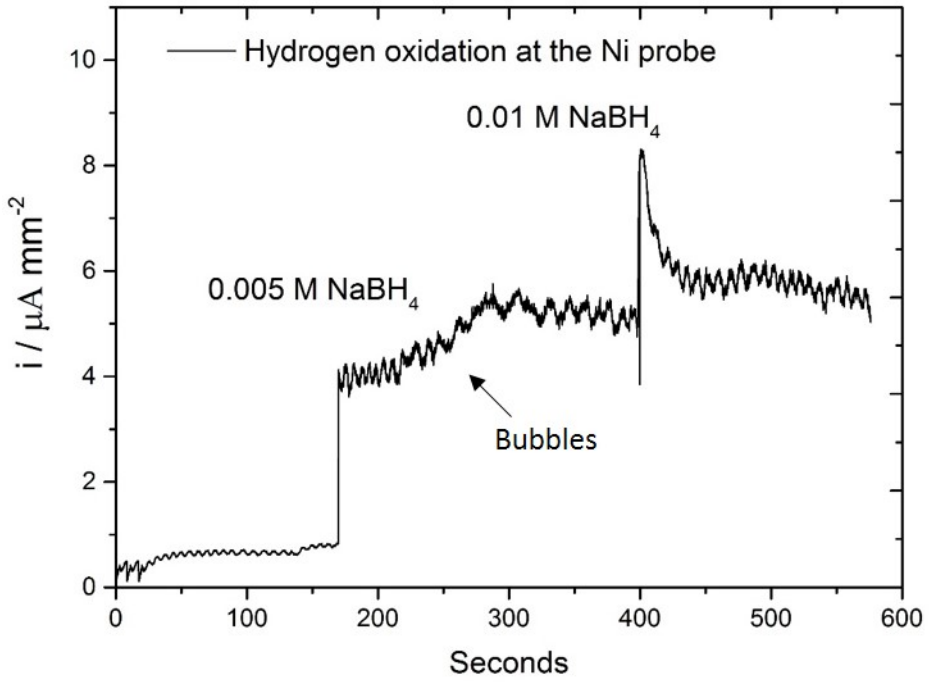

Figure 91: Hydrogen oxidation current recorded at the Ni probe using concentration of 0.005 M and 0.01 M of $NaBH_4$ in 0.1 NaOH M as a source of hydrogen generation via the catalytic spontaneous hydrolysis reaction.

7.2 Detection of Hydrogen over Au-Pt Alloy Catalysts

The results, which were previously presented to validate the utilisation of the high throughput hydrogen Probe method, demonstrated that hydrogen generated from the Pt substrate via hydrogen reduction/ borohydride hydrolysis can be oxidised at the Ni probe. Thus, the use of this electrochemical method of surface generation/ probe collection as a measure to determine the

hydrogen evolution produced by the catalytic spontaneous hydrolysis of the borohydride over Au-Pt alloy arrays as a function of composition will be reported first.

Screening for hydrogen evolution was performed to determine the hydrolysis of the borohydride (0.01 M) at the Au-Pt alloy as a function of compositions. High pH alkaline solution (NaOH 0.1 M) was used to make sure that the hydrolysis of the borohydride was not influenced by the chemical hydrolysis reaction. The probe potential at which H_2 is oxidised at the Ni probe was fixed at -1.0 V_{SCE} to avoid probing other active species such as BH_4^-, intermediates and O_2 that are electrochemically oxidised/ reduced at more positive potentials. The potential of the Au-Pt alloy arrays was fixed at potential -1.0 V_{SCE} where the only source of H_2 present between the probe and the Pt surface separation is produced by the spontaneous catalytic hydrolysis.

Before the actual hydrogen detection, the distance between the probe and the substrate was calibrated (Figure 92). The probe was alternated between an insulated layer (Si-N substrate) and the Pt surface. In addition, it should be noted that the probe can block the diffusion of BH_4^- to the Pt substrate, which affected the hydrogen evolution screening. To overcome this problem, the distance between the probe and the substrate was adjusted. Moreover, for precise hydrogen screening, it is also important to have minimal interaction with hydrogen oxidation generated by adjacent Pt substrates and therefore 50-25 distance was used to probe hydrogen throughout.

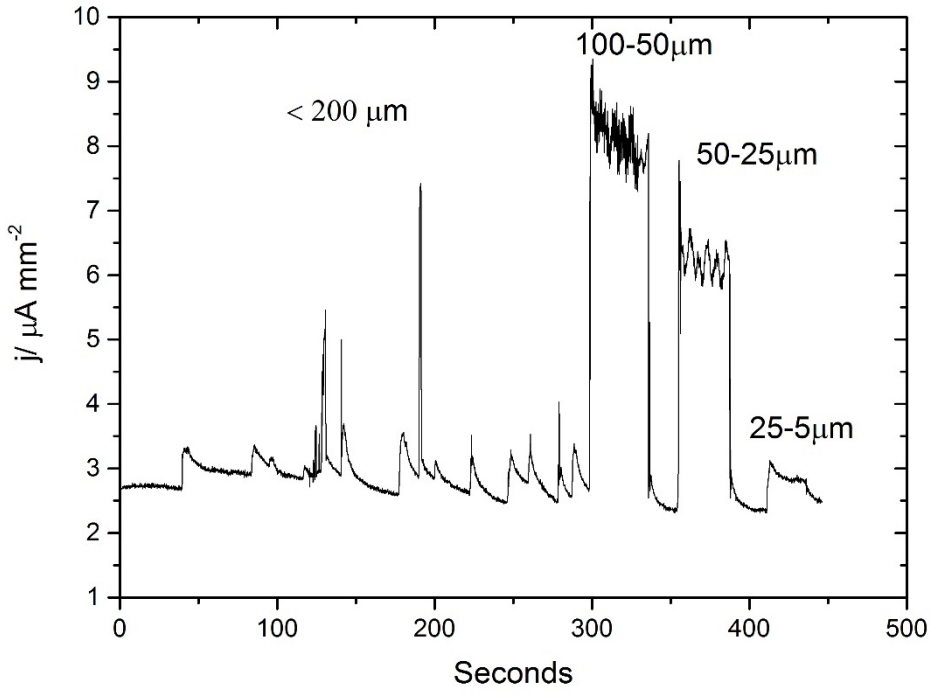

Figure 92: Distance calibration between the Ni probe and the substrate showing positive current as the probe moves closer (≤ 200) to the Pt surface and the effect of the probe on the BH_4^- diffusion for the case of 25-5 μm distance.

Figure 93 shows variations in the hydrogen oxidation current at the Ni probe using the HT-ECSP. The purpose of this experiment was to elucidate the first anodic peaks, which were referred to the H_2 oxidation seen in Chapter 6 (CVs of 0.01 M $NaBH_4$) on the Au-Pt alloy catalysts (Figure 82). By screening from Au rich to Pt rich catalysts, it could be seen that the maximum oxidation current is detected at the Ni probe for Au-Pt alloy composition between 30 and 80 Pt at. %. At this range, the hydrogen oxidation current varies between around 14 and 23 μA mm^{-2}. In addition, the hydrogen detected for the Au-Pt-alloy catalysts in the Pt range between 80 and 100 at. % showed a relatively smaller hydrogen oxidation current varying between around 8 and 17 μA mm^{-2}. On the other hand, the hydrogen oxidation current when probing at the Au-Pt alloy composition in the range between 0 and 20, showed a minimum current, ranging between 1 and 5 μA mm^{-2}. This suggests that a relatively high hydrolysis of borohydride is recorded at intermediate Au-Pt alloy compositions. This can be attributed to the electronic/ensemble effects, which enhanced the catalytic selectivity towards the hydrolysis.

Figure 94 shows a comparison of the hydrogen oxidation current versus Pt composition. The Figure demonstrates that the lowest hydrogen oxidation current was obtained when the Pt composition was ca. 1 at. %. This can be attributed to the addition of Au, which exhibited low catalytic activity towards the hydrolysis of the borohydride. This finding confirms that the presence of Pt in the alloy catalyst increases the hydrolysis rate reflected on the hydrogen oxidation and is in line with the literature found[152-153]. Furthermore, earlier findings (Chapter 6) where the anodic currents corresponding to the hydrogen oxidation was reported in the presence of $NaBH_4$, is also in consistent with this finding. Therefore, combining this data with that obtained by the CVs and high throughput electrochemical screening, it can be concluded that the Au-rich catalysts associated with the smallest H_2 evolution can be considered as an effective catalyst for BOR, while the intermediate and rich-Pt catalysts have a modest activity or are inactive for the direct BOR due to high spontaneous catalytic hydrolysis of the adsorbed BH_4^-.

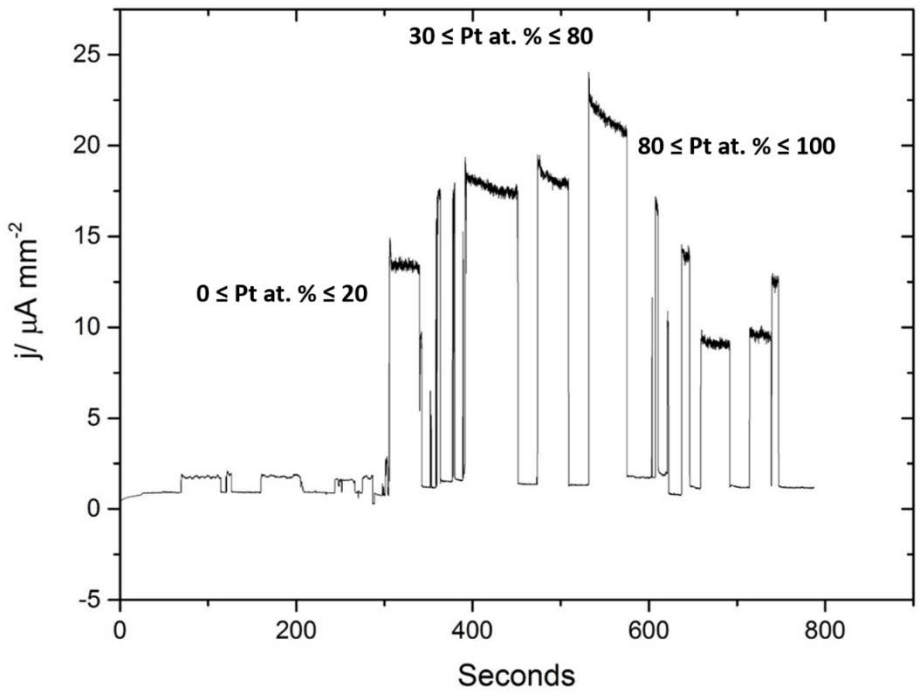

Figure 93: Hydrogen screening across the Au-Pt alloy surface using the high throughput hydrogen probe method. The probe/ Pt surface was at 50 µm. The potential of the substrate and the probe was fixed at -1.0 V_{SCE}. The electrolyte consists of 0.1 NaOH and 0.01 M of $NaBH_4$.

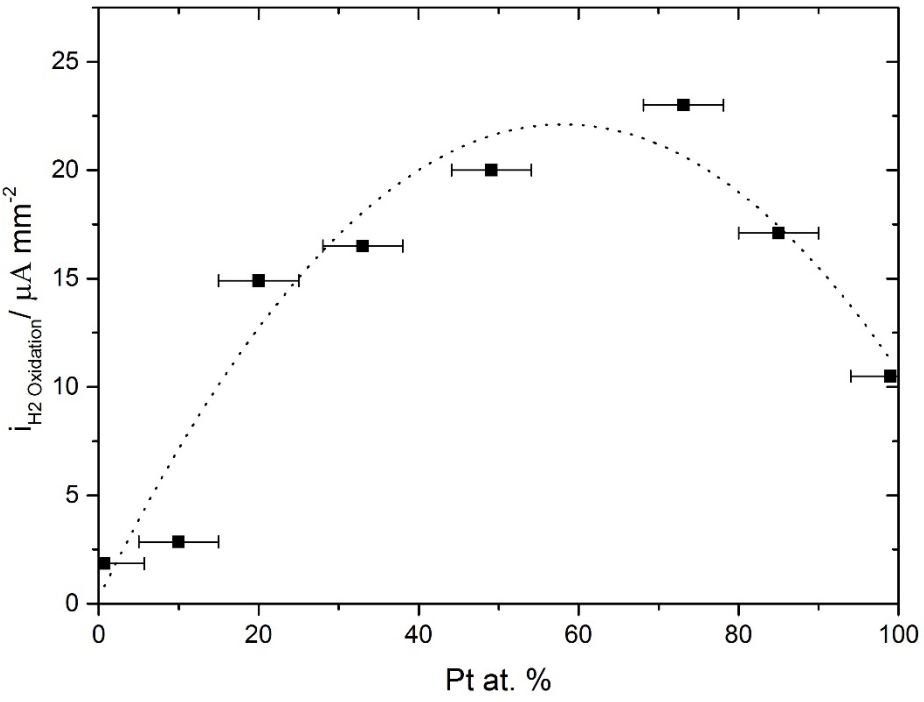

Figure 94: Variation of H_2 oxidation current extracted from the data presented in Figure 95 for determining the rate of the hydrogen evolution (due to hydrolysis) generated at the Au-Pt alloy surface as a function of electrode composition.

Chapter 8 Overall Conclusion

The overall aim of this thesis was to optimise catalysts with higher activity for DBFCs. The synthesis of combinatorial materials via the HT-PVD method led to the discovery of novel catalysts. High throughput bulk/surface techniques including SEM/EDX, XRD and XPS were used to characterise alloy catalysts as a function of composition. Specifically, gradient compositions of binary alloys of Au-Ni (Chapter 4), Au-Cu (Chapter 5) and Au-Pt alloy catalysts (Chapter 6) were synthesised, characterised and electrochemically screened to evaluate their catalytic activity for the direct BOR. Interesting catalytic trends were observed across these binary alloy systems.

The initial results discussed in Chapter 3 reveal that the direct BOR on Au and Ag metals occurred at more negative potential compared to Pt, Ni and Cu metals. The direct BOR was influenced by (1) the hydrogen evolution produced by the catalytic hydrolysis reaction (as in the case of Pt metal) that forced the onset potential of the BH_4^- oxidation to occur at higher potentials (more positive potentials) and by (2) the passivation layer formed by the adsorption of O_2/OH (as in the case of Ni, and Cu) that supresses the oxidation reaction of BH_4^-. This demonstrates the importance of alloying Au with other 3d metals to improve the catalytic activity for the direct BOR as well as reduce its cost in DBFCs

From the study on the binary alloy catalysts, XRD results showed that non-equilibrated Au-Ni solid solution materials were formed over a wide range of compositions ($98 \geq$ Au at. % ≥ 2). The equilibrated Au-Ni alloys in the composition range $85 \geq$ Au at. % ≥ 10 exhibited phase separation. XPS analysis showed that Au was segregating at the surface after thermal annealing at 300 ^{o}C.

The bulk composition of the Au-Cu alloy catalysts in the range of $5 \leq x \leq 90$ was determined by EDX. The XRD results of the unannealed Au-Cu alloy indicated single-phase alloys across the compositions. Moreover, the annealed Au-Cu (at 300 ^{o}C) showed variation in the peak intensity of the (111) Bragg peaks. The peak intensities of the (111) Bragg peaks were increased in the region of Au-rich compositions indicating an increase in the crystal size. The XPS analysis of the surface composition relative to the bulk composition before and after annealing showed no evidence of segregation of either element at any composition.

The bulk composition of the Au-Pt alloys across the surface, determined by EDX, was in the range between $1 \leq x$ at. % ≤ 99. The XRD results of the Au-Pt alloy (RT and 300 ^{o}C) exhibited a single crystalline phase across the complete composition. However, further annealing (600 ^{o}C) resulted in phase separation in the composition range between ca. 10 and 40 Pt at. %.

The surface composition of the Au-Pt alloy was compared with the bulk composition before and after annealing. The surface composition of the Au-Pt alloys showed a slight segregation of Pt atoms on the alloy surface.

The Au-Ni alloys were found to be interesting catalysts for DBFCs. The activity of the alloy catalysts varies with the addition of Ni. The value of the onset potential of the direct BOR was reasonably low for alloy compositions with small Ni additions (10 to 40 at. %) in the alloy catalysts. There were many compositions from this alloy system that have much lower onset potential than the metallic Au. This could be attractive from a cost point of view as it suggests that a low-cost catalyst could substitute Au pure metal, while still preserving high catalytic activity. The optimal catalyst was found near the Au_{65}-Ni_{35} composition. As shown in Figure 48, the Au-Ni alloy catalysts showed a decrease in the catalytic activity for the direct BOR after annealing due to surface enrichment with gold that was also observed in the XPS results. This means that the catalyst preparation method influences the Au-Ni alloy catalysts, as the non-equilibrated alloy catalysts showed better catalytic activity for the BH_4^- oxidation reaction than the equilibrated alloy catalysts.

The performance of the (unannealed and annealed) Au-Cu alloy catalysts towards the direct BOR was evaluated as a function of composition. The catalytic activity was found to be strongly associated with the alloy catalyst composition. It has been shown that adding very small amount of Au (10 to 20 at. %) to the unannealed Cu-rich catalysts increased the activity of the BH_4^- oxidation reaction. However, the presence of more Au atoms in the unannealed Cu-rich alloy catalyst showed lower BH_4^- oxidation activity shifting the onset to more positive potentials. The increase in the activity was attributed to the modification of the electronic structure and the ensembles. The $Cu_{78.3}Au_{21.7}$ alloy exhibited the highest activity followed by $Cu_{62.4}Au_{37.6}$ and $Cu_{89.7}Au_{10.3}$. For the annealed Au-Cu samples, the performance of the alloy catalysts was found to exhibit higher catalytic activity by shifting the onset potential of the direct BOR by ca. 0.15 towards lower potential compared with the unannealed Au-Cu alloy catalysts. The optimal composition for the direct BOR was found at the (annealed) Cu_{70}-Au_{30} alloy catalyst.

The presence of Pt on the Au alloy catalysts reduced the catalytic activity for the direct BOR. The catalysts in this binary alloy were favourably generating H_2 produced by the catalytic hydrolysis. There were difficulties in identifying the catalyst activity from the recorded CVs due to overlapping peaks, which placed some limitations on using the high throughput electrochemical analysis. However, this led to the development of a novel high throughput hydrogen probe technique used as an effective means for monitoring H_2 evolution produced by the catalytic hydrolysis reaction on the Au-Pt alloy catalysts (Chapter 7). The method was first used to measure the H_2 oxidation current at Ni probe. The activity of the alloy catalysts for the catalytic hydrolysis

reaction was found to be different with varying compositions. The current of the hydrogen oxidation on the Pt-rich catalysts was much higher than the Au-rich alloy catalysts, while the Pt at intermediate compositions was showing the highest H_2 oxidation current. This makes the Au-Pt alloy system unsuitable as anode materials for DBFCs.

While the surface area can be increased by surface roughening, it is believed that the increase in BOR current density is mostly attributed to the electronic/ geometric modification of the alloy catalysts when measured at low overpotential (eg. -0.8 V_{SCE}). As discussed earlier, the direct BOR was found to be dependent on the surface composition and structure. An increase/ a decrease in the composition of diluents in the Au-M alloy catalysts influence the catalytic activity for BOR. Table 5 shows the maximum current density of the unannealed and annealed Au-M (M= Ni, Cu and Pt) alloy materials for BOR extracted at a potential of -0.8 V_{SCE}, -0.5 V_{SCE} and -0.2 V_{SCE}. The results were studied to yield the following conclusions:

i. The BOR activity at -0.8 V_{SCE} on the Au-Ni alloy is optimal when a small ensemble of Ni (30%) and a large ensemble of Au are present on the alloy surface.
ii. The most active ensembles of Au-Cu (as measured at -0.8 V_{SCE}) are associated with small Au ensembles (ca. 20 % Au).
iii. With the increase in Cu contents in the annealed Au-Cu alloy, the current density of BOR at -0.2 V_{SCE} was linearly reduced. When the BOR is proceeding at higher oxidation potentials, Au becomes the most active component and the addition of Ni or Cu on the surface deactivated the reaction by the strongly adsorbed oxide species.
iv. The activity of the BOR at -0.8 V_{SCE} was affected by the addition of Pt on the Au-Pt alloy surface; the reaction follows pathways, the spontaneous catalytic hydrolysis and the BOR.
v. The current density of the BOR on the annealed Au-Pt alloy at -0.5 V_{SCE} overlaps with the HOR over a wide potential window which led to uncertainty in the activity of BOR at Pt > 50 at.%. The BH_4^- in the presence of Pt on the Au surfaces produces Pt-H_{ads}, which subsequently oxidized and the remaining of BOR may proceed at higher oxidation potentials than -0.8V_{SCE}.

Table **5** Comparison of the maximum current density values representing the activity of the BOR on Au-Ni, Au-Cu and Au-Pt alloy catalysts at different oxidation potentials including -0.8 V_{SCE}, -0.5 V_{SCE} and -0.2 V_{SCE}.

Alloy Catalyst	**Diluent at. %**	**Annealing (T, 300 °C)**	**j_{Max} (µA mm^{-2})**	**E (V_{SCE})**	**Reaction path**
Au-Ni	(Ni) 15-40 %	unannealed	ca. 15	-0.8	Direct BOR

Au-Ni	(Ni) 20-70 %	annealed	ca. 10	-0.8	Direct BOR
Au-Ni	(Ni) 1-50 %	unannealed	ca. 55	-0.5	Direct BOR
Au-Ni	(Ni) 1-35 %	annealed	ca.70-55	-0.5	Direct BOR
Au-Ni	(Ni) 1-35 %	unannealed	ca. 55-35	-0.2	Direct BOR
Au-Ni	(Ni) 1-35 %	annealed	ca. 35-17	-0.2	Direct BOR
Au-Cu	(Cu) 87-60 %	unannealed	ca. 2-3	-0.8	Direct BOR
Au-Cu	N/A	annealed	No activity	-0.8	N/A
Au-Cu	(Cu) 10-40 %	unannealed	ca. 30	-0.5	Direct BOR
Au-Cu	(Cu) 10-60 %	annealed	ca. 80-60	-0.5	Direct BOR
Au-Cu	(Cu) 70-80 %	unannealed	ca. 13-15	-0.2	Direct BOR
Au-Cu	(Cu) 10-80 %	annealed	ca. 30	-0.2	Direct BOR
Au-Pt	(Pt) 50-100 %	unannealed	ca. 30-50	-0.8	HOR/ hydrolysis
Au-Pt	(Pt) 30-100 %	annealed	ca. 50-70	-0.8	HOR/ hydrolysis
Au-Pt	(Pt) 30-80 %	unannealed	ca. 50-60	-0.5	HOR+ BOR +partial hydrolysis
Au-Pt	(Pt) 10-100 %	annealed	N/A	-0.5	uncertainty
Au-Pt	(Pt) 40-80 %	unannealed	ca. 50	-0.2	BOR
Au-Pt	(Pt) 1-30 %	annealed	ca. 50	-0.2	BOR

8.1 Future work

The gold catalyst in the DBFCs increases the system cost. This thesis focused on reducing or mitigating the dependence of the fuel cell on Au by providing promising anode candidates for DBFCs. The HT-PVD method and the HT-electrochemical screening techniques used in this work were the first to be used for exploring novel catalysts for DBFCs. Future research will focus on investigating the alloying effects on non-noble metals such as Zn, Fe, CO, also regarded as catalytic materials for the direct BOR. More effort should be extended into screening new alloy materials to be further explored. Ternary alloy materials such as Au, Ni and Zn could be an interesting catalyst to investigate.

The hydrolysis of the borohydride on other catalyst materials should be examined to better understand the mechanism of the direct BOR using the hydrogen probe. The detection of hydrogen evolution is likely to impact on the electrochemical results.

Appendix A

Table **6** Experimental detail of the alloy samples synthesised by HT-PVD on different substrate and the required surface analytical technique used for characterisation. Deposition was carried out at room temperature.

Sample number	Elements	Substrate	Mask (y/n)	Annealed (y/n)	Screening measurement
8533	Au, Ni	Si wafer	Yes	No	EDX
8539	Au, Ni	Si wafer	Yes	Yes	EDX, XRD, AFM
8540	Au, Ni	Si wafer	Yes	Yes	EDX, XRD
8542	Au, Ni	Si wafer	No	Yes	XPS, EDX
8543	Au, Ni	Si wafer	No	Yes	XPS, EDX, AFM
8545	Au, Ni	ITO/e-chem	Yes	Yes	ECS, EDX
8852	Au, Ni	ITO/e-chem	Yes	No	ECS, EDX
8855	Au, Ni	ITO/e-chem	Yes	No	ECS, EDX
8857	Au, Ni	ITO/e-chem	Yes	Yes	ECS, EDX
8869	Au, Cu	Si wafer	Yes	No	EDX
8871	Au, Cu	Si wafer	Yes	Yes	XRD, EDX
8876	Au, Ci	Si wafer	Yes	Yes	XRD, EDX
8889	Au, Cu	Si wafer	No	Yes	XPS, EDX
8892	Au, Cu	Si wafer	Yes	Yes	XRD, EDX, AFM
8884	Au, Cu	Si wafer	No	Yes	XPS, EDX,
8833	Au, Cu	Si wafer	No	No	EDX, AFM
8879	Au, Cu	ITO/e-chem	Yes	No	ECS, EDX

8883	Au, Cu	ITO/e-chem	Yes	yes	ECS, EDX
8886	Au, Cu	Au/e-chem	Yes	no	ECS
8887	Au, Cu	Au/e-chem	Yes	no	ECS
9336	Au, Pt	Si wafer	Yes	no	EDX, AFM
9337	Au, Pt	Si wafer	Yes	yes	XRD, EDX
9338	Au, Pt	Si wafer	Yes	yes	XRD, EDX
9341	Au, Pt	Si wafer	No	yes	XPS, EDX
9348	Au, Pt	Si wafer	No	yes	XPS, EDX, AFM
9345	Au, Pt	ITO/e-chem	Yes	yes	ECS, EDX
9346	Au, Pt	ITO/e-chem	Yes	no	ECS, EDX
9347	Au, Pt	ITO/e-chem	Yes	yes	ECS, EDX
9353	Au, Pt	Au/e-chem	Yes	no	ECS
9361	Au, Pt	Au/e-chem	Yes	no	ECS, H_2 Detection
9339	Au, Pt	Au/e-chem	Yes	no	ECS, H_2 Detection

AFM (a trace-retrace) data show the thickness profile at the edge of the deposited films. From this, the thickness of the binary alloy film materials was measured.

Figure 95: Trace-retrace plot of the sample number 9336 of the Au-Pt alloy system showing the film thickness.

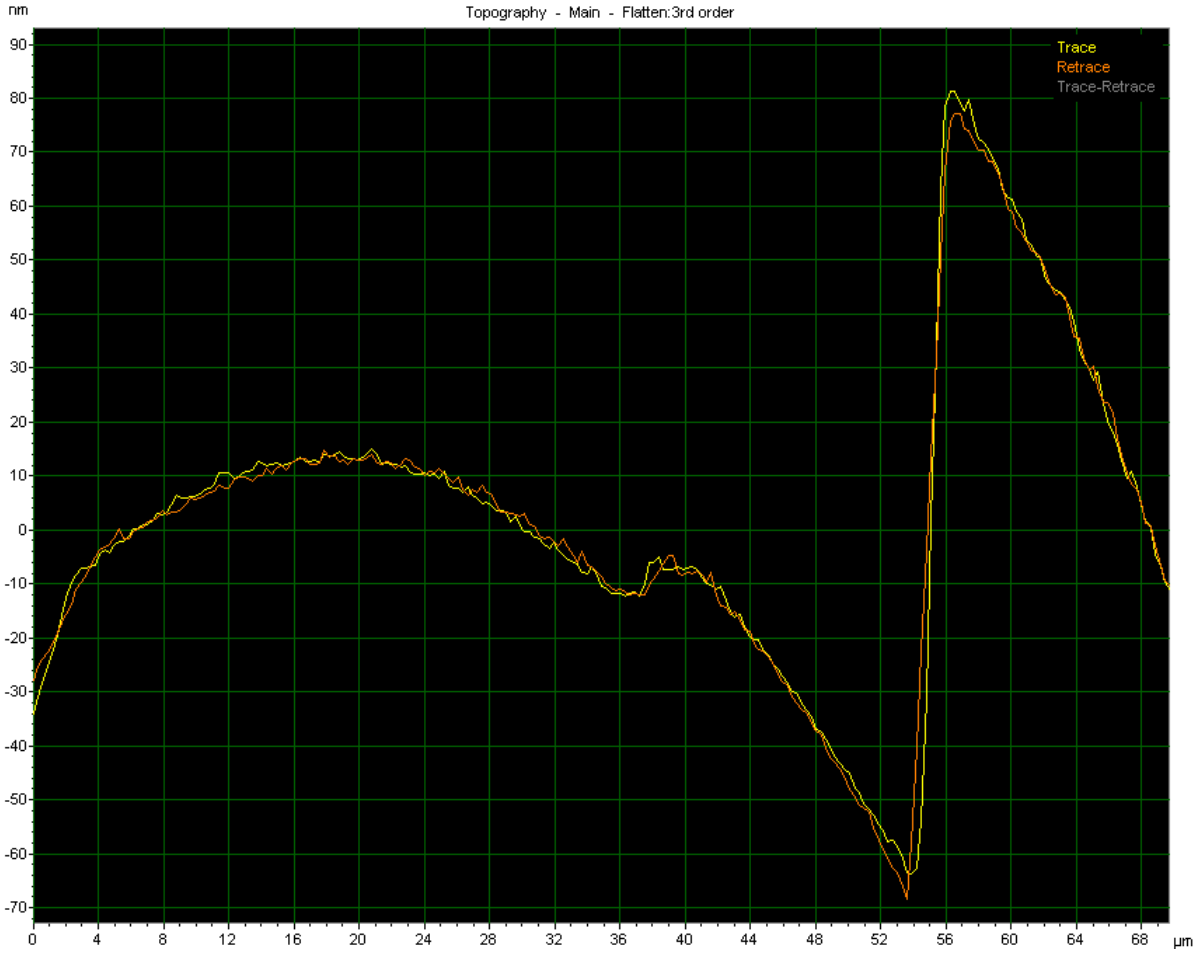

Figure 96: Trace-retrace plot of the sample number 8833 of the Au-Cu alloy system showing the film thickness.

Figure 97: Trace-retrace plot of the sample number 9539 of the Au-Ni alloy system showing the film thickness.

Appendix B

XPS data including the peak position, peak area, and atomic ratio extracted from XPS spectra using CasaXPS software.

Table **7** a summary of the XPS data analysis showing core level position, area of the Au (4f) and Ni (2p) peaks and the bulk/ surface composition calculated in atomic percentage in the unannealed Au-Ni sample (RT).

EDX **Au at. %**	**Transition**	**Binding Energy (eV)**	**Peak Area**	**At%**
15.7	Au ($4f_{7/2}$)	82.8 851.45	427.98	17.23
84.3	Ni ($2p_{3/2}$)		2056.40	86.30
34.6	Au ($4f_{7/2}$)	83.08	1391.31	38
65.4	Ni ($2p_{3/2}$)	851.63	2270.27	62.00
54.3	Au ($4f_{7/2}$)	83.72	2296.43	59.34
45.7	Ni ($2p_{3/2}$)	851.82	1567.92	40.57
79.4	Au ($4f_{7/2}$)	84.09	3038.27	80.26
20.6	Ni ($2p_{3/2}$)	852.55	747.12	19.74
89.5	Au ($4f_{7/2}$)	84.54	3038.64	87.13
10.5	Ni ($2p_{3/2}$)	852.73	448.73	12.87

Table **8** A summary of the XPS data analysis showing core level position, area of the Au (4f) and Ni (2p) peaks and the bulk/ surface composition calculated in atomic percentage in the annealed Au-Ni sample (300 ^{o}C for 15 min).

EDX **Au at. %**	**Transition**	**Binding Energy (eV)**	**Peak Area**	**At%**
15.7	Au ($4f_{7/2}$)	83.35	846.82	34.51
84.3	Ni ($2p_{3/2}$)	851.54	1606.87	65.49
34.6	Au ($4f_{7/2}$)	83.81	1414.24	67.27
65.4	Ni ($2p_{3/2}$)	852.92	688.21	32.73
54.3	Au ($4f_{7/2}$)	83.54	27471.33	88.92
45.7	Ni ($2p_{3/2}$)	851.91	308.09	11.08
79.4	Au ($4f_{7/2}$)	83.63	2306.98	92.61
20.6	Ni ($2p_{3/2}$)	853.28	184.04	7.39
89.5	Au ($4f_{7/2}$)	83.63	2424.05	96.96
10.5	Ni ($2p_{3/2}$)	852.92	76.05	3.04

Table **9** A summary of the XPS data analysis showing core level position, area of the Au($4f_{7/2}$) and Cu ($2p_{3/2}$) peaks and the concentration of each element calculated in atomic percentage in the unannealed Au-Cu alloy (RT).

EDX Cu at. %	**Transition**	**Binding Energy (eV)**	**Peak Area**	**At%**
92.7	Au ($4f_{7/2}$)	84.00	5338.94	91.08
7.3	Cu ($2pf_{3/2}$)	932.05	522.69	8.92
80.2	Au ($4f_{7/2}$)	83.63	5102.27	78.68
19.8	Cu ($2p_{3/2}$)	931.78	1382.74	21.32
58.5	Au ($4f_{7/2}$)	83.27	4061.31	57.01
41.5	Cu ($2p_{3/2}$)	931.14	3062.24	42.99
27.8	Au ($4f_{7/2}$)	83.27	2426.05	29.70
72.2	Cu ($2p_{3/2}$)	931.04	5741.40	70.30
4.4	Au ($4f_{7/2}$)	83.08	701.41	9.35
95.6	Cu ($2p_{3/2}$)	931.04	6803.64	90.65

Table **10** A summary of XPS data analysis showing core level position, area of the Au ($4f_{7/2}$) and Cu ($2p_{3/2}$) peaks and the concentration of each element calculated in atomic percentage in the annealed Au-Cu alloy (300 ^{o}C for 15 min).

EDX Cu at. %	**Transition**	**Binding Energy (eV)**	**Peak Area**	**At%**
92.7	Au ($4f_{7/2}$)	84.18	3881.78	86.06
7.3	Cu ($2pf_{3/2}$)	932.42	628.84	13.94
80.2	Au ($4f_{7/2}$)	84.27	4480.07	76.26
19.8	Cu ($2p_{3/2}$)	932.24	1394.80	23.74

58.5	Au ($4f_{7/2}$)	84.27	4061.31	59.75
41.5	Cu ($2p_{3/2}$)	932.33	3062.24	42.25
27.8	Au ($4f_{7/2}$)	84.37	3217.59	35.55
72.2	Cu ($2p_{3/2}$)	932.33	5834.33	64.45
4.4	Au ($4f_{7/2}$)	84.64	1065.95	12.03
95.6	Cu ($2p_{3/2}$)	932.42	7791.48	87.97

Table **11** A summary of XPS data analysis showing core level position, area of the Au ($4f_{7/2}$) and Pt ($4f_{7/2}$) peaks and the concentration of each element calculated in atomic percentage in the unannealed Au-Pt alloy (RT).

EDX Pt at. %	**Transition**	**Binding Energy (eV)**	**Peak Area**	**At%**
96.4	Au ($4f_{7/2}$)	84.00	2434.27	94.79
3.6	Pt ($4f_{7/2}$)	71.65	133.72	5.21
75	Au ($4f_{7/2}$)	83.54	2014.31	84.03
25	Pt ($4f_{7/2}$)	71.5	382.93	15.97
47.8	Au ($4f_{7/2}$)	83.45	947.92	56.94
52.2	Pt ($4f_{7/2}$)	70.72	716.71	43.06
11.2	Au ($4f_{7/2}$)	82.90	387.42	26.68
88.8	Pt ($4f_{7/2}$)	70.60	1064.85	73.32
3.3	Au ($4f_{7/2}$)	82.99	33.98	3.98
96.7	Pt ($4f_{7/2}$)	70.54	814.35	96.02

Table **12** XPS Data analysis showing core level locations, area of the Au ($4f_{7/2}$) and Pt ($4f_{7/2}$) peaks and the concentration of each element calculated in atomic percentage in the annealed Au-Pt alloy (300 ^{o}C for 15 min).

EDX Pt at %	**Transition**	**Binding Energy (eV)**	**Peak Area**	**At%**
96.4	Au ($4f_{7/2}$)	84.09	2421.12	90.41
3.6	Pt ($4f_{7/2}$)	74.38	256.83	9.59
75	Au ($4f_{7/2}$)	83.90	1930.26	78.96
25	Pt ($4f_{7/2}$)	74.05	514.22	21.04
47.8	Au ($4f_{7/2}$)	83.90	825.31	46.85
52.2	Pt ($4f_{7/2}$)	71.12	936.32	53.15
11.2	Au ($4f_{7/2}$)	83.90	355.67	21.34
88.8	Pt ($4f_{7/2}$)	71.21	1310.62	78.66
3.3	Au ($4f_{7/2}$)	83.90	23.50	2.53
96.7	Pt ($4f_{7/2}$)	71.48	905.20	97.47

List of References

1. Merino-Jimenez, I.; Leon, C. P. d.; Walsh, F. C., The effect of surfactants on the kinetics of borohydride oxidation and hydrolysis in the DBFC. *Electrochimica Acta* **2014,** *133* (0), 539-545.

2. Liu, B. H.; Li, Z. P.; Suda, S., Electrocatalysts for the anodic oxidation of borohydrides. *Electrochimica Acta* **2004,** *49* (19), 3097-3105.

3. Gyenge, E.; Atwan, M.; Northwood, D., Electrocatalysis of borohydride oxidation on colloidal Pt and Pt-alloys (Pt-Ir, Pt-Ni, and Pt-Au) and application for direct borohydride fuel cell anodes. *Journal of The Electrochemical Society* **2006,** *153* (1), A150-A158.

4. Höök, M.; Tang, X., Depletion of fossil fuels and anthropogenic climate change—A review. *Energy Policy* **2013,** *52*, 797-809.

5. Arioglu, M.; Selam, A. A.; Firat, S., Renewable Energy Sources: Comparison of their Use and Respective Policies on a Global Scale. 2016.

6. Chorkendorff, I.; Niemantsverdriet, J. W., *Concepts of modern catalysis and kinetics*. John Wiley & Sons: 2017.

7. Van Leeuwen, P. W., *Homogeneous catalysis: understanding the art*. Springer Science & Business Media: 2006.

8. Bravo-Suárez, J. J.; Chaudhari, R. V.; Subramaniam, B., Design of heterogeneous catalysts for fuels and chemicals processing: An overview. In *Novel materials for catalysis and fuels processing*, ACS Publications: 2013; pp 3-68.

9. Groß, A., Reactivity of bimetallic systems studied from first principles. *Topics in Catalysis* **2006,** *37* (1), 29-39.

10. Sakong, S.; Mosch, C.; Groß, A., CO adsorption on Cu–Pd alloy surfaces: ligand versus ensemble effects. *Physical Chemistry Chemical Physics* **2007,** *9* (18), 2216-2225.

11. Hammer, B.; Nørskov, J., Electronic factors determining the reactivity of metal surfaces. *Surface Science* **1995,** *343* (3), 211-220.

12. Bligaard, T.; Nørskov, J. K., Ligand effects in heterogeneous catalysis and electrochemistry. *Electrochimica Acta* **2007,** *52* (18), 5512-5516.

13. Nørskov, J. K.; Bligaard, T.; Logadottir, A.; Kitchin, J.; Chen, J. G.; Pandelov, S.; Stimming, U., Trends in the exchange current for hydrogen evolution. *J. Electrochem. Soc.* **2005,** *152* (3), J23-J26.

14. Al-Odail, F. A.; Anastasopoulos, A.; Hayden, B. E., The hydrogen evolution reaction and hydrogen oxidation reaction on thin film PdAu alloy surfaces. *Physical Chemistry Chemical Physics* **2010,** *12* (37), 11398-11406.

15. Wang, Y.; Chen, K. S.; Mishler, J.; Cho, S. C.; Adroher, X. C., A review of polymer electrolyte membrane fuel cells: Technology, applications, and needs on fundamental research. *Applied Energy* **2011,** *88* (4), 981-1007.

16. Boudghene Stambouli, A.; Traversa, E., Fuel cells, an alternative to standard sources of energy. *Renewable and Sustainable Energy Reviews* **2002,** *6* (3), 295-304.

17. Grove, W. R., XXIV. On voltaic series and the combination of gases by platinum. *The London, Edinburgh, and Dublin Philosophical Magazine and Journal of Science* **1839,** *14* (86-87), 127-130.

18. Ma, J.; Choudhury, N. A.; Sahai, Y., A comprehensive review of direct borohydride fuel cells. *Renewable and Sustainable Energy Reviews* **2010,** *14* (1), 183-199.

19. Li, Q. F.; He, R. H.; Gao, J. A.; Jensen, J. O.; Bjerrum, N. J., The CO poisoning effect in PEMFCs operational at temperatures up to 200 degrees C. *Journal of the Electrochemical Society* **2003,** *150* (12), A1599-A1605.

20. Gottesfeld, S.; Pafford, J., A new approach to the problem of carbon monoxide poisoning in fuel cells operating at low temperatures. *Journal of the Electrochemical Society* **1988,** *135* (10), 2651-2652.

21. Iulianelli, A.; Ribeirinha, P.; Mendes, A.; Basile, A., Methanol steam reforming for hydrogen generation via conventional and membrane reactors: a review. *Renewable and Sustainable Energy Reviews* **2014,** *29*, 355-368.

22. Dalebrook, A. F.; Gan, W.; Grasemann, M.; Moret, S.; Laurenczy, G., Hydrogen storage: beyond conventional methods. *Chemical Communications* **2013,** *49* (78), 8735-8751.

23. Liu, B. H.; Li, Z. P.; Arai, K.; Suda, S., Performance improvement of a micro borohydride fuel cell operating at ambient conditions. *Electrochimica Acta* **2005,** *50* (18), 3719-3725.

24. Choudhury, N. A.; Raman, R. K.; Sampath, S.; Shukla, A. K., An alkaline direct borohydride fuel cell with hydrogen peroxide as oxidant. *Journal of Power Sources* **2005,** *143* (1–2), 1-8.

25. Aricò, A. S.; Srinivasan, S.; Antonucci, V., DMFCs: from fundamental aspects to technology development. *Fuel Cells* **2001,** *1* (2), 133-161.

26. Qi, Z.; Kaufman, A., Open circuit voltage and methanol crossover in DMFCs. *J. Power Sources* **2002,** *110* (1), 177-185.

27. Scott, K.; Taama, W.; Argyropoulos, P.; Sundmacher, K., The impact of mass transport and methanol crossover on the direct methanol fuel cell. *J. Power Sources* **1999,** *83* (1-2), 204-216.

28. Ferguson, A.; Ugursal, V. I., Fuel cell modelling for building cogeneration applications. *J. Power Sources* **2004,** *137* (1), 30-42.

29. Demirci, U. B., Direct borohydride fuel cell: Main issues met by the membrane–electrodes-assembly and potential solutions. *Journal of Power Sources* **2007,** *172* (2), 676-687.

30. Duteanu, N.; Vlachogiannopoulos, G.; Shivhare, M. R.; Yu, E. H.; Scott, K., A parametric study of a platinum ruthenium anode in a direct borohydride fuel cell. *J Appl Electrochem* **2007,** *37* (9), 1085-1091.

31. Li, Z. P.; Liu, B. H.; Arai, K.; Suda, S., Development of the direct borohydride fuel cell. *Journal of Alloys and Compounds* **2005,** *404–406* (0), 648-652.

32. Schlesinger, H. I.; Brown, H. C.; Finholt, A. E.; Gilbreath, J. R.; Hoekstra, H. R.; Hyde, E. K., Sodium borohydride, its hydrolysis and its use as a reducing agent and in the generation of hydrogen1. *Journal of the American Chemical Society* **1953,** *75* (1), 215-219.

33. Amendola, S. C.; Sharp-Goldman, S. L.; Janjua, M. S.; Spencer, N. C.; Kelly, M. T.; Petillo, P. J.; Binder, M., A safe, portable, hydrogen gas generator using aqueous borohydride solution and Ru catalyst. *International Journal of Hydrogen Energy* **2000,** *25* (10), 969-975.

34. Elder, J. P.; Hickling, A., Anodic behaviour of the borohydride ion. *Transactions of the Faraday Society* **1962,** *58* (0), 1852-1864.

35. de Leon, C. P.; Walsh, F. C.; Pletcher, D.; Browning, D. J.; Lakeman, J. B., Direct borohydride fuel cells. *Journal of Power Sources* **2006,** *155* (2), 172-181.

36. Morris, J. H.; Gysling, H. J.; Reed, D., Electrochemistry of boron compounds. *Chemical Reviews* **1985,** *85* (1), 51-76.

37. Liu, B. H.; Suda, S., Hydrogen storage alloys as the anode materials of the direct borohydride fuel cell. *Journal of Alloys and Compounds* **2008,** *454* (1), 280-285.

38. Wang, K.; Lu, J.; Zhuang, L., A Current−Decomposition Study of the Borohydride Oxidation Reaction at Ni Electrodes. *The Journal of Physical Chemistry C* **2007,** *111* (20), 7456-7462.

39. Gyenge, E., Electrooxidation of borohydride on platinum and gold electrodes: implications for direct borohydride fuel cells. *Electrochimica Acta* **2004,** *49* (6), 965-978.

40. Feng, R.; Dong, H.; Cao, Y.; Ai, X.; Yang, H., Agni-catalyzed anode for direct borohydride fuel cells. *International Journal of Hydrogen Energy* **2007,** *32* (17), 4544-4549.

41. Gardiner, J. A.; Collat, J. W., Polarography of the tetrahydroborate ion. The effect of hydrolysis on the system. *Inorganic chemistry* **1965,** *4* (8), 1208-1212.

42. Santos, D. M. F.; Sequeira, C. A. C., Zinc anode for direct borohydride fuel cells. *Journal of The Electrochemical Society* **2010,** *157* (1), B13-B19.

43. Simões, M.; Baranton, S.; Coutanceau, C., Electrooxidation of Sodium Borohydride at Pd, Au, and PdxAu1−x Carbon-Supported Nanocatalysts. *The Journal of Physical Chemistry C* **2009,** *113* (30), 13369-13376.

44. Liu, B. H.; Li, Z. P.; Suda , S., Anodic oxidation of alkali borohydrides catalyzed by nickel. *Journal of The Electrochemical Society* **2003,** *150* (3), A398-A402.

45. Duan, D. H.; Zhao, Y. F.; Liu, S. B.; Wu, A. L. In *Electrochemical Oxidation of Borohydride on Cu Electrode*, Advanced Materials Research, Trans Tech Publ: 2012; pp 3264-3267.

46. Indig, M. E.; Snyder, R. N., Sodium borohydride, an interesting anodic fuel (1). *Journal of The Electrochemical Society* **1962,** *109* (11), 1104-1106.

47. Okinaka, Y., An Electrochemical Study of Electroless Gold-Deposition Reaction. *J. Electrochem. Soc.* **1973,** *120* (6), 739-744.

48. Mirkin, M. V.; Yang, H. J.; Bard, A. J., Borohydride oxidation at a gold electrode. *Journal of the Electrochemical Society* **1992,** *139* (8), 2212-2217.

49. Merino Jimenez, I. Investigation of the use of sodium borohydride for fuel cells. University of Southampton, 2013.

50. Chatenet, M.; Micoud, F.; Roche, I.; Chainet, E., Kinetics of sodium borohydride direct oxidation and oxygen reduction in sodium hydroxide electrolyte: Part I. BH4− electro-oxidation on Au and Ag catalysts. *Electrochimica Acta* **2006,** *51* (25), 5459-5467.

51. Amendola, S. C.; Onnerud, P.; Kelly, M. T.; Petillo, P. J.; Sharp-Goldman, S. L.; Binder, M., A novel high power density borohydride-air cell. *Journal of Power Sources* **1999,** *84* (1), 130-133.

52. Atwan, M. H.; Macdonald, C. L. B.; Northwood, D. O.; Gyenge, E. L., Colloidal Au and Au-alloy catalysts for direct borohydride fuel cells: Electrocatalysis and fuel cell performance. *Journal of Power Sources* **2006,** *158* (1), 36-44.

53. Pei, F.; Wang, Y.; Wang, X.; He, P.; Chen, Q.; Wang, X.; Wang, H.; Yi, L.; Guo, J., Performance of supported Au–Co alloy as the anode catalyst of direct borohydride-hydrogen peroxide fuel cell. *International Journal of Hydrogen Energy* **2010,** *35* (15), 8136-8142.

54. Yi, L.; Wei, W.; Zhao, C.; Tian, L.; Liu, J.; Wang, X., Enhanced activity of Au–Fe/C anodic electrocatalyst for direct borohydride-hydrogen peroxide fuel cell. *J. Power Sources* **2015,** *285*, 325-333.

55. He, P.; Wang, X.; Liu, Y.; Liu, X.; Yi, L., Comparison of electrocatalytic activity of carbon-supported Au–M (M = Fe, Co, Ni, Cu and Zn) bimetallic nanoparticles for direct borohydride fuel cells. *International Journal of Hydrogen Energy* **2012,** *37* (16), 11984-11993.

56. Oliveira, R. C.; Vasić, M.; Santos, D. M.; Babić, B.; Hercigonja, R.; Sequeira, C. A.; Šljukić, B., Performance assessment of a direct borohydride-peroxide fuel cell with Pd-impregnated faujasite X zeolite as anode electrocatalyst. *Electrochimica Acta* **2018,** *269*, 517-525.

57. Hernández-Ramírez, V.; Alatorre-Ordaz, A.; de Lourdes Yépez-Murrieta, M.; Ibanez, J. G.; Ponce-de-León, C.; Walsh, F. C., Oxidation of the Borohydride Ion at Silver Nanoparticles on a Glassy Carbon Electrode (GCE) Using Pulsed Potential Techniques. *ECS Transactions* **2009,** *20* (1), 211-225.

58. Hosseini, M. G.; Abdolmaleki, M.; Ashrafpoor, S., Electrocatalytic Oxidation of Sodium Borohydride on a Nanoporous Ni/Zn-Ni Electrode. *Chinese Journal of Catalysis* **2012,** *33* (11–12), 1817-1824.

59. He, P.; Wang, X.; Liu, Y.; Liu, X.; Yi, L., Comparison of electrocatalytic activity of carbon-supported Au–M (M= Fe, Co, Ni, Cu and Zn) bimetallic nanoparticles for direct borohydride fuel cells. *international journal of hydrogen energy* **2012,** *37* (16), 11984-11993.

60. Moreno, J. E. D.; García-Rodríguez, D. E.; Ordaz, M. A. A.; Esquivel, I. R. G.; de León, C. P.; Herrasti, P.; Mendoza-Huizar, L. H. In *Comparative Study of Borohydride Oxidation, at Polycrystalline and Nanostructured Copper Electrodes*, Meeting Abstracts, The Electrochemical Society: 2014; pp 2253-2253.

61. Merrifield, R. B., Solid phase peptide synthesis. I. The synthesis of a tetrapeptide. *Journal of the American Chemical Society* **1963,** *85* (14), 2149-2154.

62. Hanak, J. J., The “multiple-sample concept” in materials research: Synthesis, compositional analysis and testing of entire multicomponent systems. *Journal of Materials Science* **1970,** *5* (11), 964-971.

63. Xiang, X.-D.; Sun, X.; Briceño, G.; Lou, Y.; Wang, K.-A.; Chang, H.; Wallace-Freedman, W. G.; Chen, S.-W.; Schultz, P. G., A combinatorial approach to materials discovery. *Science* **1995,** *268* (5218), 1738-1740.

64. Schultz, P. G.; Xiang, X.-D., Combinatorial approaches to materials science. *Current Opinion in Solid State and Materials Science* **1998,** *3* (2), 153-158.

65. Xiang, X. D.; Schultz, P. G., The combinatorial synthesis and evaluation of functional materials. *Physica C: Superconductivity* **1997,** *282–287, Part 1*, 428-430.

66. Cooper, J. S.; Zhang, G.; McGinn, P. J., Plasma sputtering system for deposition of thin film combinatorial libraries. *Review of Scientific Instruments* **2005,** *76* (6), 062221.

67. Danielson, E.; Golden, J. H.; McFarland, E. W.; Reaves, C. M.; Weinberg, W. H.; Wu, X. D., A combinatorial approach to the discovery and optimization of luminescent materials. *Nature* **1997,** *389* (6654), 944-948.

68. Senkan, S., Combinatorial heterogeneous catalysis—a new path in an old field. *Angewandte Chemie International Edition* **2001,** *40* (2), 312-329.

69. Reddington, E.; Sapienza, A.; Gurau, B.; Viswanathan, R.; Sarangapani, S.; Smotkin, E. S.; Mallouk, T. E., Combinatorial electrochemistry: a highly parallel, optical screening method for discovery of better electrocatalysts. *Science* **1998,** *280* (5370), 1735-1737.

70. Prochaska, M.; Jin, J.; Rochefort, D.; Zhuang, L.; DiSalvo, F. J.; Abruña, H. D.; Van Dover, R., High throughput screening of electrocatalysts for fuel cell applications. *Review of scientific instruments* **2006,** *77* (5), 054104.

71. Simon, U.; Sanders, D.; Jockel, J.; Heppel, C.; Brinz, T., Design strategies for multielectrode arrays applicable for high-throughput impedance spectroscopy on novel gas sensor materials. *Journal of combinatorial chemistry* **2002,** *4* (5), 511-515.

72. Jiang, R.; Chu, D., A combinatorial approach toward electrochemical analysis. *Journal of Electroanalytical Chemistry* **2002,** *527* (1), 137-142.

73. Sullivan, M. G.; Utomo, H.; Fagan, P. J.; Ward, M. D., Automated electrochemical analysis with combinatorial electrode arrays. *Analytical chemistry* **1999,** *71* (19), 4369-4375.

74. Warren, C. J.; Haushalter, R. C.; Matsiev, L., Electrochemical deposition and testing system consisting of individually addressable electrode arrays to create a library of semiconductor-containing materials on said array. Google Patents: 2001.

75. Anastasopoulos, A.; Hannah, L.; Hayden, B. E., High throughput optimisation of PdCu alloy electrocatalysts for the reduction of nitrate ions. *Journal of Catalysis* **2013,** *305*, 27-35.

76. Al-Odail, F. A.; Anastasopoulos, A.; Hayden, B. E., Hydrogen evolution and hydrogen oxidation on palladium bismuth alloys. *Topics in Catalysis* **2011,** *54* (1-4), 77-82.

77. Guerin, S.; Hayden, B. E., Physical vapor deposition method for the high-throughput synthesis of solid-state material libraries. *Journal of Combinatorial Chemistry* **2005,** *8* (1), 66-73.

78. Guerin, S.; Hayden, B. E.; Lee, C. E.; Mormiche, C.; Owen, J. R.; Russell, A. E.; Theobald, B.; Thompsett, D., Combinatorial electrochemical screening of fuel cell electrocatalysts. *Journal of combinatorial chemistry* **2004,** *6* (1), 149-158.

79. Guerin, S.; Hayden, B. E.; Lee, C. E.; Mormiche, C.; Russell, A. E., High-throughput synthesis and screening of ternary metal alloys for electrocatalysis. *The Journal of Physical Chemistry B* **2006,** *110* (29), 14355-14362.

80. An introduction to surface analysis by XPS and AES. *Scitech Book News* Dec 2003, 2003.

81. Daubinger, P.; Kieninger, J.; Unmüssig, T.; Urban, G. A., Electrochemical characteristics of nanostructured platinum electrodes–a cyclic voltammetry study. *Physical Chemistry Chemical Physics* **2014,** *16* (18), 8392-8399.

82. Finkelstein, D. A.; Mota, N. D.; Cohen, J. L.; Abruña, H. D., Rotating disk electrode (RDE) investigation of BH4− and BH3OH− electro-oxidation at Pt and Au: implications for BH4− fuel cells. *The Journal of Physical Chemistry C* **2009,** *113* (45), 19700-19712.

83. He, P.; Wang, Y.; Wang, X.; Pei, F.; Wang, H.; Liu, L.; Yi, L., Investigation of carbon supported Au–Ni bimetallic nanoparticles as electrocatalyst for direct borohydride fuel cell. *Journal of Power Sources* **2011,** *196* (3), 1042-1047.

84. Grinberg, V. A.; Mayorova, N. A.; Korlyukov, A. A.; Pasynskii, A. A., Direct borohydride oxidation electrocatalysts based on Ni-Ru/C and Ni-Ru-F/C alloys. *Russian Journal of Electrochemistry* **2010,** *46* (11), 1289-1296.

85. Aytaç, A.; Gürbüz, M.; Sanli, A. E., Electrooxidation of hydrogen peroxide and sodium borohydride on Ni deposited carbon fiber electrode for alkaline fuel cells. *International Journal of Hydrogen Energy* **2011,** *36* (16), 10013-10021.

86. Molina Concha, B.; Chatenet, M., Direct oxidation of sodium borohydride on Pt, Ag and alloyed Pt–Ag electrodes in basic media. Part I: Bulk electrodes. *Electrochimica Acta* **2009,** *54* (26), 6119-6129.

87. ZAAFARANY, I.; BOLLER, H., Electrochemical behavior of copper electrode in sodium hydroxide solutions. *Curr World Environ* **2009,** *4* (2), 8.

88. Donato Moreno, J. E.; García-Rodríguez, D. E.; Alatorre Ordaz, M. A.; Galindo Esquivel, I. R.; Ponce de León, C.; Herrasti, P.; Mendoza-Huizar, L. H., Comparative Study of Borohydride Oxidation, at Polycrystalline and Nanostructured Copper Electrodes. *Meeting Abstracts* **2014,** *MA2014-02* (49), 2253.

89. Yu, W.; Porosoff, M. D.; Chen, J. G., Review of Pt-based bimetallic catalysis: from model surfaces to supported catalysts. *Chemical Reviews* **2012,** *112* (11), 5780-5817.

90. Baker, H.; Okamoto, H., ASM Handbook, Volume 03 - Alloy Phase Diagrams. ASM International.

91. Wang, J.; Lu, X.-G.; Sundman, B.; Su, X., Thermodynamic assessment of the Au–Ni system. *Calphad* **2005,** *29* (4), 263-268.

92. Bienzle, M.; Oishi, T.; Sommer, F., Thermodynamics and local atomic arrangements of gold-nickel alloys. *Journal of Alloys and Compounds* **1995,** *220* (1–2), 182-188.

93. Wolverton, C.; Zunger, A., Ni-Au: A testing ground for theories of phase stability. *Computational materials science* **1997,** *8* (1), 107-121.

94. Clinton, J. R.; Tyler, E.; Luo, H., Electrical and magnetic properties of Au-Ni alloys. *Journal of Physics F: Metal Physics* **1974,** *4* (8), 1162.

95. Abadias, G.; Schuster, I.; Marty, A.; Gilles, B., Epitaxial-strain-stabilized ordering in Au 1− x Ni x alloy thin films grown by MBE. *Physical Review B* **2000,** *61* (10), 6495-6506.

96. Zhenyin, Y.; Lichtenwalner, D. J.; Morris, A. S.; Krim, J.; Kingon, A. I., Comparison of Au and Au–Ni alloys as contact materials for MEMS switches. *Microelectromechanical Systems, Journal of* **2009,** *18* (2), 287-295.

97. Zafeiratos, S.; Kennou, S., Gold/nickel ultrathin bimetallic overlayers on yttria-stabilized ZrO2 (100). *The Journal of Physical Chemistry B* **2002,** *106* (1), 41-48.

98. Yang, F.; Yao, Y.; Yan, Z.; Min, H.; Goodman, D. W., Preparation and characterization of planar Ni–Au bimetallic model catalysts. *Applied Surface Science* **2013,** *283*, 263-268.

99. Chin, Y.-H.; King, D. L.; Roh, H.-S.; Wang, Y.; Heald, S. M., Structure and reactivity investigations on supported bimetallic AuNi catalysts used for hydrocarbon steam reforming. *Journal of Catalysis* **2006,** *244* (2), 153-162.

100. Keane, M. A.; Gómez-Quero, S.; Cárdenas-Lizana, F.; Shen, W., Alumina-Supported Ni–Au: Surface Synergistic Effects in Catalytic Hydrodechlorination. *ChemCatChem* **2009,** *1* (2), 270-278.

101. Knudsen, J.; Merte, L. R.; Peng, G.; Vang, R. T.; Resta, A.; Lægsgaard, E.; Andersen, J. N.; Mavrikakis, M.; Besenbacher, F., Low-temperature CO oxidation on Ni (111) and on a Au/Ni (111) surface alloy. *ACS Nano* **2010,** *4* (8), 4380-4387.

102. Zhou, S.; Yin, H.; Schwartz, V.; Wu, Z.; Mullins, D.; Eichhorn, B.; Overbury, S. H.; Dai, S., In situ phase separation of NiAu alloy nanoparticles for preparing highly active Au/NiO CO oxidation catalysts. *ChemPhysChem* **2008,** *9* (17), 2475-2479.

103. Tamašauskaitė-Tamašiūnaitė, L.; Balčiūnaitė, A.; Čekavičiūtė, R.; Selskis, A., Investigation of titanium supported nanostructured Au-Ni and Pt-Ni thin layers as electrocatalysts for DBFC. *Journal of The Electrochemical Society* **2012,** *159* (5), B611-B618.

104. Waseda, Y.; Matsubara, E.; Shinoda, K., Diffraction from Polycrystalline Samples and Determination of Crystal Structure. In *X-Ray Diffraction Crystallography: Introduction, Examples and Solved Problems*, Springer Berlin Heidelberg: Berlin, Heidelberg, 2011; pp 107-167.

105. Haas, P.; Tran, F.; Blaha, P., Calculation of the lattice constant of solids with semilocal functionals. *Physical Review B* **2009,** *79* (8), 085104.

106. Davey, W. P., Precision Measurements of the Lattice Constants of Twelve Common Metals. *Physical Review* **1925,** *25* (6), 753-761.

107. Asami, K., A precisely consistent energy calibration method for X-ray photoelectron spectroscopy. *Journal of Electron Spectroscopy and Related Phenomena* **1976,** *9* (5), 469-478.

108. Nemoshalenko, V.; Didyk, V.; Krivitskii, V.; Senekevich, A., Study of the Change State of Atoms in Iron, Cobalt and Nickel Phosphides. *Zhurnal Neorganicheskoi Khimii* **1983,** *28*, 2182.

109. Weininger, J.; Breiter, M., Hydrogen evolution and surface oxidation of nickel electrodes in alkaline solution. *J. Electrochem. Soc.* **1964,** *111* (6), 707-712.

110. Grubač, Z.; Petrović, Ž.; Katić, J.; Metikoš-Huković, M.; Babić, R., The electrochemical behaviour of nanocrystalline nickel: A comparison with polycrystalline nickel under the same experimental condition. *Journal of electroanalytical chemistry* **2010,** *645* (2), 87-93.

111. Motori, A.; Sandrolini, F.; Davolio, G., Electrical properties of nickel hydroxide for alkaline cell systems. *J. Power Sources* **1994,** *48* (3), 361-370.

112. Dmochowska, M.; Czerwiński, A., Behavior of a nickel electrode in the presence of carbon monoxide. *Journal of Solid State Electrochemistry* **1998,** *2* (1), 16-23.

113. Alsabet, M.; Grdeń, M.; Jerkiewicz, G., Electrochemical growth of surface oxides on nickel. Part 3: Formation of β-NiOOH in relation to the polarization potential, polarization time, and temperature. *Electrocatalysis* **2015,** *6* (1), 60-71.

114. Pissinis, D. E.; Sereno, L. E.; Marioli, J. M., Utilization of special potential scan programs for cyclic voltammetric development of different nickel oxide-hydroxide species on Ni based electrodes. **2012**.

115. Okamoto, H.; Chakrabarti, D.; Laughlin, D.; Massalski, T., The Au− Cu (gold-copper) system. *Journal of Phase Equilibria* **1987,** *8* (5), 454-474.

116. Silva, K. S. B. D.; Gentle, A.; Arnold, M.; Keast, V. J.; Cortie, M. B., Dielectric function and its predicted effect on localized plasmon resonances of equiatomic Au–Cu. *Journal of Physics D: Applied Physics* **2015,** *48* (21), 215304.

117. Tynkova, A.; Katona, G. L.; Langer, G. A.; Sidorenko, S. I.; Voloshko, S. M.; Beke, D. L., Formation of CuxAu1-x phases by cold homogenization of Au/Cu nanocrystalline thin films. *Beilstein Journal of Nanotechnology* **2014,** *5* (1), 1491-1500.

118. Losch, W.; Kirschner, J., Surface composition of polycrystalline Au–Cu alloys as a function of temperature. *Journal of Vacuum Science and Technology* **1978,** *15* (4), 1541-1548.

119. Völker, E.; Williams, F. J.; Calvo, E. J.; Jacob, T.; Schiffrin, D. J., O 2 induced Cu surface segregation in Au–Cu alloys studied by angle resolved XPS and DFT modelling. *Physical Chemistry Chemical Physics* **2012,** *14* (20), 7448-7455.

120. König, D.; Richter, K.; Siegel, A.; Mudring, A. V.; Ludwig, A., High-Throughput Fabrication of Au–Cu Nanoparticle Libraries by Combinatorial Sputtering in Ionic Liquids. *Advanced Functional Materials* **2014,** *24* (14), 2049-2056.

121. Liu, X.; Wang, A.; Zhang, T.; Su, D.-S.; Mou, C.-Y., Au–Cu alloy nanoparticles supported on silica gel as catalyst for CO oxidation: Effects of Au/Cu ratios. *Catalysis today* **2011,** *160* (1), 103-108.

122. Liu, X.; Wang, A.; Li, L.; Zhang, T.; Mou, C.-Y.; Lee, J.-F., Structural changes of Au–Cu bimetallic catalysts in CO oxidation: in situ XRD, EPR, XANES, and FT-IR characterizations. *Journal of catalysis* **2011,** *278* (2), 288-296.

123. Bauer, J. C.; Mullins, D.; Li, M.; Wu, Z.; Payzant, E. A.; Overbury, S. H.; Dai, S., Synthesis of silica supported AuCu nanoparticle catalysts and the effects of pretreatment conditions for the CO oxidation reaction. *Physical Chemistry Chemical Physics* **2011,** *13* (7), 2571-2581.

124. Della Pina, C.; Falletta, E.; Rossi, M., Highly selective oxidation of benzyl alcohol to benzaldehyde catalyzed by bimetallic gold–copper catalyst. *Journal of Catalysis* **2008,** *260* (2), 384-386.

125. Li, W.; Wang, A.; Liu, X.; Zhang, T., Silica-supported Au–Cu alloy nanoparticles as an efficient catalyst for selective oxidation of alcohols. *Applied Catalysis A: General* **2012,** *433*, 146-151.

126. Yi, L.; Song, Y.; Liu, X.; Wang, X.; Zou, G.; He, P.; Yi, W., High activity of Au–Cu/C electrocatalyst as anodic catalyst for direct borohydride-hydrogen peroxide fuel cell. *international journal of hydrogen energy* **2011,** *36* (24), 15775-15782.

127. Tamašauskaitė-Tamašiūnaitė, L.; Balčiūnaitė, A.; Zabielaitė, A.; Stankevičienė, I.; Kepenienė, V.; Selskis, A.; Juškėnas, R.; Norkus, E., Investigation of electrocatalytic activity of the nanostructured Au–Cu catalyst deposited on the titanium surface towards borohydride oxidation. *Journal of Electroanalytical Chemistry* **2013,** *700*, 1-7.

128. Wang, L.; Chen, H.; Chen, M., Facile synthesis and characterization of Au–Cu, Pt–Cu nanotubes by sacrificial template method. *Materials Research Bulletin* **2014,** *53*, 185-189.

129. Elmer, J.; Palmer, T.; Specht, E. D., Direct observations of rapid diffusion of Cu in Au thin films using in situ x-ray diffraction. *Journal of Vacuum Science & Technology A: Vacuum, Surfaces, and Films* **2006,** *24* (4), 978-987.

130. Jones, R.; Stafford, F. E.; Whitmore, D., Mass spectrometric study of the thermodynamic properties of solid Au− Pt alloys. *Metallurgical and Materials Transactions B* **1970,** *1* (2), 403-413.

131. Brown, B.; Wolter, S. D.; Stoner, B. R.; Glass, J. T., Alloying effects of cosputtered gold-platinum thin films on the oxygen reduction reaction in acidic electrolyte. *J. Electrochem. Soc.* **2008,** *155* (8), B852-B859.

132. Mihut, C.; Descorme, C.; Duprez, D.; Amiridis, M. D., Kinetic and spectroscopic characterization of cluster-derived supported Pt–Au catalysts. *Journal of Catalysis* **2002,** *212* (2), 125-135.

133. Mott, D.; Luo, J.; Smith, A.; Njoki, P. N.; Wang, L.; Zhong, C.-J., Nanocrystal and surface alloy properties of bimetallic Gold-Platinum nanoparticles. *Nanoscale research letters* **2007,** *2* (1), 12.

134. Wanjala, B. N.; Luo, J.; Loukrakpam, R.; Fang, B.; Mott, D.; Njoki, P. N.; Engelhard, M.; Naslund, H. R.; Wu, J. K.; Wang, L., Nanoscale Alloying, Phase-Segregation, and Core− Shell Evolution of Gold− Platinum Nanoparticles and Their Electrocatalytic Effect on Oxygen Reduction Reaction. *Chemistry of Materials* **2010,** *22* (14), 4282-4294.

135. Skelton, D.; Tobin, R.; Lambert, D. K.; DiMaggio, C. L.; Fisher, G. B., A surface-science-based model for the selectivity of platinum–gold alloy electrodes in zirconia-based NOx sensors. *Sensors and Actuators B: Chemical* **2003,** *96* (1-2), 46-52.

136. Irissou, E.; Laplante, F.; Garbarino, S.; Chaker, M.; Guay, D., Structural and electrochemical characterization of metastable PtAu bulk and surface alloys prepared by crossed-beam pulsed laser deposition. *The Journal of Physical Chemistry C* **2010,** *114* (5), 2192-2199.

137. Kumar, S. S.; Phani, K., Exploration of unalloyed bimetallic Au–Pt/C nanoparticles for oxygen reduction reaction. *J. Power Sources* **2009,** *187* (1), 19-24.

138. Hernández-Fernández, P.; Rojas, S.; Ocón, P.; Gómez de La Fuente, J.; San Fabián, J.; Sanza, J.; Pena, M.; García-García, F.; Terreros, P.; Fierro, J., Influence of the preparation route of bimetallic Pt− Au nanoparticle electrocatalysts for the oxygen reduction reaction. *The Journal of Physical Chemistry C* **2007,** *111* (7), 2913-2923.

139. Lou, Y.; Maye, M. M.; Han, L.; Luo, J.; Zhong, C.-J., Gold–platinum alloy nanoparticle assembly as catalyst for methanol electrooxidation. *Chemical Communications* **2001,** (5), 473-474.

140. Suntivich, J.; Xu, Z.; Carlton, C. E.; Kim, J.; Han, B.; Lee, S. W.; Bonnet, N. p.; Marzari, N.; Allard, L. F.; Gasteiger, H. A., Surface composition tuning of Au–Pt bimetallic nanoparticles

for enhanced carbon monoxide and methanol electro-oxidation. *Journal of the American Chemical Society* **2013,** *135* (21), 7985-7991.

141. Du, C.; Gao, X.; Zhuang, Z.; Cheng, C.; Zheng, F.; Li, X.; Chen, W., Epitaxial growth of zigzag PtAu alloy surface on Au nano-pentagrams with enhanced Pt utilization and electrocatalytic performance toward ethanol oxidation reaction. *Electrochimica Acta* **2017,** *238*, 263-268.

142. Gan, Q.-M.; Tao, L.; Zhou, L.-N.; Zhang, X.-T.; Wang, S.; Li, Y.-J., Directional coalescence growth of ultralong Au 93 Pt 7 alloy nanowires and their superior electrocatalytic performance in ethanol oxidation. *Chemical Communications* **2016,** *52* (29), 5164-5166.

143. da Silva, S. G.; Silva, J. C. M.; Buzzo, G. S.; De Souza, R. F.; Spinacé, E. V.; Neto, A. O.; Assumpção, M. H., Electrochemical and fuel cell evaluation of PtAu/C electrocatalysts for ethanol electro-oxidation in alkaline media. *International Journal of Hydrogen Energy* **2014,** *39* (19), 10121-10127.

144. Iotov, P.; Kalcheva, S.; Kanazirski, I., On the enhanced electrocatalytic performance of PtAu alloys in borohydride oxidation. *Electrochimica Acta* **2013,** *108*, 540-546.

145. Kalcheva, S.; Kanazirski, I., KINETICS OF BOROHYDRIDE ELECTROOXIDATION: REVISITED. *Journal of Chemical Technology & Metallurgy* **2014,** *49* (6).

146. Tegou, A.; Armyanov, S.; Valova, E.; Steenhaut, O.; Hubin, A.; Kokkinidis, G.; Sotiropoulos, S., Mixed platinum–gold electrocatalysts for borohydride oxidation prepared by the galvanic replacement of nickel deposits. *Journal of Electroanalytical Chemistry* **2009,** *634* (2), 104-110.

147. Geng, X.; Zhang, H.; Ma, Y.; Zhong, H., Borohydride electrochemical oxidation on carbon-supported Pt-modified Au nanoparticles. *J. Power Sources* **2010,** *195* (6), 1583-1588.

148. Jusys, Z.; Behm, R. J., Borohydride electrooxidation over Pt/C, AuPt/C and Au/C catalysts: Partial reaction pathways and mixed potential formation. *Electrochemistry Communications* **2015,** *60*, 9-12.

149. Seah, M.; Smith, G.; Anthony, M., AES: Energy calibration of electron spectrometers. I—an absolute, traceable energy calibration and the provision of atomic reference line energies. *Surface and interface analysis* **1990,** *15* (5), 293-308.

150. Janin, E.; Björkqvist, M.; Grehk, T. M.; Göthelid, M.; Pradier, C. M.; Karlsson, U. O.; Rosengren, A., Hydrogen adsorption on the Pt(111)(3 × 3)R30°-Sn surface alloy studied by high resolution core level photoelectron spectroscopy. *Applied Surface Science* **1996,** *99* (4), 371-378.

151. Bard, A. J.; Fan, F. R. F.; Kwak, J.; Lev, O., Scanning electrochemical microscopy. Introduction and principles. *Analytical Chemistry* **1989,** *61* (2), 132-138.

152. Lam, V.; Kannangara, D.; Alfantazi, A.; Gyenge, E., Electrochemical quartz crystal microbalance study of borohydride electro-oxidation on Pt: the effect of borohydride concentration and thiourea adsorption. *The Journal of Physical Chemistry C* **2011,** *115* (6), 2727-2737.

153. Lima, F. H.; Pasqualeti, A. M.; Concha, M. B. M.; Chatenet, M.; Ticianelli, E. A., Borohydride electrooxidation on Au and Pt electrodes. *Electrochimica Acta* **2012,** *84*, 202-212.